


Fall 12-15-2018

Elevated Temperature Progressive Damage and Failure of Duplex Stainless Steel

Darren P. Luke

University of New Mexico - Main Campus

Follow this and additional works at: https://digitalrepository.unm.edu/ce_etds

 Part of the [Applied Mechanics Commons](#), [Computational Engineering Commons](#), [Heat Transfer, Combustion Commons](#), [Structural Engineering Commons](#), and the [Structural Materials Commons](#)

Recommended Citation

Luke, Darren P. "Elevated Temperature Progressive Damage and Failure of Duplex Stainless Steel." (2018).
https://digitalrepository.unm.edu/ce_etds/218

This Dissertation is brought to you for free and open access by the Engineering ETDs at UNM Digital Repository. It has been accepted for inclusion in Civil Engineering ETDs by an authorized administrator of UNM Digital Repository. For more information, please contact disc@unm.edu.

Darren P. Luke

Candidate

Civil Engineering

Department

This dissertation is approved, and it is acceptable in quality and form for publication:

Approved by the Dissertation Committee:

Dr. Tang-Tat Ng, Chairperson

Dr. Fernando Moreu

Dr. Yu-Lin Shen

Dr. Hugh Denham

ELEVATED TEMPERATURE PROGRESSIVE DAMAGE AND FAILURE OF DUPLEX STAINLESS STEEL

by

DARREN P. LUKE

B.S., Civil Engineering, University of New Mexico, 2004
M.S., Civil Engineering, University of New Mexico, 2006

DISSERTATION

Submitted in Partial Fulfillment of the
Requirements for the Degree of

**Doctor of Philosophy
Engineering**

The University of New Mexico
Albuquerque, New Mexico

December 2018

DEDICATIONS

To my wife, Emily, without your love, support and patience over the years this would not have been possible. You have been a pillar for our family, your accomplishments as a wife, mother and in your career are amazing. You are a true blessing, I love you!

To my son, Kaleb, and daughter, Amber, you bring great joy to my life and have made your mother and me very proud. To my late father, Larry, and to my mother, Vicky, you've always motivated me to work hard and I'm very grateful for your love and support.

ACKNOWLEDGEMENTS

First, I would like to thank Dr. Tang-Tat Ng for believing in my academic ability and providing me with the opportunity to attend graduate school which has led to an exciting career in scientific research. I would like to thank Dr. Fernando Moreu, Dr. Yu-Lin Shen and Dr. Hugh Denham for serving on my dissertation committee.

I would like to thank Stanford Research Institute, Rocky Mountain Laboratories, Thermophysical Properties Research Laboratory, Ball Aerospace and Technologies, and the Air Force Research Laboratory for their contributions to the experimental results found in this manuscript. In particular, I would like to thank Dr. Brian Hyde, Mrs. Courtney Lay, Dr. John Jungk, Dr. Dale Doering, Dr. Takao Kobayashi, and Mr. Robert Ulibarri for their contributions to the experimental efforts.

I would like to thank my colleagues Dr. Choon Tham and Mr. Hoang-Nam Nguyen who were instrumental in the pursuit of elevated temperature fracture research. I would also like to thank Mr. Jacob Koester for his extremely valuable contributions to this research and for his contribution to my career growth while we were both in our early careers at Ball Aerospace.

This work and educational opportunity would not have been possible without the support of the Air Force Research Laboratory, particularly Mr. Robert Roybal and Major Joshua Burger, and the Department of Civil Engineering at the University of New Mexico.

Darren P. Luke
University of New Mexico
December 2018

ELEVATED TEMPERATURE PROGRESSIVE DAMAGE AND FAILURE OF DUPLEX STAINLESS STEEL

by

DARREN P. LUKE

B.S., Civil Engineering, University of New Mexico, 2004

M.S., Civil Engineering, University of New Mexico, 2006

Ph.D., Engineering, University of New Mexico, 2018

ABSTRACT

Ductile failure of metals has been the focus of detailed research efforts both within academia and industry for many years since it is tremendously important for understanding the failure of structures under extreme loading conditions. However, a limited amount of research has been dedicated to elevated temperature ductile failure which is critical for evaluating catastrophic events such as industrial, structural or shipping vessel fires as well as high temperature applications in welding, machining and power generation. The research presented in this dissertation focuses on the structural response of a Duplex Stainless Steel material at elevated temperatures, the development of a calibrated continuum damage plasticity model, validation testing and assessment of the model for predicting the failure of loaded structures subjected to transient heating.

Rectangular cross-section tensile specimens with various edge notches were tested to measure the change in elastic modulus, yield strength, ultimate strength, and

ductility of duplex stainless steel at elevated temperatures up to 1000°C. The reduction in cross-sectional area during strain localization was measured using Digital Image Correlation which enabled direct calculation of true stress and strain. The yield and hardening curves were then used in conjunction with the load versus displacement curve to characterize a general continuum damage plasticity model. The damage initiation and evolution were calibrated to best fit the notched tensile specimen response. The known mesh dependency of modeling strain localization and failure in ductile metals was reduced using fracture energy defined by effective plastic displacement and considering the element size to be a “material property”.

Validation experiments were conducted using panel specimens under constant tensile load subjected to local transient heating. The panels were tested at several different heating rates and pre-loads. The characterized damage model was then used to simulate the panel experiments and the failure times and crack initiation locations were compared. The model captured crack initiation locations, observed near the edge of the heated zone, and predicted failure times within 8% for all cases.

A second validation experiment was used to evaluate the predictive capability for pressure vessel failure during rapid heating. The catastrophic failure of pressure vessels subjected to accidental fire has been shown to be very destructive when a boiling liquid expanding vapor explosion (BLEVE) occurs. Pressure vessel failure can occur in less than 20 minutes when exposed to fully engulfing fuel fires, resulting in a significant hazard for industrial fires in petroleum and chemical processing plants, among others. The experiments were designed to identify the critical pressure ratio when the failure mode

transitions from a local to catastrophic failure at a given heated zone size, providing insight into the criticality analysis of thermal protection system failure. The tests resulted in an empirical correlation between critical pressure ratio and heated zone ratio for potential application to other geometries and materials. The damage model was shown to be capable of predicting the failure time and temperature within 6% as well as the failure mode transition line. This is the first known capability presented in the literature for predicting local and catastrophic failure in un-cracked pressure vessels and pipelines due to localized heating, which has historically focused on the criticality of existing cracks under ambient conditions.

CONTENTS

DEDICATIONS	iii
ACKNOWLEDGEMENTS.....	iv
ABSTRACT.....	v
LIST OF FIGURES.....	xi
LIST OF TABLES.....	xviii
Chapter 1 : Introduction	1
1.1 Background and Motivation.....	1
1.2 Research Objectives	3
1.3 Structure of the Dissertation.....	5
Chapter 2 : Literature Review	7
2.1 Ductile Fracture Initiation Modeling.....	7
2.1.1 Uncoupled Void Growth Models for Fracture Initiation	8
2.1.2 Coupled Porous Metal Plasticity and Fracture Model.....	11
2.1.3 Cohesive Zone Fracture Models	14
2.1.4 Uncoupled Semi-Empirical Fracture Indicator Models	17
2.1.5 Continuum Damage Modeling for Ductile Fracture	20
2.1.6 Summary of Ductile Fracture Modeling for Un-cracked Bodies	25
2.2 Elevated Temperature Ductile Fracture.....	26
2.2.1 Elevated Temperature Plasticity	27
2.2.2 Elevated Temperature Fracture Initiation.....	36
Chapter 3 : Material Selection and Characterization	40
3.1 Composition and Microstructural Analysis	41
3.2 Thermal Properties at Elevated Temperatures.....	44
3.3 Thermal Expansion at Elevated Temperatures	47
3.4 Elastic Properties of DSS.....	48
3.5 Total Reflectance at Elevated Temperatures.....	50
3.6 Summary	52
Chapter 4 : Elevated Temperature Tensile Testing	53
4.1 Tensile Specimen Geometry	56
4.2 Tensile Test Diagnostics	59

4.3 Test Configuration and Procedure	61
4.4 C-Notch Test Results	68
4.4.1 Digital Image Correlation Results	69
4.4.2 Temperature Dependent Stress-Strain Response	73
4.4.3 Uncertainty Analysis for Elevated Temperature True Stress-Strain.....	76
4.5 V-Notch Test Results	80
4.6 Fracture Surface Analysis	82
4.7 Summary	88
Chapter 5 : Elevated Temperature Fracture Modeling.....	90
5.1 Constitutive Model for Ductile Failure.....	91
5.1.1 Progressive Damage Model.....	91
5.1.2 Elevated Temperature Flow Stress.....	96
5.2 Finite Element Model	102
5.2.1 Explicit Solver and Mass Scaling	102
5.2.2 Finite Element Mesh.....	107
5.2.3 Element Type and Hourglass Control	111
5.3 Material Model Calibration	116
5.3.1 Constitutive Model Calibration	116
5.3.2 Progressive Damage Model Calibration	122
5.4 PDM Model Summary	129
Chapter 6 : Panel Specimen Validation.....	130
6.1 Elevated Temperature Panel Experiments.....	130
6.1.1 Panel Test Articles	131
6.1.2 Panel Test Configuration	133
6.1.3 Panel Test Matrix.....	137
6.1.4 Laser Beam Results.....	138
6.1.5 Thermal Results	142
6.1.6 Mechanical Results.....	143
6.1.7 Panel Validation Test Summary.....	151
6.2 Panel Validation Models	152
6.2.1 Thermal Model	152

6.2.2 Thermal-Mechanical Model	162
6.2.3 Panel Validation Modeling Summary	175
Chapter 7 : Pressure Vessel Validation	177
7.1 Elevated Temperature Pressure Vessel Experiments	178
7.1.1 Pressure Vessel Test Articles	180
7.1.2 Test Configuration	183
7.1.3 Pressure Vessel Test Conditions.....	188
7.1.4 Pressure Vessel Test Results.....	190
7.1.5 Pressure Vessel Test Summary.....	209
7.2 Pressure Vessel Validation Models	210
7.2.1 Pressure Vessel Mesh.....	211
7.2.2 Thermal Model for Laser Heating of Pressure Vessels.....	214
7.2.3 Thermal-Mechanical Model of Pressure Vessel Failure	223
7.2.4 Pressure Vessel Validation Modeling Summary.....	238
Chapter 8 : Summary and Recommendations.....	240
8.1 Summary	240
8.2 Recommendations and Future Work.....	243
REFERENCES.....	245
Appendix A: Example Files for the Analysis of Notched Specimens.....	259
A.1 Abaqus Input File Example for C-Notch Specimen	259
A.2 Abaqus Python Script to Extract C-Notch Model Results	261
A.3 Abaqus File for Thermal and Mechanical Properties of DSS	264
Appendix B: Example Files for the Analysis of Panel Specimens.....	270
B.1 Pseudo-code for Irregular Beam Subroutine Implementation.....	270
B.2 Abaqus Input File Example for Panel Specimen Thermal Model.....	272
B.3 Abaqus Input File Example for Panel Specimen Thermal-Mechanical Model.....	274
Appendix C: Example Files for the Analysis of Pressure Vessels	277
C.1 Abaqus User Subroutines for Axisymmetric Flux Profile on a Curved Surface.....	277
C.2 Abaqus Input File Example for Pressure Vessel Thermal Model	286
C.3 Abaqus Python Script for Extracting Temperature History at TC Locations	287
C.4 Abaqus Input File Example for Pressure Vessel Thermal-mechanical Model.....	288

LIST OF FIGURES

FIGURE 2.1: MCCLINTOCK VOID GROWTH AND COALESCENCE MODEL GEOMETRY	9
FIGURE 2.2: RICE-TRACEY VOID GROWTH MODEL GEOMETRY	10
FIGURE 2.3: TRACTION-SEPARATION FUNCTION EXAMPLES	15
FIGURE 2.4: HILLERBORG'S FICTITIOUS CRACK MODEL	16
FIGURE 2.5: TRACTION-SEPARATION LAWS WITH HARDENING AND SOFTENING CURVES A) TVERGAARD AND HUTCHINSON (1992) B) SCHEIDER AND BROCKS (2003).....	17
FIGURE 2.6: DIAGRAM FOR EFFECTIVE STRESS CONCEPT USED IN CONTINUUM DAMAGE MODELING	21
FIGURE 3.1: SCANNING ELECTRON MICROSCOPE IMAGE OF THE ETCHED DSS CROSS-SECTION SHOWING DISTINCT DUPLEX STRUCTURE OF FERRITE AND AUSTENITE PHASES FOR A CROSS-SECTION PARALLEL TO THE ROLLING DIRECTION	43
FIGURE 3.2: SCANNING ELECTRON MICROSCOPE IMAGE OF THE ETCHED DSS CROSS-SECTION SHOWING DISTINCT DUPLEX STRUCTURE OF FERRITE AND AUSTENITE PHASES FOR A CROSS-SECTION PERPENDICULAR TO THE ROLLING DIRECTION.....	44
FIGURE 3.3: TEMPERATURE DEPENDENT SPECIFIC HEAT USING DIFFERENTIAL SCANNING CALORIMETER	45
FIGURE 3.4: TEMPERATURE DEPENDENT THERMAL CONDUCTIVITY DETERMINED FROM LASER FLASH METHOD	47
FIGURE 3.5: TEMPERATURE DEPENDENT THERMAL EXPANSION	48
FIGURE 3.6: TENSILE SPECIMEN FOR ROOM TEMPERATURE ELASTIC PROPERTIES.....	48
FIGURE 3.7: AXIAL AND TRANSVERSE STRAIN WHILE LOADING THE SPECIMEN IN THE ELASTIC REGIME ...	49
FIGURE 3.8: CALCULATED STRESS BASED ON FORCE HISTORY CORRESPONDING TO STRAIN MEASUREMENT	49
FIGURE 3.9: TRAM LABORATORY CONFIGURATION USED TO DETERMINE TEMPERATURE DEPENDENT SURFACE REFLECTANCE.....	51
FIGURE 3.10: TEMPERATURE DEPENDENT ABSORPTANCE OF BLACK STOVE BRIGHT® PAINT AT 1.07 μM .	52
FIGURE 4.1: POSSIBLE TENSILE SPECIMEN HEATING DEVICES: A) GLEEBLE 3500 (RESISTIVE HEATING) B) MTS MODEL 653 (FURNACE HEATING) C) HI-TEMPIR MODEL 5209 (BROADBAND IR HEATING) D) IPG PHOTONICS YLS-6000 (LASER HEATING)	54
FIGURE 4.2: GEOMETRY OF THE NOTCHED TENSILE SPECIMENS. C-NOTCH SPECIMEN (TOP) AND V-NOTCH SPECIMEN (BOTTOM)	58
FIGURE 4.3: CAMERA CONFIGURATION FOR DIC IMAGING OF WIDTH AND THICKNESS REDUCTION AND THE ELONGATION OF THE NOTCH SHOULDER	60
FIGURE 4.4: TENSILE TEST CONFIGURATION SHOWING MOVEABLE CARRIAGE FOR HEATER HEAD AND POWER CONTROL UNIT	62
FIGURE 4.5: HEATER HEAD WITH THERMAL INSULATION ATTACHED	63
FIGURE 4.6: HEATER HEAD PLACEMENT IN CLOSE PROXIMITY TO SAMPLE PRIOR TO TESTING	63
FIGURE 4.7: C-NOTCH SPECIMEN GEOMETRY, HIGHLIGHTING THE APPROXIMATE GRIP AREA, HEATED ZONE AND TC PLACEMENT	64
FIGURE 4.8: CAMERA CONFIGURATION FOR DIC MEASUREMENT OF THICKNESS, WIDTH, AND SHOULDER DISPLACEMENT	65
FIGURE 4.9: EXAGGERATED GEOMETRY OF DIFFUSE AND LOCALIZED NECKING AND THE "BOW-TIE" OR "CUSHION" DEFORMATION OBSERVED IN RECTANGULAR CROSS-SECTION SPECIMENS.....	67
FIGURE 4.10: LOAD VERSUS GRIP DISPLACEMENT FOR C-NOTCH SPECIMENS AT VARIOUS TEMPERATURES	69
FIGURE 4.11: EXAMPLE OF THE WIDTH, THICKNESS, AND SHOULDER DISPLACEMENT CAMERA IMAGES USED FOR DIC ANALYSIS FOR THE C-NOTCHED SPECIMEN AT 1000°C	70
FIGURE 4.12: LOAD VERSUS RELATIVE SHOULDER DISPLACEMENT FOR C-NOTCH SPECIMENS AT VARIOUS TEMPERATURES.....	71

FIGURE 4.13: LOAD VERSUS NORMALIZED THICKNESS FOR C-NOTCH SPECIMENS AT VARIOUS TEMPERATURES.....	72
FIGURE 4.14: LOAD VERSUS NORMALIZED WIDTH FOR C-NOTCH SPECIMENS AT VARIOUS TEMPERATURES	72
FIGURE 4.15: TRUE STRESS-STRAIN CURVES AT VARIOUS TEMPERATURES DETERMINED FROM C-NOTCH SPECIMENS	73
FIGURE 4.16: PROGRESSION OF INTERNAL VOID FORMATION DURING LOCALIZED NECKING OF 800° C-NOTCH SPECIMEN AS CAPTURED BY WIDTH REDUCTION DIC CAMERA	74
FIGURE 4.17: TEMPERATURE DEPENDENCE OF ELASTIC MODULUS.....	75
FIGURE 4.18: TEMPERATURE DEPENDENCE OF YIELD STRESS AND ULTIMATE STRENGTH	76
FIGURE 4.19: ENLARGED IMAGE OF C-NOTCH SHOULDER EDGE WITH PIXEL UNCERTAINTY ESTIMATE	77
FIGURE 4.20: FORCE-DISPLACEMENT CURVE FOR C-NOTCH EXPERIMENTS WITH UNCERTAINTY BOUNDS	79
FIGURE 4.21: TRUE STRESS-STRAIN CURVES FOR THE C-NOTCH EXPERIMENTS WITH UNCERTAINTY BOUNDS	80
FIGURE 4.22: COMPARISON OF NOMINAL STRESS VERSUS SHOULDER DISPLACEMENT FOR THE C-NOTCH AND V-NOTCH SAMPLES AT ELEVATED TEMPERATURES	81
FIGURE 4.23: CONTRAST IMAGE OF CONJUGATE SURFACES FOR ROOM TEMPERATURE C-NOTCH SPECIMEN	83
FIGURE 4.24: PERSPECTIVE VIEW OF FRASTA TOPOLOGY FOR CONJUGATE FRACTURE SURFACES FROM ROOM TEMPERATURE C-NOTCH SPECIMEN	84
FIGURE 4.25: ESTIMATION OF FRACTURE PROGRESSION BASED ON OVERLAPPING FRACTURE SURFACE TOPOGRAPHY MAPS.....	85
FIGURE 4.26: SEM IMAGE OF THE CONJUGATE FRACTURE SURFACES FOR A ROOM TEMPERATURE C-NOTCH SPECIMEN	86
FIGURE 4.27: CONTRAST IMAGE OF THE FRACTURE SURFACE SHOWING A REDUCTION IN CENTRAL THINNING WITH INCREASING TEMPERATURE	86
FIGURE 4.28: FAPP OVERLAID ON THE SEM IMAGE ON FRACTURE SURFACE A FOR THE ROOM TEMPERATURE C-NOTCH SPECIMEN	87
FIGURE 4.29: SEM IMAGES OF THE FRACTURE SURFACE NEAR THE CENTRAL REGION WHERE CRACK INITIATION OCCURS.....	88
FIGURE 4.30: SEM IMAGES OF THE FRACTURE SURFACE NEAR THE SAMPLE EDGE WHERE SHEAR FAILURE IS OBSERVED.....	88
FIGURE 5.1: STRESS-STRAIN RESPONSE WITH PROGRESSIVE DAMAGE AND FAILURE (ABAQUS DOCUMENTATION, 2008).....	94
FIGURE 5.2: ROOM TEMPERATURE FLOW STRESS COMPARISON TO VARIOUS FUNCTIONAL FORMS OF $F(\epsilon)$	97
FIGURE 5.3: NORMALIZED STRESS VERSUS HOMOLOGOUS TEMPERATURE FOR DETERMINING FLOW STRESS TEMPERATURE MODIFIER TERM	98
FIGURE 5.4: COMPARISON OF TEMPERATURE MODIFIER TERMS WITH DATA FROM CLAUSEN (2004) ON ALUMINUM AND CHEN (2006) ON HIGH STRENGTH STEEL	99
FIGURE 5.5: COMPARISON OF MULTIPLICATIVE CONTRIBUTION MODELS WITH ELEVATED TEMPERATURE DATA FROM C-NOTCH EXPERIMENT	100
FIGURE 5.6: COMPARISON OF ELEVATED TEMPERATURE DATA TO COUPLED FLOW STRESS EQUATION BASED ON TANH HARDENING SHAPE	101
FIGURE 5.7: COMPARISON OF EXPLICIT DYNAMIC SIMULATION OF C-NOTCH SPECIMEN AT VARIOUS MASS SCALING LEVELS.....	104
FIGURE 5.8: ROOT MEAN SQUARE ERROR AS A FUNCTION OF MASS SCALING FACTOR IN COMPARISON TO MODEL WITH NO MASS SCALING	104

FIGURE 5.9: COMPARISON OF IMPLICIT AND EXPLICIT SOLUTION SCHEMES FOR THE TENSILE TEST SIMULATIONS	106
FIGURE 5.10: COMPARISON OF LOAD VERSUS DISPLACEMENT BETWEEN THE SINGLE AND DOUBLE PRECISION SOLVER FOR TWO DIFFERENT MASS SCALING LEVELS	107
FIGURE 5.11: FINITE ELEMENT MESH FOR C-NOTCH SPECIMEN MESH SHOWING ELEMENT SIZE IN THE LOCALIZATION ZONE	110
FIGURE 5.12: FINITE ELEMENT MESH FOR V-NOTCH SPECIMEN MESH SHOWING ELEMENT SIZE IN THE LOCALIZATION ZONE	110
FIGURE 5.13: NOTIONAL DEFORMATION OF 2-D PANEL UNDER TENSILE LOAD: (A) UN-DEFORMED MESH; (B) DEFORMED MESH WITHOUT HOURGLASS MODE; (C) DEFORMED MESH WITH HOURGLASS MODE	112
FIGURE 5.14: THREE ELEMENT FINITE ELEMENT MODEL FOR EVALUATION OF HOURGLASS CONTROL TECHNIQUES.....	113
FIGURE 5.15: FORCE VERSUS DISPLACEMENT OF THREE ELEMENT MODEL USING VARIOUS HOURGLASS CONTROL TECHNIQUES	113
FIGURE 5.16: DEFORMED SHAPE COLORED WITH EFFECTIVE PLASTIC STRAIN: (A) TYPICAL DEFORMED SHAPE WITHOUT HOURGLASS MODE; (B) DEFORMED SHAPE USING VISCOUS HOURGLASS CONTROL WHICH WAS UNABLE TO SUPPRESS HOURGLASS MODE	114
FIGURE 5.17: DEFORMED SHAPE OF THREE ELEMENT MODEL WITH MORE CONFINING BOUNDARY CONDITIONS, COLORED WITH EFFECTIVE PLASTIC STRAIN.....	114
FIGURE 5.18: FORCE VERSUS DISPLACEMENT CURVES USING VARIOUS HOURGLASS CONTROL TECHNIQUES WITH THE THREE ELEMENT MODEL AND INCREASED CONFINEMENT OF THE END BOUNDARIES....	115
FIGURE 5.19: EXPERIMENTALLY DERIVED HARDENING CURVES AND EXTRAPOLATED HARDENING CURVES USED IN THE FEA SIMULATIONS.....	117
FIGURE 5.20: COMPARISON OF LOAD-DISPLACEMENT RESPONSE OF C-NOTCH FEA SIMULATIONS USING EXTRAPOLATED HARDENING CURVES	118
FIGURE 5.21: COMPARISON OF LOAD-DISPLACEMENT RESPONSE OF C-NOTCH FEA SIMULATIONS USING MODIFIED HARDENING CURVES.....	119
FIGURE 5.22: COMPARISON OF MODIFIED HARDENING CURVES USED IN FEA ANALYSIS TO THE EXPERIMENTAL CURVES WITH UNCERTAINTIES.....	120
FIGURE 5.23: DEFORMATION OF C-NOTCH SAMPLE AT 1000°C COMPARED TO FEA RESULTS USING MODIFIED HARDENING CURVE WITHOUT MATERIAL DAMAGE	121
FIGURE 5.24: ITERATIVE PROCESS FOR CALIBRATING THE PROGRESSIVE DAMAGE MODEL PARAMETERS USING GLOBAL LOAD-DISPLACEMENT	122
FIGURE 5.25: LOAD DISPLACEMENT CURVES USING THE MODIFIED HARDENING CURVES TO IDENTIFY DAMAGE INITIATION POINT	123
FIGURE 5.26: LOAD-DISPLACEMENT RESPONSE OF ELEVATED TEMPERATURE C-NOTCH SPECIMENS USING PDM MODEL WITH DAMAGE INITIATION AND EVOLUTION	124
FIGURE 5.27: EFFECTIVE PLASTIC STRAIN CONTOURS FOR THE C-NOTCH SPECIMEN AT 400°C: A) INCREMENT PRIOR TO FAILURE B) INCREMENT AFTER FAILURE (ELEMENT DELETION)	125
FIGURE 5.28: FEA RESULTS FOR C-NOTCH SPECIMEN AT 400°C WITH HALF SPECIMEN REMOVED USING AXIAL CROSS-SECTION. SOLUTION CONTOURS FOR INCREMENT JUST PRIOR TO FAILURE; A) EQUIVALENT PLASTIC STRAIN B) DAMAGE LEVEL C) MISES STRESS.....	125
FIGURE 5.29: DAMAGE EVOLUTION CURVES AT VARIOUS TEMPERATURES DETERMINED FROM OPTIMIZING LOAD-DISPLACEMENT RESPONSE OF C-NOTCH SPECIMENS.....	126
FIGURE 5.30: V-NOTCH SPECIMEN RESULTS USING PDM MODEL WITH TRIAXIALITY DEPENDENT DAMAGE INITIATION STRAIN	127
FIGURE 5.31: TRIAXIALITY DEPENDENCE ON THE DAMAGE INITIATION STRAIN FOR VARIOUS TEMPERATURES.....	128

FIGURE 6.1: PANEL TEST GEOMETRY INCLUDING HOLE LOCATIONS FOR CUSTOM MOUNTING FIXTURE	132
FIGURE 6.2: GRIP ADAPTER WITH 24 BOLT PATTERN AND CLEVIS MOUNT PIN TO LIMIT SLIP AND ALLOW FOR SAMPLE ROTATION	132
FIGURE 6.3: SPECKLE PATTERN PAINT APPLIED TO REAR SURFACE OF PANEL SPECIMEN TO ENABLE FULL FIELD STRAIN CALCULATIONS	133
FIGURE 6.4: TEST CONFIGURATION SHOWING LASER DIAGNOSTICS AND BEAM PATH	134
FIGURE 6.5: LABORATORY CONFIGURATION OF OPTICAL ELEMENTS AND BEAM DIAGNOSTICS FOR THE PANEL TESTS	135
FIGURE 6.6: CAMERA CONFIGURATION FOR PANEL EXPERIMENTS	136
FIGURE 6.7: LABORATORY CONFIGURATION WITH PANEL SAMPLE MOUNTED IN THE MTS MACHINE	137
FIGURE 6.8: LASER BEAM PROFILES FOR PANEL TEST PT1 AND PT2	139
FIGURE 6.9: LASER BEAM PROFILES FOR PANEL TEST PT3 AND PT4	140
FIGURE 6.10: BEAM PROFILE DATA IN THE VERTICAL DIMENSION FOR PT3 WITH BEAM SHAPE APPROXIMATION	141
FIGURE 6.11: TEMPERATURE HISTORY OF CENTER THERMOCOUPLES FOR PANEL TESTS PT1 AND PT2	142
FIGURE 6.12: TEMPERATURE HISTORY OF CENTER THERMOCOUPLES FOR PANEL TESTS PT3 AND PT4	143
FIGURE 6.13: LOAD AND DISPLACEMENT HISTORIES OF PANEL TESTS PT1 AND PT2	144
FIGURE 6.14: FIRST FRAME OF CRACK GROWTH CAPTURED BY THE FULL-FIELD STRAIN CAMERA FOR PT1 AND PT2	145
FIGURE 6.15: IMAGE AT THE MID-POINT OF FAILURE PROCESS CAPTURED BY THE FULL-FIELD STRAIN CAMERA FOR PT1 AND PT2	146
FIGURE 6.16: FULL-FIELD STRAIN MAP IN THE FINAL FRAME PRIOR TO CRACK INITIATION FOR PT1	147
FIGURE 6.17: LOAD AND DISPLACEMENT HISTORIES OF PANEL TESTS PT3 AND PT4	148
FIGURE 6.18: FIRST FRAME OF CRACK GROWTH CAPTURED BY THE FULL-FIELD STRAIN CAMERA FOR PT3 AND PT4	149
FIGURE 6.19: IMAGE AT THE MID-POINT OF FAILURE PROCESS CAPTURED BY THE FULL-FIELD STRAIN CAMERA FOR PT3 AND PT4	150
FIGURE 6.20: CLOSE-UP OF THE IMAGE AT THE MID-POINT OF FAILURE PROCESS CAPTURED BY THE FULL-FIELD STRAIN CAMERA FOR PT4	150
FIGURE 6.21: DIAGRAM OF UNIFORMLY SPACED IRRADIANCE VALUES FROM SWIR IMAGERY	153
FIGURE 6.22: INVERSE DISTANCE WEIGHTING METHOD APPLIED TO THE FOUR CLOSEST IRRADIANCE POINTS WITH ONE PER QUADRANT	154
FIGURE 6.23: PANEL MESH AND LASER BEAM MAPPING APPLIED TO THERMAL MODEL	156
FIGURE 6.24: MWIR IMAGERY USED TO DETERMINE HORIZONTAL SHIFT OF LASER POSITION; A) PRIOR TO SATURATION USED TO DETERMINE LASER CENTROID B) IMAGE AFTER SATURATION USED TO DETERMINE PANEL EDGE LOCATIONS	157
FIGURE 6.25: TEMPERATURE HISTORY COMPARISON OF THE ABAQUS THERMAL MODEL TO THE THERMOCOUPLE DATA FOR PT1	158
FIGURE 6.26: THERMAL PROFILES FROM THE ABAQUS SIMULATION AT SELECT TIMES DURING THE LASER HEATING OF PT1	158
FIGURE 6.27: TEMPERATURE HISTORY COMPARISON AND THERMAL PROFILES FROM THE ABAQUS THERMAL MODEL OF PT2	159
FIGURE 6.28: TEMPERATURE HISTORY COMPARISON AND THERMAL PROFILES FROM THE ABAQUS THERMAL MODEL OF PT3	160
FIGURE 6.29: TEMPERATURE HISTORY COMPARISON AND THERMAL PROFILES FROM THE ABAQUS THERMAL MODEL OF PT4	160
FIGURE 6.30: OPTIMIZED ABSORPTION USED IN THE ABAQUS MODEL COMPARED TO THE ELEVATED TEMPERATURE ABSORPTION, INCLUDING UNCERTAINTY ESTIMATE, FROM THE TRAM EXPERIMENT WHEN USING A 1.07 μM PROBE LASER	161

FIGURE 6.31: LOADING AND BOUNDARY CONDITIONS FOR THE ABAQUS THERMAL-MECHANICAL MODEL OF THE PANEL EXPERIMENTS	162
FIGURE 6.32: LOAD HISTORY RESULTS FROM ABAQUS PDM SIMULATION COMPARED TO EXPERIMENTAL RESULTS FOR PT1.....	163
FIGURE 6.33: DISPLACEMENT HISTORY FROM THE ABAQUS PDM SIMULATION COMPARED TO EXPERIMENTAL RESULTS FOR PT1.....	164
FIGURE 6.34: TEMPERATURE SOLUTION AT CRACK INITIATION TIME FOR PT1.....	165
FIGURE 6.35: DAMAGE INITIATION CRITERION, DAMAGE VARIABLE, EQUIVALENT PLASTIC STRAIN AND VON MISES STRESS SOLUTIONS AT CRACK INITIATION TIME FOR PT1 (SOLUTION ONLY SHOWN FOR REGION OF INTEREST DEFINED IN FIGURE 6.34).....	166
FIGURE 6.36: FRACTURE INITIATION PREDICTION FOR PT1 COMPARED TO THE EXPERIMENTAL RESULTS	167
FIGURE 6.37: SECONDARY CRACK INITIATION PREDICTION FOR PT1 COMPARED TO THE EXPERIMENTAL RESULTS	168
FIGURE 6.38: LOAD AND DISPLACEMENT HISTORY FOR PT2 COMPARED TO THE PDM MODEL RESULTS .	169
FIGURE 6.39: OVERLAID IMAGE OF THE PDM MODEL AND PT2 TEST RESULT FOR THE CRACK INITIATION LOCATION	170
FIGURE 6.40: LOAD AND DISPLACEMENT HISTORY FOR PT3 COMPARED TO THE PDM MODEL RESULTS .	172
FIGURE 6.41: OVERLAID IMAGE OF THE PDM MODEL AND PT3 TEST RESULT FOR THE CRACK INITIATION LOCATION	172
FIGURE 6.42: LOAD AND DISPLACEMENT HISTORY FOR PT4 COMPARED TO THE PDM MODEL RESULTS .	173
FIGURE 6.43: OVERLAID IMAGE OF THE PDM MODEL AND PT4 TEST RESULT FOR THE CRACK INITIATION LOCATION	173
FIGURE 7.1: NOTIONAL PLOT OF THE FAILURE RESPONSE AS A FUNCTION OF HEATED ZONE SIZE AND INTERNAL PRESSURE	179
FIGURE 7.2: CAD GEOMETRY DRAWING FOR CYLINDRICAL PRESSURE VESSEL WITH REUSABLE END FLANGES	181
FIGURE 7.3: PRESSURE VESSEL TOP FLANGE WITH THERMOCOUPLE FEEDTHROUGH AND PRESSURIZATION SYSTEM	181
FIGURE 7.4: THERMOCOUPLE PATTERN FOR THE INTERIOR SURFACE OF THE PRESSURE VESSELS.....	182
FIGURE 7.5: EXAMPLE OF ONE OF THE CYLINDERS AFTER ROLLING AND WELDING WITHOUT THE END CAPS ATTACHED	183
FIGURE 7.6: ENCLOSURE FOR THE PRESSURE VESSEL EXPERIMENTS	184
FIGURE 7.7: INSTRUMENTED PRESSURE VESSEL MOUNTED IN THE TEST FIXTURE	185
FIGURE 7.8: PRESSURIZATION SYSTEM WITH REMOTE OPERATION SWITCHES.....	186
FIGURE 7.9: TEST CONFIGURATION FOR ELEVATED TEMPERATURE PRESSURE VESSEL EXPERIMENTS	188
FIGURE 7.10: PREDICTED FAILURE MODE TRANSITION LINE AND TEST RANGES FOR THREE DIFFERENT LASER BEAM SIZES.....	189
FIGURE 7.11: EXPERIMENTAL RESULTS SHOWING THE FAILURE MODE TRANSITION AS THE PRESSURE RATIO IS INCREASED	192
FIGURE 7.12: IMAGES OF THE FAILURE MODE FOR EACH PRESSURE VESSEL EXPERIMENT	193
FIGURE 7.13: TEMPERATURE HISTORY FOR HIGHEST THERMOCOUPLE READINGS FROM TEST #12 WHEN LASER OPERATION WAS ABORTED	194
FIGURE 7.14: TEST ARTICLE USED IN TEST #12 SHOWING DAMAGE TO THE PAINTED SURFACE CAUSED BY LASER HEATING PRIOR TO THE TEST BEING TERMINATED OVER LASER HEALTH CONCERNS.....	195
FIGURE 7.15: LASER BEAM PROFILE FOR PRESSURE VESSEL TEST #1	196
FIGURE 7.16: LASER BEAM PROFILES FOR THE PRESSURE VESSEL EXPERIMENTS WHICH WERE ANALYZED WITH THE PDM MODEL.....	197

FIGURE 7.17: HORIZONTAL AND VERTICAL PROFILE OF THE LASER BEAM FOR PRESSURE VESSEL TEST #9 SHOWING HOT SPOTS	198
FIGURE 7.18: HIGH SPEED IMAGERY OF FRACTURE PROCESS FOR TEST #12.....	199
FIGURE 7.19: HIGH SPEED IMAGERY OF THE FRACTURE PROCESS FOR TEST #9	199
FIGURE 7.20: HIGH SPEED IMAGERY OF THE FRACTURE PROCESS FOR TEST #6	200
FIGURE 7.21: THERMOCOUPLE HISTORIES FOR PRESSURE VESSEL TEST #1	201
FIGURE 7.22: THERMOCOUPLE HISTORIES FOR PRESSURE VESSEL TEST #12	202
FIGURE 7.23: FLOW CHART FOR IDENTIFYING THE LASER BEAM CENTROID LOCATION USING THE BEAM PROFILE AND TC DATA.....	203
FIGURE 7.24: PRESSURE HISTORY FOR TEST #1 SHOWING STABLE PRESSURE AND LOW SINGLE-TO-NOISE RATIO	204
FIGURE 7.25: PRESSURE HISTORY FOR TEST #1 SHOWING A DECAY IN PRESSURE FOLLOWING LOCAL FAILURE	205
FIGURE 7.26: PRESSURE HISTORY FOR TEST #6 SHOWING A RAPID DECREASE IN PRESSURE FOLLOWING A CATASTROPHIC FAILURE.....	206
FIGURE 7.27: PRESSURE HISTORY FOR TEST #1 ZOOMED TO SHOW THE GRADUAL PRESSURE INCREASE AS THE CYLINDER IS HEATED	206
FIGURE 7.28: RELATIVE PRESSURE INCREASE BEFORE FAILURE AS A FUNCTION OF THE APPLIED LASER ENERGY	207
FIGURE 7.29: FAILURE MODE TRANSITION ESTIMATE FOR HEATED PRESSURE VESSELS	208
FIGURE 7.30: EXAMPLE OF 2:1 TRANSITION MESH.....	212
FIGURE 7.31: PRESSURE VESSEL MESH SHOWING THE TRANSITION MESH AND SOLID-SHELL COUPLING LOCATIONS ALONG WITH THE APPROXIMATE MESH SIZE	212
FIGURE 7.32: SOLID TO SHELL COUPLING INTERFACE USED TO REDUCE PRESSURE VESSEL MESH	213
FIGURE 7.33: COMPLETE PRESSURE VESSEL MESH WITH APPROXIMATE HEATED ZONE SIZE	214
FIGURE 7.34: COSINE CORRECTION FOR FLUX BASED ENERGY DEPOSITION FOR ELEMENTS ON A CURVED SURFACE	216
FIGURE 7.35: THERMAL CONTOURS FROM THE ABAQUS HEAT TRANSFER ANALYSIS OF 3 PRESSURE VESSEL EXPERIMENTS WITH VARIOUS LASER BEAM SIZES, SHOWN AFTER THE INITIAL INCREMENT AND FINAL INCREMENT OF THE ANALYSIS	217
FIGURE 7.36: TEMPERATURE HISTORY COMPARISON BETWEEN THERMOCOUPLE READINGS AND ABAQUS THERMAL MODEL RESULTS	218
FIGURE 7.37: COMPARISON OF THE ABAQUS THERMAL PROFILE AND THE THERMOCOUPLE MEASUREMENTS ALONG AN AXIAL PATH AT VARIOUS TIMES IN THE HEATING PROCESS FOR PRESSURE VESSEL TEST #4	219
FIGURE 7.38: TEMPERATURE HISTORY AND THERMAL PROFILE COMPARISON BETWEEN THE ABAQUS THERMAL SOLUTION AND THERMOCOUPLE MEASUREMENTS FOR TEST#7	220
FIGURE 7.39: TEMPERATURE HISTORY COMPARISON BETWEEN ABAQUS SIMULATION AND CENTER THERMOCOUPLE TRACE FOR TEST #7	221
FIGURE 7.40: ABAQUS THERMAL PROFILE COMPARISON TO THERMOCOUPLE DATA ALONG AN AXIAL PATH FOR TEST #11.....	221
FIGURE 7.41: TEMPERATURE DEPENDENT LASER ABSORPTION USED IN ABAQUS THERMAL MODELS COMPARED TO TRAM DATA.....	222
FIGURE 7.42: FLOW CHART DESCRIBING THE SEQUENTIALLY COUPLED THERMAL-MECHANICAL ANALYSIS OF PRESSURE VESSEL FAILURE INDUCED BY LOCALIZED HEATING	223
FIGURE 7.43: EXAMPLE OF A LOCAL FAILURE PREDICTION WITH AND WITHOUT THE USE OF VDLOAD COMPARED TO A TYPICAL FAILURE OBSERVED IN THE EXPERIMENTS	225
FIGURE 7.44: TEST #9 FRACTURE COMPARISON BETWEEN HIGH SPEED VIDEO AND ABAQUS PREDICTIONS (TEMPERATURE CONTOURS).....	228

FIGURE 7.45: TEMPERATURE CONTOURS FOR TEST #9 DURING FAILURE	229
FIGURE 7.46: MISES STRESS CONTOURS FOR TEST #9 DURING FAILURE	230
FIGURE 7.47: EQUIVALENT PLASTIC STRAIN CONTOURS FOR TEST #9 DURING FAILURE	230
FIGURE 7.48: DAMAGE INITIATION CRITERIA CONTOURS FOR TEST #9 DURING FAILURE	231
FIGURE 7.49: DAMAGE VARIABLE CONTOURS FOR TEST #9 DURING FAILURE.....	232
FIGURE 7.50: COMPARISON OF FAILURE RESPONSE BETWEEN THE EXPERIMENT AND PDM SIMULATION FOR TEST #4	233
FIGURE 7.51: TEMPERATURE CONTOURS FOR TEST #4 DURING FAILURE	234
FIGURE 7.52: MISES STRESS CONTOURS FOR TEST #4 DURING FAILURE.....	234
FIGURE 7.53: EQUIVALENT PLASTIC STRAIN CONTOURS FOR TEST #4 DURING FAILURE	235
FIGURE 7.54: DAMAGE INITIATION CRITERION CONTOURS FOR TEST #4 DURING FAILURE	236
FIGURE 7.55: DAMAGE VARIABLE CONTOURS FOR TEST #4 DURING FAILURE.....	236
FIGURE 7.56: COMPARISON OF FAILURE RESPONSE BETWEEN THE EXPERIMENT AND PDM SIMULATION FOR TEST #12	238

LIST OF TABLES

TABLE 2.1: VARIOUS STRAIN AND STRAIN RATE DEPENDENT FLOW STRESS MODIFIER TERMS	33
TABLE 2.2: VARIOUS TEMPERATURE DEPENDENT FLOW STRESS MODIFIER TERMS.....	34
TABLE 2.3: COUPLED FLOW STRESS MODELS FOR STRAIN, STRAIN RATE, AND TEMPERATURE DEPENDENCE	35
TABLE 3.1: CHEMICAL COMPOSITION AND PHASE PERCENTAGE OF DSS SAMPLE FROM OES.....	42
TABLE 4.1: CONTRIBUTORS WITH UNCERTAINTY ESTIMATE FOR DETERMINATION OF LOAD-DISPLACEMENT AND TRUE STRESS-STRAIN	78
TABLE 4.2: C-NOTCH SPECIMEN DIMENSIONS.....	82
TABLE 4.3: V-NOTCH SPECIMEN DIMENSIONS.....	82
TABLE 6.1: PANEL TEST MATRIX INCLUDING LOAD AND LASER CONDITIONS	138
TABLE 6.2: MEASURED LASER BEAM POWER, IRRADIANCE, AND SIZE	140
TABLE 6.3: PDM MODEL COMPARISON TO PT1 RESULTS	169
TABLE 6.4: PDM MODEL COMPARISON TO PT2 RESULTS	171
TABLE 6.5: PDM MODEL COMPARISON TO PT3 RESULTS	172
TABLE 6.6: PDM MODEL COMPARISON TO PT4 RESULTS	173
TABLE 7.1: CYLINDRICAL PRESSURE VESSEL TEST ARTICLE THICKNESSES	180
TABLE 7.2: RESULTS SUMMARY FOR ELEVATED TEMPERATURE PRESSURE VESSEL FAILURES.....	191
TABLE 7.3: EXAMPLE ANALYSIS SEQUENCE INCLUDING COMPUTATION TIME ASSOCIATED WITH EACH MASS SCALING LEVEL.....	224
TABLE 7.4: COMPARISON OF ABAQUS FAILURE PREDICTIONS USING PDM WITH EXPERIMENTAL RESULTS	227

Chapter 1 : Introduction

1.1 Background and Motivation

Ductile failure of metals has been the focus of detailed research efforts both within academia and industry for the past 50 years due to the common use of ductile metals within many designs. Significant investments have been made to improve the understanding of the ductile failure process to evaluate system performance during catastrophic failure events, such as vehicle collisions, where sudden extreme loading can result in costly reconstruction expenses and even loss of life. Failures of this type are observed in vehicle collisions, industrial accidents, structural fires, natural disasters, train derailments and collisions, as well as terror and military attacks. Extreme environments are also common for emerging applications in space, deep sea, energy, and hypersonic technologies. The study of material failure is critical for preventing and mitigating the loss of property and potentially the loss of life in these extreme environments.

Although material failure was previously studied, the concept of fracture mechanics was first introduced by Griffith in the 1920's to understand the failure process in a quantifiable manner (Lassen and Recho, 2006). In the decades of research that followed, the research community primarily focused on the analysis of pre-existing cracks, including prediction of critical crack length and propagation of the crack tip using various analytical and numerical approaches. However, pre-existing cracks may not be present when sudden and extreme conditions are responsible for failure. This limits the utility of

traditional fracture mechanics techniques for these applications. The prediction of crack initiation (formation) is thus a critical factor for analyzing the failure of engineered systems subjected to sudden and extreme conditions.

In the last several decades, various approaches have been developed to predict fracture initiation in uncracked bodies for brittle and ductile materials. The initiation of fracture is a complex process that is dependent on the material type, stress state, strain rates, geometry and temperature. In ductile metals, the initiation of fracture is further complicated by micromechanical deformations that result in void nucleation, growth and coalescence which can cause the material to exhibit diffuse necking and strain localization prior to macroscopic crack development. The majority of the predictive models rely on numerical methods such as the Finite Element Method to evaluate the crack initiation criterion and subsequent crack propagation. As a result, simulation of diffuse necking and strain localization during material softening creates a numerical problem (bifurcation) which introduces strong mesh dependencies in the prediction of crack formation (Needleman, 1988). Furthermore, the ductility of metals generally increases with temperature which further exasperates the mesh dependency when analyzing extreme thermal environments.

Although progress continues to be made in predicting ductile fracture, a definitive solution to this problem has not been identified, which is evident by the vast number of approaches in the literature. While there are many approaches, the current emphasis in ductile failure research is mostly on the quantification of stress state and strain rate dependency at ambient temperature. Research on predicting elevated temperature crack

initiation in ductile metals is very limited. As a result, there is a gap in the research for analyzing elevated temperature failure during catastrophic thermal events such as industrial, structural or shipping vessel fires as well as high temperature applications in welding, machining and power generation.

The need exists for predicting ductile crack formation at elevated temperatures to perform risk analysis, improve designs, and develop risk mitigation methods. Ideally, a predictive modeling capability will account for the temperature dependence of strength, ductility, strain localization and the corresponding mesh dependency. The approach should be easy to integrate into large scale structural analysis tools such that relevant and realistic predictions can be conducted.

1.2 Research Objectives

Although significant investments have been made to understand the response of ductile metals at ambient and elevated temperature conditions over the past several decades, it is apparent that no universally accepted approach has been adopted. The literature includes simple functional relationships, phenomenological models with many calibration parameters, void growth/coalescence models, and dislocation mechanics based models. Interestingly, after proper calibration many are capable of reproducing laboratory experiments with reasonable accuracy. However, limited emphasis has been placed on model validation beyond the calibration experiments. Moreover, even less emphasis has been placed on the prediction of ductile fracture initiation at elevated temperatures. The intent of this research is to characterize a constitutive model and

fracture approach at elevated temperatures to predict the fracture initiation and crack growth in pipelines and pressure vessels under extreme thermal conditions. The following objectives were used to guide the research documented in this dissertation:

- Identify a material of interest for pipeline and pressure vessels used in chemical, oil/gas, nuclear, power, and industrial applications where extreme thermal conditions can result in catastrophic damage
- Characterize the microstructure, chemical composition, thermal properties, and room temperature strength using established testing methods
- Perform elevated temperature calibration experiment for deriving the isothermal constitutive response of the material from room temperature to 70% of the melt temperature (larger range than found in the literature)
- Calibrate an elevated temperature constitutive model and fracture initiation method at each temperature condition
- Perform transient heating of panel specimens under constant uniaxial tension to validate constitutive/fracture model for predicting failure time and crack initiation location in uncracked bodies with high thermal gradients
- Perform transient heating of pipeline/pressure vessel to validate constitutive/fracture model for predicting failure times and failure mode

1.3 Structure of the Dissertation

The focus of this dissertation is to study the elevated temperature fracture initiation of ductile metals. Chapter 1 provides the background, motivation, and research objectives. Chapter 2 provides a comprehensive literature review on fracture initiation methods, elevated temperature constitutive models, and elevated temperature fracture research. Chapter 3 will provide an in-depth material characterization using traditional testing methods for microstructure, chemical composition, elevated temperature thermal properties, and room temperature strength characteristics.

Chapter 4 will focus on elevated temperature tensile testing of notched specimens with rectangular cross-sections, manufactured from rolled sheet material. Chapter 5 will detail the elevated temperature constitutive model and fracture initiation approaches used in this research. The calibration of the material model based upon the isothermal tensile test data will be described in detail.

Chapter 6 will describe the panel validation experiments under constant load and rapid transient heating. The model predictions for crack initiation location and time to failure will be compared to the experiments. Chapter 7 will describe the pipeline/pressure vessel validation experiments. The failure response as a function of heated zone size and internal pressure will be investigated to determine the transition from local failure to catastrophic failure. The predicted failure mode and failure time will be used as validation metrics for evaluating the material model developed in this manuscript.

Chapter 8 will provide a summary and evaluation of the methodology developed within this dissertation for predicting fracture initiation of uncracked bodies subjected to extreme thermal conditions and recommendations for future research.

Chapter 2 : Literature Review

2.1 Ductile Fracture Initiation Modeling

Numerous strategies have been developed to understand and model the characteristics of ductile failure, namely; material hardening and softening, void formation and coalescence, dislocations, crack initiation and propagation. Many researchers have attempted to address limitations in Linear Elastic Fracture Mechanics (LEFM) for application to materials which display a non-linear response, such as ductile metals. Rice (1968) defined a path independent strain energy release rate, later known as the J-integral, to predict propagation of an existing crack within a plastic process zone. Fracture toughness was derived from the LEFM work by Irwin (1957) on stress intensity factors for crack propagation. The Crack Tip Opening Displacement (CTOD) between the two crack faces was proposed by Wells (1963) for predicting crack tip advancement and later modified to the Crack Tip Opening Angle (CTOA) by Kanninen et al. (1981) for thin walled materials. Hahn et al. (1969) derived an empirical model for predicting the critical crack length for ductile fracture of pipelines and pressure vessels. Each of these methods require a pre-existing crack with a defined size, location, and orientation which limits their utility when considering un-cracked bodies. In addition, these methods are limited to isothermal conditions or at least a material process zone that does not span a large thermal gradient. The limitations of these methods has led the fracture community to investigate constitutive material models for simulating crack initiation in ductile metals.

2.1.1 Uncoupled Void Growth Models for Fracture Initiation

The role of void growth in ductile failure of metals was identified early in the study of fracture mechanics (Tipper, 1949; Puttick, 1959; Rogers, 1960). In ductile metals, it was observed that microvoids nucleated and coalesced during the necking and localization process leading up to failure. While in brittle metals, the crack was observed to propagate by cleavage, which is the failure of atomic bonds along the crystallographic planes, without generation of microvoids.

McClintock (1968) used the experimental observations of Tipper (1949) and Rhines (1961) on copper and plasticine, respectively, to formulate a fracture criterion based on the growth of preexisting cylindrical voids with elliptical cross-sections. Although the analysis was simplified to a power-law plastic hardening rule and void orientations parallel to the applied stress, this would form the first theoretical fracture initiation model for ductile metals based on void growth and coalescence.

Figure 2.1 shows the void geometry considered by McClintock where the voids are parallel to the applied stress, σ_z , the major and minor transverse hole sizes are defined by a and b , and the hole separation in the transverse directions are defined by l_a and l_b . The fracture is assumed to occur when a pair of voids touch as defined by the relative growth factor, F , which can occur in one of 6 possible modes. As an example, the relative growth factor in the b -direction due to a stress in the z -direction is given by, $F_{zb} = (b/l_b)/(b_o/l_{b_o})$. Coalescence occurs when $b = l_b/2$, resulting in a critical growth factor to

achieve fracture initiation of $F_{zb}^f = l_{bo}/2b_o$. The increment of the accumulated damage, $\eta_{zb} = F_{zb}/F_{zb}^f$, can then be expressed as,

$$\frac{d\eta_{zb}}{d\bar{\epsilon}} = \frac{1}{\ln(F_{zb}^f)} \left[\frac{\sqrt{3}}{2(1-n)} \sinh\left(\frac{\sqrt{3}(1-n)(\sigma_a + \sigma_b)}{2\bar{\sigma}}\right) + \frac{3(\sigma_a - \sigma_b)}{4\bar{\sigma}} \right] \quad (2.1)$$

where n is the power-law hardening exponent, σ_a and σ_b are the transverse principal stresses, $\bar{\epsilon}$ is the equivalent strain and $\bar{\sigma}$ is the von Mises stress. Fracture is estimated to occur when $\eta=1$ (*i.e.* $F=F^f$). The McClintock model is considered to be an uncoupled void growth factor model because the accumulation of damage, *i.e.* growth of the voids, has no direct impact on the constitutive material response. The damage is simply evaluated after each increment based on the stress state and the occurrence of fracture initiation is determined.

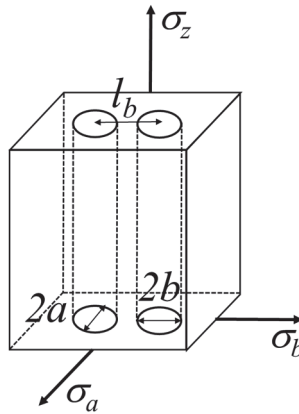


Figure 2.1: McClintock void growth and coalescence model geometry

Rice and Tracey (1969) performed a similar investigation for the growth of a spherical void within an infinite media, as depicted in Figure 2.2. The void growth from an initial radius, R_o , to a deformed radius of R , was found to be enhanced by the superposition of hydrostatic tension, as one might expect.

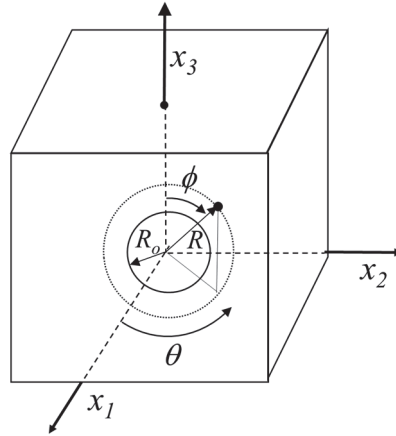


Figure 2.2: Rice-Tracey void growth model geometry

The analysis also showed that the void growth was strongly dependent on the dilatation and less dependent on the shape change of the void. Based on these findings, the Rice-Tracey void growth model is commonly reduced to the following exponential relationship:

$$\ln \frac{R}{R_0} = \int \alpha \exp\left(\frac{3\sigma_m}{2\sigma_{eq}}\right) d\varepsilon_{eq}^p \quad (2.2)$$

where σ_m is the hydrostatic stress, σ_{eq} is the equivalent von Mises stress, ε_{eq}^p is the equivalent plastic strain, and α is the growth factor approximated using a Rayleigh-Ritz analysis. The original two term approximation by Rice-Tracey estimated α to be 0.283 while a converged analysis by Huang (1990) found α to be 0.427 which was consistent with later finite element solutions by Huang (1991) for higher triaxiality values. Similar to the McClintock model, the fracture is estimated to occur when a critical void growth ratio is reached, $(R/R_0)^c$. Since the model is only based on the growth of a single void, the critical void ratio cannot be directly correlated to deformation where two voids begin to

interact (coalesce). As a result, the critical void growth ratio is most commonly determined by calibrating the numerical model to experimental data.

The uncoupled void growth models, such as McClintock (1968) and Rice-Tracey (1969), provide a fundamental understanding of how voids grow in simplified geometries and are trivial to implement in numerical simulations due to the uncoupled nature. However, they lack the complexity to capture the interaction of voids as they coalesce and do not consider the nucleation of voids or the process of void sheeting along shear bands between voids. The uncoupled approach also lacks the ability to simulate the loss in load carrying capacity during localization which limits the applicability to highly ductile behavior often exhibited in elevated temperature metals.

2.1.2 Coupled Porous Metal Plasticity and Fracture Model

Coupled porous metal plasticity models attempt to relate the constitutive material behavior to void nucleation, growth and coalescence during the ductile failure process, enabling the simulation of strain localization and loss in load carrying capacity at failure. The role of void nucleation and growth on ductile failure was initially investigated in the 1960's, including the pioneering work of McClintock and Rice described in Section 2.1.1. Based on these early void growth concepts, Gurson (1977) developed one of the first constitutive models to make flow stress dependent on the void content of the material during failure. The Gurson model was subsequently improved upon by Tvergaard (1981) and Tvergaard & Needleman (1984) to form what is commonly known as the Gurson-Tvergaard-Needleman (GTN) model.

The GTN is the most popular of the coupled porous metal plasticity models and is essentially a variation of the von Mises plasticity theory, commonly used for metals, modified to account for the growth of primary voids, nucleation of secondary voids, and coalescence of voids leading to fracture initiation. The effects of void growth and nucleation are taken into account at the material level with a modified plastic flow potential or yield function, requiring the implementation to be implemented into the constitutive model. The modified plastic flow potential is defined as:

$$\Phi = \left(\frac{\sigma_{eq}}{\bar{\sigma}_y} \right)^2 + 2q_1 f^*(f) \cosh \left(\frac{3q_2 \sigma_m}{2\bar{\sigma}_y} \right) - (1 + q_1^2 f^*(f)^2) \quad (2.3)$$

Where σ_{eq} is the equivalent von Mises stress, $\bar{\sigma}_y$ is the flow stress, σ_m is the mean stress, and $f^*(f)$ is the void volume function. Note, when $f^*(f) = 0$ the plastic flow potential is reduced to the standard Mises plasticity model. The GTN model was initially defined by Gurson (1977) and the parameters q_1 and q_2 were introduced by Tvergaard (1981) to fit experimental data more easily for the plane strain analysis of a plate containing cylindrical holes. At this point the model was still based on the growth of primary voids and did not account for the nucleation of secondary voids.

Further study by Tvergaard and Needleman (1984) introduced the function $f^*(f)$ to account for the nucleation of voids and rapid void coalescence at failure.

$$f^*(f) = \begin{cases} f & \text{for } f \leq f_c \\ f_c + \frac{1/q_1 - f_c}{f_f - f_c} (f - f_c) & \text{for } f_c < f \leq f_f \\ 1/q_1 & \text{for } f > f_f \end{cases} \quad (2.4)$$

$$\dot{f} = \dot{f}_{growth} + \dot{f}_{nucleation} \quad (2.5)$$

$$\dot{f}_{growth} = (1 - f) \dot{\epsilon}^{pl} : I \quad (2.6)$$

$$\dot{f}_{nucleation} = A_N \dot{\bar{\epsilon}}^{pl} \quad (2.7)$$

Where $\bar{\epsilon}^{pl}$ is the effective plastic strain, f_c is the void volume fraction at coalescence, and f_f is the void volume fraction at full damage. The rate of change of the void volume fraction, \dot{f} , is defined as a function of $\dot{\epsilon}^{pl}$, the time derivative of the plastic strain.

The coefficient A_N , first proposed by Chu and Needleman (1980), defines strain-controlled nucleation:

$$A_N(\bar{\epsilon}^{pl}) = \frac{f_N}{s_N \sqrt{2\pi}} \exp\left[-\frac{1}{2}\left(\frac{\bar{\epsilon}^{pl} - \epsilon_N}{s_N}\right)^2\right] \quad (2.8)$$

Where f_N is the void volume fraction due to the nucleation of particles and the nucleation function follows a normal distribution with a mean value, ϵ_N , and standard deviation, s_N . Due to the contributions of Tvergaard and Needleman the modified formulation is named the Gurson-Tvergaard-Needleman model.

Numerous modified GTN models have been used in the literature, such as the one proposed by Nahshon and Hutchinson (2008) to correct for shear dominated failure. However, each model technically requires counting of voids at various stages of the deformation process and relating the microscopic behavior to the global response during testing. The process has been found to be tedious and expensive to implement since up to 10 parameters may be required to fully define the constitutive model. As a result, the constitutive model parameters are typically fit to match the global response (load vs. displacement) of the test specimen with no regard for the actual void behavior (Alegre

and Gutierrez-Solana, 2004). A comprehensive review of the GTN model and its adaptations has been provided by Benzerga et al. (2016).

2.1.3 Cohesive Zone Fracture Models

Cohesive Zone Models (CZM) use an interface/cohesive element to describe the stress-displacement relationship in terms of the cohesive law, sometimes referred to as the traction-separation law. CZM models are based on the early work on fracture energy by Griffith and Eng (1921) and cohesive force approaches by Dugdale (1960), Barenblatt (1962) and Hillerborg et al. (1976). The approach by Hillerborg defines a fracture energy per unit area of the newly generated crack surface as follow:

$$G_f = \int_0^{\delta_c} \sigma d\delta \quad (2.9)$$

Where G_f is the fracture energy per unit area, σ is the stress and δ is the crack separation. The beginning of failure is assumed to occur when the stress reaches the material tensile strength for Mode I failure. The stress carrying capacity of the material then follows the traction-separation law definition, $\sigma(\delta)$. Several examples are shown in Figure 2.3, but no definitive function has been defined in the literature. The stress carrying capacity is lost when the separation is equal to δ_c , however the fracture process begins after the tensile stress is reached.

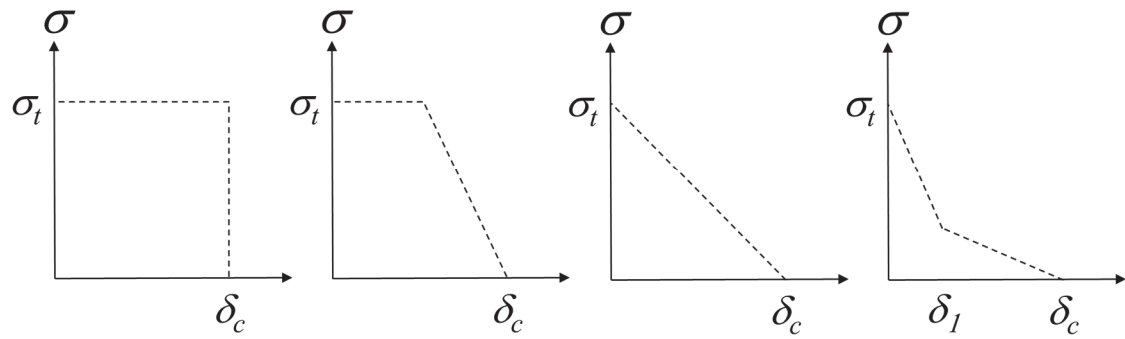


Figure 2.3: Traction-separation function examples

The pseudo-damaged zone between $\delta=0$ and $\delta=\delta_c$ is commonly termed the fracture process zone (FPZ) where the displacement is discontinuous but stress continuity is maintained by the cohesive traction. Since the simulated crack tip is located at $\delta=\delta_c$ but the effective crack tip and peak stress are located at $\delta=0$, this approach is commonly referred to as the fictitious crack model. Figure 2.4 shows a depiction of the Hillerborg's fictitious crack model. Although Hillerborg's model was developed for concrete applications, an earlier approach by Dugdale followed a similar logic for metals with a cohesive force acting near the vicinity of the crack tip to simulate softening.

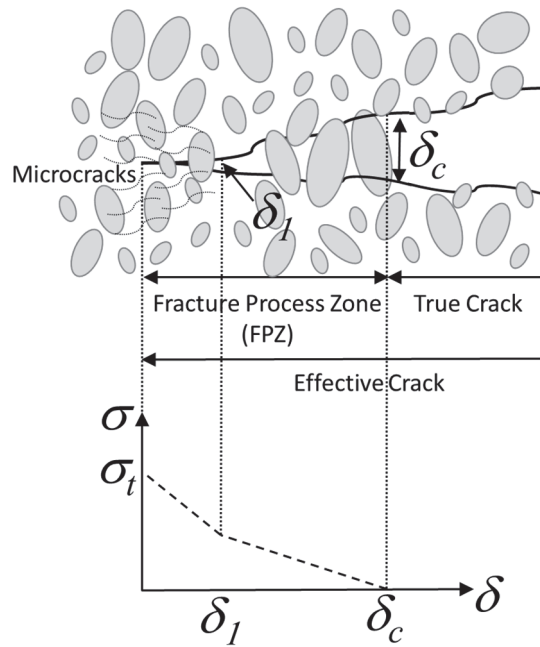


Figure 2.4: Hillerborg's fictitious crack model

Many definitions for the traction-separation law for metals can be found in the literature in the decades since the work of Hillerborg, including Tvergaard & Hutchinson (1992) and Scheider & Brocks (2003). As shown in Figure 2.5, these two methods also include a hardening portion at the beginning of the traction-separation law. Bazant (2002) and Elices et al. (2002) point out that this approach lacks objectivity and is only acceptable for fixed crack paths and suggest any hardening be handled in the constitutive response of the bulk material. Cornec et al. (2003) suggests the hardening portion is needed for numerical stability between the continuum element and cohesive interface and also suggests $\delta_1 \ll \delta_c$. The need for a hardening portion in the traction-separation law is arguable and appears to be a function of how the model is implemented into the structural analysis code.

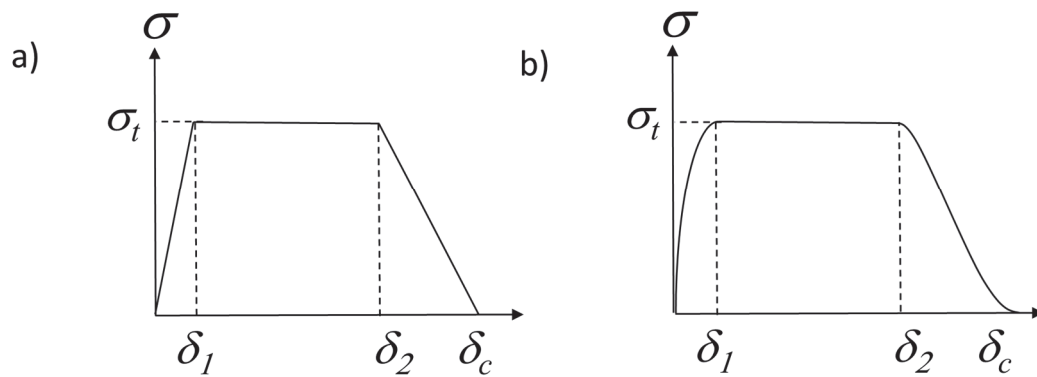


Figure 2.5: Traction-separation laws with hardening and softening curves a) Tvergaard and Hutchinson (1992) b) Scheider and Brocks (2003)

Nevertheless, the cohesive zone fracture models all contain a softening portion which progressively degrades the stress carrying capacity of the cohesive interface, generally cast in terms of normal traction for Mode I failure. Although some approaches for mixed mode softening have been presented in Camanho and Davila (2002) as well as Scheider and Brocks (2003), limited evidence is provided for either method. Scheider and Brocks (2003) also showed the predicted cup-cone fracture of aluminum bars were sensitive to the aspect ratio and orientation of the cohesive surface and suggest the element inclination should be in the direction of the maximum tangential stress. As a result, cohesive zone fracture models appear to be most applicable to Mode I fracture simulations or cases where the crack locations and orientations are known.

2.1.4 Uncoupled Semi-Empirical Fracture Indicator Models

The uncoupled fracture indicator models are the simplest of the fracture modeling approaches which are empirically calibrated using an estimated fracture quantity which can take various forms. The approaches emerged from the metal forming community and

gained popularity because of their computational efficiency in large-scale finite element simulations. The uncoupled void growth models by McClintock (1968) and Rice (1969), described previously, can be considered damage indicator models since they are not coupled to the constitutive response of the material.

Cockcroft and Latham (1968) proposed a simple fracture indicator quantity for ductile metals based upon the maximum tensile stress integrated over the equivalent strain path as follows:

$$C_f = \int_0^{\varepsilon^f} \sigma^* d\bar{\varepsilon} \quad (2.10)$$

where σ^* is the maximum tensile stress, $\bar{\varepsilon}$ is the equivalent strain, ε^f is the fracture strain and C_f is the empirically derived fracture constant.

Oyane et al. (1980) proposed a damage indicator model for porous metals with an integral quantity related to the equivalent strain at void initiation and the relative density of the material during deformation. Assuming a homogenous, pore-free material, the damage indicator can be reduced to the following equation:

$$C_f = \int_0^{\bar{\varepsilon}^f} \left(1 + \frac{\sigma_m}{A \sigma_{eq}} \right) d\bar{\varepsilon} \quad (2.11)$$

where σ_m is the hydrostatic stress, $\bar{\varepsilon}$ is the equivalent strain, σ_{eq} is the yield stress, $\bar{\varepsilon}^f$ is the equivalent strain at fracture, C_f and A are the empirically derived fracture constant.

Brozzo et al. (1972) proposed a damage indicator for formability of sheet-metals based on the maximum principal stress, σ_1 , and the hydrostatic stress, σ_m , integrated over the plastic strain, ε_p , as follows:

$$C_f = \int \frac{2\sigma_1}{3(\sigma_1 - \sigma_m)} d\varepsilon_p \quad (2.12)$$

The value of C_f is an empirically derived fracture constant, sometimes referred to as the tearing parameter. A modified version of the tearing parameter was proposed by Wellman (2012) to improve correlation with notched aluminum tensile specimen data. The Heaviside brackets were included to correct for compressive states and the exponent was added to improve correlation with test data, resulting in the modified Brozzo model:

$$C_f = \int \left\langle \frac{2\sigma_1}{3(\sigma_1 - \sigma_m)} \right\rangle^4 d\varepsilon_p \quad (2.13)$$

Johnson and Cook (1985) developed an elaborate damage indicator as a function of stress triaxiality, σ^* , dimensionless strain rate, $\dot{\varepsilon}^*$, and homologous temperature, T^* , using empirical trends to establish a functional form for the fracture strain, ε^f . The Johnson and Cook fracture strain criterion is as follows:

$$\varepsilon^f = [D_1 + D_2 \exp D_3 \sigma^*][1 + D_4 \ln \dot{\varepsilon}^*][1 + D_5 T^*] \quad (2.14)$$

Where the 5 damage variables, D_i , are fitting parameters used to correlate the model to empirical results. The first term in the expression is based on the work of Hancock and Mackenzie (1976).

Additional damage indicator models can be found in the literature with various levels of complexity and sophistication. The majority are based upon an engineering estimate for the functional form of the fracture quantity and contain empirical calibration parameters rather than a characterization of the physical mechanisms of the fracture process. In addition, they are uncoupled from the constitutive material model which limits the ability to model the softening response. Nonetheless, the damage indicator models are widely used due to their ease of implementation and low computational cost.

2.1.5 Continuum Damage Modeling for Ductile Fracture

Continuum Damage Models (CDM) acknowledge the microscopic mechanisms of ductile damage, such as void nucleation, growth and coalescence, that ultimately lead to material failure but choose to address them in a phenomenological manner due to the complexity of the microscopic response under various loading conditions. The work of Lemaitre and Chaboche (1978), Chaboche (1984), Lemaitre (1984, 1985), and Rousselier (1987) established the foundation for early isotropic CDM models that have since been used extensively by European researchers to predict ductile fracture, such as Borvik et al. (1999) and Tanguy and Besson (2002). CDM models assume that as the microscopic damage increases, the macroscopic response of the material exhibits a decrease in stiffness and observable strength (Lemaitre, 1985) which can be characterized by a damage evolution law.

The concept of a damage variable was first introduced by Kachanov (1958) to account for micro-cracking and the concept of an effective stress was later introduced by Rabotnov et al. (1970) as follows:

$$\sigma = (1 - D)\bar{\sigma} \quad (2.15)$$

where, D is the overall damage in the material, σ is the observable stress in the material, and $\bar{\sigma}$ is the effective stress if no damage was present. The damage is assumed to be isotropic in this case (D is a scalar value), which assumes the micro-cracking and internal void orientations/distributions are uniformly distributed in all directions. Figure 2.6 shows a diagram of the effective stress concept where the effective stress is calculated using the undamaged constitutive response model and the observable stress is then calculated based on the evolution of the damage variable which corrects for a reduction in effective area due to internal defects.

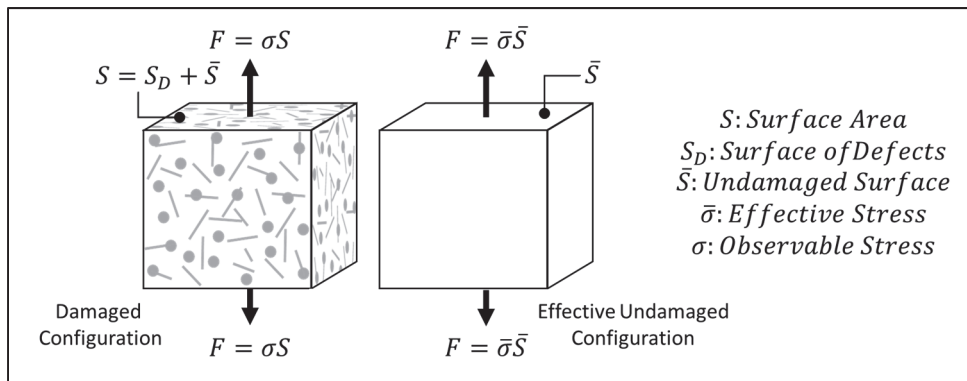


Figure 2.6: Diagram for effective stress concept used in continuum damage modeling

Using the strain equivalence hypothesis of Lemaitre (1972), the strain developed under the observed stress acting on the surface area is equal to the strain developed

under the effective stress acting on the effective area. Assuming linear thermo-elasticity with isotropic damage, the elastic strains can then be defined as (Lemaitre, 1984):

$$\varepsilon_{ij}^e = \frac{\sigma_{ij}(1+\nu)}{E(1-D)} - \frac{\nu}{E} \frac{\sigma_{kk}\delta_{ij}}{(1-D)} \quad (2.16)$$

where, ε^e is the elastic strain tensor, σ is the observable stress tensor, E is the modulus of elasticity and ν is the Poisson's ratio. The damage strain energy release rate, Y , is then defined as (Lemaitre 1984):

$$Y = -\frac{\sigma_{eq}^2}{2E(1-D)^2} f\left(\frac{\sigma_m}{\sigma_{eq}}\right) \quad (2.17)$$

$$f\left(\frac{\sigma_m}{\sigma_{eq}}\right) = \frac{2}{3}(1+\nu) + 3(1-2\nu)\left(\frac{\sigma_m}{\sigma_{eq}}\right)^2 \quad (2.18)$$

where σ_m is the mean (hydrostatic) stress and σ_{eq} is the equivalent stress. The constitutive equation for the kinetic law of damage evolution is then derived based upon the assumption of a dissipation potential and using the normality property of that potential, as described in Lemaitre (1984):

$$\dot{D} = -\frac{\partial\varphi}{\partial Y} \quad (2.19)$$

where φ is the dissipation potential and \dot{D} is the damage evolution law. The dissipation potential function, and corresponding damage evolution law, have not been definitively characterized in the literature. As such, a significant amount of the research has been devoted to defining various forms of the dissipation potential that lead to improved correlations with experimental data.

The dissipation potential defined by Lemaitre is one of the earliest CDM models based on dissipation potential. The approach is sometimes referred to as the Unified Damage Law because it attempts to include ductile damage, creep damage, fatigue damage, and quasi-brittle damage (Lemaitre, 2005). The dissipation potential and damage evolution law are as follows:

$$\varphi = \frac{S}{(s+1)} \left(\frac{-Y}{S} \right)^{s+1} \dot{p} \quad (2.20)$$

$$\dot{D} = \left(\frac{-Y}{S} \right)^s \dot{p} \quad (2.21)$$

where, S and s are material parameters that can be temperature dependent and \dot{p} is the equivalent plastic strain rate.

Tai and Yang (1987) developed an alternative criterion for the dissipation potential as follows:

$$\varphi = \frac{S}{2} \left(\frac{-Y}{S} \right)^2 D \dot{p} \quad (2.22)$$

$$\dot{D} = -\frac{Y}{S} D \dot{p} \quad (2.23)$$

Wang (1992) suggested another form of the dissipation potential, assuming a Ramberg-Osgood hardening law:

$$\varphi = \frac{S}{2(1-D)} \left(-\frac{Y}{S} \right)^2 \frac{(p_c - p)^{\alpha-1}}{p^{2N}} \quad (2.24)$$

$$\dot{D} = \frac{1}{1-D} \left(-\frac{Y}{S} \right) \frac{(p_c - p)^{\alpha-1}}{p^{2N}} \quad (2.25)$$

where, α is a damage coefficient, N is the hardening constant, and p_c is the critical value of the equivalent plastic strain at the critical damage level, D_c .

Chandranth and Pandey (1993) introduced another form of the dissipation potential as follows:

$$\varphi = \frac{S}{2} \left(-\frac{Y}{S} \right)^2 \left[\frac{1}{(1-D)^N} - (1-D) \right] \dot{p} \quad (2.26)$$

$$\dot{D} = \left(-\frac{Y}{S} \right) \left[\frac{1}{(1-D)^N} - (1-D) \right] \dot{p} \quad (2.27)$$

Bonora (1997) devised yet another form of the dissipation potential as follows:

$$\varphi = \frac{S}{2(1-D)} \left(-\frac{Y}{S} \right)^2 \frac{(D_c - D)^{\alpha-1/\alpha}}{P^{(2+N)/N}} \quad (2.28)$$

$$\dot{D} = \left(-\frac{Y}{S} \right) \frac{(D_c - D)^{\alpha-1/\alpha}}{P^{(2+N)/N}} \frac{1}{(1-D)} \quad (2.29)$$

It can be seen that numerous CDM models can be found in the literature with different functional forms for the dissipation potential and damage evolution law. Each of these models assumes isotropic damage where voids and micro cracks are uniformly distributed in all directions. This approach is commonly termed “scalar damage” and is the most commonly used due to simplicity in the implementation. However, the damage may take the form of a 4th order tensor for fully anisotropic damage such as the work of Chaboche

(1984) and Chow and Wang (1987). However, fully anisotropic damage is more challenging to characterize and is rarely used in the literature.

The CDM models presented in this section focus on stress triaxiality and accumulated plastic strain dependencies. However, a more recent approach developed within the MIT Impact and Crashworthiness Laboratory (Xue, 2007; Xue and Wierzbicki, 2008) incorporates the lode angle and hydrostatic stress dependency to improve predictions for a broader range of loading conditions. The number of CDM variants continues to grow as it seems to be the leading candidate for fracture simulations of un-cracked bodies.

2.1.6 Summary of Ductile Fracture Modeling for Un-cracked Bodies

Although progress continues to be made in predicting ductile fracture initiation, a definitive solution has not been identified which is evident by the vast number of approaches in the literature. In addition, only the Johnson and Cook failure strain model includes temperature dependence explicitly, indicating a potential gap in the literature. The blind assessment of various ductile failure models in the Sandia Fracture Challenges (Boyce et al., 2014; Boyce et al., 2016) has demonstrated that various approaches performed equally well in predicting the fracture quantities of interest for ductile failure in complex specimen geometries. Despite the various physical or phenomenological underpinnings, the research indicates that calibration of the model parameters to match the global response, such as load versus displacement, is necessary for all constitutive/fracture models and may be more significant than the form of the model

itself. To the author's knowledge, no research has demonstrated a predictive failure model for ductile metals purely derived from a physical basis such as the evolution of voids and/or dislocations without calibration. As a result, a phenomenological model is assessed to be equally sufficient for describing ductile failure as the physically-based models.

2.2 Elevated Temperature Ductile Fracture

Investigation of the elevated temperature mechanical response of metals emerged in the early to middle part of the 20th century with the increasing demand for applications in energy, nuclear, military and aircraft research. In 1924, the American Society of Mechanical Engineers (ASME) and American Society for Testing Materials (ASTM) identified a need for elevated temperature data which ultimately led to the joint publication on elevated temperature properties of metals in 1932. Creep failure associated with long exposure times were the focus of much of the early research that followed, as summarized in Dorn (1955). Some of the first comprehensive investigations into isothermal tensile strength after short exposure times and yield/rupture temperatures under constant load and rapid heating were first reported by NACA, the National Advisory Committee for Aeronautics (Heimerl et al. 1955, 1956, 1957). However, elevated temperature creep behavior still dominated the literature until the 1970's when research progressed to include fatigue crack growth for estimating elevated temperature service life (Haigh, 1975; Harrison and Sandor, 1971; James 1972a, 1972b; Liaw and Swaminathan, 1989; Raj and Ashby, 1975).

The temperature dependence of the constitutive models to include modifications to the elastic modulus, yield strength, ultimate strength and hardening response has largely been developed in the last several decades. Similarly, there was limited research focused on the development of elevated temperature ductile fracture initiation prior to 1980 as the focus was primarily on isothermal crack propagation. The following sections describe some of the existing approaches to characterize elevated temperature plasticity and fracture initiation.

2.2.1 Elevated Temperature Plasticity

Increasing the temperature of a material is generally thought to decrease the elastic modulus and strength (retract the yield surface) while increasing the strain at fracture (greater ductility). This type of response has been shown experimentally in Heimerl (1956), Gerberich et al. (1962) and Hawkyard et al. (1968) and more recently by Borvik et al. (2005), Erice et al. (2012) and Guo and Nemat-Nasser (2006), among others. Several numerical approaches to describe this response can be found in the literature using various semi-empirical correlations as well as dislocation theory.

The approach most commonly seen in the literature follows the experimental and numerical modeling work of Johnson and Cook (1985) which incorporates a flow stress modifier term based on the homologous temperature, T^* , as follows:

$$\sigma = [A + B\epsilon^n][1 + C \ln \dot{\epsilon}^*][1 - T^{*m}] \quad (2.30)$$

where, σ is the von Mises tensile flow stress, ϵ is the equivalent plastic strain, and $\dot{\epsilon}^* = \dot{\epsilon}/\dot{\epsilon}_0$ is the dimensionless plastic strain rate for $\dot{\epsilon}_0 = 1.0s^{-1}$. The homologous

temperature is defined as $T^*=(T-T_{room})/(T_{melt}-T_{room})$. The material constants A , B , n , C , and m are then used to fit experimental data. The temperature contribution term is simple in nature which has led to its widespread use for elevated temperature research (Borvik et al., 2005; Clausen et al., 2004; Florando et al., 2015). However, the functional form of the modifier term often produces a poor correlation with experimental data, as shown in Clausen (2004). The fit typically captures the response at lower homologous temperatures ($T^*<0.3$) or higher homologous temperatures ($T^*>0.6$) but rarely captures the entire range for ductile metals. Florando et al. (2015) identifies this limitation and suggests a “dual-condition” model where the fitting parameters abruptly change near $T^*=0.5$ to improve experimental correlation. However, the correlation with the dual-condition model is never provided. Nevertheless, the Johnson-Cook (J-C) model is frequently used due to its simplicity even though the functional form of the temperature correction term may require modification in order to capture the response of ductile metals across a broad temperature range.

Zerilli and Armstrong (1987) utilized the experimental results from Johnson and Cook to derive a temperature dependent constitutive model based upon dislocation mechanics in FCC and BCC materials. A formulation for HCP materials, such as titanium, was later introduced by the same authors (Zerilli and Armstrong, 1996). The constitutive model for flow stress in FCC materials is given as follows:

$$\sigma = \sigma_0 + C_2\sqrt{\varepsilon} \exp(-C_3T + C_4T \ln\varepsilon) \quad (2.31)$$

Where, σ_0 is the athermal term associated with Hall-Petch hardening as a function of grain size, ε is the equivalent plastic strain, and T is the temperature. The coefficients C_2 , C_3 , and C_4 are material constants used to fit experimental data. The athermal term is also frequently considered a fitting parameter as the grain size dependency is rarely known.

The Zerilli and Armstrong (Z-A) model provides a coupled strain rate and temperature term which has been reported to improve experimental correlations. The applicability of the model is estimated to be $T^* < 0.5$ (Zerilli and Armstrong, 1987). However, the correlation across the entire temperature range for BCC and FCC materials has been demonstrated using various modified versions of the Z-A model (Voyiadjis and Abed, 2005). The approach isn't clear when analyzing dual phase materials such as duplex stainless steel where a 50-50 distribution of ferrite (BCC) and austenite (FCC) grains are present. Recent attempts have been made to simulate the response of dual phase brass (Farabi et al., 2015) with a modified Z-A model with moderate success using a high reference temperature. Based upon the literature, research is continuing in this area to improve correlations with experimental data.

Another method based on dislocation mechanics is the Mechanical Threshold Stress (MTS) model (Follansbee and Kocks, 1988). The model gets its name based upon the idea of a mechanical threshold which is defined as an extrapolated flow stress at absolute zero where the thermal activation of dislocations is absent. The MTS flow stress is defined as follows (Goto et al., 2000):

$$\sigma = \sigma_0 + (S_i \sigma_i + S_e \sigma_e) \frac{\mu(p,T)}{\mu_0} \quad (2.32)$$

where, σ_0 is the athermal component of the threshold stress, σ_i is the intrinsic component of the flow stress associated with thermally activated dislocations, σ_e is the strain hardening component, p is the pressure, T is the temperature, μ is the shear modulus and μ_0 is the reference shear modulus at absolute zero and ambient pressure. The temperature and strain rate dependent scaling factors (S_i and S_e) are defined as follows (Goto et al., 2000):

$$S_j = \left(1 - \left(\frac{k_b T}{g_j \mu b^3} \ln \frac{\dot{\epsilon}_j}{\dot{\epsilon}} \right)^{1/q_j} \right)^{1/p_j} \quad (2.33)$$

where g_j is a normalized activation energy, b is the Burgers vector, $\dot{\epsilon}$ is the strain rate, $\dot{\epsilon}_j$ is a reference strain rate, k_b is the Boltzmann constant, T is absolute temperature, p and q are fitting parameters. The strain hardening component, σ_e , of the MTS model typically takes the form of a Voce (1948) hardening law while the athermal component, σ_0 , of the threshold stress can be defined as follows (Zerilli and Armstrong, 1987):

$$\sigma_0 = \left(\sigma_f + C_1 \varepsilon_p^n + \frac{k}{\sqrt{d}} \right) \frac{\mu(p,T)}{\mu_0} \quad (2.34)$$

where, σ_f is associated with far field dislocations, C_1 and n are material constants associated with the dislocation density, d is the grain size and k is a material constant associated with the Hall-Petch effect. Similar to the Z-A model, the athermal component is often assumed to be constant and is calibrated to experimental data (Goto et al., 2000).

The MTS model is relatively complex in its description of temperature dependent metal plasticity using dislocation mechanics theory when compared to the phenomenological model of Johnson and Cook. Banerjee (2007) provides a comprehensive comparison of the MTS and J-C model for simulating the strain rate and temperature dependence of high strength 4340 steel with several interesting observations. The MTS model is more complex which led to longer computation times however he found the MTS fitting parameters were easier to calibrate than the J-C model. Banerjee also found remarkable correlations with Taylor impact tests for both the MTS and J-C models even though they are conceptually very different.

Another technique which has seen an increased emphasis in recent years follows the work of Zener and Hollomon (1944). The concept was initially proposed for room temperature and below, but has recently been used to describe the behavior at elevated temperatures (Ashtiani and Shahsavari, 2016; Khamei and Dehghani, 2015; Lin et al., 2010; Rajput et al., 2016; Zhang and Baker, 2004). The Zener-Holloman (Z-H) model assumes that the change in hardening response depends on a single dimensionless parameter, Z , which is a function of strain rate, $\dot{\epsilon}$, and temperature, T , as follows:

$$Z = \dot{\epsilon} e^{-Q/RT} \quad (2.35)$$

where, R is the universal gas constant and Q is the activation energy for deformation. The proposed Z-H hardening law then takes the form $\sigma = f(\epsilon, Z(\dot{\epsilon}, T))$. The most common correlation found in the literature is as follows:

$$\sigma = \frac{1}{\alpha} \ln \left\{ \left(\frac{Z}{A} \right)^{1/n} + \left[\left(\frac{Z}{A} \right)^{2/n} + 1 \right]^{1/2} \right\} \quad (2.36)$$

where, the factors α , n , and A are dependent upon ε and generally are assumed to follow a 6 or 7 term polynomial expansion. An example for α is provided as follows (Ashtiani and Shahsavari, 2016; Lin et al., 2010):

$$\alpha = F_0 + F_1\varepsilon + F_2\varepsilon^2 + F_3\varepsilon^3 + F_4\varepsilon^4 + F_5\varepsilon^5 + F_6\varepsilon^6 \quad (2.37)$$

where, F_i are fitting constants. Although some authors assume α , n , and A are constants (Khamei and Dehghani, 2015), up to 35 parameters must be calibrated when each variable is assumed to follow a 7 term polynomial expansion (Ashtiani and Shahsavari, 2016).

The models described above for Z-A, MTS, and Z-H follow a more complex coupled form of the equations for flow stress while many of the other models found in the literature take a multiplicative contribution form, similar to the J-C model:

$$\sigma = f(\varepsilon)f(\dot{\varepsilon})f(T) \quad (2.38)$$

Table 2.1 shows a subset of potential strain and strain rate dependent terms used for approximating the flow stress. The strain dependency is generally cast in terms of effective plastic strain with the exception of the Prager and Hollomon models which are cast in terms of total logarithmic strain as they were early attempts to capture the elastic and plastic response in a single equation. The parameters C_i represent material constants used for fitting data and the reference strain rate, $\dot{\varepsilon}_0$, can also be considered a fitting parameter.

Table 2.1: Various strain and strain rate dependent flow stress modifier terms

$f(\epsilon)$		$f(\dot{\epsilon})$	
Ludwik (1909)	$\sigma = C_1 + C_2 \epsilon^{C_3}$	Cowper and Symonds (1957)	$1 + \left(\frac{\dot{\epsilon}}{\dot{\epsilon}_0}\right)^{1/C_1}$
Zener (1946)	$\sigma = C_1 \left(\frac{\epsilon}{C_2}\right)^{C_3}$	Ludwik (1909)	$\log\left(\frac{\dot{\epsilon}}{\dot{\epsilon}_0}\right)$
Prager (1938)	$\sigma = C_1 \tanh\left(\frac{E\epsilon}{C_1}\right)$	Sokolowsky (1948)	$\log\left(1 + \frac{\dot{\epsilon}}{\dot{\epsilon}_0}\right)$
Voce (1948)	$\sigma = C_1 + C_2 \epsilon + C_3 (1 - e^{-C_4 \epsilon})$	Johnson and Cook (1985)	$1 + C_1 \ln\left(\frac{\dot{\epsilon}}{\dot{\epsilon}_0}\right)$
Swift (1952)	$\sigma = C_1 (\epsilon + C_2)^{C_3}$	Kobayashi and Dodd (1989)	$\dot{\epsilon}^{C_1}$
Schreyer (2005)	$\sigma = C_1 + C_2 \tanh(C_3 \epsilon)$		

The temperature dependent flow stress modifier term has been proposed by many researchers using various forms, as shown in Table 2.2, where T_o represents a reference temperature and T_m is the melt temperature. Many of the terms are slight modifications or simplifying cases of one another, generally chosen to best fit experimental data. Using any combination of the strain, strain rate and temperature modifier terms provides a different multiplicative contribution model. For instance, the J-C model can be reproduced using the strain hardening function of Ludwik with the strain rate and temperature modifier terms developed in Johnson and Cook. Likewise, the model proposed in Kobayashi and Dodd (1989) is roughly the combination of the Hollomon, Kobayashi, and Litonsky terms. Other models certainly exist in the literature that may have been overlooked however this provides a general overview based upon the summary found in Hor et al. (2013).

Table 2.2: Various temperature dependent flow stress modifier terms

$f(T)$	
Johnson and Cook (1983)	$1 - \left(\frac{T - T_0}{T_m - T_0}\right)^{C_1}$
Litonsky (1977)	$1 - \frac{T}{T_m}$
Vihn et al. (1980)	$\exp\left(\frac{C_1}{T}\right)$
Zhao and Gary (1996)	$1 + C_1(T - T_0)$
Hor et al. (2013)	$1 - C_1\left(\frac{T - T_0}{T_m - T_0}\right)^{C_2}$
Hensel and Spittel (1979)	$\exp(C_1T)$
Chen et al. (2006)	$C_1 - \frac{(T - C_2)^{C_3}}{C_4}$
Zener and Hollomon (1944)	$\exp\left(\frac{Q}{RT}\right)$

The multiplicative contribution models garner much of the attention within the literature due to ease of implementation and simplified calibration process with each term being uncoupled. However, many researchers have focused on coupled models, such as the Z-A, MTS, and Z-H models, to improve experimental correlations. Another common approach to developing a coupled constitutive model is to simply make the calibration factors within a multiplicative contribution model a function of the other variables such that the cross-correlation between strain hardening, strain-rate and temperature are quantified. A select number of the coupled flow stress models are provided in Table 2.3.

Table 2.3: Coupled flow stress models for strain, strain rate, and temperature dependence

$\sigma(\varepsilon, \dot{\varepsilon}, T)$	
Lechler et al. (2008)	$\sigma = C_1 \exp\left(\frac{C_2}{T}\right) (C_3 + \varepsilon)^{C_4(T)} \dot{\varepsilon}^{C_5(T)}$
Hensel and Spittel (1979)	$\sigma = C_1 e^{C_2 T} \varepsilon^{C_3} \dot{\varepsilon}^{C_4} e^{\left(\frac{C_5}{\dot{\varepsilon}}\right)} (1 + \varepsilon)^{C_6 T} e^{C_7 \varepsilon} \dot{\varepsilon}^{C_8 T} T^{C_9}$
Baker (2006)	$\sigma = C_1(T) \varepsilon^{C_2(T)} \left(1 + C_3 \ln\left(\frac{\dot{\varepsilon}}{\dot{\varepsilon}_0}\right)\right)$
Tari and Worswick (2015)	$\sigma = \left(C_1 + C_2 \left(1 - \exp\left(C_3 * \frac{T - T_r}{T_m}\right)\right)\right) (\varepsilon + \varepsilon_0)^{C_4(T)} \dot{\varepsilon}^{C_5(T)}$
Mulyadi et al. (2006)	$\sigma = C_1 \lambda Z^{C_2} (1 - \exp(-C_3 \varepsilon)) \text{ where, } Z = \dot{\varepsilon} \exp\left(\frac{Q}{RT}\right)$
Hor et al. (2013)	$\sigma = (C_1 + C_2 \varepsilon^n) \left(D + (1 - D) \tanh\left(\frac{1}{\varepsilon + \varepsilon_a}\right)\right) \left(1 - C_3 \left(\frac{T - T_0}{T_m - T_0}\right)^{C_4}\right)$ $\text{where, } D = 1 - \left(\frac{p\varepsilon}{1+p\varepsilon}\right) \tanh\left(\frac{T - T_0}{T_{rec} - T_0}\right)$

The literature shows a vast number of approaches for simulating the temperature dependence of the plastic response in ductile metals. Surprisingly, the models can be vastly different yet the authors report close correlation (generally within 10%) with experimental data in almost all cases. However, the applicability of the model may be a result of the material behavior and limited conditions for which they are calibrated and used. In addition, physically based models (MTS) and phenomenological models (J-C) were shown to provide comparable results when calibrated to the same data, resulting in close correlations with experiments for both models (Banerjee, 2007). As a result, it seems the calibration process may be the most important consideration, suggesting the constitutive approach should be selected as the simplest model capable of simulating the material and conditions of interest.

2.2.2 Elevated Temperature Fracture Initiation

A considerable amount of research has been presented in the literature on the temperature dependent constitutive behavior of metals as a function of temperature. However, the constitutive model development has largely focused on understanding and modeling the plastic response with limited concern for post-peak behavior. The primary result is often a goodness-of-fit with empirical data from which the models were calibrated. Although some researchers have provided correlations with cutting force (Baker, 2006), deep drawing force-displacement (Tari and Worswick, 2015), and deformation during Taylor impact tests (Johnson and Cook, 1985; Banerjee, 2007), there has been little research on temperature dependent fracture initiation which is required for analyzing catastrophic damage of uncracked bodies.

Elevated temperature fracture research has primarily focused on creep (Cowan and Khandelwal, 2014; Mukherjee et al., 1968; Saxena, 1991; Zhang and Lee, 1993), fatigue crack growth (Haigh, 1975; Harrison and Sandor, 1971; James 1972; Liaw as Swaminathan, 1989), and traditional crack extension models such as J-integral (Lee and Park, 1992; Mills, 1980; Provenzano et al., 1981), Crack-tip Opening Displacement (Schweizer, 2016; Tran et al., 2001), and fracture toughness/resistance (Choe et al., 2001). The following summary describes some of the few elevated temperature fracture initiation experiments and models found in the literature since the influential work of Johnson and Cook (1985) on temperature dependent fracture strain.

Tang et al. (2016) calibrated a Hensel-Spittel Model (Table 2.3) with a modified Lemaitre CDM dissipation potential (Bouchard et al. 2011) to simulate the response of high strength steel during hot stamping. The model was calibrated and applied in the 550°C to 850°C temperature range where ferrite phase transformation is assumed to be suppressed. The model was validated against Nakajima tests and the force-displacement curves were compared along with the crack initiation, propagation and coalescence paths.

Borvik et al. (2005) calibrated a modified J-C flow stress model for Weldox 460E steel where the J-C strain rate dependency term was replaced with a Cowper-Symonds term (Table 2.1). The model was then coupled with a simple linear damage evolution law proposed by Borvik et al. (2001). The calibrated models were compared back to the tensile specimens with reasonable correlations. However, the authors acknowledge the temperature dependency term of Johnson and Cook may be inadequate for the temperature range of interest (100-500°C) based on experimental observations for Weldox 460E.

Barton et al. (1994) calibrated the fracture strain of pure iron and copper between room temperature and 400°C using a modified damage indicator model. The model is based on a parameterized version of the Rice-Tracey criterion with the addition of a linear correlation of fracture strain with temperature. Although a fracture initiation criterion is determined, no temperature dependence of the flow stress is characterized and no validation is performed. Similarly, Tinetti et al. (2004) characterized a GTN void growth

model for 304 stainless steel and Bonora and Milella (2000) characterized a custom flow stress and CDM model at elevated temperatures without providing validation.

Calamaz et al. (2010) characterized a modified J-C model for hot machining of titanium alloys. The model was used to simulate hot machining and the cutting force/speed were compared with experiments. Umbrello et al. (2004) characterized a modified J-C model with a Brozzo damage indicator model for hot machining and compared well with cutting force and chip morphology. Umbrello (2008) also attempts to simulate high speed machining of titanium alloy using a traditional J-C model. Other researchers (Clausen et al., 2004; Erice et al., 2012; Florando et al., 2015; Seidt and Gilat, 2013; Ulacia et al., 2011) have calibrated different forms of the J-C model at elevated temperatures without providing validation for fracture initiation.

Dempsey et al. (2012) characterized a tabular thermo-elastic constitutive model for 304L stainless steel along with a modified Brozzo damage indicator model. The model was validated for predicting critical pressure in locally heated pressure vessels at a steady thermal condition (near isothermal in a local region). However, the crack initiation location and failure pattern were not provided. Similarly, Manu et al. (2009) investigated the failure time predictions for pressure vessels subjected to fully engulfing fuel fires using a creep damage model however crack initiation and growth was not predicted.

Review of the literature produced a limited number of investigations to predict crack initiation in un-cracked bodies under elevated temperature conditions, with even fewer performing model validation. The existing techniques are heavily influenced by the

Johnson-Cook model even though several authors have acknowledged the limitations of the temperature dependent flow stress modifier term. The literature also shows the majority of researchers have chosen to use damage indicator or continuum damage approaches for simulating fracture initiation at elevated temperatures. The choice to use continuum damage modeling is not surprising since it appears to be a leading candidate for fracture initiation under ambient conditions (Boyce et al., 2016). A general form of the CDM approach is proposed for this research to quantify the effect of stress triaxiality and temperature on the yield, hardening and material damage for predicting elevated temperature failure of a ductile metal.

Chapter 3 : Material Selection and Characterization

Ductile metals are extensively used in structural designs because of their cost and manufacturability characteristics. For this reason, large structures, ships, pipelines and pressure vessels have traditionally been made of steel alloys. Within the past 50 years there has been an increased demand for metals with greater resistance to corrosion from harsh environments such as offshore oil fields or low-grade petroleum wells with high amounts of hydrogen sulfide. Duplex Stainless Steel (DSS) emerged as a key corrosion resistant material for offshore drilling in the North Sea during the late 1970's. DSS has near equal proportions of ferrite and austenite which combines several beneficial properties of ferritic and austenitic steels resulting in high strength and ductility while also having good resistance to corrosion, abrasion, and fatigue.

The excellent strength and corrosion resistant properties of DSS, particularly with respect to stress corrosion cracking, led to a widespread increase in use for power plants, industrial plants, chemical containment, petrochemical, desalination, nuclear, storage and transportation industries (Chung, 1992; Tucker et al., 2015). Failure of DSS components in these industries due to extreme thermal conditions caused by fire or terror/military attack could result in catastrophic loss of life and property. As a result, DSS was chosen as the focus of this study with the expectation that the resulting method could be applied to other ductile metals at elevated temperatures.

While there are several established commercial DSS products, new grades are constantly emerging for specialized applications. For example, numerous patents have

been submitted within the past 20 years for new alloy compositions and manufacturing methods (Azuma and Ogawa, 1997; Park et al., 2000; Bergstrom et al., 2004; Yamada et al., 2012; Motoya et al., 2017). The remainder of this chapter will focus on characterization of the DSS used in this study which was selected based on material availability. The chemical composition, microstructure, room temperature strength, coefficient of thermal expansion, thermal conductivity, specific heat, and absorption will be detailed in the following sections. The elevated temperature strength and fracture characteristics will be reported in later chapters, as it is the primary focus of this dissertation.

3.1 Composition and Microstructural Analysis

The various grades of DSS tend to favor a different mix of ferrite and austenite phase based on the constituents of “Ferritizers” such as Cr (chromium), Si (silicon), Mo (molybdenum), W (tungsten), Ti (titanium), Nb (niobium) and “Austenitizers” such as C (carbon), Ni (nickel), Mn (manganese), N (nitrogen), Cu (copper). As a result, the material composition and microstructure are used to define the material. The chemical composition describes the percent of material constituents while the microstructure describes the percent of austenite and ferrite.

The compositions were obtained by spark Optical Emission Spectroscopy (OES) and Energy Dispersive X-Ray Spectroscopy (EDX). OES is a technique that creates an electrical arc on the material resulting in vaporization which emits characteristic light. The light is then separated by wavelength using a diffraction grating and the intensity is

measured to determine the concentration of each element. EDX is a technique that is used in conjunction with a Scanning Electron Microscope (SEM) that detects x-ray emission during bombardment of the sample with an electron beam. The x-ray energy spectrum is then evaluated to determine the elemental composition. The results of the OES measurements are provided in Table 3.1. The EDX device is not sensitive to lower atomic number elements such as copper and nitrogen so it was used as a secondary measurement. The EDX measured 70.8% Fe, 22.7% Cr, 5.2% Ni, 0.6% Mn, 0.57% Si, and 0.22% Ti. The EDX results were consistent with the OES for the largest constituents although some variation was seen for the measured Mn and Si content.

Table 3.1: Chemical composition and phase percentage of DSS sample from OES

Element	Symbol	Weight %
Chromium	Cr	23.3
Nickel	Ni	5.1
Silicon	Si	0.37
Titanium	Ti	0.23
Manganese	Mn	0.3
Copper	Cu	0.3
Carbon	C	0.08
Molybdenum	Mo	0.04
Phosphorus	P	0.025
Nitrogen	N	0.02
Cobalt	Co	0.09
Tungston	W	0.02
Niobium	Nb	0.01
Sulfur	S	0.007
Aluminum	Al	<0.01
Vanadium	V	<0.01
Tin	Sn	<0.01
Iron	Fe	Remainder (~70)

In order to determine the microstructure, small samples were cut parallel and perpendicular to the rolling direction of the sheet material. The small samples were then embedded in phenolic resin and ground using progressively finer grinding paper (180, 240, 320, 400, 600, and 800 grits). After grinding, the samples were polished with 3 μm ,

1 μm , and 0.25 μm diamond particles. The polished samples were then chemically etched using cupric chloride and hydrochloric acid solution (CuCl_2 – 5 g, HCl – 100 ml, ethyl alcohol – 100 ml, H_2O – 100 ml). The solution interacts with the ferrite phase more readily than the austenite phase resulting in distinct contrast that can be observed via Scanning Electron Microscope (SEM). The etched cross-section parallel to the rolling direction is shown in Figure 3.1 and the cross-section perpendicular to the rolling direction is shown in Figure 3.2. The ferrite phases interact with the solution more which results in a darker appearance due to a deeper etching. The austenitic phases are lighter in color since they protrude slightly. The distinct duplex phase can be seen in the SEM images with alternating layers of ferrite and austenite phases. In addition, the layers appear to be mainly single phase with few inclusions.

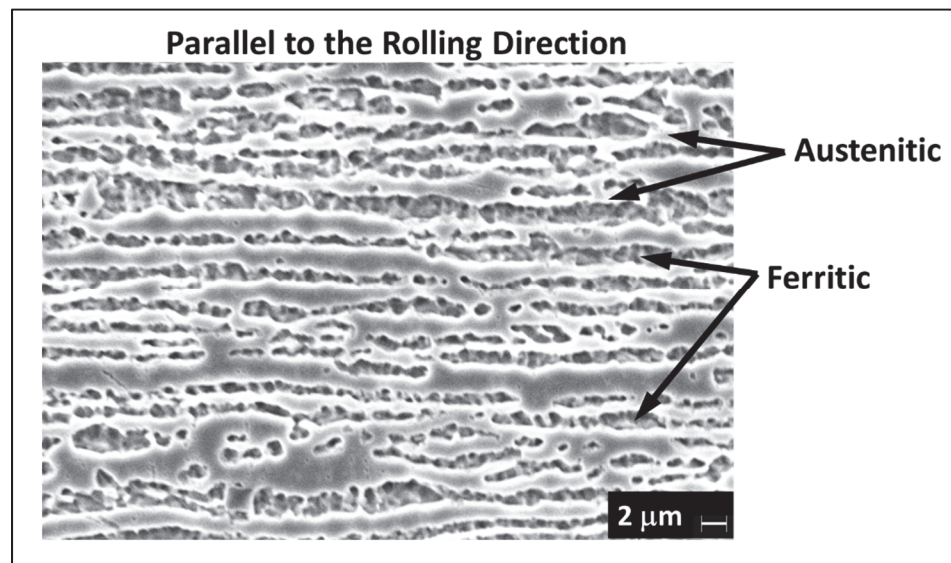


Figure 3.1: Scanning Electron Microscope image of the etched DSS cross-section showing distinct duplex structure of ferrite and austenite phases for a cross-section parallel to the rolling direction

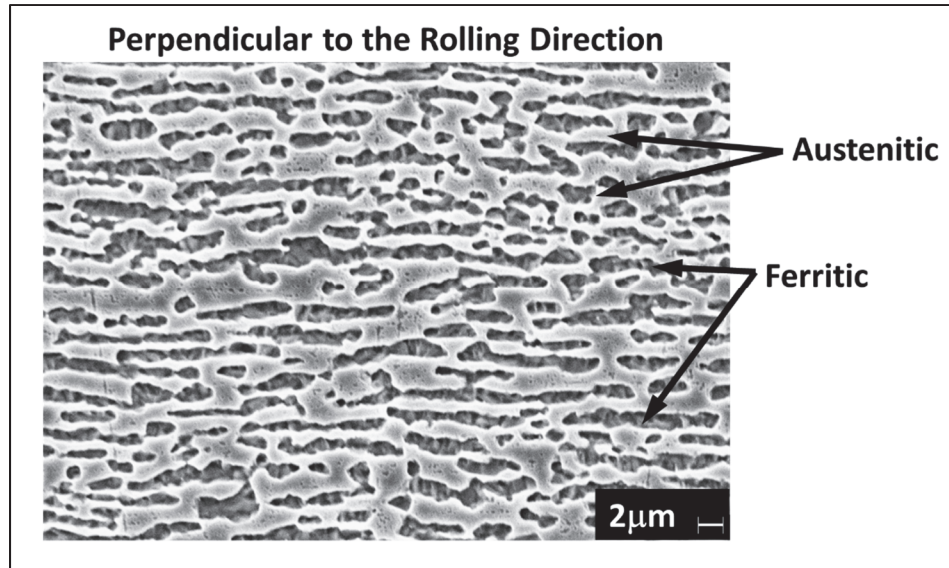


Figure 3.2: Scanning Electron Microscope image of the etched DSS cross-section showing distinct duplex structure of ferrite and austenite phases for a cross-section perpendicular to the rolling direction

The percent of austenite and ferrite phase was determined by contrast segregation of the SEM images using digital image analysis software. The microstructure was determined to be approximately 44% ferrite and 56% austenite. The near equal proportions of each phase is not surprising as this is a characteristic of most DSS material.

3.2 Thermal Properties at Elevated Temperatures

The thermal-physical properties are needed to properly simulate the transient thermal conditions that will be observed in the experiments designed for validation of the fracture initiation model, which will be discussed in a later chapter. The specific heat and density of the material must be determined as a function of temperature to define the heat capacity of the material which describes the amount of energy required to raise the temperature of the material. A Differential Scanning Calorimeter (DSC) method, following ASTM E1269, was used in this study since DSC is one of the most common and accurate

methods for determining specific heat at elevated temperatures. Using the Netzsch Model 404 DSC, the specific heat was determined from room temperature to 1200°C. The results are shown in Figure 3.3.

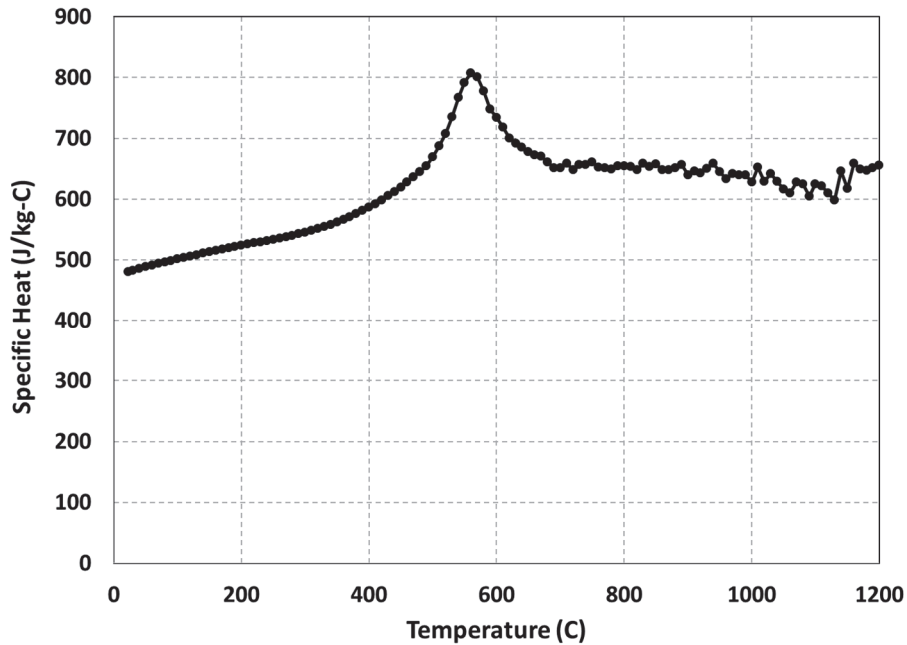


Figure 3.3: Temperature dependent specific heat using differential scanning calorimeter

The melt temperature was determined using a graphite tube furnace to melt the sample while monitoring the sample temperature. The onset of melt was observed at 1466°C and was completed at 1476°C. Since the specific heat was not determined in the range of 1200°C to 1476°C, a constant specific heat corresponding the last measured value was assumed and a latent heat of fusion of 285 kJ/kg was added in the range of 1466-1476°C.

The thermal diffusivity was determined using the laser flash method, following ASTM E1461. A custom device at the Thermophysical Properties Research Laboratory Inc. (TPRL) was used to determine diffusivity at time durations down to 40 microseconds. The

apparatus consists of a Korad K2 laser, vacuum system, and metallic heater tube surrounding the sample. The bulk density was determined to be 7685 g/cm³ based on sample volume and mass. Although the density is lower than the 7810 g/cm³ often used for traditional steel, it is consistent with values reported for other DSS variants (International Molybdenum Association, 2009). The thermal conductivity was then calculated from the diffusivity, specific heat, and density using the following relationship:

$$\alpha = \frac{\kappa}{\rho C_p} \quad (3.1)$$

where, α is the thermal conductivity, κ is the thermal diffusivity and ρ is the bulk density. The results are shown in Figure 3.4. The data is sparser for conductivity than specific heat because each data point represents one experiment while the DSC dataset is collected during a single experiment. The sample must be brought up to the target temperature in the heater tube then the laser impulse adds radiant energy and the rear surface temperature history is used to determine diffusivity. Similar to the specific heat, a constant conductivity was assumed above 1200°C corresponding the last measured value. Although linear extrapolation may be more representative, temperatures above 1200°C are not anticipated as the structural loads will likely induce failure below this temperature.

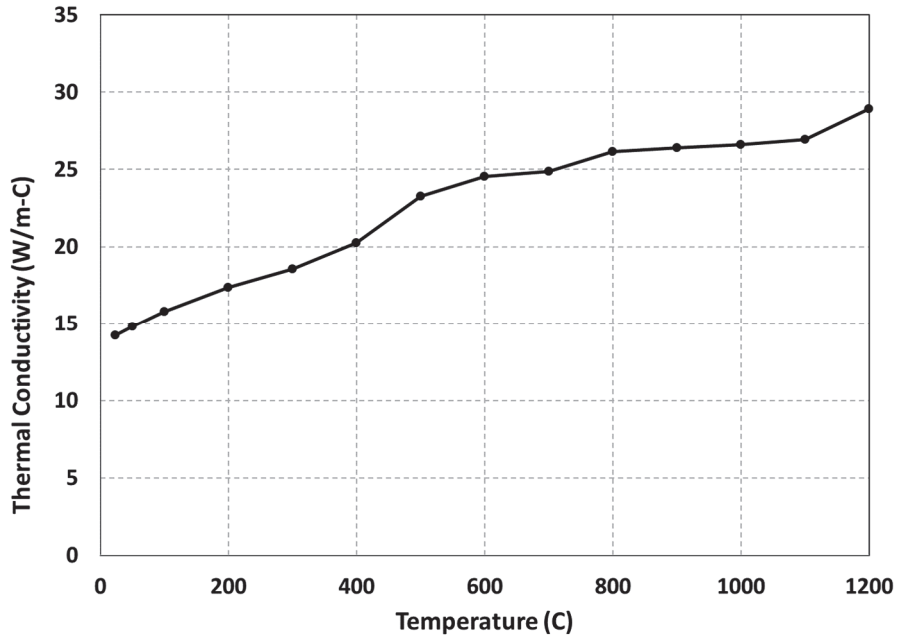


Figure 3.4: Temperature dependent thermal conductivity determined from laser flash method

3.3 Thermal Expansion at Elevated Temperatures

The coefficient of thermal expansion (CTE) will play a role in the deformation behavior of the pipeline and vessels subjected to localized heating. As the local temperature changes, the metal will attempt to expand while being confined by the cooler material outside of the heated zone resulting in a local bulge associated with material expansion and internal pressure, as discussed in Birk et al. (2006) and Romero et al. (2014). The CTE was determined using a dual push-rod dilatometer (Theta Dilatronics II) from 100°C to 1100°C, following ASTM E228. The results, shown in Figure 3.5, were consistent with published values for DSS in the range of 100-500°C (International Molybdenum Association, 2009).

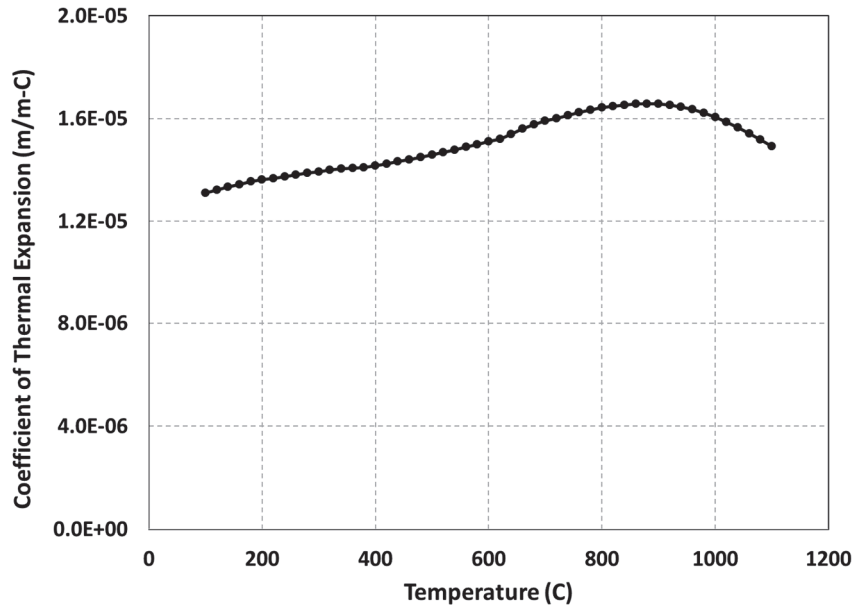


Figure 3.5: Temperature dependent thermal expansion

3.4 Elastic Properties of DSS

In order to characterize the room temperature elastic properties, Young's modulus and Poisson's ratio, a standard tensile specimen was mounted with strain gages and tested in a tensile MTS system. The strain gages (EA-06-125BZ-350 by Micro Measurements) were placed in the axial and transverse directions with one set mounted to the front and one set mounted to the back surface of the specimen (Figure 3.6). The strain gages were connected as two active arms on opposite positions in the Wheatstone bridge circuit of a Dynamics Model 7600A transducer signal conditioner/amplifier.

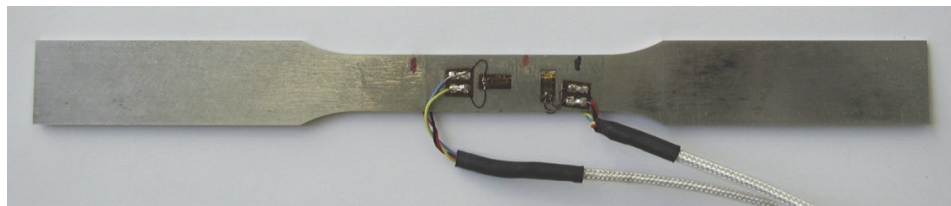


Figure 3.6: Tensile specimen for room temperature elastic properties

The specimen was then loaded while recording the force as a function of time via the MTS software and strain gage output via Nicholet oscilloscope. The results of strain versus time and stress versus time are shown in Figure 3.7 and Figure 3.8, respectively.

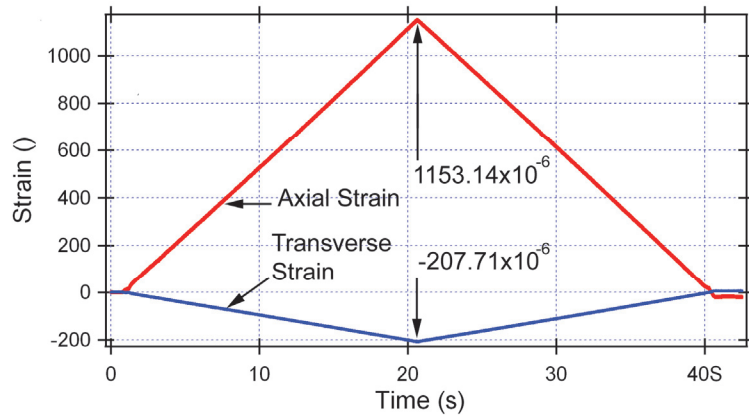


Figure 3.7: Axial and transverse strain while loading the specimen in the elastic regime

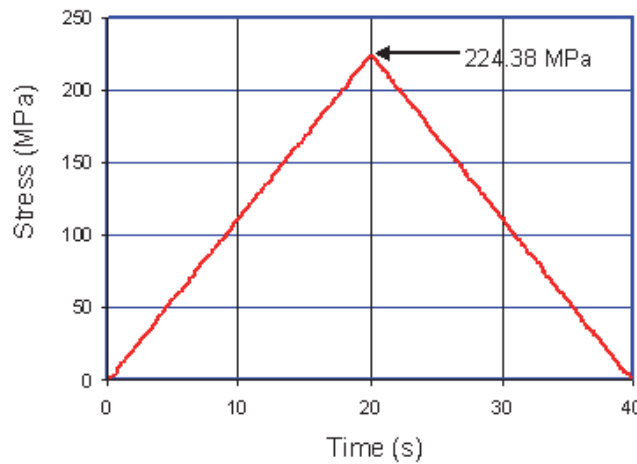


Figure 3.8: Calculated stress based on force history corresponding to strain measurement

The Poisson's ratio was obtained by dividing the peak transverse strain by the peak axial strain resulting in a value of 0.18. The Poisson's ratio is lower than a traditional value for steel of 0.3 but was consistent with values found in the literature for other stainless steels (Tane et al., 2003). The modulus was obtained by dividing the peak stress by the

peak strain resulting in a value of 194.6 GPa, which is consistent with the traditional range for steels (180-210 GPa).

3.5 Total Reflectance at Elevated Temperatures

The absorption of thermal energy is a critical factor for simulating transient heating and elevated temperature failure. In many extreme thermal environments, the structural loads are constant and thermal weakening of the structure ultimately leads to failure. As a result, the prediction of critical exposure time is highly dependent on the absorbed thermal energy. Several heating methods will be discussed in subsequent chapters but a Near-InfraRed (NIR) laser source was ultimately chosen for the validation experiments due to the accuracy and adjustability of the impinging heat flux as compared to high intensity heat lamps or fuel burning methods. Since metals are surface absorbers, the reflectance, R , as a function of temperature can be used to determine the absorptance, α , using:

$$\alpha(T) = 1 - R(T) \quad (2.2)$$

The wavelength specific surface absorptance (corresponding to the laser wavelength) was determined using a custom device at the Temperature-dependent Reflectance of Aerospace Materials (TRAM) laboratory at the Air Force Research Laboratory (AFRL), as this is a non-standard measurement. The TRAM device consists of heater and probe lasers of varying wavelengths, a gold coated hemi-ellipsoid dome, beam shaping optics and a multitude of diagnostics to monitor the laser characteristics as well

as the sample temperature and total reflected energy as a function of time. The general layout of the TRAM laboratory is shown in Figure 3.9.

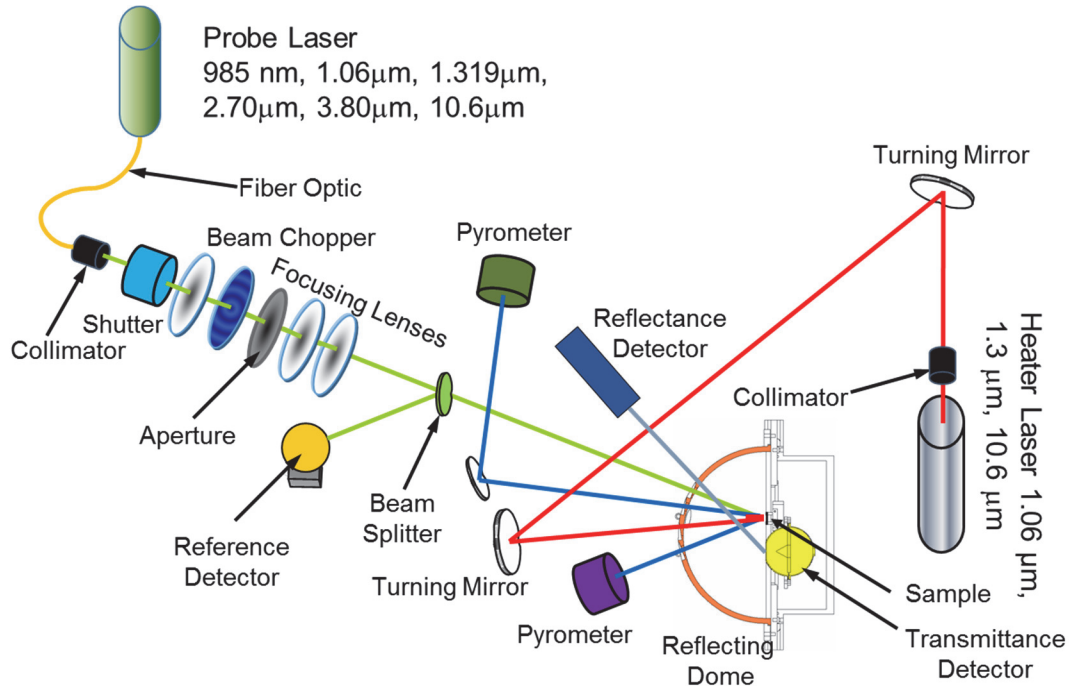


Figure 3.9: TRAM laboratory configuration used to determine temperature dependent surface reflectance

The DSS test articles were painted black for the validation experiments using high temperature paint to increase energy absorption and surface uniformity in comparison to the as-received condition. The TRAM experiments were able to capture the total reflectance up to 600°C and then the absorptance was calculated using Equation 2.2. Figure 3.10 shows the increase in absorptance from a typical value of approximately 50% for the as-received condition up to 80-85% with the black paint, along with relatively good stability over the temperature range. The measurement uncertainty was approximately 9% based on the measurement uncertainty for total applied power and reflected power.

The absorption up to 1000°C was desired but this was not achievable with the available heater source so the higher temperature values were extrapolated.

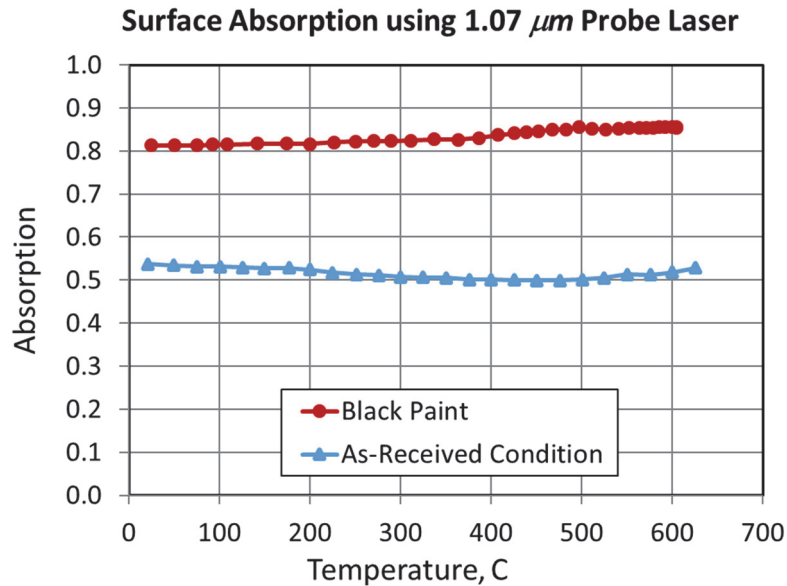


Figure 3.10: Temperature dependent absorptance of black Stove Bright® paint at 1.07 μm

3.6 Summary

The material characterization in this chapter focused on the measurements that are common in the literature, with the exception of the temperature dependent reflectance measurements. The material composition, microstructure, thermal conductivity, specific heat, density, melt temperature, coefficient of thermal expansion, optical absorption, and room temperature elastic properties were all determined.

The following chapter details the elevated temperature tensile testing which will be used to determine the change in elastic modulus, yield strength and ultimate strength with temperature as well as capturing the post peak behavior for characterizing the continuum damage model for simulating elevated temperature fracture.

Chapter 4 : Elevated Temperature Tensile Testing

Elevated temperature material strength characterization in metals traditionally begins with pseudo-static tension tests to determine the elastic modulus, yield and ultimate strengths. The stress-strain response is commonly used to define the plastic flow curve and is extrapolated to multi-axial stress states using the von Mises stress and equivalent plastic strain. Tensile tests also provide a stress state which corresponds well to the panel validation experiments, which will be discussed later in this manuscript. Alternative elevated temperature tests found in the literature include isothermal split Hopkinson and hot compression tests which are used for high strain rate and metal forming applications, respectively. Tensile testing provides the most representative load case and will be used in this study for determining the elevated temperature elastic modulus, yield strength, ultimate strength, and material damage characterization.

Numerous researchers have demonstrated the ability to perform high temperature tensile testing for characterization of the material response up to ultimate strength (Antoun 2004; Coer et al., 2011; Colley et al., 2004; Florando et al., 2015; Gerberich et al., 1962; Manu 2008; Sajjadi et al., 2002; Sakumoto et al. 1996; Ulacia et al., 2011). However, the literature is lacking in the description of the post-peak behavior of materials at elevated temperatures. Most of the approaches provide mechanical loading with an electro-mechanical universal testing machine commonly used for room temperature measurements with the addition of a sample heater. The heating methods

can be separated into four basic categories; resistive, furnace, broadband InfraRed (IR), and laser heating.

Resistive heating leverages the electrical resistance of a metallic material to heat the sample by controlling the applied current. Feedback from a thermocouple located at the point of minimum cross-section, where heating will be greatest, is used to adjust the electrical current to raise and then stabilize the sample temperature. The Gleeble 3500 (Figure 4.1), by Dynamic Systems Incorporated, is a common thermomechanical testing apparatus that utilizes a resistive heating technique. The manufacturer specification for the Gleeble 3500 system advertises heating rates in excess of 10,000°C/s. However, the heat uniformity in the sample is compromised once strain localization occurs due to a reduction in cross-sectional area. The area reduction results in higher temperature in the localization zone than the rest of the gage length. As a result, the technique is adequate for characterizing elevated temperature mechanical response up to the ultimate tensile strength but is unable to maintain isothermal conditions after peak load is reached.

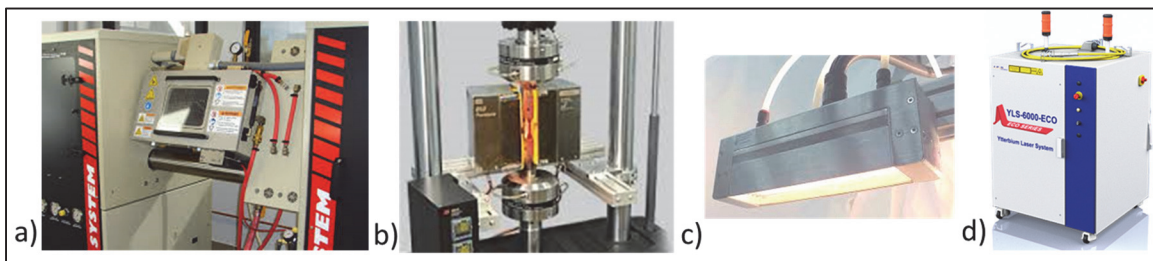


Figure 4.1: Possible tensile specimen heating devices: a) Gleeble 3500 (resistive heating) b) MTS Model 653 (Furnace heating) c) Hi-TempIR Model 5209 (Broadband IR heating) d) IPG Photonics YLS-6000 (Laser heating)

Furnace heating is a more traditional approach accomplished with electrical heating elements within a thermal isolation enclosure commonly constructed with ceramic. The enclosure is preheated and then placed around the gage length of the tensile sample and the heating elements are controlled using thermocouple feedback of the surface temperature. The MTS Systems Corporation Model 653 furnace (Figure 4.1) is one example of a furnace specifically designed for tensile testing configurations. Furnace heating is capable of maintaining isothermal sample temperature through the process of strain localization and failure. The heating rate is several orders of magnitude smaller than resistive heating, at approximately 100°C/min, but provides a similar heating rate to experiments for pressure vessels within an engulfing fuel fire (Birk et al., 2006). The primary limitation of furnace heating is the sample enclosure which does not allow for imaging based measurements such as digital image correlation displacement measurements or stereoscopic full field strain measurements.

Broadband IR heating is another heating method which uses a light emitting source, typically a quartz-halogen lamp, to produce a broadband emission that usually encompasses the visible and near IR spectrums. The heating is caused by surface absorption of the emitted light so a controlled and localized heating can be easily achieved. An example of a broadband IR heater is the Hi-TempIR Model 5209 (Figure 4.1) which produces 6 KW of power output and heating rates in excess of 100°C/min. Since IR heating does not rely on enclosure radiation, heating can be done from a single side of the sample which enables imaging-based diagnostic methods. However, the temperature

gradient through the thickness may require cycling of the IR sources to reach temperature uniformity for high heating rates.

The final method uses laser radiation to provide a similar heating approach to broadband IR with the exception that they are able to produce extremely high heating rates in excess of 10,000°C/s. An example of a common high energy industrial laser is the IPG Photonics YLS-6000 (Figure 4.1). In contrast to broadband IR sources, laser emission is in a very narrow spectrum with a typical line width of less than 20 nm. The energy can be collimated using optics and the energy distribution can be adjusted using a beam integrator, resulting in a well characterized and uniform heat flux on the sample. The primary limitations of using a laser based heating system are the cost and additional laboratory safety measures needed to operate a class 4 laser system.

An electro-mechanical universal testing system load frame from MTS Systems Incorporated (Model 312.22) and a broadband IR heating system from Hi-TempIR, model 5209 described above, was selected to perform the elevated temperature tensile tests. Using the broadband IR heating system provided heating rates representative of an engulfing fuel fire while enabling imaging of the sample during testing. Further discussion of the imaging based diagnostics will be provided later in this chapter.

4.1 Tensile Specimen Geometry

Standard tensile specimen geometries are defined in ASTM E21-09 for elevated temperature tension tests of metallic materials. Although circular cross-section specimens are preferred, an exception is made for sheet and strip materials which allow

for a rectangular cross-section since the rolling process may modify the strength characteristics. The ASTM standard also specifies the sample to be fabricated such that the axis of the specimen is in the direction of fabrication (i.e. the rolling direction for sheet material). In this study, the validation experiments were constructed of 1.5 mm thick rolled sheet material for the panel and pressure vessel geometries therefore rectangular cross-sections were used.

The emphasis of this work on post-peak mechanical behavior introduces several challenges which impact the specimen geometry. Firstly, it is challenging to capture the deformation in the localization zone due to the randomness of the fracture location in a traditional flat specimen, sometimes occurring along a 45° shear band. Secondly, the study of fracture in ductile metals at room temperature has shown that the rate of damage accumulation and the effective plastic strain at fracture are functions of triaxiality (Bao 2004; Bonora et al., 2005; Mackenzie et al., 1977). Researchers have most commonly used round bar tensile specimens with varying notch radii to investigate this phenomenology. However, Bron et. al. (2004) demonstrated a similar phenomenology in the rupture of sheet material by varying the notch severity in rectangular cross-section samples. The use of edge notched samples allows for variation in the triaxiality but it also forces the localization and fracture to occur perpendicular to the loading direction and at the location of minimum sample width, greatly simplifying measurement of the instantaneous cross-sectional area.

In this study, rectangular cross-section specimens with two different edge notches were used to characterize the elevated temperature response of DSS. The samples were

machined such that the loading direction is parallel to the rolling direction of the sheet material. The larger notch, called the C-notch specimen, has a semi-circular shape with a 1 cm radius and 5 mm minimum cross-sectional width (Figure 4.2). This geometry provides a nearly uniform stress across the width whilst being sufficiently narrow to induce necking perpendicular to the axis of the specimen. Furthermore, the C-notch provides visual access to the minimum cross-sectional area for monitoring deformation in both the width and thickness directions using digital image correlation.

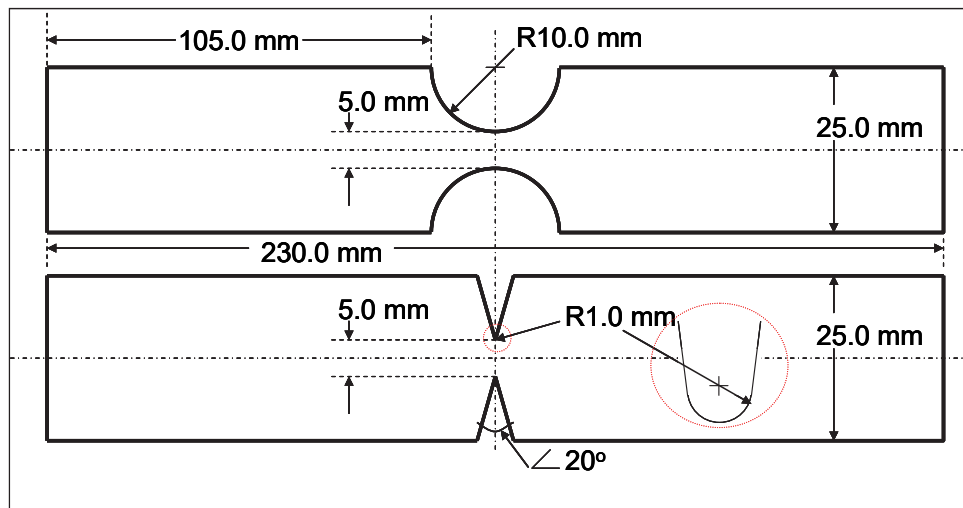


Figure 4.2: Geometry of the notched tensile specimens. C-notch specimen (top) and V-notch specimen (bottom)

Additionally, a V-notched specimen was tested to provide a higher triaxiality, more representative of what may be experienced at the tip of a propagating crack in a panel or thin wall pressure vessel. The V-notched specimen has a 1-mm radius at the notch root, as shown in Figure 4.2. The severity of the notch introduces non-uniformity in stress and strain distribution at the narrow cross-section. Thus, it is less suitable for determining the hardening response and damage evolution, which will be discussed in Chapter 5. Therefore, the C-notch specimen was used to determine the hardening response and the

lower triaxiality damage evolution while the V-notch specimen was used to determine a higher triaxiality damage initiation condition for estimating crack propagation.

4.2 Tensile Test Diagnostics

The research emphasis on post peak mechanical behavior and the elevated temperature testing environment introduces several diagnostics challenges. The tensile test procedure, as described in the ASTM E8 standard, only provides true stress-true strain until necking occurs due to the shortcomings of the measurement techniques and the randomness of where the material localizes. For round bar specimens, Bridgman's (1952) semi-empirical correction is used to infer true stress in the necked region from the global displacement to avoid the difficulty in measuring the radial displacement in the localization zone. Bridgman's correction has been studied by many researchers with mixed results. Needleman (1972) concluded that the Bridgman's correction works well during early necking but underestimates later stages of necking. Garcia-Garino et al. (2006) compared test data, FE simulation results, and Bridgman's correction on aluminum and found good agreement. However, for rectangular cross-section specimens used for sheet materials, such as that used in pressure vessels and large diameter pipes, a Bridgman-type correction has not been found. As a result, the deformation in the localization zone must be measured to quantify area reduction, true stress and true strain during material damage.

The elevated temperature testing environment eliminates the possibility of using strain gages due to adhesive failure and makes the use of an extensometer or dilatometer

more challenging. Furthermore, an extensometer only captures the global response of the sample and is unable to capture the area reduction during localized deformation. Digital Image Correlation (DIC) has grown in popularity for measuring local strain and deformations as digital cameras and image processing tools continue to advance. Researchers have begun correlating entire strain fields to FEA simulations (Tarigopula et al., 2008; Lava et al. 2010) which was previously limited to a few strain gage locations. In addition, it has been used in a stereo camera arrangement to measure out-of-plane deformation for area reduction estimates (Grytten et al., 2009) and also for measuring strain fields at elevated temperature (Florando et al., 2015). In this study, a three camera arrangement (Figure 4.3) was used for measuring the width and thickness reductions during localized deformation as well as elongation of the notch shoulder in order to quantify the necking behavior in detail.

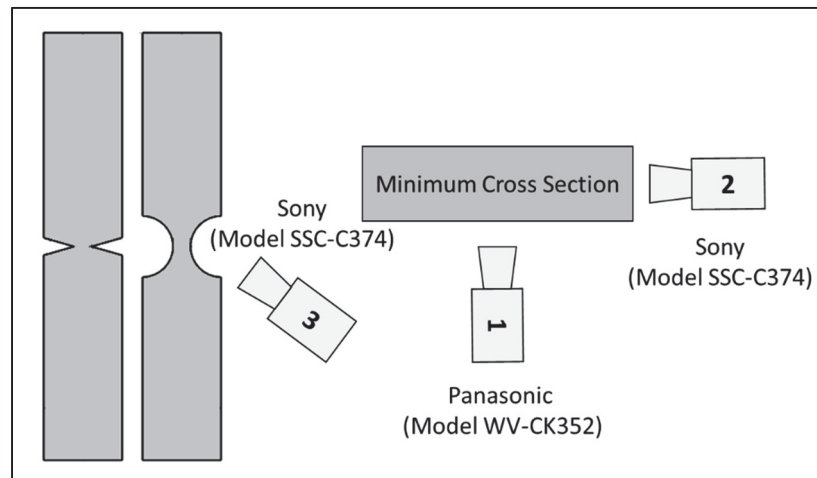


Figure 4.3: Camera configuration for DIC imaging of width and thickness reduction and the elongation of the notch shoulder

In addition to deformation measurements, the sample temperature was measured using a high temperature thermocouple (Type K from Omega Engineering)

rated up to 1250°C. Type K thermocouples have excellent weldability to DSS and provide one of the highest temperature ranges. The thermocouple was used to provide feedback to the power control system for the Hi-TempIR heater in order to modulate the lamp and control the sample temperature. The load was measured from the calibrated MTS Model 661.21A-C3 load cell. The Linear Variable Differential Transformer (LVDT) displacement was also recorded as a redundancy, even though additional displacement from outside of the notch region was included in the measurement. The tensile specimens were evaluated after the experiment to determine the final cross-sectional area and to investigate the fracture surface using the FRActure Surface Topographic Analysis (FRASTA) procedure developed at Stanford Research Institute.

4.3 Test Configuration and Procedure

The heater system consisted of a Hi-TempIR (Model 5209) heater module and power controller. The heater module contains six 127 mm long quartz halogen lamps arranged in parallel with a specular reflector, generating up to 6 kW. The power to the heater module was controlled by a Model 915 Power Control System allowing the user to set the desired temperature with a digital set point adjuster and the percentage of power with a ten-turn dial gauge. The controller used temperature feedback from the Type-K thermocouple (TC) to adjust the electrical power applied to the heater module.

In order to place the heater module close to the specimen in the tensile machine, a movable carriage was built for the heater head and power control unit. Figure 4.4 shows a picture of the assembled heating system mounted to the moveable carriage. The video

cameras were placed close to the specimen so there was concern the heat source could potentially damage the video cameras. In order to prevent damage to the cameras and prevent saturation of the sensors with the high-intensity broadband light, it was necessary to place a shield in front of the heater. Figure 4.5 shows the thermal insulation that was cut in the shape of the specimen and placed in front of the heater module. The thermal insulation successfully blocked both the intense heat and light from the surrounding area. Figure 4.6 shows the placement of the heater module in close proximity to the specimen prior to testing.

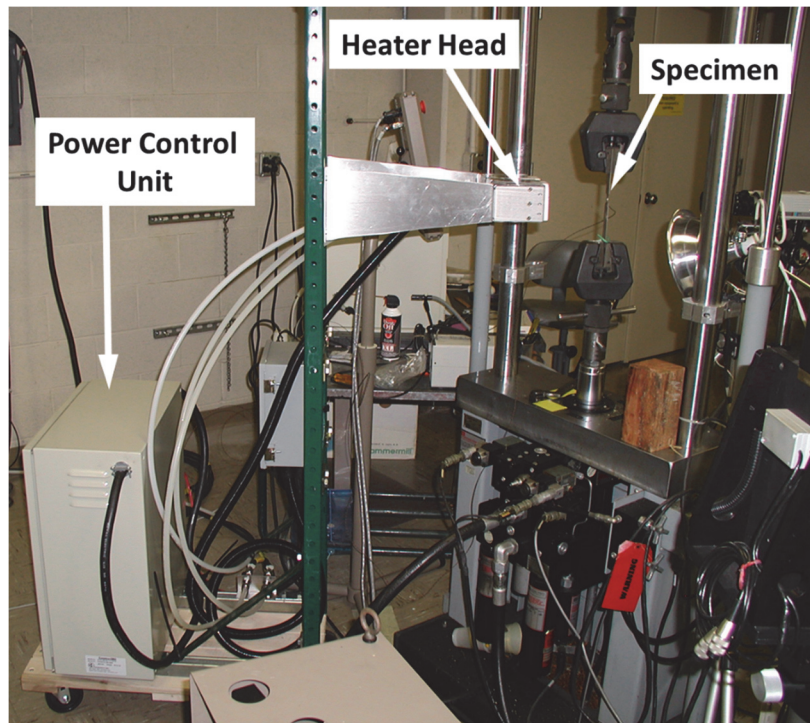


Figure 4.4: Tensile test configuration showing moveable carriage for heater head and power control unit

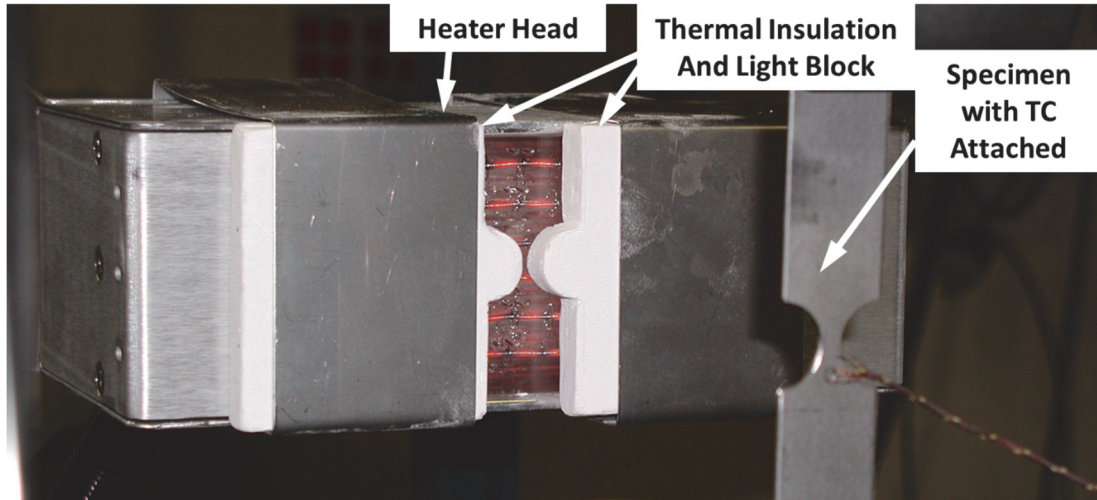


Figure 4.5: Heater head with thermal insulation attached

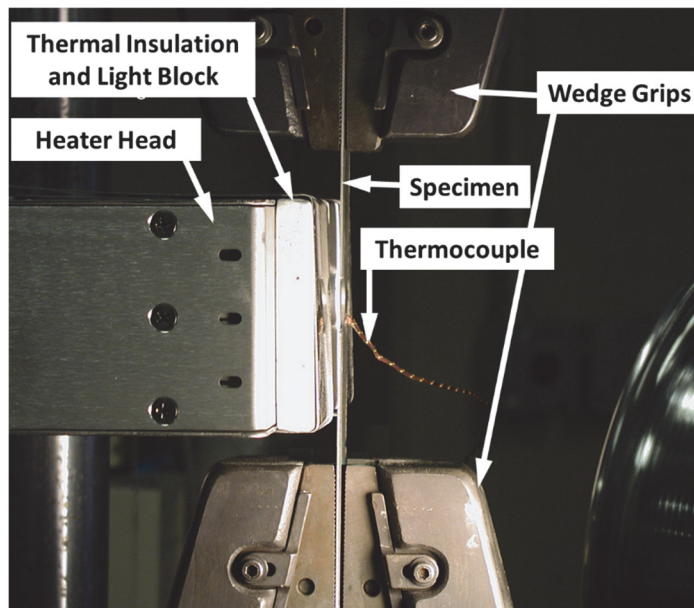


Figure 4.6: Heater head placement in close proximity to sample prior to testing

The heater was configured to illuminate an area of 75 mm in the vertical direction and 25mm in the horizontal direction. Figure 4.7 illustrates the placement of thermocouples and size of the heated zone during testing.

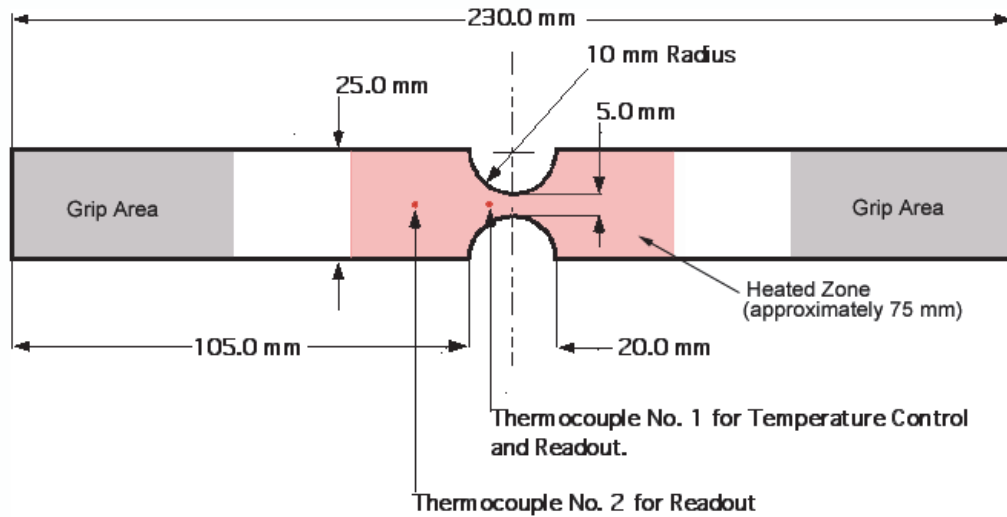


Figure 4.7: C-Notch specimen geometry, highlighting the approximate grip area, heated zone and TC placement

The applied load was provided by a 100 kN (22 kip) MTS Model 312.22 with ± 75 mm piston displacement. During each experiment a small load was applied to the test specimen and held constant to prevent buckling due to thermal expansion. The heater was then turned on and the specimen was brought to the desired temperature level as determined by the centermost thermocouple. Once the set temperature was reached and stabilized, the sample was loaded at a constant displacement rate of 0.01 inch per second (0.254 mm/s). At this rate, failure occurred in 10-20 seconds for the majority of the experiments.

Video cameras were positioned to capture both the width and thickness of the specimen simultaneously. An attempt was made to use a single video camera with turning mirrors to measure both the width and thickness dimensions but the thickness image was slightly out of focus due to the optical path length difference and the shallow depth of focus of the optical system. In addition, the magnification of the thickness image

could not be changed independently which limited the pixel resolution. Therefore, multiple video cameras and a digital video multiplexer unit were used instead.

The video setup is shown in Figure 4.8. Video camera #1 was a Panasonic (Model WV-CL352) with a zoom lens (12.5-75mm F1.8). In addition, a +4 close-up lens was also used to view the width change of the specimen. Video camera #2 was a Sony CCD (Model SSC-C374) with a Questar telescope Model QM1 attached for recording the thickness change. The Questar telescope is capable of capturing a 3.5×2.3 mm region into a full video window at a 56 cm stand-off distance. Video camera #3 was a Sony CCD camera (Model SSC-C374) with a zoom lens (18-108 mm F2.5) for recording the overall deformation of the notched area by capturing the deformation of the notch shoulders. The signals from the three cameras were fed into a digital video multiplexer, 4-Channel MPEG-2 DVR, and the images were recorded with 720 by 480 pixel resolution at 30 frames per second for each channel.

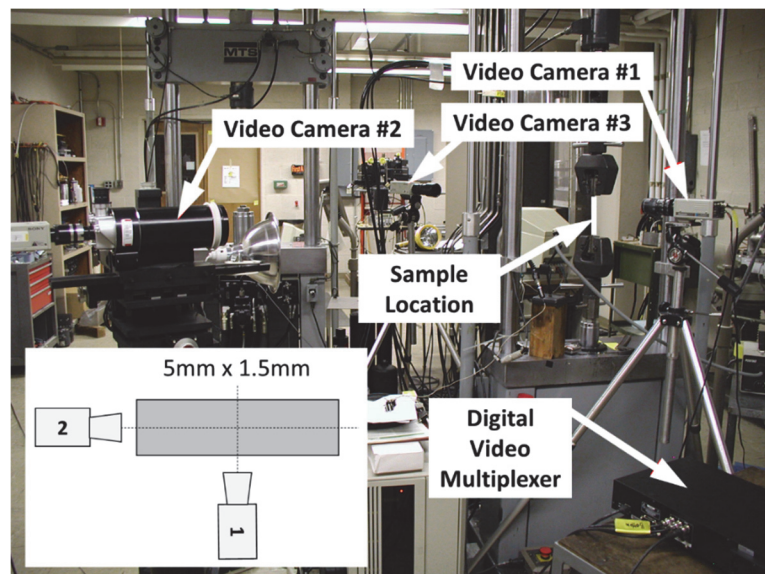


Figure 4.8: Camera configuration for DIC measurement of thickness, width, and shoulder displacement

Video images from each camera were downloaded and stored in TIFF format for post-processing. Selected images of width, thickness, and shoulder spacing were then examined using Adobe Photoshop software. The Photoshop dimension-measuring capability was then used to read the width, thickness, and shoulder spacing in pixel counts. The pixel counts were then converted to length for true stress and true strain computation based on the reference dimension prior to testing. If greater contrast was achieved, this process could be automated using digital image analysis software.

In the C-notched test, the central region in which necking occurs is large enough in the axial direction that the stress distribution across the minimum section approximates the distribution in a traditional tensile specimen prior to necking. Given the uniformity in the C-notch specimens prior to localization, the average true stress and true strain in the cross-section was determined using the assumption of a rectangular cross-section. The true stress was obtained by dividing the total force by the instantaneous cross-sectional area, determined from the width and thickness measurements. The true stress is defined by the following equation:

$$\sigma_{true} = \frac{F}{w \times t} \quad (4.1)$$

where, w and t are instantaneous measurements of width and thickness of the cross-section, respectively. The true strain is defined as follows:

$$\epsilon_{true} = \ln\left(\frac{A_0}{A}\right) = \ln\left(\frac{w_0 \times t_0}{w \times t}\right) \quad (4.2)$$

where, w_o and t_o are original width and thickness of the cross-section, respectively. However, this only represents the average axial strain and does not accurately represent the maximum strain in the minimum cross-section after localized necking because of the non-uniform strain distribution. In addition, rectangular cross-sections tend to deform into a “bow-tie” shape (Figure 4.9), particularly at lower temperatures, which results in over-prediction of the area and under-prediction of the true stress and strain. Thus, the true stress and strain as defined above should be considered a lower bound after necking occurs.

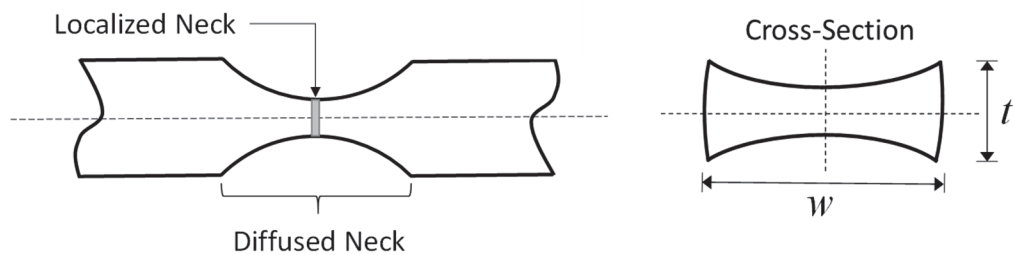


Figure 4.9: Exaggerated geometry of diffuse and localized necking and the "bow-tie" or "cushion" deformation observed in rectangular cross-section specimens

In the absence of a correction similar that of Bridgman for round bars, the determination of actual true stress and strain during necking is challenging. Ling (1996) proposed obtaining true stress-true strain via Finite Element (FE) simulation by iteratively changing the input stress-strain curve until the calculated load-displacement matches experimental results. Zhang et al. (1999) developed a methodology for correlating true stress-true strain to load-thickness reduction curves for rectangular cross-sections by FE simulation. Schneider et al. (2004) also used FE analysis together with digital image correlation (DIC), measuring surface displacement to arrive at correction factors for true stress in the localization zone. Similarly, Cabezas and Celentano (2004) used FE simulation

to obtain a correction factor for SAE 1045 steel in tension specimens via comparison of the global load-displacement, thickness and width reduction. The combination of experimentation and FE analysis is currently the preferred method for obtaining true stress-true strain during necking of rectangular cross-sections and will be adopted in this study, as discussed in Chapter 5.

4.4 C-Notch Test Results

The C-Notch specimens were successfully tested at Room Temperature (RT), 200, 400, 600, 800, and 1000°C. The load versus grip displacement response of the C-notch specimens at various temperatures is shown in Figure 4.10. The overall displacement at failure tended to decrease from the RT value until a temperature of 600°C, with the lowest displacement at failure observed at 400°C. The reduction in ductility can be attributed to the decomposition of ferrite and increased tendency for precipitation of nitrides and carbides (Tane et al., 2003; Boyer and Gall, 1985), commonly referred to as the “475°C embrittlement”. At 800°C and 1000°C, minimal strain hardening is observed so peak load is reached quickly followed by a large amount of diffuse necking prior to localization and failure.

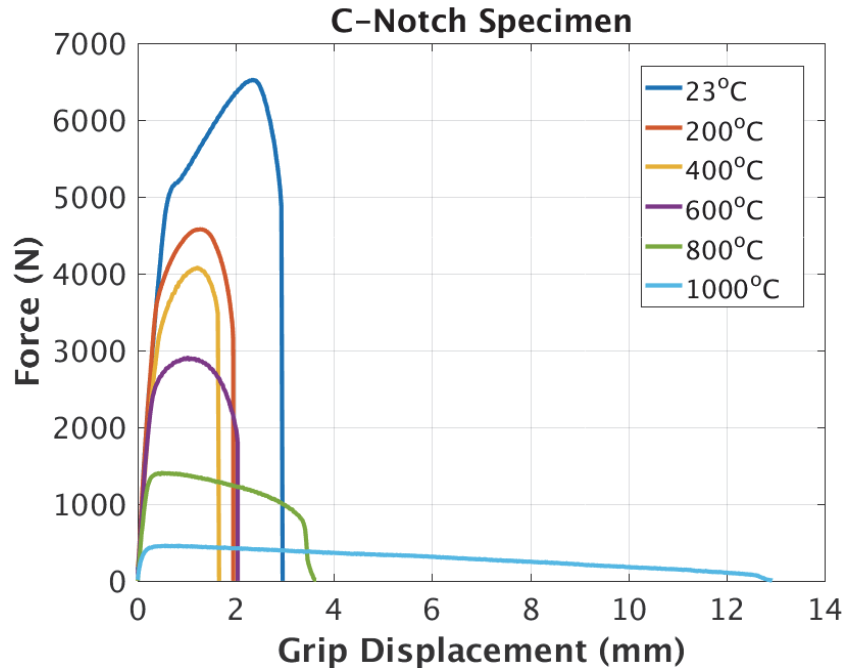


Figure 4.10: Load versus grip displacement for C-notch specimens at various temperatures

4.4.1 Digital Image Correlation Results

The load-displacement curve provided in Figure 4.10 gives a general indication of the sample response as a function of temperature. However, the grip displacement includes grip slip and deformation outside of the notched region. As a result, the shoulder displacement was determined by Digital Image Correlation (DIC) along with the width and thickness reductions. A select number of images from the width, thickness and shoulder displacement cameras are shown in Figure 4.11 for the 1000°C sample. The images progress in time from left-to-right with an increasing amount of observable deformation.

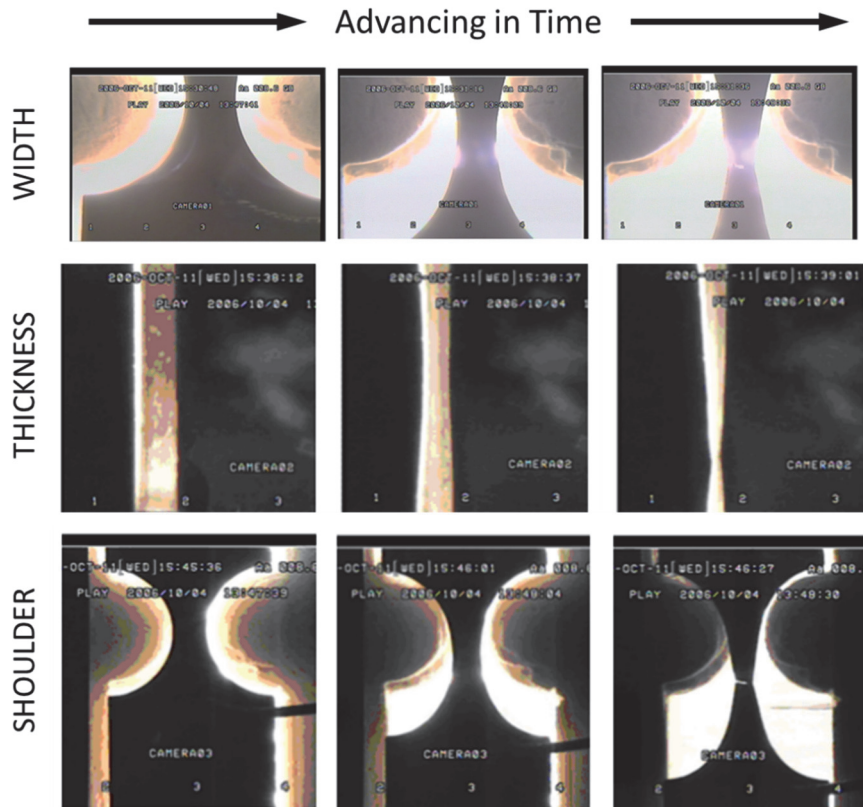


Figure 4.11: Example of the width, thickness, and shoulder displacement camera images used for DIC analysis for the C-Notched specimen at 1000°C

A load-displacement curve, similar to Figure 4.10, was then created with respect to relative shoulder displacement, as shown in Figure 4.12. The data resolution is significantly less for the shoulder displacement than grip displacement since each point is manually analyzed using digital image software. However, the same trends are observed with respect to “475°C Embrittlement” at intermediate temperatures and the significant diffuse necking at 800°C and 1000°C.

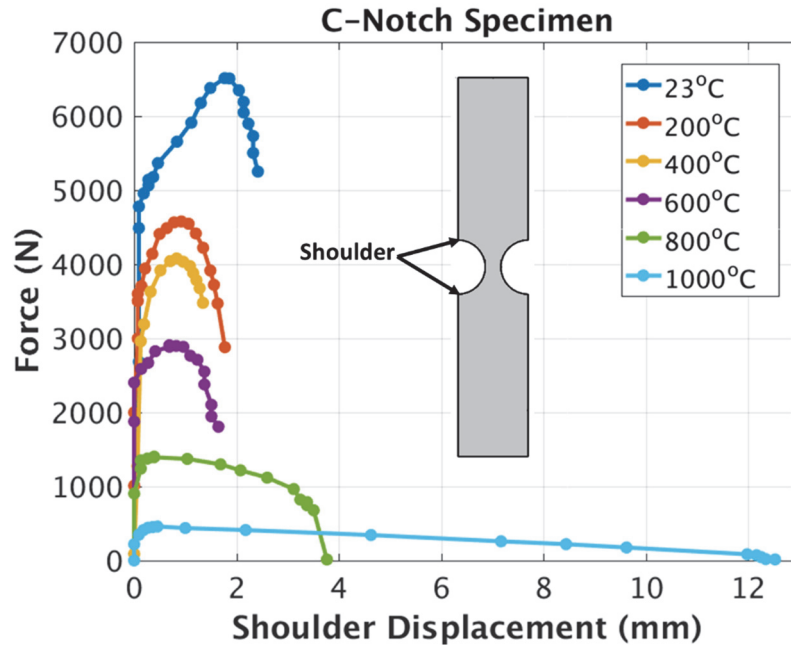


Figure 4.12: Load versus relative shoulder displacement for C-notch specimens at various temperatures

The normalized thickness and width reduction were then determined using DIC, as shown in Figure 4.13 and Figure 4.14, respectively. Similar to the shoulder displacement, the thickness and width reductions at 800°C and 1000°C were substantially larger than the RT values. A greater increase in thickness ratio was observed above 400°C which may be attributed to a transition from a “bow-tie” deformation at lower temperatures to a uniform deformation at higher temperatures. Analysis of the final fracture surface will be discussed in greater detail later in this chapter.

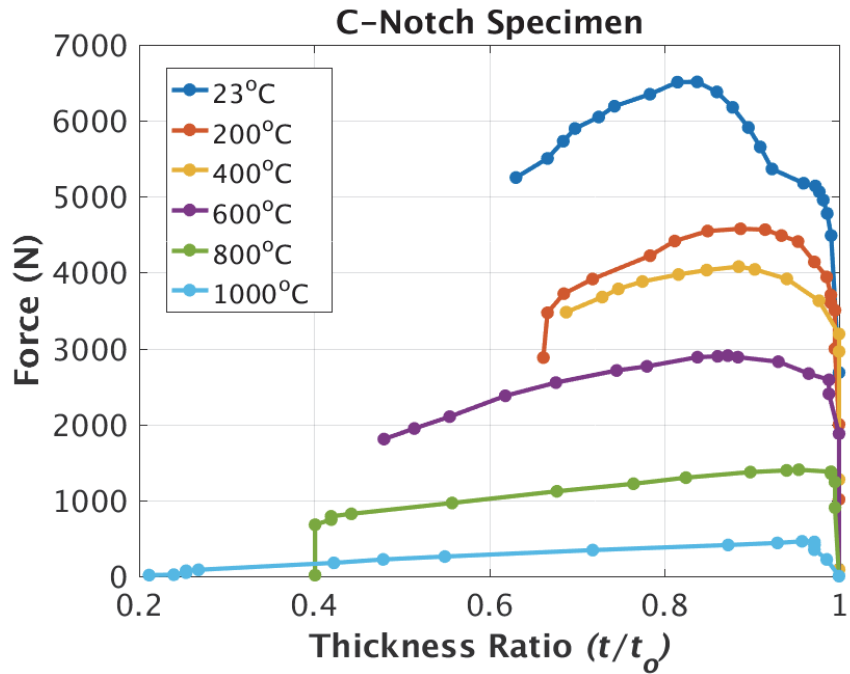


Figure 4.13: Load versus normalized thickness for C-Notch specimens at various temperatures

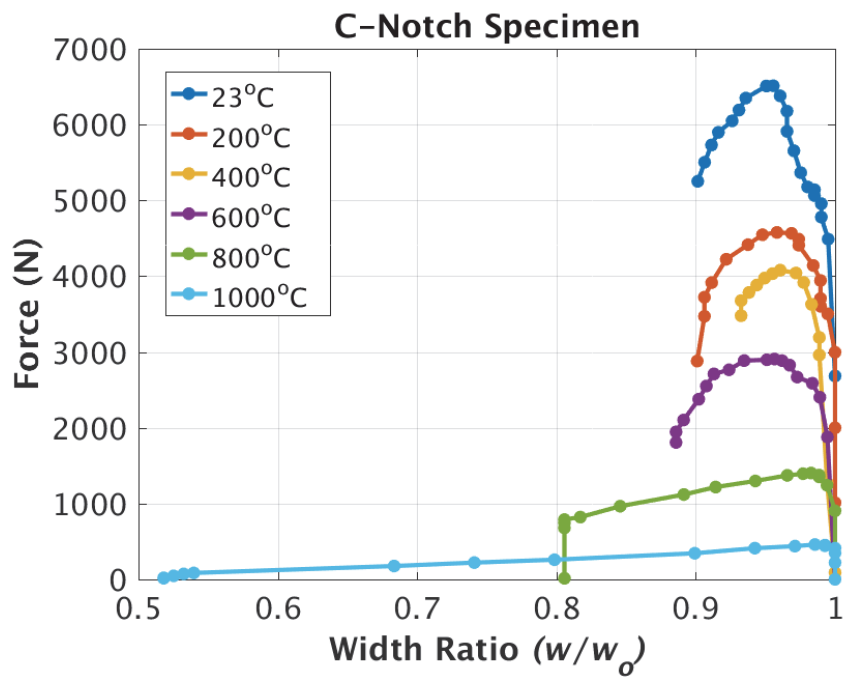


Figure 4.14: Load versus normalized width for C-Notch specimens at various temperatures

4.4.2 Temperature Dependent Stress-Strain Response

The instantaneous area reduction was determined using the change in thickness and width determined from digital image correlation. The corresponding force and initial area were then used to calculate the true stress and true strain, respectively. The resultant true stress-strain curve is provided in Figure 4.15 for each temperature. The true stress is increasing even though the applied load is decreasing due to the reduction in cross-sectional area during necking. The strain hardening is shown to be considerable for temperatures of 600 °C and lower. On the other hand, strain hardening is relatively small but the fracture strain is significantly higher above 600°C.

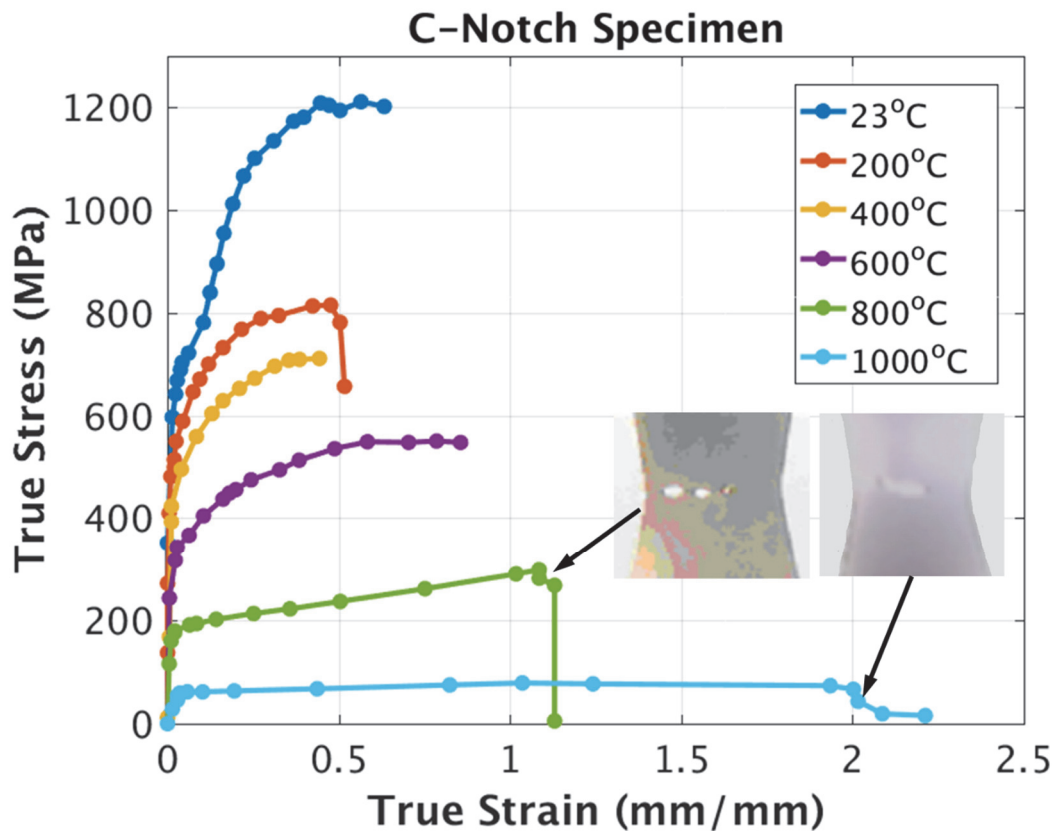


Figure 4.15: True stress-strain curves at various temperatures determined from C-Notch specimens

In general, the true stress-strain hardening response increases monotonically. However, a drop in the true stress-strain curve just prior to fracture is seen in Figure 4.15 for temperatures of 200, 800, and 1000 °C. The cause for the drop in the true stress near the end of the curve is attributed to significant void formation and coalescence. Large voids were observed in the central portion of the specimen width before complete material separation was achieved. An example for 800°C and 1000°C is shown in the inset pictures of Figure 4.15. The progression through time of macroscopic void formation and growth for the 800°C sample is shown in Figure 4.16, as captured by the width reduction DIC camera.

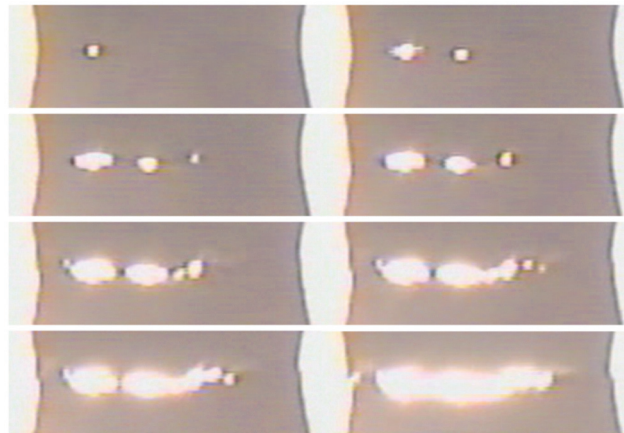


Figure 4.16: Progression of internal void formation during localized necking of 800° C-Notch specimen as captured by width reduction DIC camera

Due to the presence of macroscale voids, the cross-sectional area is not well defined by the reduced width and thickness of the specimen. A drop would be expected since the instantaneous cross-sectional area is overestimated when large internal voids are present. However, the drop is not realistic for material hardening so the curves will need to be extrapolated in those regions of the curves.

The elastic modulus, yield and ultimate strength were also estimated from the C-Notch specimens as shown in Figure 4.17 and Figure 4.18, respectively. The elastic modulus shows an abrupt drop between 200°C and 400°C which is greater than seen in existing literature for traditional stainless steels (Chen and Young 2006, Sakumoto et al. 1996). However, there is limited elevated temperature data on duplex stainless steel variants and no prior data on this particular DSS composition which makes it difficult to confirm the observed trend. The DIC measurement sensitivity is also poor for evaluating small displacements in the elastic regime, which will be evident from the uncertainty analysis in the following section. However, the fracture energy will not be extremely sensitive to the modulus since the majority of the energy is in the plastic regime for ductile metals.

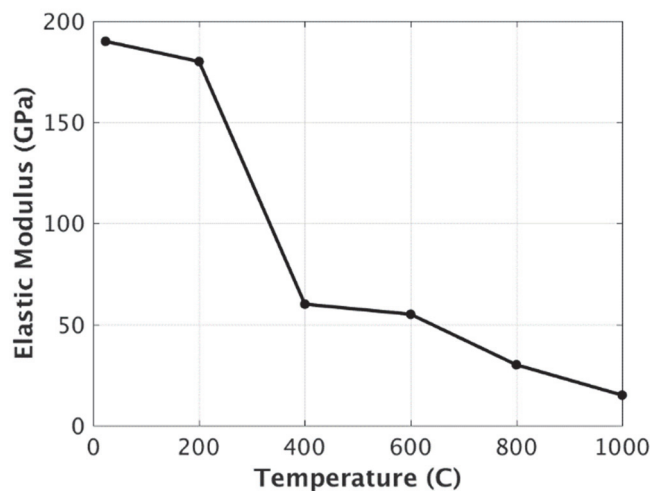


Figure 4.17: Temperature dependence of elastic modulus

The temperature dependence of the yield and ultimate strength demonstrated a rapid decline between RT and 200°C followed by a second rapid decline after 600°C. A

similar trend was observed by Chen and Young (2006) and Sakumoto et al. (1996) which increases confidence in the results and approach used during this research.

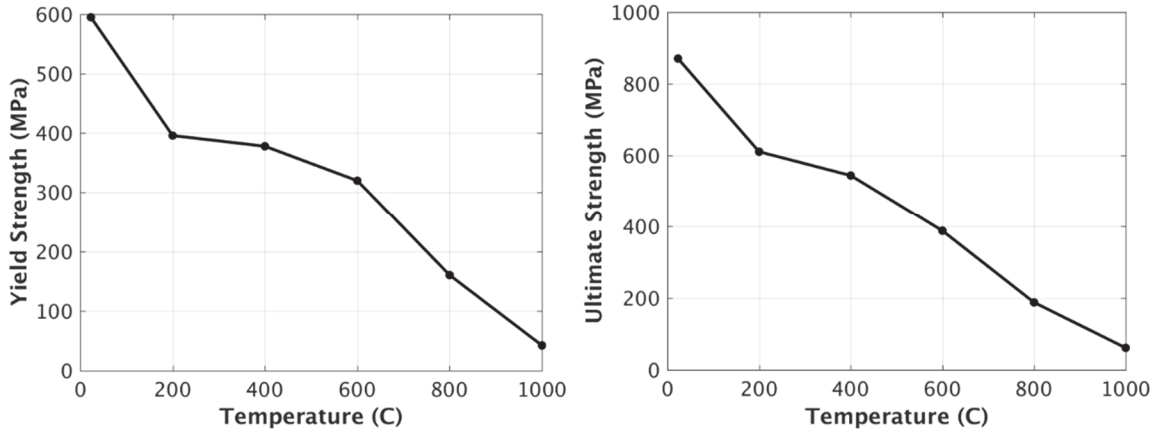


Figure 4.18: Temperature dependence of yield stress and ultimate strength

4.4.3 Uncertainty Analysis for Elevated Temperature True Stress-Strain

The uncertainty in the true stress-strain curve was investigated using guidance from the International Organization for Standardization (ISO) (GUM 2008) and National Institute of Standards and Technology (NIST) (Taylor and Kuyatt, 1994). The uncertainty contributors include the load cell, pixel measurements, and the micrometer used to determine initial dimensions.

The pixel measurement uncertainty was quantified in two separate ways: measuring distance and measuring change in distance. Figure 4.19 shows an enlarged image of a specimen's notch edge. The contrast between the specimen and the background is not abrupt but rather transitions over a few pixels. An assumption is necessary for which shade of color is representative of a pixel containing the notch edge. It was estimated that an edge location could be determined within ± 2 pixels and thus the

distance between two edges ± 4 pixels. The shade of color chosen to represent the edge could be tracked closely regardless if the pixel actually contained the edge. Therefore, the uncertainty was determined to be ± 1 pixel for tracking movement of an edge and thus ± 2 pixels for tracking displacement between two edges.

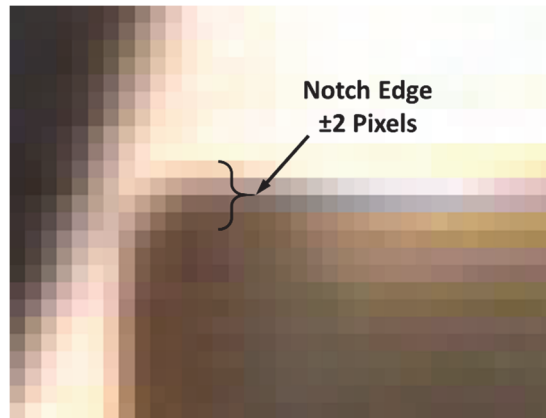


Figure 4.19: Enlarged image of C-Notch shoulder edge with pixel uncertainty estimate

Table 4.1 summarizes the contributors and associated uncertainty estimates for load-displacement determination. The percent of relative uncertainty for the displacement changed during the experiment, i.e. percent uncertainty decreases as displacement increases. Also, the percent uncertainty for the distance and micrometer measurements changed between test cases, e.g. camera placement changes the pixel dimensions.

Table 4.1: Contributors with uncertainty estimate for determination of load-displacement and true stress-strain

Contribution	Uncertainty
Displacement	± 2 pixels
Distance	± 4 pixels
Load Cell	± 1.0% of Reading
Micrometer	± 0.0005 in.

A uniform distribution of the uncertain variables is assumed based on the minimum limits criterion (bounding limits are known), 100% containment criterion and uniform probability criterion. The uniform probability criterion is arguable but without substantiating data a uniform or normal distribution is most often used. A coverage factor of 2 will be used, as recommended by NIST, resulting in an expanded uncertainty with confidence of approximately 95%. The combined uncertainty of the measured value was then determined using the following equation:

$$U = 2 \sqrt{\sum_{i=0}^n \left[\frac{u(x_i)}{\sqrt{3}} \right]^2} \quad (3.3)$$

where, n is the number of contributors and u is relative uncertainty percentage. The calculation provides a 95% probability that the measurand lies within the interval specified by U , using a uniform probability distribution for each contributor.

The displacement measurement has three contributors: the observation of displacement, the initial pixel-distance of the notch spacing, and the micrometer measurement of the initial distance. The uncertainty bounds for displacement in conjunction with that of the load cell provides the uncertainties shown in Figure 4.20 for the C-notch specimen at each temperature.

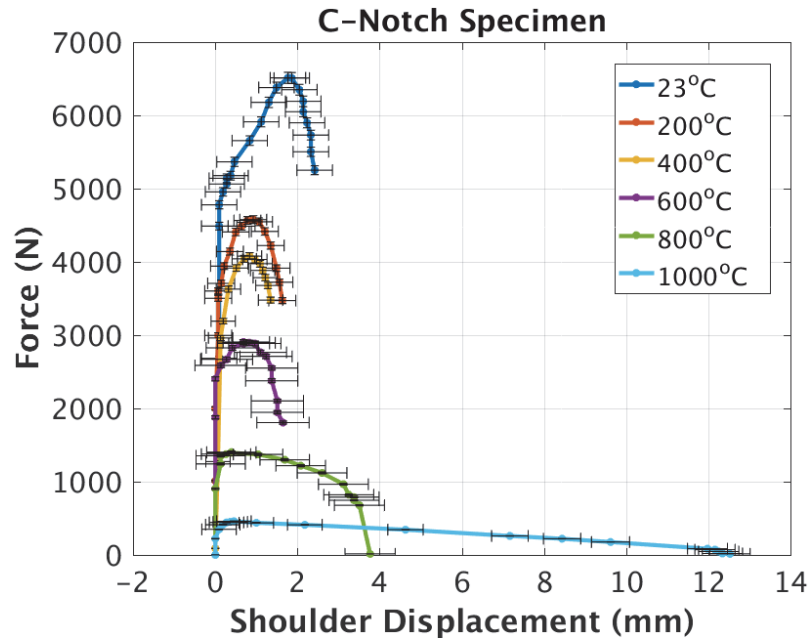


Figure 4.20: Force-displacement curve for C-Notch experiments with uncertainty bounds

The contributors for the strain measurement includes the uncertainty in the number of pixels in the initial area as well as the change in pixel measurements for the width and thickness dimension. These two contributors also apply to the true stress measurement with the addition of the load cell and micrometer measurement of initial cross-sectional area. The resulting uncertainty bounds for the true stress-strain curves for the C-notch specimens are provided in Figure 4.21.

The aforementioned bowtie deformation will be shown in Section 4.6 to increase uncertainty in true stress and true strain in the lower temperature experiments (<600 °C) for the portion beyond the ultimate tensile strength. The effect is an increase in both true stress and true strain which has not been reflected in Figure 4.21. Since this phenomenon occurs in a limited portion of the stress-strain curves, this uncertainty does not

significantly influence the resulting mechanical response curves determined from the FE modeling discussed in the following chapter.

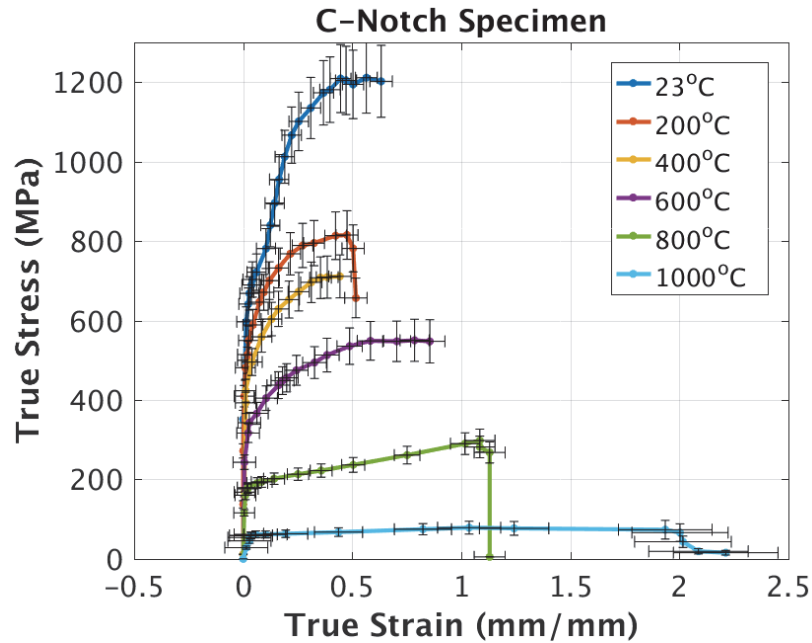


Figure 4.21: True stress-strain curves for the C-Notch experiments with uncertainty bounds

4.5V-Notch Test Results

The V-Notch specimens were tested in a similar manner and using identical equipment and diagnostics to the C-Notch specimens. Based on the literature, a lower displacement at failure was anticipated for the V-notch specimen due to the additional confinement and higher triaxiality near the notch root. The nominal stress versus shoulder displacement for the V-Notch specimens is shown in Figure 4.22, along with the C-Notch results.

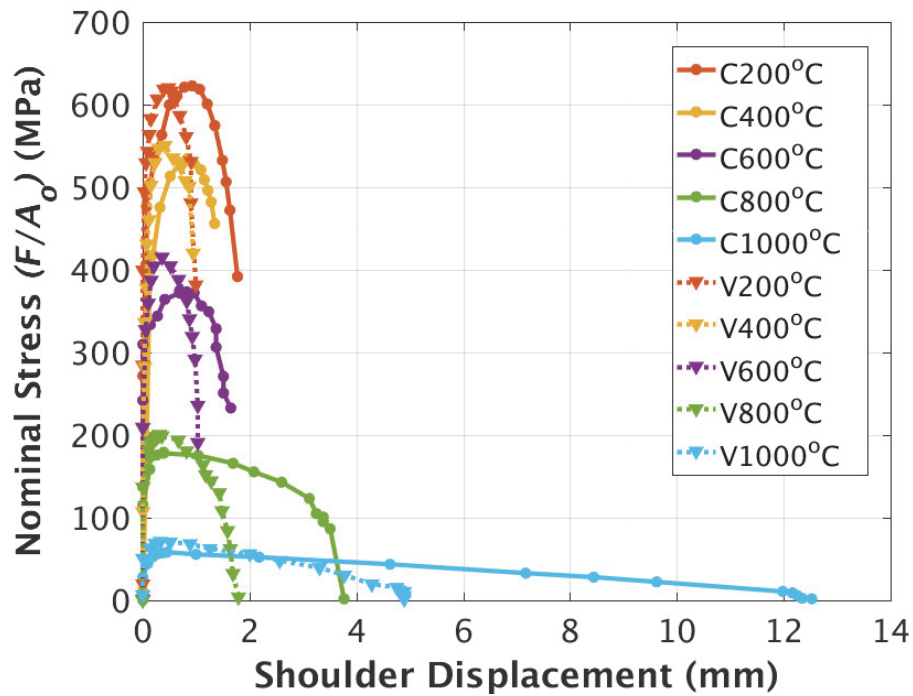


Figure 4.22: Comparison of nominal stress versus shoulder displacement for the C-Notch and V-Notch samples at elevated temperatures

The nominal stress, based on the initial cross-sectional area, is used for the comparison instead of the applied force due to variability in the initial thickness and width of the samples. The thickness and width of the C-Notch and V-Notch samples are provided in Table 4.2 and Table 4.3, respectively. While the majority of the samples were machined to near tolerance, the V-Notch samples for 200, 400 and 1000°C were larger in the width dimension than specified by the design drawings. In addition, the comparison using shoulder displacement in Figure 4.22 also assumes the majority of the plastic deformation occurs in the region of the minimum cross-section where strain localizes. The difference in initial shoulder lengths and the non-homogeneous strain fields within the notched region requires the use of finite element simulation to properly determine whether the V-Notch indeed has a reduced fracture strain. This will be evident if a lower

damage initiation strain is required to match the displacement at failure for the V-Notch specimens. Further discussion will be provided in Chapter 5.

Table 4.2: C-Notch specimen dimensions

C-Notch

Temperature (°C)	Thickness (mm)	Width (mm)	Notch Shoulder Distance (mm)
RT	1.52	5.0	20.0
200	1.5	5.0	20.0
400	1.52	5.0	20.1
600	1.54	5.04	20.2
800	1.54	5.06	20.3
1000	1.55	5.08	20.3

Table 4.3: V-Notch specimen dimensions

V-Notch

Temperature (°C)	Thickness (mm)	Width (mm)	Notch Shoulder Distance (mm)
200	1.5	5.57	5.17
400	1.51	5.52	5.17
600	1.54	5.04	5.09
800	1.54	5.06	5.22
1000	1.55	5.31	5.35

4.6 Fracture Surface Analysis

The fracture surface was analyzed following the completion of all experiments using the FRActure Surface Topographic Analysis (FRASTA) procedure developed at Stanford Research Institute. The FRASTA technique uses a confocal optical scanning laser microscope to determine surface topology. A topographic map of the conjugate fracture surfaces for a room temperature C-notch sample is provided in Figure 4.23.

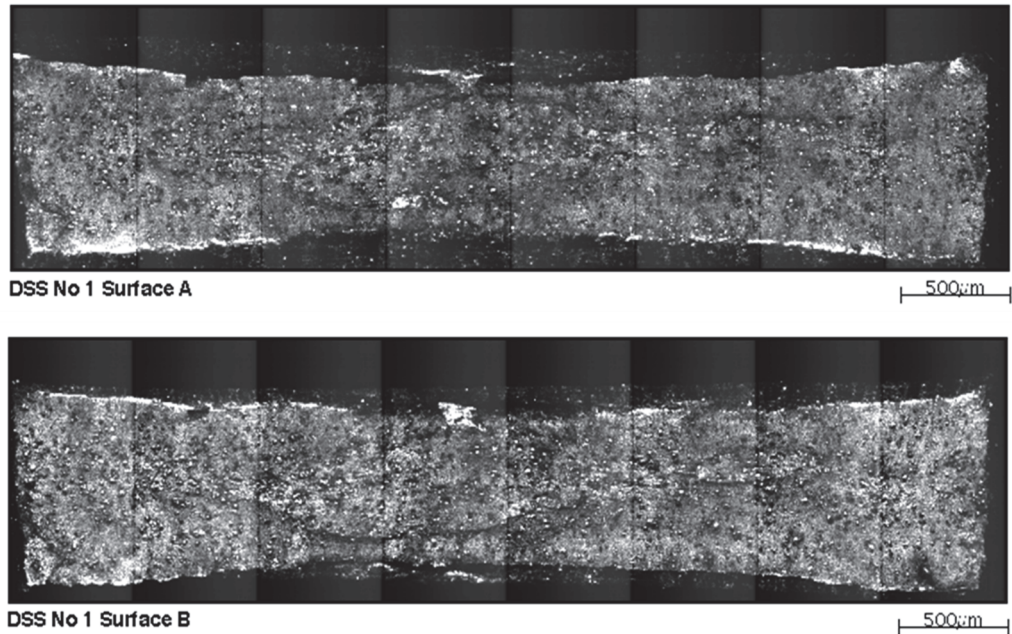


Figure 4.23: Contrast image of conjugate surfaces for room temperature C-Notch specimen

The perspective view of the surface topography is shown in Figure 4.24. The overall surface topography was generated from 24 fine resolution images in an 8 by 3 grid. The surface height is magnified for plotting purposes to improve evaluation of the surface topology. The image for Surface B was also flipped horizontally to simplify comparison of the conjugate surfaces. A nearly horizontal fracture area is observed in the central region of the fractured specimens which is likely to be the location of initial failure. The failure becomes more shear dominated as the fracture propagates toward the edges in the width direction.

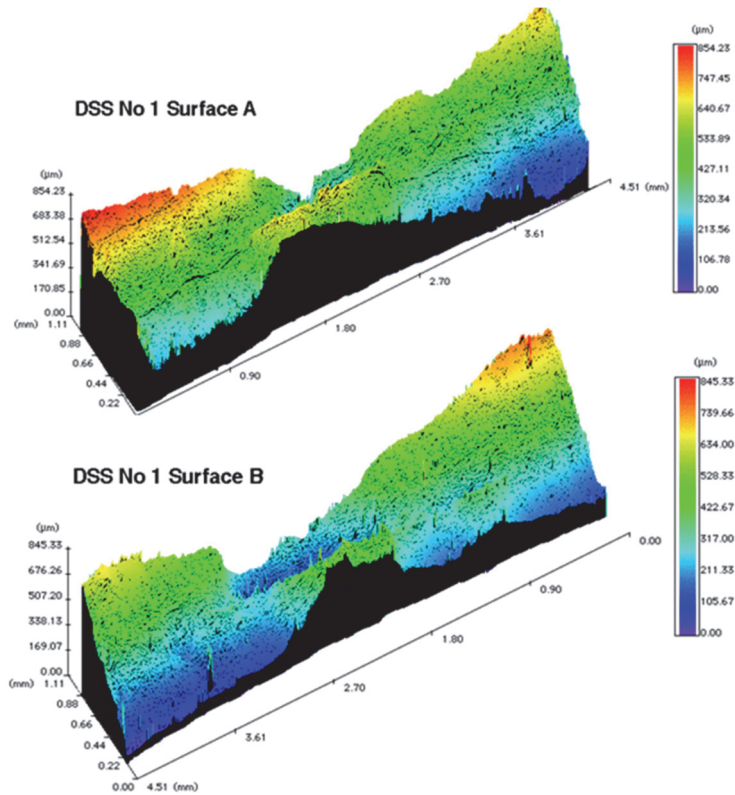


Figure 4.24: Perspective view of FRASTA topology for conjugate fracture surfaces from room temperature C-Notch specimen

The progression of the fracture process is estimated with Fracture Area Projection Plots (FAPP) by overlaying the fracture surface topography maps and increasing the separation between the images until a gap is formed, representing the location of initial failure. As the separation is increased, the area of the gap increases which gives some indication of the progression of the crack propagation, as shown in Figure 4.25 for various surface separation distances. The black color represents the area where the surfaces would still be connected and the white color represents areas of separation. The fracture is seen to initiate near the center of the specimen, where triaxiality is highest, followed by propagation to the free surface in the thickness direction and finally propagation along the shear plane toward the free surface in the width direction.

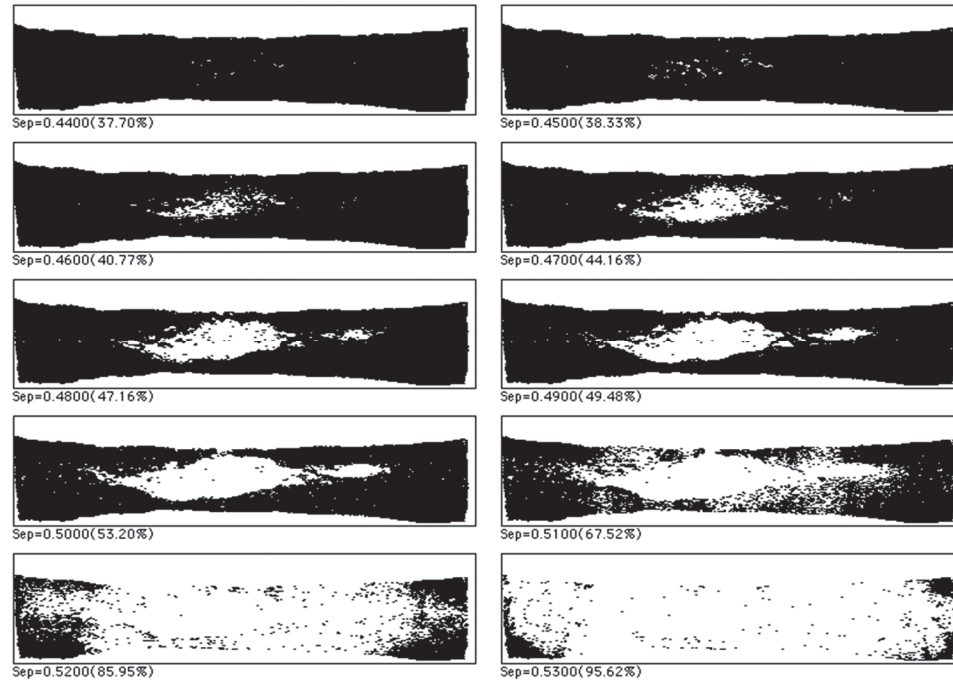


Figure 4.25: Estimation of fracture progression based on overlapping fracture surface topography maps

The final deformed shape, shown in Figure 4.26, shows a non-rectangular cross-section in the fracture zone with increased thinning in the central region. The deformation forms a “bow-tie” shape which introduces error of approximately 17% at room temperature when compared to the area calculation using instantaneous width and thickness measurements based on DIC. However, the error can only be evaluated for the final fracture state and measuring the instantaneous thinning of the central region is very challenging, especially at elevated temperatures. The bow-tie error is assumed to be minimal prior to strain localization which decreases the overall impact on elevated temperature fracture predictions.

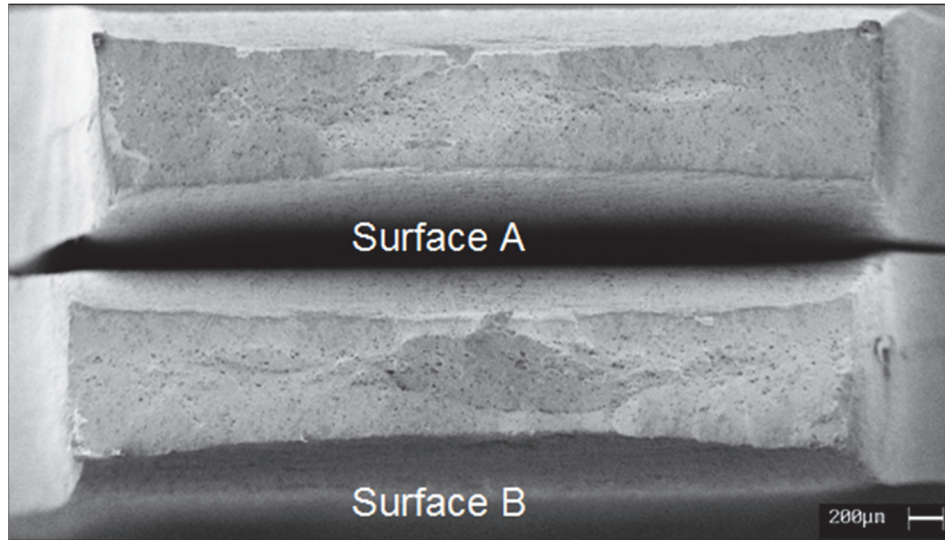


Figure 4.26: SEM image of the conjugate fracture surfaces for a room temperature C-notch specimen

In addition, the bowtie shape deformation becomes less significant at elevated temperatures. Figure 4.27 shows contrast images of the deformed shape for 23, 400 and 800°C. Although the length scales are not equal between images, the bow-tie shape deformation is most noticeable at room temperature. Based on the contrast images, the error associated with calculating area from the DIC thickness and width is reduced to less than 10% at elevated temperatures.

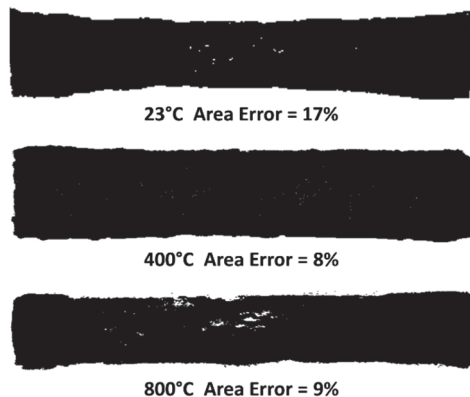


Figure 4.27: Contrast image of the fracture surface showing a reduction in central thinning with increasing temperature

The SEM images were also superimposed with the FAPP plots at various separations to visualize the failure progression of the central crack (Figure 4.28). The location and size of the initial micro-cracks and the region of primary void growth can be estimated.

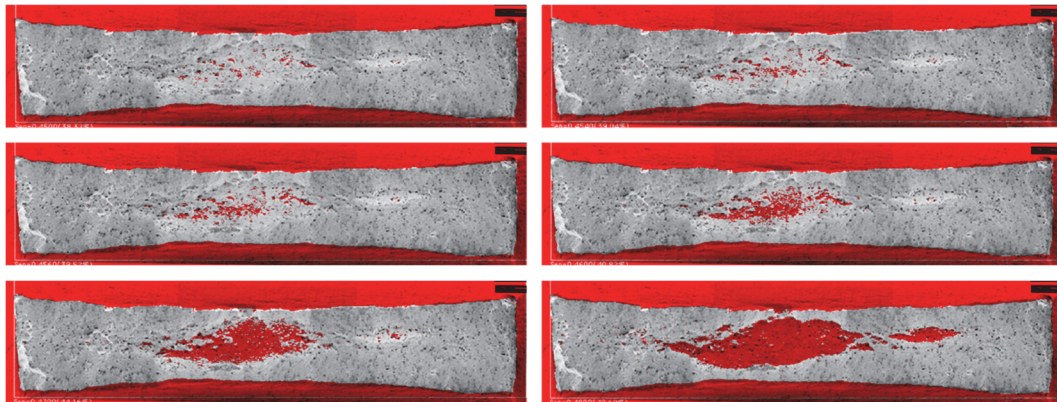


Figure 4.28: FAPP overlaid on the SEM image on fracture surface A for the room temperature C-Notch specimen

SEM images were also taken of the central region where initial crack formation is estimated (Figure 4.29) and the edge of the sample where shear dominated propagation is observed (Figure 4.30). A significant number of large (dark) voids are seen in both regions where void, nucleation and growth are likely mechanisms of the failure. Small dimples cover the surface where small voids have grown without coalescing. Large voids also tended to form around more significant inclusions. Elliptic (elongated) shaped deformation of the voids are observed near the edge which is a sign of shear failure in this region.

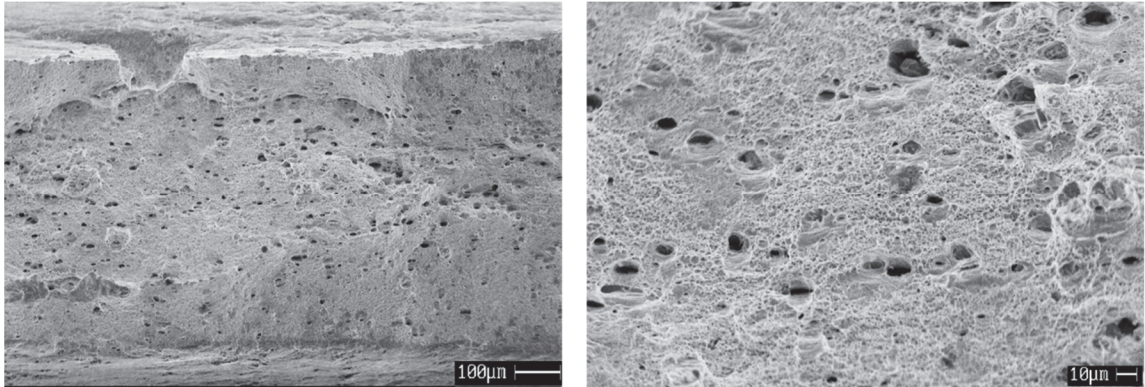


Figure 4.29: SEM images of the fracture surface near the central region where crack initiation occurs

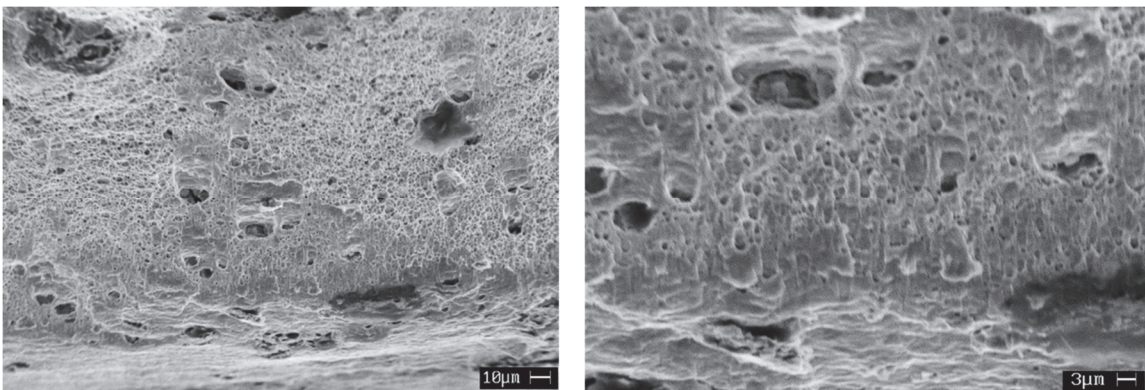


Figure 4.30: SEM images of the fracture surface near the sample edge where shear failure is observed

The FRASTA analysis for elevated temperature experiments show a similar result with the fracture initiation occurring in the central region and propagating outward, although the propagation along the shear plane becomes less apparent as temperature increases.

4.7 Summary

The experimental study of the strength of DSS sheet material has been conducted at elevated temperatures up to 1000°C ($T^* \approx 0.7$) in a manner that allows measurement of

the macroscopic deformations in the localization zone. The C-Notch tensile tests led to a relationship between true stress and true strain from room temperature up to 1000°C. The temperature dependency of the elastic modulus, yield strength and ultimate strength were also examined. In addition, elevated temperature tensile tests of a sharper V-Notch specimen were conducted to assess the effects of higher stress triaxiality on the fracture response of DSS. Further examination of the triaxiality dependence will be provided in the next chapter as the ductile failure response will be characterized using finite element simulations. Also, a close examination of the fracture surface revealed the failure progression via void formation, an indication of a ductile failure mode, at all temperature levels. The “bow-tie” deformation was found to be most prevalent at room temperature with nearly uniform deformation observed at higher temperatures.

Chapter 5 : Elevated Temperature Fracture Modeling

Significant investments have been made to improve the understanding of ductile fracture and to develop predictive models for failure analysis, as described in Chapter 2. Over this period, numerous strategies have been developed to understand and model the characteristics of ductile failure, namely; material hardening and softening, void formation and coalescence, dislocations, crack initiation and propagation. Many researchers have attempted to use modified LEM methods, uncoupled void growth models, damage indicator models, cohesive zone models, coupled void growth plasticity/damage models, and continuum damage models.

In the literature, the models are often shown to closely correlate with the test data for which they are derived but validation is rarely provided. When validation is conducted, it has been shown that several models with different physical or phenomenological underpinnings can capture the same general trends, indicating the model calibration may be the critical success factor. This is clearly shown in the results of the Sandia Fracture Challenges (SFC) (Boyce et al., 2014; Boyce et al., 2016) and Banerjee (2007). Nevertheless, Continuum Damage Models (CDM) have seemed to emerge as one of the preferred methods due to the ease of implementation, calibration, and accuracy (providing some of the closest predictions in the SFC).

The application of these models at elevated temperatures is relatively limited when compared to room temperature, as described in Chapter 2. The primary focus of elevated temperature research in the literature has been on the temperature

dependence of the elastic modulus, yield and ultimate strength with very little emphasis placed on the post-peak behavior. In this study, a CDM model will be calibrated to capture the elevated temperature damage (post-peak) behavior for simulating fracture initiation and growth in ductile DSS material.

5.1 Constitutive Model for Ductile Failure

CDM models define a flow stress dependency on the material damage level based upon a damage initiation criterion along with a damage evolution function. The damage evolution is often simplified to a scalar function for isotropic damage where voids and micro cracks are assumed to be uniformly distributed in all directions. The evolution function is commonly defined as a function of strain rate, stress triaxiality, lode angle, and temperature. The Progressive Damage Model in the commercial FE code Abaqus provides a general framework to account for the dependencies that have been reported by many researchers, as described in Chapter 2, and has been used in this research to develop an elevated temperature damage model for DSS.

5.1.1 Progressive Damage Model

The Abaqus Finite Element Analysis software provides a general analysis capability for simulating structural dynamics, thermal transport and coupled thermal-mechanical processes, among other things. Abaqus includes dozens of constitutive material models including Mises, Hill, and user defined yield criteria with isotropic, kinematic, Johnson-Cook, Gurson-Tvergaard-Needleman, and other hardening models. Abaqus also includes several damage and failure models including traction separation, shear damage, Johnson-

Cook, Gurson-Tvergaard-Needleman, ductile damage and Forming Limit Diagrams (FLD) based damage. The ductile damage model implementation in Abaqus follows the continuum damage concept with progressive accumulation of damage in the material and thus will be termed the Progressive Damage Model (PDM) in this work.

As previously mentioned, the Progressive Damage Model has been implemented such that the initiation of damage can be defined as a function of stress triaxiality, strain rate, lode angle, and temperature. The generality of the PDM model captures the critical parameters found in the CDM literature (Chaboche, 1984; Lemaitre, 1985; Rousselier, 1987; Tai and Yang, 1987; Wang, 1992; Chandrakanth and Panday, 1993; Bonora, 1997; Wierzbicki et al., 2005), with the exception of any variation with respect to hydrostatic stress, such as the work by Xue (2007). The damage initiation can be used in conjunction with the Isotropic Mises (J2) plasticity model to define the undamaged material response which has been shown to adequately represent the yield behavior of metals (Dowling, 1999). The initiation of failure occurs when the cumulative equivalent plastic strain reaches the critical equivalent plastic strain at the onset of damage, $\bar{\varepsilon}_D^{pl}$, as shown in the following equation:

$$\omega_D = \int \frac{d\bar{\varepsilon}^{pl}}{\bar{\varepsilon}_D^{pl}(\eta, \xi(\Theta), \dot{\varepsilon}^{pl}, T)} = 1 \quad (5.1)$$

where, η is the stress triaxiality, ξ is the lode parameter, Θ is the lode angle, $\dot{\varepsilon}^{pl}$ is the effective plastic strain rate, and T is the temperature. The effect of lode angle and strain rate will not be studied in this work since temperature and stress triaxiality are assumed

to be the primary contributors for the anticipated loading conditions. The damage state variable ω_D increases monotonically with plastic deformation and the increment is computed as follows:

$$\Delta\omega_D = \frac{\Delta\bar{\varepsilon}^{pl}}{\bar{\varepsilon}_D^{pl}(\eta, \xi(\Theta), \dot{\bar{\varepsilon}}^{pl}, T)} \geq 0 \quad (5.2)$$

Once the criterion for damage initiation is met, the material response follows the continuum damage approach for the damage evolution which describes the rate of degradation of the material stiffness. Damage evolution is tracked with the progression of the damage variable, D , and the stress at the material point is then defined as follows:

$$\sigma = (1 - D)\bar{\sigma} \quad (5.3)$$

where, $\bar{\sigma}$ is the stress tensor of the undamaged element for the current increment. Figure 5.1 illustrates the effect of damage on the material response and highlights the so-called damaged modulus which is consistent with the CDM model and experimental observation by Lemaitre (1985) for pure copper.

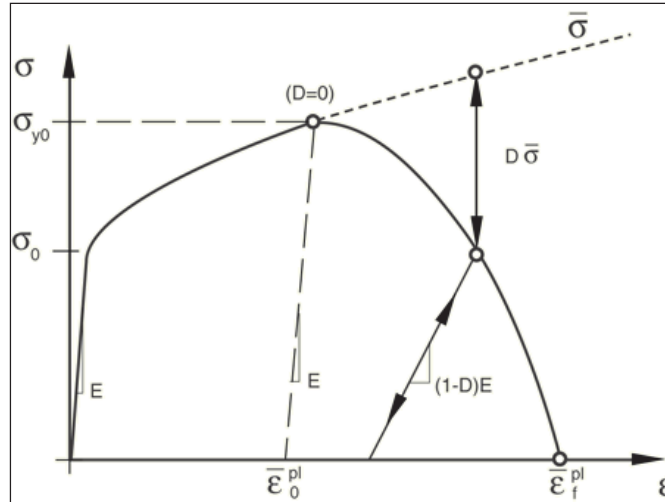


Figure 5.1: Stress-strain response with progressive damage and failure (Abaqus Documentation, 2008)

The evolution of D directly reduces the stiffness and load-carrying capacity of the element. By default, the element is removed from further calculations if all section points at any one integration point have lost all load-carrying capacity, i.e. $D=1$. The evolution of D as a function of strain rate, temperature or field variables can be input using tabular, exponential, or a linear form which enables flexibility to capture the various damage evolution functions found in the literature.

Once damage initiation occurs, the softening response leads to a strong mesh dependency (Besson et al., 2003; Bonora, 1999; van den Boogaard and Huetink, 2006) as material stability is lost, often referred to as loss of ellipticity or bifurcation. In the literature, mesh convergence is frequently only shown up to the point of peak load which is especially misleading if the paper is describing a model for material softening and failure. Many researchers have investigated bifurcation (Gasteble and May, 2000; Schreyer and Neilsen, 1996; Becker, 2002) during strain localization and some have even

suggested using bifurcation as a crack propagation indicator, including the work of Rabczuk and Belytschko (2004). However, it's unclear whether instability of a mathematical model should actually correlate to a physical mechanism at the material level if the model does not capture material level features such as dislocations and voids. Nevertheless, the material instability calculation is computationally expensive which has led researchers to investigate non-local constitutive models (Reusch and Svendsen, 2004; Ramaswamy and Aravas, 1998) among other methods of reducing the mesh dependency during material softening.

Using fracture energy, as proposed by Hillerborg (1976), the mesh dependency can be reduced, but not eliminated, by introducing the equivalent plastic displacement quantity, \bar{u}^{pl} , as the characteristic element length (L_c) times the effective plastic strain ($\bar{\varepsilon}^{pl}$), as shown in the following equation:

$$G_f = \int_{\bar{\varepsilon}_0^{pl}}^{\bar{\varepsilon}_f^{pl}} L_c \sigma_y d\bar{\varepsilon}^{pl} = \int_0^{\bar{u}_f^{pl}} \sigma_y d\bar{u}^{pl} \quad (5.4)$$

The rate of change in effective plastic displacement, $\dot{\bar{u}}^{pl}$, is zero prior to damage initiation and then evolves with effective plastic strain, $\dot{\bar{u}}^{pl} = L_c \dot{\bar{\varepsilon}}^{pl}$. The evolution of the damage variable can then be defined as a function of effective plastic displacement, $D(\bar{u}^{pl}) = [0,1]$. This form of the equation helps to maintain a constant fracture energy and displacement in the localization zone as the element size is refined. However, a

length scale still remains as the definition of characteristic length becomes a critical feature.

In Abaqus, a characteristic length equal to the cube root of the element volume is proposed to account for the possibility of a crack forming in an arbitrary location and direction. This approach then requires a perfectly cubic element in order to maintain a consistent fracture energy and some mesh dependency will still remain due to the orientation of the mesh relative to the localization zone. In addition, using cubic elements is not practical for most applications and presents a challenge for simulating pressure vessels in this research where the thickness dimension is much smaller than the largest dimension. Therefore, the proposed method is to use a damage evolution based on effective plastic displacement where the element size used during calibration is considered to be a “material property” (Baaser and Gross, 2000; Hutchinson, 1997), enabling higher aspect ratio elements to be used for the sheet material while maintaining the fracture energy.

5.1.2 Elevated Temperature Flow Stress

The definition of the flow stress can be cast in a number of different forms, as discussed in Chapter 2. The impact of strain hardening, strain rate and temperature are often modeled using an uncoupled multiplicative combination (such as the Johnson-Cook Model), where $\sigma = f(\varepsilon)f(\dot{\varepsilon})f(T)$. Using this basic formulation assumes the shape of the hardening response does not change with temperature but rather it is uniformly scaled. Using this concept, the room temperature C-Notch data was used to assess the validity of the multiplicative contribution models. The various forms of the strain hardening curves, $f(\varepsilon)$, were

manually optimized to fit the experimental results, as shown in Figure 5.2. Although a more rigorous optimization could be used, the general outcome is expected to be the same.

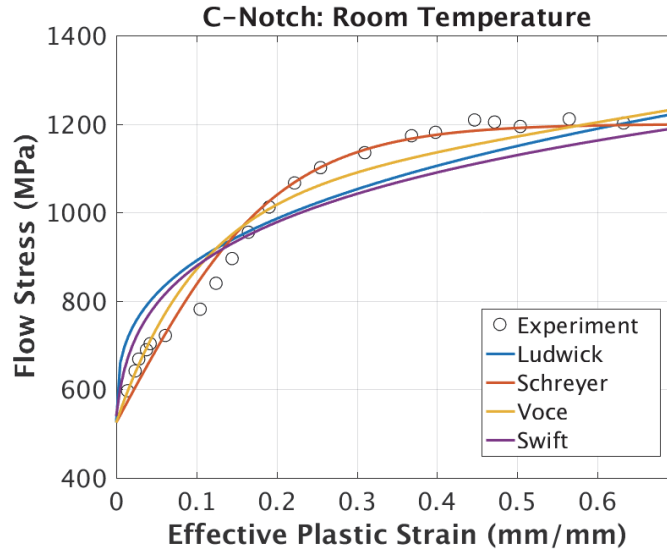


Figure 5.2: Room temperature flow stress comparison to various functional forms of $f(\epsilon)$

The best correlation between the flow stress function and room temperature results is given by the *tanh* hardening curve found in Schreyer and Maudlin (2005), although they indicate it was published previously which may be referring to the early work of Prager (1938).

The temperature modifier function, $f(T)$, was then characterized using the normalized ultimate stress ratio versus homologous temperature (Figure 5.3). The Litonsky modifier, which is simply a linear decay in strength, was found to provide a poor correlation across the entire temperature range. The Hensel and Johnson-Cook modifiers under/over predict for around half of the temperature range. The Zhao model has the best correlation up to T^* of 0.7 but over predicts strength at 200°C ($T^* \approx 0.15$) and predicts

zero strength around 1050°C ($T^* \approx 0.73$) which may result in unrealistic crack initiation locations.

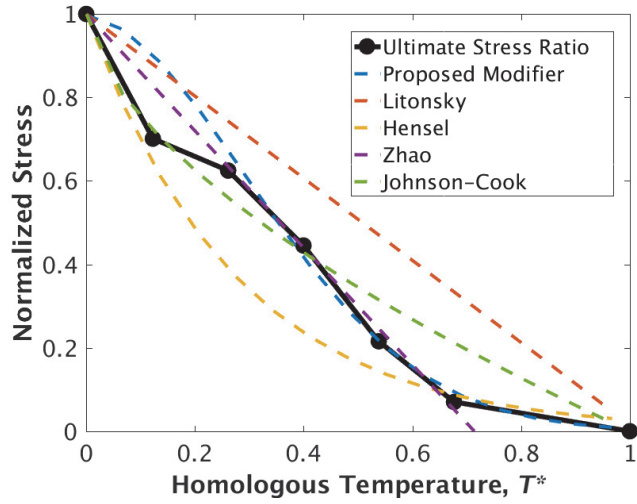


Figure 5.3: Normalized stress versus homologous temperature for determining flow stress temperature modifier term

A new temperature modifier term is also proposed which improves correlations at higher temperatures but over predicts strength in the 200°C region. The new modifier takes the following form:

$$f(T) = \exp\left(-C_1 \left(\frac{T}{T_m}\right)^{C_2}\right) \quad (5.5)$$

where, C_1 and C_2 are fitting constants and T_m is the melt temperature. The poor correlation at 200°C is due to the immediate decline in strength for stainless steels which has also been observed by Chen and Young (2006) and Sakumoto et al. (1996). The various temperature modifier terms were also compared to results for aluminum (Clausen et al., 2004) and high strength steel (Chen et al., 2006), as shown in Figure 5.4.

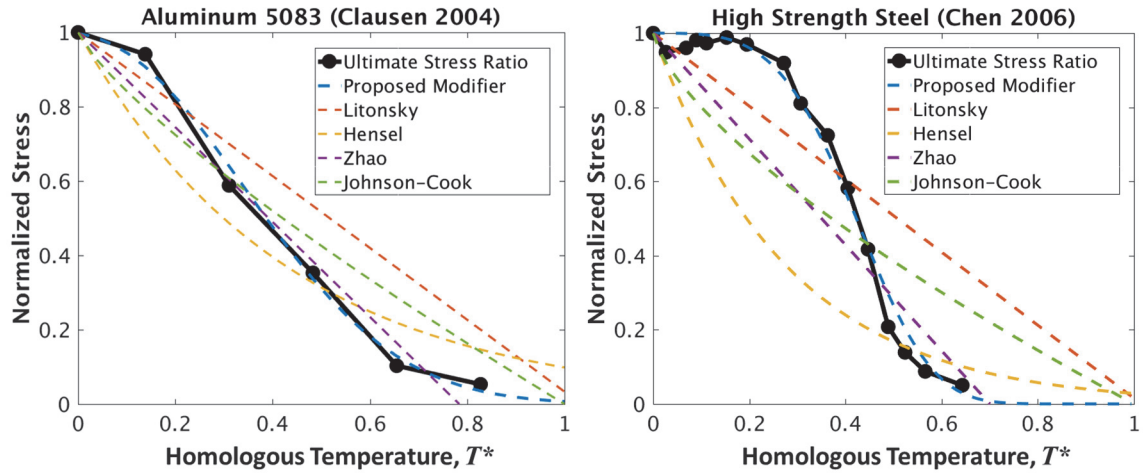


Figure 5.4: Comparison of temperature modifier terms with data from Clausen (2004) on aluminum and Chen (2006) on high strength steel

The proposed temperature modifier term results in a significant improvement over the other approaches for the two additional datasets where the strength is maintained at lower temperatures and the rapid decline is observed at intermediate temperatures. However, the proposed modifier did not compare as well for the DSS dataset and the concept of a multiplicative contribution, $\sigma = f(\varepsilon)f(T)$, must still be assessed. The *tanh* hardening fit from Figure 5.2 was combined with the Zhao and proposed modifier fits from Figure 5.3 to estimate the hardening curves for the elevated temperature C-Notch experiments, as shown in Figure 5.5.

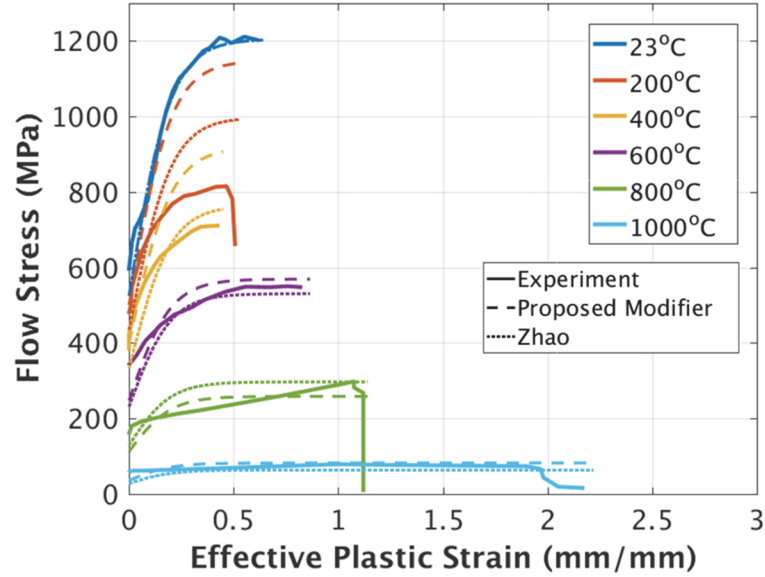


Figure 5.5: Comparison of multiplicative contribution models with elevated temperature data from C-Notch experiment

Neither temperature modifier term provides a close correlation with the experimental data across the entire temperature range, indicating a coupled flow stress equation, $\sigma = f(\varepsilon, T)$, may be needed for this material to account for changes in the shape of the hardening curve with temperature. As a result, a temperature dependent \tanh hardening function was used to fit the experimental data.

$$\sigma = C_1(T) + C_2(T) \tanh(C_3(T)\varepsilon) \quad (5.6)$$

where, fitting constants C_1 , C_2 and C_3 are now functions of temperature. The comparison with experimental data is significantly improved over the multiplicative equation, as shown in Figure 5.6. However, there are still discrepancies at 200, 400, and 800°C that could not be resolved. Moreover, the overall fit could not be improved when attempting other forms of the hardening function, as described in Table 2.1, due to the differences in the hardening shapes across the entire temperature range.

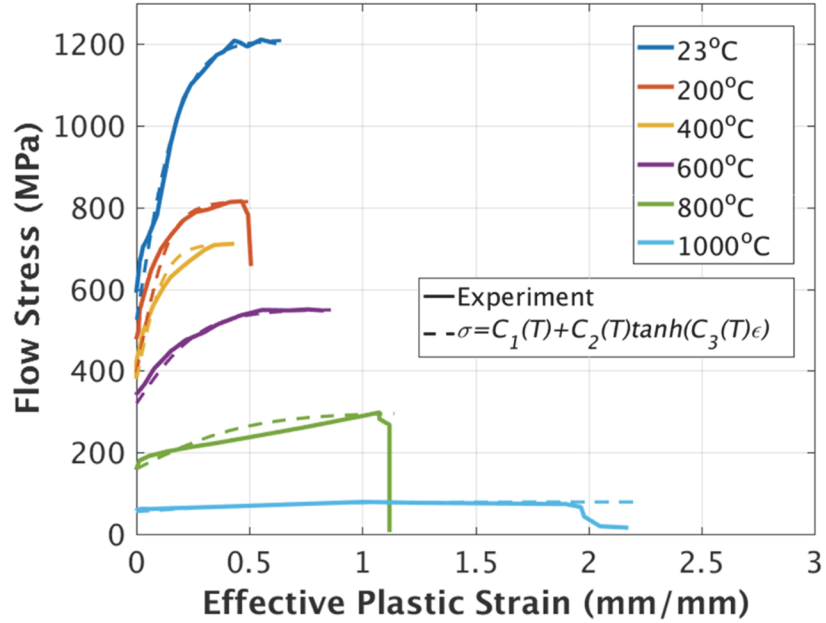


Figure 5.6: Comparison of elevated temperature data to coupled flow stress equation based on *tanh* hardening shape

Although it can be convenient to have a functional form of the hardening response for conveying large datasets and performing analytical analysis, it is generally not required for large scale finite element models where tabular data can be used for greater flexibility. Further investigation into multiplicative models is warranted since it is widely used in the literature, particularly variations of the Johnson-Cook model, but it appears the unique response of DSS does not fit within that construct. In this study, a tabular form of the hardening curves will be used to increase flexibility to capture the change in shape and amplitude of the hardening curve at elevated temperatures that could not be easily captured, even when using a coupled hardening function. Further discussion of the hardening curves will be provided in Section 5.3.

5.2 Finite Element Model

Simply selecting and calibrating a material model does not ensure accurate results will be achieved when simulating thermal-mechanical failure. Commercial FEA codes, such as Abaqus, are designed for ease-of-use but should not be used as a “black box” where all solutions can be trusted. In order to increase confidence in the model results, a number of features were investigated during this research, including; time integration, mass scaling, hourglass control techniques, mesh design, and solver precision.

5.2.1 Explicit Solver and Mass Scaling

Modeling crack initiation and propagation requires the use of dynamic solver with explicit time integration to capture inertial effects and maintain stability, respectively. However, an implicit solver could potentially be used prior to damage initiation and changed to an explicit scheme before fracture. During the explicit solver execution, a stability criterion for the time increment must be enforced to avoid oscillatory solutions with increasing amplitude. The stability requirement is dictated by the wave speed in the material as well as the element size. The stability requirement for the Abaqus/Explicit solver is as follows:

$$\Delta t = \min \left(L_e \sqrt{\frac{\rho}{\lambda + 2\mu}} \right) \quad (5.7)$$

where, L_e is the characteristic length of the finite element, ρ is the density of the material, λ and μ are Lamé’s material constants. The stability requirement can result in a large number of increments and excessive computation time when simulating quasi-static

events. In such cases, a mass scaling technique can be used to increase the stable time increment. However, this approach must be used with caution to ensure the problem is indeed quasi-static (i.e. accelerations are small). A kinetic energy criterion is often used to check the effect of mass scaling on the model. The ratio of kinetic energy to internal energy of the model should be less than approximately 5% for a problem to be considered quasi-static. Discussions by Kutt et al. (1998) on techniques and guidelines in minimizing dynamic effects provide useful insights. The problems of interest for this research were determined to be pseudo-static until material damage occurs which enables the use of mass scaling for a large portion of the analysis. As a result, a sensitivity study on mass scaling was conducted to identify a maximum mass scaling level.

The C-Notch specimen at 200°C was analyzed using an approximate hardening response based on the experimentally determined true-stress strain data. The simulation was conducted at the experimental stroke rate of 2.54 mm/s and various fixed mass scaling levels, defined by the Abaqus keyword *FIXED MASS SCALING. The mass scaling (MS) was varied from 1 to 1,000,000 and the load versus shoulder displacement was compared until just prior to the final load drop (*i.e.* $\delta \approx 1.7\text{mm}$, $F \approx 2800\text{ N}$). The load versus displacement results are shown in Figure 5.7 and the Root Mean Square Error (RMSE) is shown in Figure 5.8.

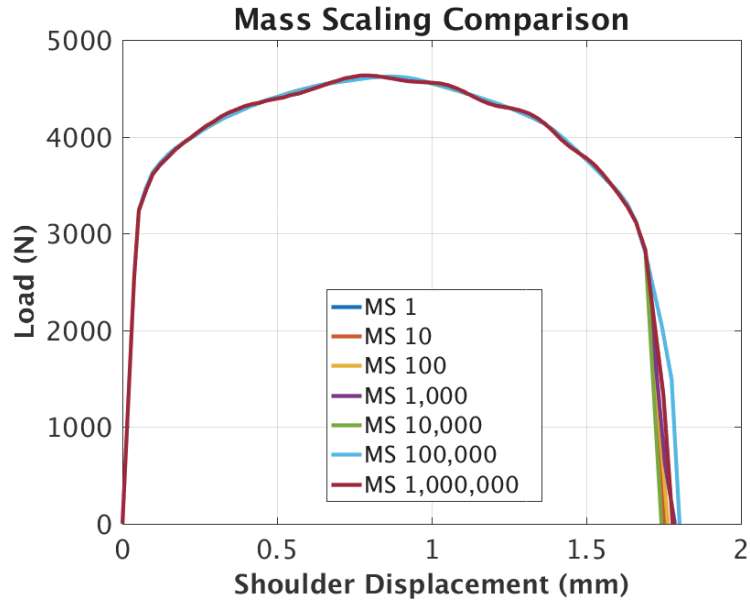


Figure 5.7: Comparison of explicit dynamic simulation of C-Notch specimen at various mass scaling levels

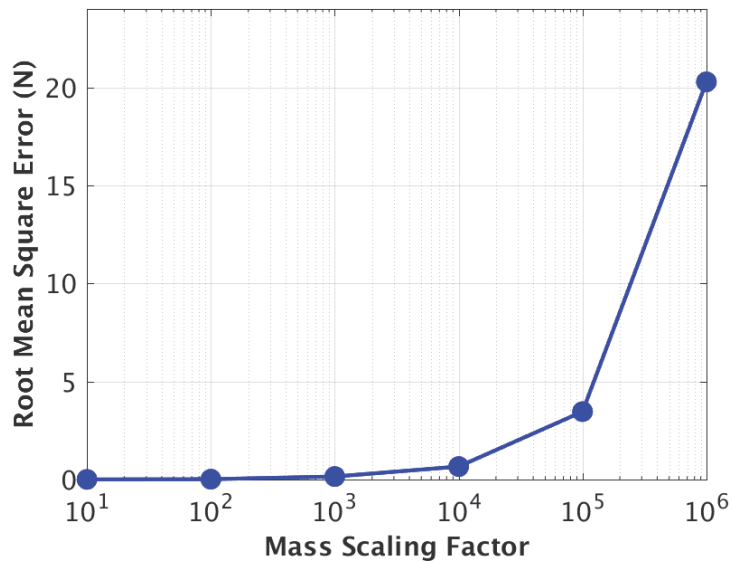


Figure 5.8: Root mean square error as a function of mass scaling factor in comparison to model with no mass scaling

The general trend in the load versus displacement response was captured at all mass scaling levels. However, oscillations in the force at MS of 1,000,000 can be easily seen in Figure 5.7 and even some small oscillations were observable at MS of 100,000. A mass scaling of 10,000 was identified as a maximum mass scaling level since oscillations

were nearly eliminated and the RMSE was beginning to level off. However, MS of 1,000 was used for the majority of the analyses presented in this study.

To help validate the use of the explicit solver and mass scaling, a comparative study was conducted for static and dynamic approaches to simulating the tensile tests. For most of the experiment, the tensile tests may be considered quasi-static and thus can be adequately solved using a static assumption ($\sum F = 0$). However, the experiment becomes dynamic during localized necking and the implicit solver is unstable during crack propagation which dictates the use of an explicit dynamic solver. The inertial effect due to model mass, m , and acceleration, a , in a dynamic analysis ($\sum F = ma$) necessitates great care when analyzing quasi-static problems. For instance, the load must be applied gradually to avoid unrealistic inertial effects and stress waves that would otherwise be ignored in an implicit solver where loads can be applied instantaneously. In the case of the tensile test specimens, the stroke rate was gradually increased to the experimental rate using Abaqus keyword “*Amplitude, Definition=Smooth Step” to eliminate any large stress waves induced by instantaneous application of boundary conditions.

The implicit static, implicit dynamic, and explicit dynamic solution procedures were compared using the C-notch test at 200 °C in order to show that the explicit solution of the dynamic equation with mass scaling and smooth application of the boundary condition can be used to analyze a quasi-static uniaxial tension test. Material damage was not considered because the PDM model becomes unstable in the implicit solver near the point of failure. The results are shown in Figure 5.9 with negligible difference between

the three methods, indicating the approach can properly capture the quasi-static behavior of the test specimen.

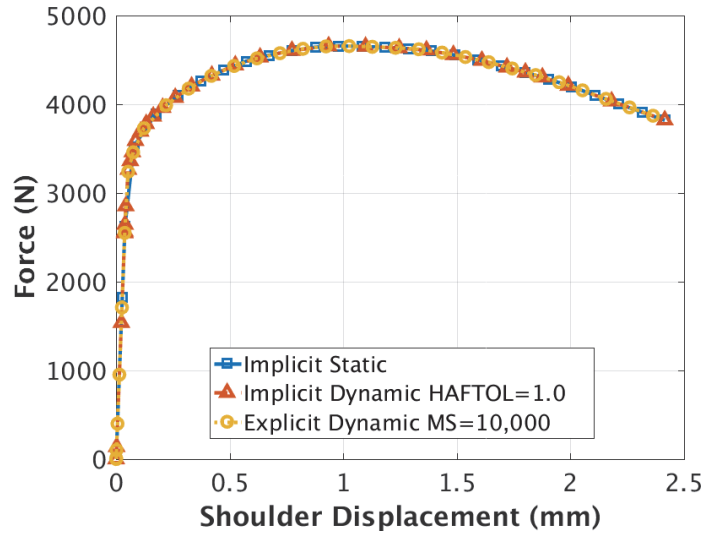


Figure 5.9: Comparison of implicit and explicit solution schemes for the tensile test simulations

When conducting Abaqus/Explicit simulations with mass scaling, the solver precision should also be considered. The stable time increment increases with mass scaling, effectively reducing the number of solver increments required for the analysis. As the mass scaling is decreased near fracture initiation, the time increment will be drastically reduced. As a result, the number of increments increases which leads to compounding error when using single precision. A comparison of the results for MS=10,000 (1.1 Million increments) and MS=10 (37 Million increments) is shown in Figure 5.10. The results show a significant error is introduced when using single precision near fracture initiation. The results are also consistent with the Abaqus recommendation to use the double precision solver when the number of increments exceeds 2 Million. Given these findings, the double precision Abaqus/Explicit solver is used throughout this study.

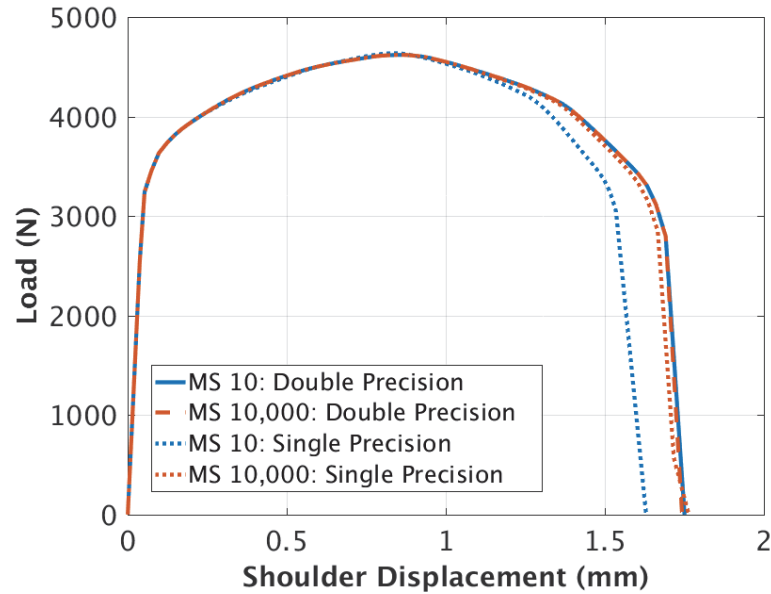


Figure 5.10: Comparison of load versus displacement between the single and double precision solver for two different mass scaling levels

5.2.2 Finite Element Mesh

Local continuum damage mechanics models, such as the PDM approach, have a known pathological mesh-size dependence because of strain localization, i.e. the material softening behavior exhibited in localized necking is ill-posed due to loss of ellipticity of the governing equations. Analytical solutions to softening models predict damage localization into an infinitesimal volume, which is contrary to experimental observation of the ductile failure process. Thus, in the finite element method, localization depends upon the initial mesh discretization, and continuing mesh refinement leads to a non-physical solution as localization occurs in an infinitely thin cross-section. In order to alleviate mesh size dependence, an intrinsic material length scale based on material microstructure is often introduced into the governing equations which forms the basis of nonlocal continuum models and gradient damage models. In nonlocal models, the

equivalent plastic strain is integrated over a characteristic domain instead of a single element typically used in FEA based continuum models. A more comprehensive discussion on the two models and issues associated with localization modeling can be found in Peerlings et al. (2001, 2002) and Jirasek & Rolshoven (2003).

Since there is no well-defined methodology for determination of intrinsic material length scale, numerical simulations are often used to calibrate the length scale to match experimental observations. Similarly, a local continuum damage model can be used with the initial dimensions of the finite elements defined as a “material property” together with the calibrated damage parameters to match experimental observations. Then, the element dimensions and damage parameters can be applied to the analysis of more complex structures. This engineering approach has been used successfully by Xia et al. (1995) to simulate failure of various notched plates and more recently by Borvik et al. (2003) to study the influence of stress triaxiality and strain rate on the behavior of Weldox 460 E structural steel, and has been adopted for the development of the progressive damage model in this study.

Given that the mesh size is considered a “material property”, the element size must be selected to appropriately represent the geometry of the notched tensile specimens while being adequate in size for the larger panels and pressure vessels used in the validation experiments. If the mesh is highly refined in the notched specimens it could result in excessive runtime for the larger validation tests. If the elements are too large then the notched specimen geometry will not be adequately captured. In addition to size, the orientation of the element can cause inconsistencies between the calibration

experiment and the validation experiments. Since the tensile tests, panel tests, and pressure vessels are all expected to fail in Mode I, the mesh can be designed to align with the anticipated crack direction.

The smallest dimension in the three experiments is the sheet material thickness (1.5 mm) while the largest dimension is the pressure vessel (pipeline) length (1 m) which are almost three orders of magnitude different. A minimum of three elements through the thickness was identified as a minimum for capturing thermal gradients during transient heating of the validation experiments and the non-uniform stress and strain field during localization. In the plane of the sheet material, an element size of 1mm x 1mm was selected as the coarsest mesh which still resolved the notch specimen geometry. Given this element size, the mesh for the pressure vessel would be greater than 2.5 Million elements without implementing additional meshing strategies, which will be discussed in more detail in Chapter 7. As a result, this was found to be the smallest mesh size possible for enabling simulations of larger scale systems such as pressure vessels.

The mesh for the C-Notch and V-Notch specimens are shown in Figure 5.11 and Figure 5.12 along with the approximate element dimensions in the localization zone (minimum cross-section width). The mesh is transitioned to a larger size in the tab regions of the C-Notch specimen however the central 3 rows, where localization occurs, are very close to the target dimensions. In the V-notch specimen, the element size in the central region is set to the target dimensions and the remaining geometry is meshed to have a relatively uniform element size over the entire sample. More sophisticated transition

meshing strategies could be used to reduce the number of elements but it wasn't necessary since the total number of elements was relatively small (<9,000).

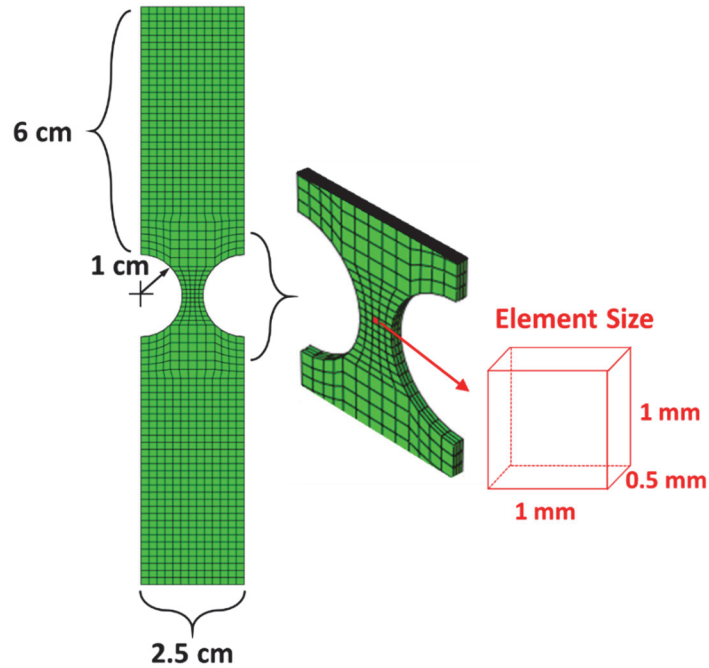


Figure 5.11: Finite element mesh for C-Notch specimen mesh showing element size in the localization zone

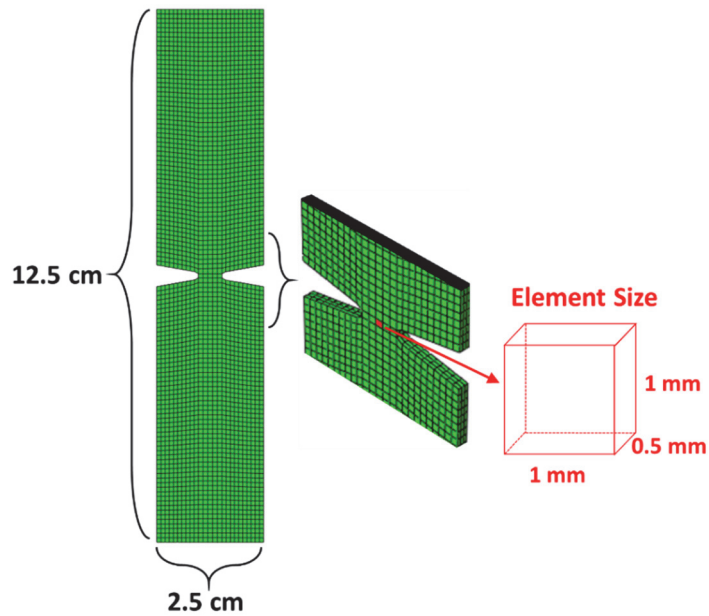


Figure 5.12: Finite element mesh for V-Notch specimen mesh showing element size in the localization zone

5.2.3 Element Type and Hourglass Control

The element type is also a critical consideration for any FEA model since there are many solid, shell, and reduced order structural elements one can choose. Even within a particular type, such as a 4-noded shell, one will find many different integration approaches. Although some shell elements can resolve the thickness change during large deformation, a solid element is preferred so that the thinning of the sheet material can be discretely captured. As an example, almost an order of magnitude in thickness reduction was observed for the experiments conducted at 1000°C.

Within the solid element options, the FEA community has slowly trended toward reduced integration hexagonal elements for large plasticity and failure problems due to their performance, relative accuracy, and the reduction in volumetric/shear locking. An overly stiff response may be observed when using full integration with a material response that tends toward incompressible such as large deformation plasticity problems. Belytschko, Liu, and Moran (2000) provide a comprehensive description of various element technologies along with some of the advantages and disadvantages. The primary concern when using reduced order elements is the associated hourglass deformation mode, as shown in Figure 5.13.

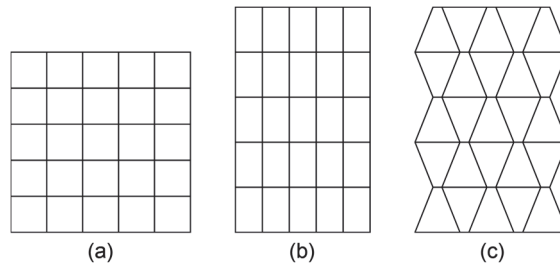


Figure 5.13: Notional deformation of 2-D panel under tensile load: (a) Un-deformed mesh; (b) Deformed mesh without hourglass mode; (c) Deformed mesh with hourglass mode

The issue arises from the rank deficiency in the element stiffness matrix such that nodal displacements can occur unrelated to rigid body motion and induce no additional stress in the element. The hourglass mode results in excessive and unrealistic mesh distortion which has led to the development of a wide variety of hourglass control techniques such as artificial stiffness, artificial damping and the enhanced assumed strain techniques. Technical discussion on the different techniques can be found in papers by Flanagan & Belytschko (1981), Belytschko et al. (1983), Belytschko & Bindeman (1993), Wriggers & Reese (1996), Reese & Wriggers (2000), Puso (2000), and within the Abaqus documentation.

The various hourglass control approaches available in Abaqus were evaluated to better understand solution sensitivity. The 8-noded reduced order brick element (C3D8R) within Abaqus/Explicit can be used with relaxed stiffness, total stiffness, enhanced, viscous or a combined method of hourglass control. When using the implicit solver, Abaqus/Standard, the brick element can only be used with total stiffness and enhanced hourglass controls. A simple three element model was created to evaluate the hourglass techniques using 1 x 1 x 1 cm elements. The deformation was imposed by a constant

velocity of the top surface and the boundary conditions allowed for uniform cross-section reduction, as shown in Figure 5.14.

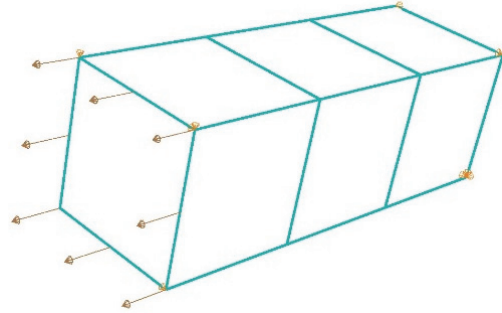


Figure 5.14: Three element finite element model for evaluation of hourglass control techniques

Each of the available hourglass control technique were analyzed and the load versus displacement curves were extracted, as shown in Figure 5.15. In most cases, the overall force-displacement response is very similar and the plot must be enhanced near the peak load to discern between the various methods. However, the exception is the viscous hourglass control technique which failed to control the hourglass mode.

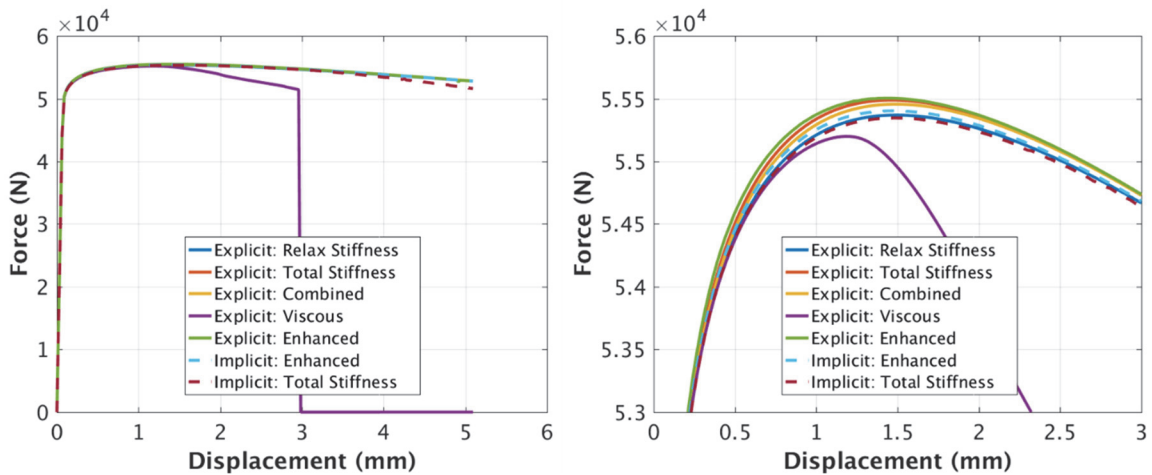


Figure 5.15: Force versus displacement of three element model using various hourglass control techniques

The typical deformation behavior was nearly uniform along all three elements while the viscous hourglass control resulted in non-uniform deformation as the solution became unstable, as shown in Figure 5.16.

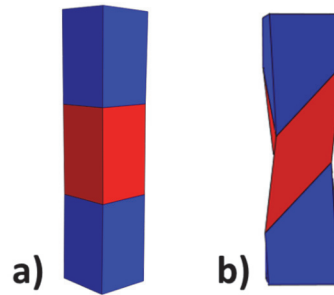


Figure 5.16: Deformed shape colored with effective plastic strain: (a) Typical deformed shape without hourglass mode; (b) Deformed shape using viscous hourglass control which was unable to suppress hourglass mode

A second test case was used to further evaluate the hourglass control techniques with more confined boundaries. The “roller” boundaries were replaced by “pins” such that the top and bottom surfaces were not allowed to deform, resulting in an hourglass deformation of the top and bottom element and increased strain localization in the center element. A representative deformed shape is shown in Figure 5.17.

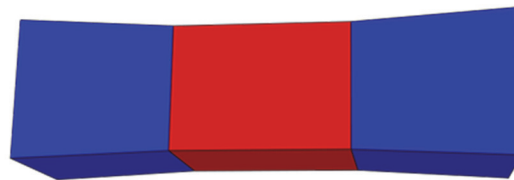


Figure 5.17: Deformed shape of three element model with more confining boundary conditions, colored with effective plastic strain

The resultant force versus displacement curves are provided in Figure 5.18 which shows a significant difference between the various hourglass control techniques. Once again, the viscous hourglass control is the least stable method while the enhanced, total

stiffness and combined stiffness using Abaqus/Explicit now show a considerable increase in system stiffness.

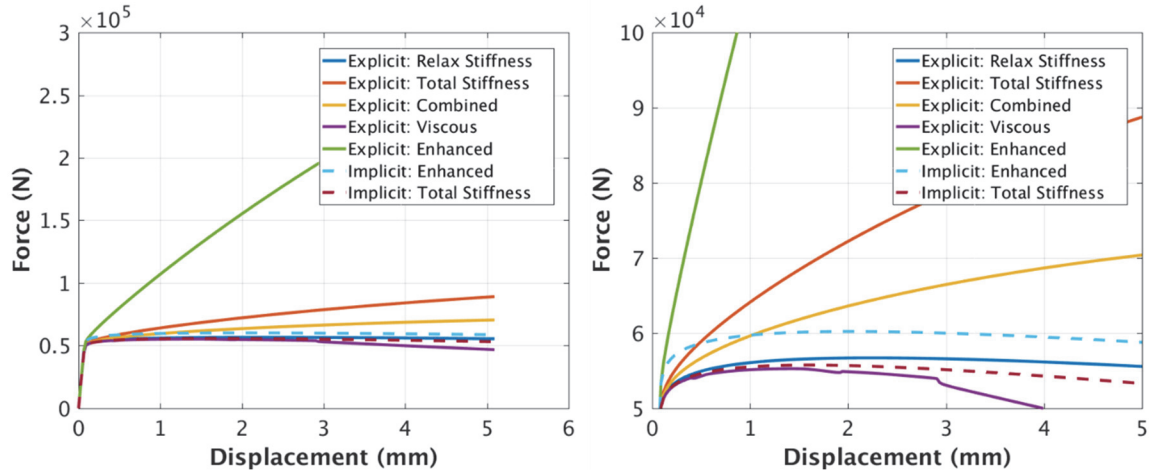


Figure 5.18: Force versus displacement curves using various hourglass control techniques with the three element model and increased confinement of the end boundaries

Of the remaining hourglass control methods, the Implicit/Total Stiffness and Explicit/Relax Stiffness methods had comparable results and happen to be the default hourglass control techniques for their respective solvers. Contrary to the Abaqus documentation, the enhanced hourglass control technique had the largest difference in structural response between the explicit and implicit solver, most likely due to differences in the implementation. The large variation in response indicates that not only the mesh size but also the element technology must be constant to maintain a consistent material response during fracture. Given these findings, the default hourglass control technique for Abaqus/Explicit, relaxed stiffness, was used for the remainder of the study to inhibit hourglass modes in the reduced integration brick element (C3D8R).

5.3 Material Model Calibration

As discussed in Chapter 2, the constitutive model calibration for sheet material has been heavily investigated for application to metal forming. The work of Ling (1996), Zhang et al. (1999), Schneider et al. (2004), Cabezas & Celentano (2004), and others have demonstrated the combination of experimentation and FE analysis is currently the preferred method for obtaining true stress-true strain during necking for rectangular cross-sections. Similarly, the evolution of damage is generally derived by comparing the results of FE analysis to the post-peak response of tensile specimens. Based on the experimental results in Chapter 4, the true stress-strain material hardening curve was estimated using the instantaneous cross-sectional area calculated from the DIC measurements of the thickness and width reduction. In this section, the experimentally derived true stress-strain curves will be used in the FE analysis and the results will be compared to the global load-displacement response of the specimens prior to peak load. The damage initiation strain and evolution curves will then be determined as a function of temperature using the post peak response of the specimens.

5.3.1 Constitutive Model Calibration

The FE simulations were conducted using the FE mesh described in Section 5.2.2 with C3D8R brick elements, relax stiffness hourglass control, Abaqus/Explicit solver, double-precision, and mass scaling of 1,000. The mass scaling was gradually decreased after damage initiation such that no mass scaling was present at fracture. The hardening curves, derived from the C-Notch experiments in Chapter 4, were used with the Isotropic

J2 (Mises) Plasticity model with associated plastic flow (*Plastic, Hardening=Isotropic). The experimentally derived hardening curves are shown in Figure 5.19 along with the extrapolated hardening curves used in the FEA simulations. The curves were extrapolated where the hardening unrealistically decreases due to the presence of macro-scale voids prior to final material separation.

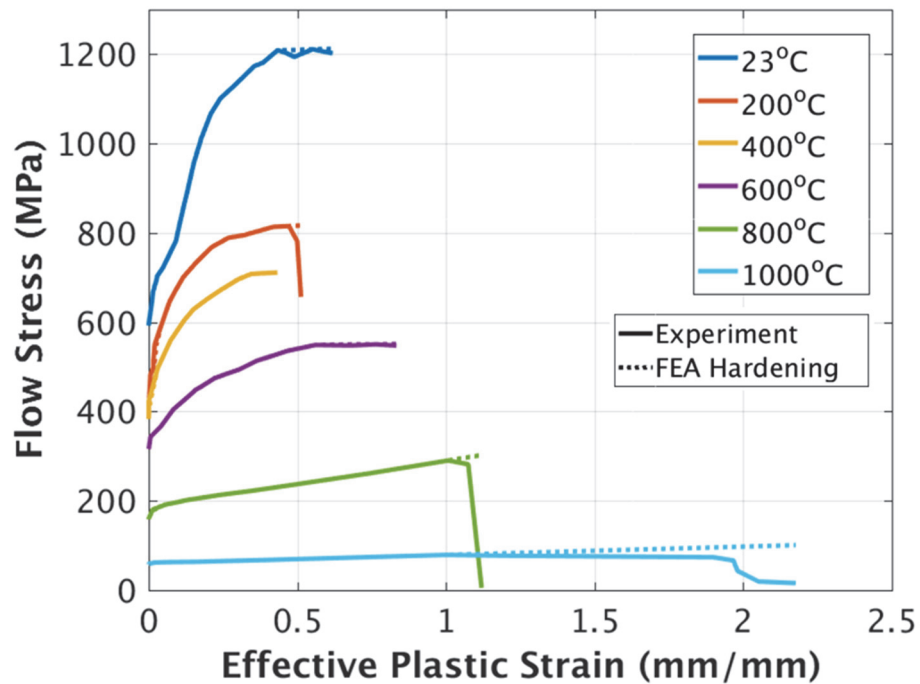


Figure 5.19: Experimentally derived hardening curves and extrapolated hardening curves used in the FEA simulations

The resulting load displacement response based on the extrapolated hardening curves are shown in Figure 5.20.

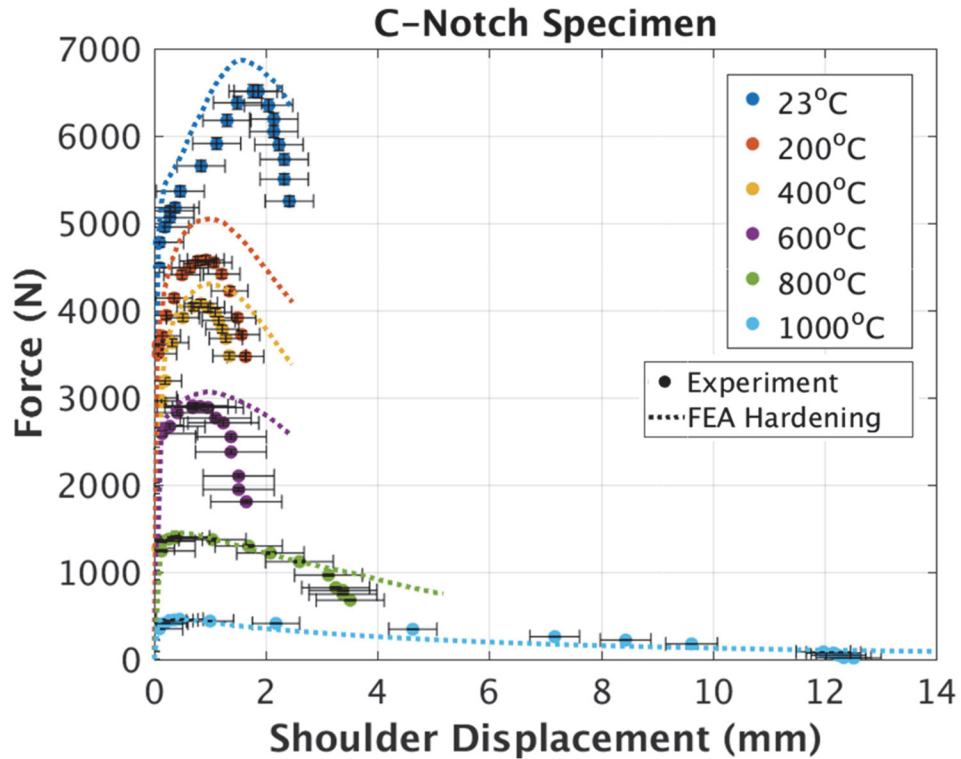


Figure 5.20: Comparison of load-displacement response of C-Notch FEA simulations using extrapolated hardening curves

The FEA simulations predict higher peak loads than the experiment for temperatures in the 23-600°C range while having close correlation at 800°C and slight under prediction at 1000°C. The peak load has significantly lower uncertainty than the displacement, therefore the hardening curves were adjusted within the uncertainty of the experimental results to capture the peak load for each experiment. The results using the modified hardening curves capture the point of peak load in the experiment within the uncertainty of the measurement, as shown in Figure 5.21. However, the experimental peak is not necessarily the same as the peak load in the model, as seen for 200°C, since material damage has yet to be included.

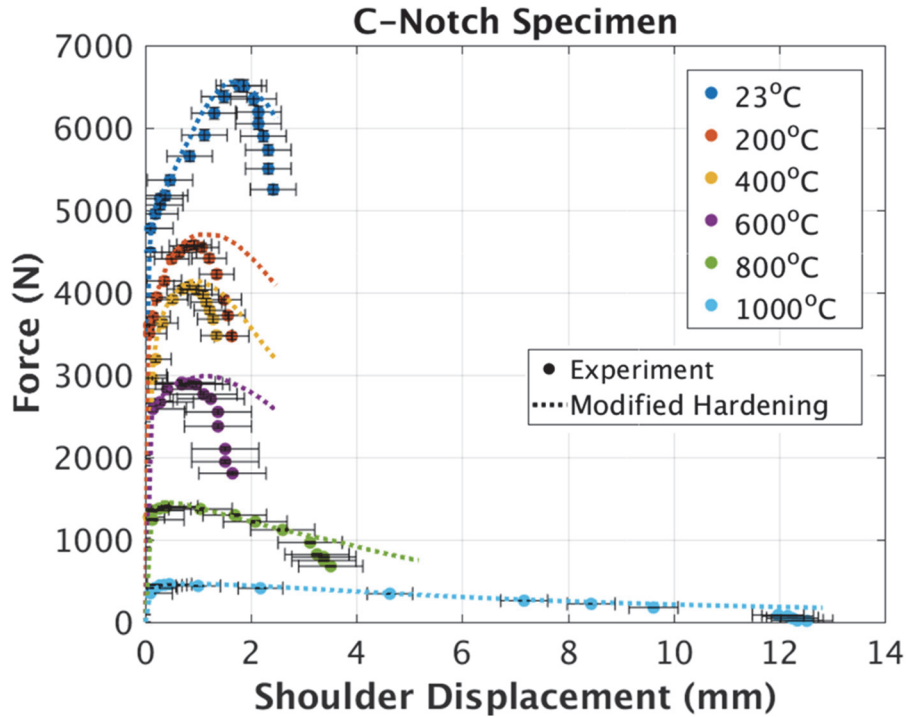


Figure 5.21: Comparison of load-displacement response of C-Notch FEA simulations using modified hardening curves

The modified hardening curves are shown in Figure 5.22 in comparison to the experimentally derived curves, including measurement uncertainties. Minimal modification was needed for the 600 and 800°C curves. However, a decrease in the hardening response was needed for 23-400°C while an increase was needed for 1000°C. The majority of the hardening curves were modified within the experimental uncertainty to capture the peak load with the exception of 1000°C where minimal hardening was observed and diffuse necking begins almost immediately. Although the original comparison in Figure 5.20 was reasonable for 1000°C, the hardening response had to be increased beyond the experimental uncertainties to properly capture the load-displacement response (Figure 5.21). This may be due to limitations in the FEA model to

capture large diffuse necking behavior or underestimation of uncertainties for this particular experiment.

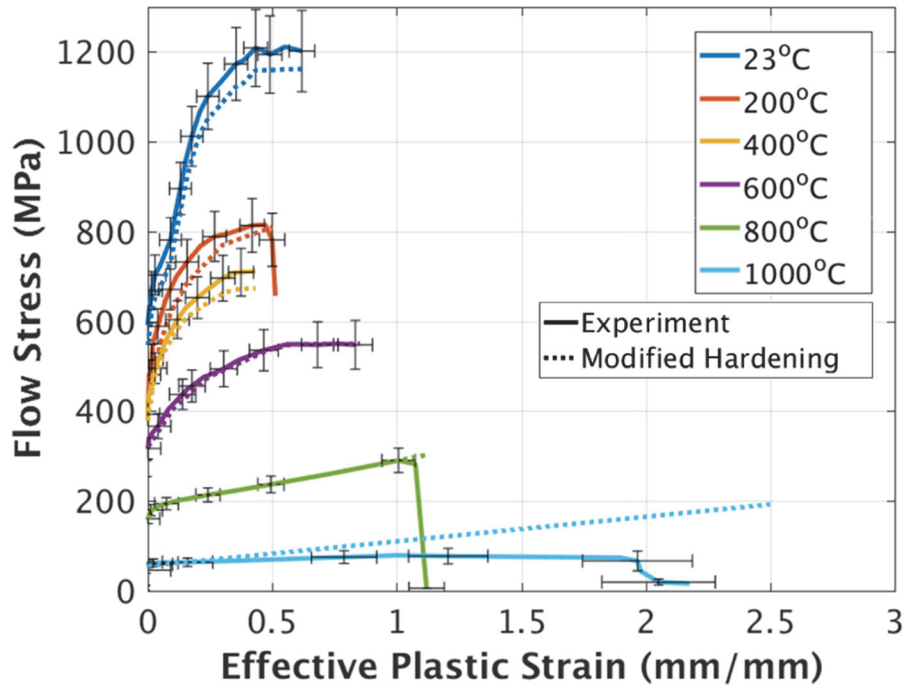


Figure 5.22: Comparison of modified hardening curves used in FEA analysis to the experimental curves with uncertainties

As previously mentioned, mesh dependency is an inherent issue when modeling ductile failure. Ideally, the element size would be close to the true localization dimension for the material, loading condition and temperature such that localization occurs over a similar length scale in the model. However, this approach does not account for large amounts of diffuse necking because the plastic strain will typically localize across a single element as the area reduction begins to outpace the hardening, effectively combining the diffuse and localized necking into a single element. Figure 5.23 shows a comparison of the deformed shape of the C-Notch specimen at 1000°C to the FEA results using the modified hardening curve. The strain is shown to localize in the center element even

when no damage model is used. The FEA model also results in diffuse necking which is not as evenly distributed as the experiment and a localization band which is not as sharp.

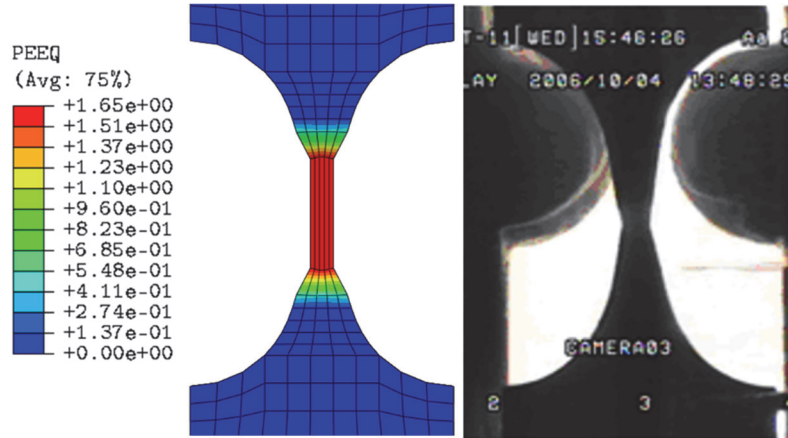


Figure 5.23: Deformation of C-Notch sample at 1000°C compared to FEA results using modified hardening curve without material damage

An alternative approach based on a non-local material model could potentially improve the ability to capture the diffuse necking. However, a length scale still exists to control the smoothing which may still result in challenges for capturing both the diffuse necking and localization band since they may require two different length scales.

In this study, the choice to make the element size a material property requires the use of the modified hardening curve at 1000°C to properly capture the load carrying capacity observed in the experiment. Since the peak load is relatively low and the elongation at failure is higher at 1000°C, this choice may have relatively low impact on crack initiation predictions as the stress is likely to redistribute to cooler material. The modified hardening curves, shown in Figure 5.22 and tabulated in Appendix A.3, will be used in the remainder of this study as it provides a global load-displacement response which correlates well with the experimental results up to the peak load.

5.3.2 Progressive Damage Model Calibration

The damage model calibration was then performed using the same basic modeling approach in Abaqus/Explicit with C3D8R brick elements, relax stiffness hourglass control, double-precision, and initial mass scaling of 1,000. The damage initiation and evolution were calibrated such that a best fit between computed and measured global load-displacement response was obtained for the post-peak behavior. An iterative trial and error technique was used to first calibrate the damage initiation strain and then the damage evolution curve (Figure 5.24). However, a parametric optimization software, such as DAKOTA, has been used in subsequent studies.

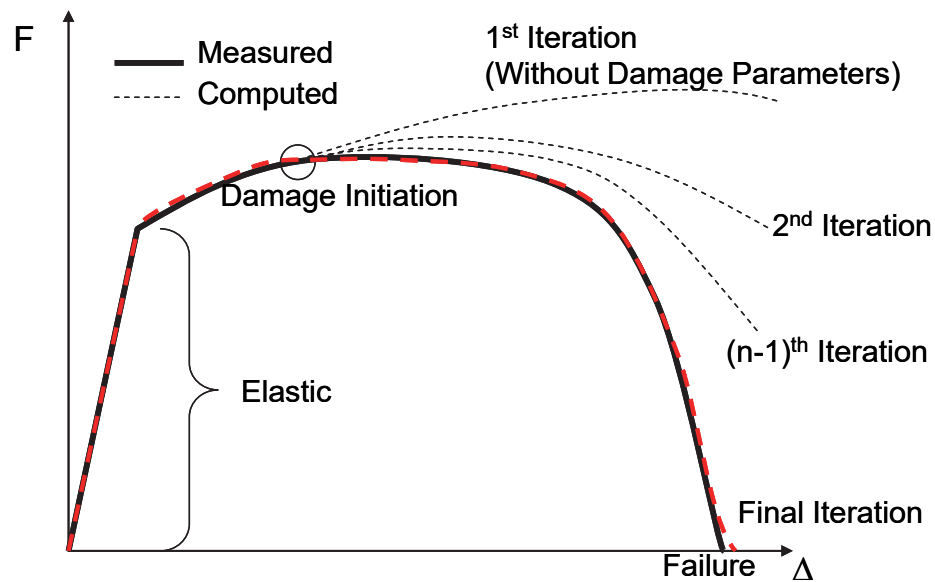


Figure 5.24: Iterative process for calibrating the progressive damage model parameters using global load-displacement

The C-Notch results from the hardening curve calibration were used to determine the damage initiation strain. As previously mentioned, the peak load from the model was not necessarily the same as the experiment even after calibration of the hardening curve. The point where the model begins to diverge from the experimental results is where the damage initiation is assumed to occur. Figure 5.25 shows the load-displacement curves for each temperature with the estimated damage initiation point. At lower temperatures, the initiation point is close to the point of peak load in the experiment. At 800 and 1000°C, the initiation is estimated to be later in the deformation due to the greater diffuse necking. After the damage initiation point was identified from the load-displacement curve, the corresponding maximum effective plastic strain was determined from the model.

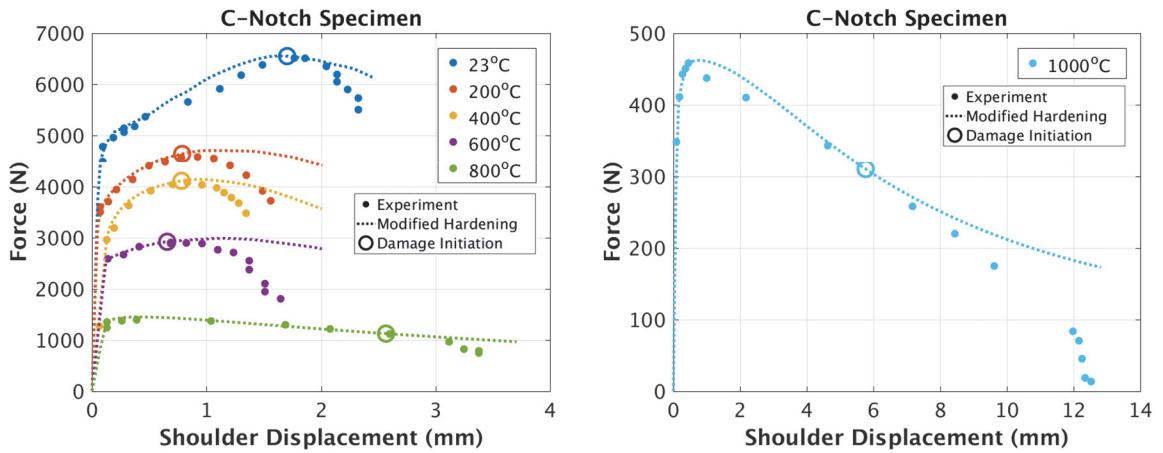


Figure 5.25: Load displacement curves using the modified hardening curves to identify damage initiation point

Once the effective plastic strain at the onset of damage was identified, the damage evolution curve was iteratively calibrated to best fit the post-peak behavior of the C-Notch specimens. The damage evolution was typically determined within 10

iterations. The load-displacement response is shown in Figure 5.26 with the inclusion of damage initiation (*Damage Initiation, Criterion=Ductile) and damage evolution (*Damage Evolution, type=displacement, softening=tabular).

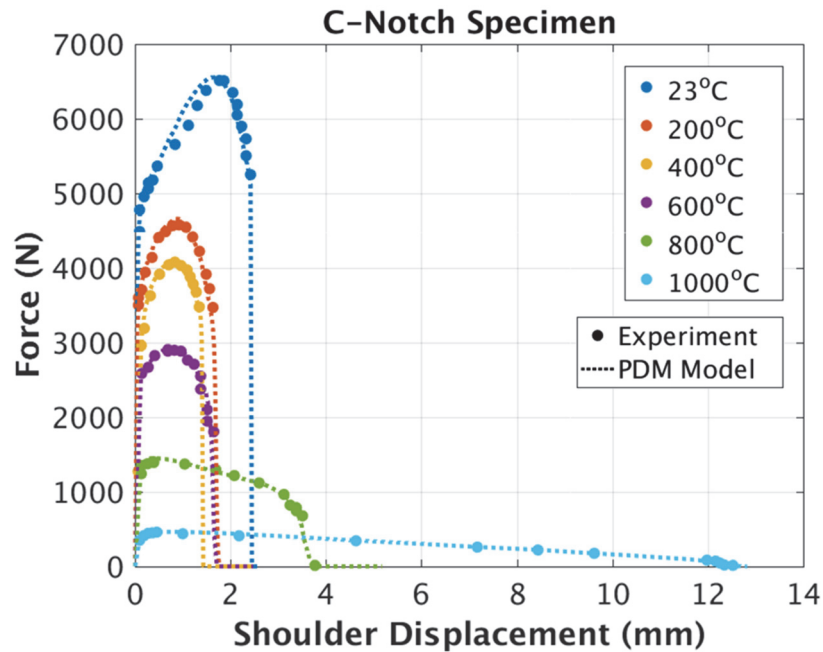


Figure 5.26: Load-displacement response of elevated temperature C-Notch specimens using PDM model with damage initiation and evolution

The incorporation of the PDM model allows the FEA analysis to capture the loss in load carrying capacity during material damage and the final loss in load carrying capacity prior to failure. An example result at 400°C is shown in Figure 5.27 with the equivalent plastic strain (PEEQ) contours for the increment before and after failure of the C-Notch specimen. The solution contours for PEEQ, damage level (SDEG), and von Mises stress (SMISES) are also provided in Figure 5.28 for the increment just prior to failure. The specimen has been cross-sectioned along the loading axis to see the variation in stress and damage within the central portion of the localization zone. The damage is highest

and fracture initiates in the centermost element which is consistent with the fracture evaluation using the FRASTA technique, described in Section 4.6.

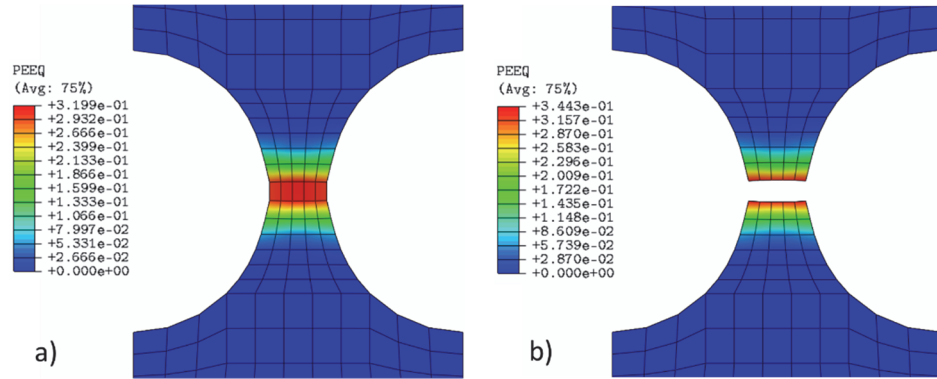


Figure 5.27: Effective plastic strain contours for the C-Notch specimen at 400°C: a) Increment prior to failure b) Increment after failure (element deletion)

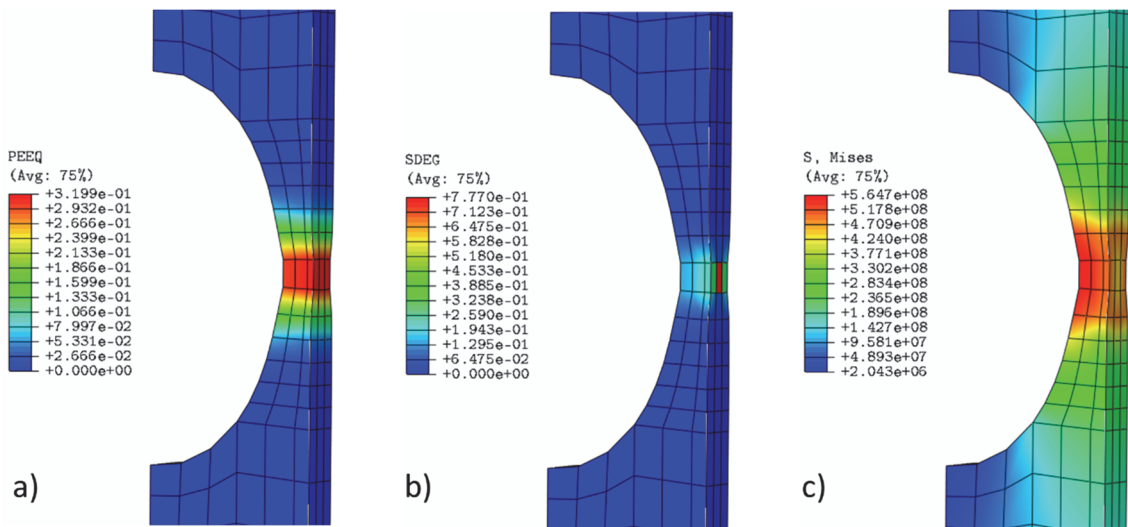


Figure 5.28: FEA results for C-Notch specimen at 400°C with half specimen removed using axial cross-section. Solution contours for increment just prior to failure; a) Equivalent plastic strain b) Damage level c) Mises stress

The damage evolution, corresponding to the load-displacement results in Figure 5.26, are provided in Figure 5.29. The damage evolution curves are similar for 23 and 400°C as well as 200 and 600°C which is reasonable when comparing the difference between the shoulder displacement at failure and shoulder displacement at peak load

(Figure 5.25). The 800°C damage evolution curve is fortuitously close to the lower temperature curves since the damage initiation was selected at a point later in the diffuse necking regime (around 75% of fracture displacement). Likewise, the 1000°C damage evolution curve was selected in the diffuse necking regime but at a point closer to 50% of the fracture displacement (Figure 5.25) which results in an extended damage evolution curve, as shown in Figure 5.29.

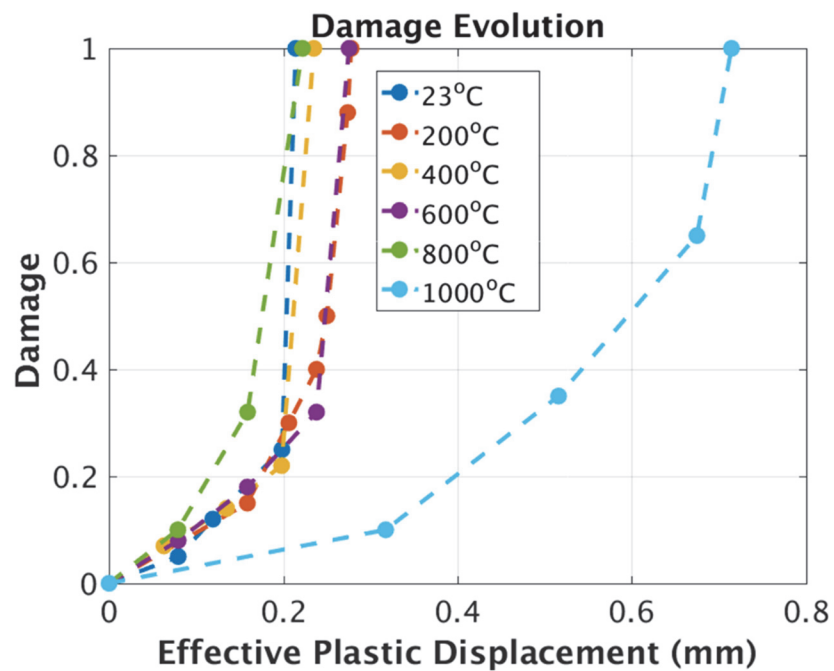


Figure 5.29: Damage evolution curves at various temperatures determined from optimizing load-displacement response of C-Notch specimens

Overall, the PDM model was able to significantly improve the correlation with the global load-displacement response of the C-Notch specimens (Figure 5.26). The V-Notch specimens were then analyzed using the same hardening and damage evolution curves used for the C-Notch specimens while modifying the damage initiation strain as a function of triaxiality to match the global displacement at failure. Although the damage evolution could also be modified with stress triaxiality using a field variable and user subroutine

(VUSDFLD), it greatly increases the data regularization requirement for the Abaqus/Explicit solver which introduces additional interpolation error. The results of the triaxiality dependent damage initiation strain results are provided in Figure 5.30. The displacement at failure is captured well and the peak load is within approximately 5% of measured values.

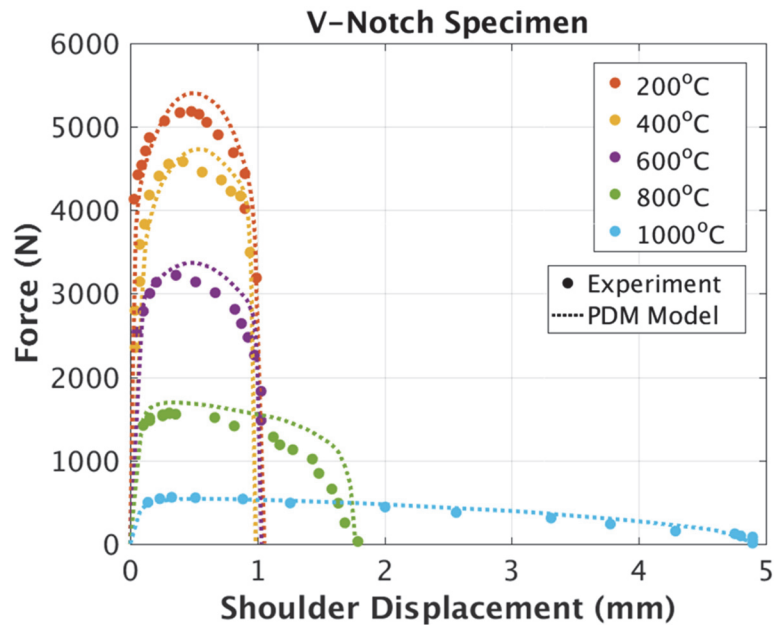


Figure 5.30: V-Notch specimen results using PDM model with triaxiality dependent damage initiation strain

Closer correlation with the post-peak response could be achieved by using triaxiality dependent damage evolution but was judged to be unnecessary as the C-Notch response is likely to control the fracture initiation in the problems of interest for this study. The V-Notch data will primarily contribute to the propagation of the crack as the confinement (triaxiality) will be higher in those conditions, resulting in a lower effective plastic displacement at failure for elements at the tip of a propagating crack than elements at a crack initiation location.

The triaxiality dependent damage initiation strain is provided in Figure 5.31. The higher triaxiality values at each temperature correspond to the V-Notch specimen and the lower triaxiality value at each temperature corresponds to the C-Notch specimen. The triaxiality is not uniform through the cross-section, particularly for the V-notch specimen, so the triaxiality values represent a nominal value for each case based on the Abaqus solution.

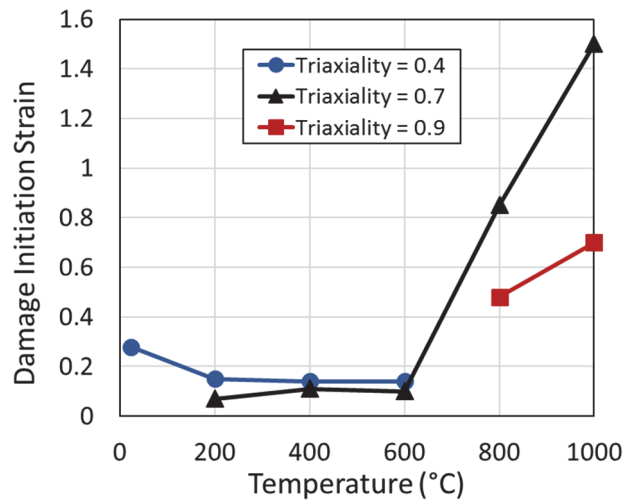


Figure 5.31: Triaxiality dependence on the damage initiation strain for various temperatures

The triaxiality and the damage initiation strains are higher for the 800 and 1000°C cases due to the significant amount of necking allowed prior to damage initiation. Due to the significant change in displacement at failure between the two specimen geometries at 800 and 1000°C, as shown in Figure 4.20, the delayed initiation for the C-Notch specimen was required to capture the lower fracture displacement in the V-Notch specimen. As previously mentioned, this may be due limitations in capturing large amounts of diffuse necking when using a local approach to simulate fracture within the

FEM framework. Nevertheless, the PDM model was capable of being calibrated to closely match the response of both the C-Notch and V-notch specimens.

5.4 PDM Model Summary

The result of a combined experimental and numerical analysis has resulted in a complete set of calibrated temperature and stress triaxiality dependent material hardening and progressive damage model parameters for simulating elevated temperature failure of DSS sheet material. The PDM model within Abaqus was capable of being calibrated to match the load-displacement response of both the C-Notch and V-Notch specimens which provides a Continuum Damage Mechanics approach to simulating crack initiation and propagation in initially un-cracked bodies.

An example input file for Abaqus simulations of the notched specimens is provided in Appendix A along with a python script used to extract the load, displacement, and maximum effective plastic strain at each increment. The complete set of material properties for DSS is also provided in Appendix A, including; density, elastic modulus, Poisson's ratio, coefficient of thermal expansion, specific heat, thermal conductivity, isotropic hardening, damage initiation as a function of triaxiality, and damage evolution as a function of temperature. To the Author's knowledge, this represents a first-of-its-kind dataset for characterizing the elevated temperature response of Duplex Stainless Steel for predicting fracture initiation during transient heating.

Chapter 6 : Panel Specimen Validation

The temperature dependent thermal and mechanical properties of DSS was characterized, including calibration of the progressive damage model. The model must also be validated to demonstrate utility for simulating realistic system level response. Model validation is often lacking in the literature where most often the calibration is presented with no application to real systems. Simply calibrating the model without comparison to additional load cases provides limited evidence for a models merit, even though non-validated models are common in the literature. In this study, model validation testing and analysis was conducted to evaluate the predictive capability of the PDM model for simulating elevated temperature component failure during transient heating. The first validation experiment was conducted using constant tensile load panels subjected to transient heating until failure. The PDM model was then used to simulate the panel response and the time-to-failure and crack initiation location were compared. No modifications were made to the material model during the validation simulations.

6.1 Elevated Temperature Panel Experiments

The panel experiments consisted of flat panels specimens subjected to uniaxial tension at a constant prescribed load, chosen to be within the elastic regime at room temperature. The prescribed force was applied with a universal testing machine followed by rapid heating until failure, using a high energy fiber laser to achieve heating rates in excess of 100°C/sec. The test was designed to capture the following critical measurements; load and displacement history, temperature history, crack initiation

location and crack propagation, and irradiance distribution. The irradiance distribution and temperature history are critical for characterizing the transient thermal state of the panel during the experiment while the crack initiation location and load-displacement are critical measurements for model comparison.

6.1.1 Panel Test Articles

The panels were constructed of the same sheet stock of duplex stainless steel used for model calibrations, with a thickness of 1.5 ± 0.1 mm, and manufactured such that the rolling direction was parallel to the loading direction. A custom grip adapter was fabricated to reduce grip slip and enable rotational motion during crack propagation. A diagram of the panel geometry and hole locations for mounting the custom fixture are shown in Figure 6.1. The CAD design for the panel, grip adapter and clevis is shown in Figure 6.2.

The front side of each sample was painted with Forrest Paint “Stove Bright” high temperature stove paint (Flat Black #6304) to help increase the surface absorption of the samples at the laser wavelength ($1.07 \mu\text{m}$). Painting the panels helped to increase the laser energy absorption from 50% to roughly 85%, as described in Section 3.5. The paint also provides a near uniform surface finish across the sample which reduces spatial variation in absorption commonly seen with unfinished materials in the as-received condition.

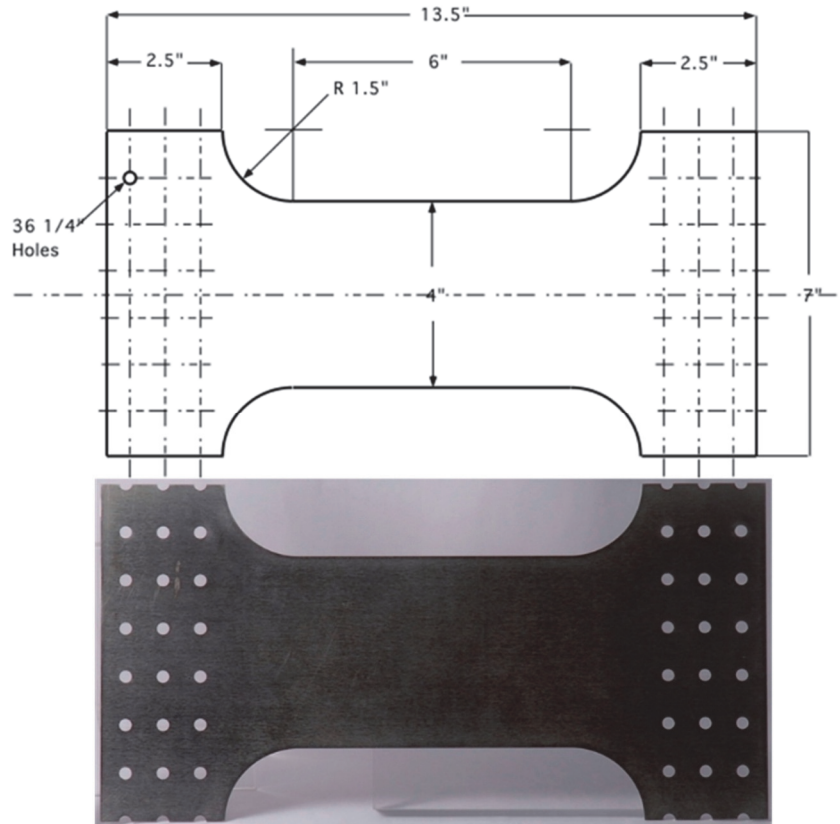


Figure 6.1: Panel test geometry including hole locations for custom mounting fixture

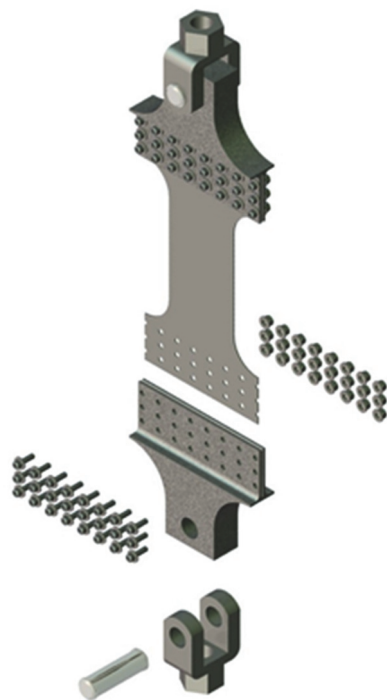


Figure 6.2: Grip adapter with 24 bolt pattern and clevis mount pin to limit slip and allow for sample rotation

The rear surfaces of the panels were prepared with high temperature speckled paint to facilitate full-field strain imaging. The speckled paint is used to track movement in the panel which enabled calculation of temporally varying strain distribution across the panel. The surface was painted with a background of light-colored Stove Bright paint (Almond #6283) and then dried. Black paint (Flat Black #6304) was then applied in a speckle pattern as shown in Figure 6.3 below.

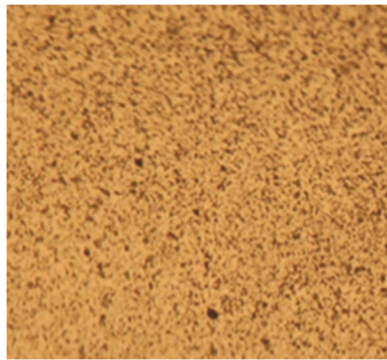


Figure 6.3: Speckle pattern paint applied to rear surface of panel specimen to enable full field strain calculations

The only contact measurements on the panel specimens were thermocouples used to capture the transient heating of the panel. Two type-K thermocouples (Omega Engineering) were spot welded to the rear surface, centered at the laser alignment location. One was perfectly centered and the second was placed as closely as possible just above the center point. Type-K thermocouples provide a measurement range up to 1250°C with standard error of 2.2°C or 0.75% of the reading, whichever is greater.

6.1.2 Panel Test Configuration

Transient heating of the test articles was provided by a 20 KW fiber laser manufactured by IPG Photonics, model YLS-20000. The laser provides a well

characterized surface flux in comparison to the IR-heaters used in the notched tension tests and significant improvement over fuel burning methods used by Birk et al. (2006) which resulted in notably difficult to characterize flux profiles, requiring simplification for modeling purposes (Manu, 2008). The basic layout of the beam train and laser diagnostics used in the panel experiments are provided in Figure 6.4. The laser beam is propagated through collimating optics to reduce beam divergence then through a coated wedge optic to split approximately 0.4% of the laser energy along multiple partial reflections used for laser diagnostics.

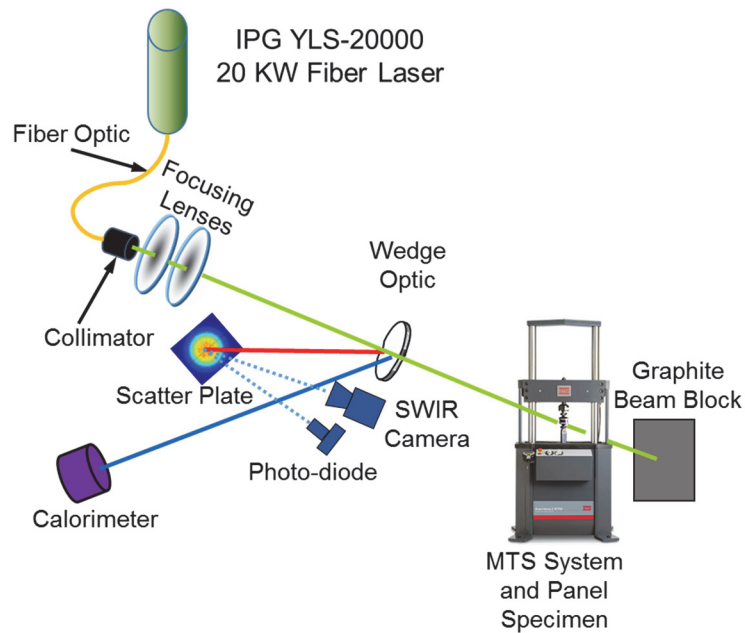


Figure 6.4: Test configuration showing laser diagnostics and beam path

The first partial reflection was used to measure the temporal and spatial variation of the laser irradiance profile using a 30 cm by 30 cm diffuse Macor scatter plate and an Indigo Alpha Short Wave InfraRed (SWIR) camera. The average power in the irradiance profile was determined from the second partial reflection using an 8 inch Scientech

calorimeter. A secondary power estimate was provided by a photo-detector (Judson J22 InGaAs) viewing the reflected energy from the scatter plate. The power measurements were calibrated to a NIST traceable ball calorimeter (BB2GP1), along the primary beam path, to determine the split ratio of the partial reflection. The scatter plate, calorimeter and test article were placed at equal distances from the wedge to capture any remaining divergence in the beam not removed by the collimator. An image of the laboratory configuration for the optical components is shown in Figure 6.5.

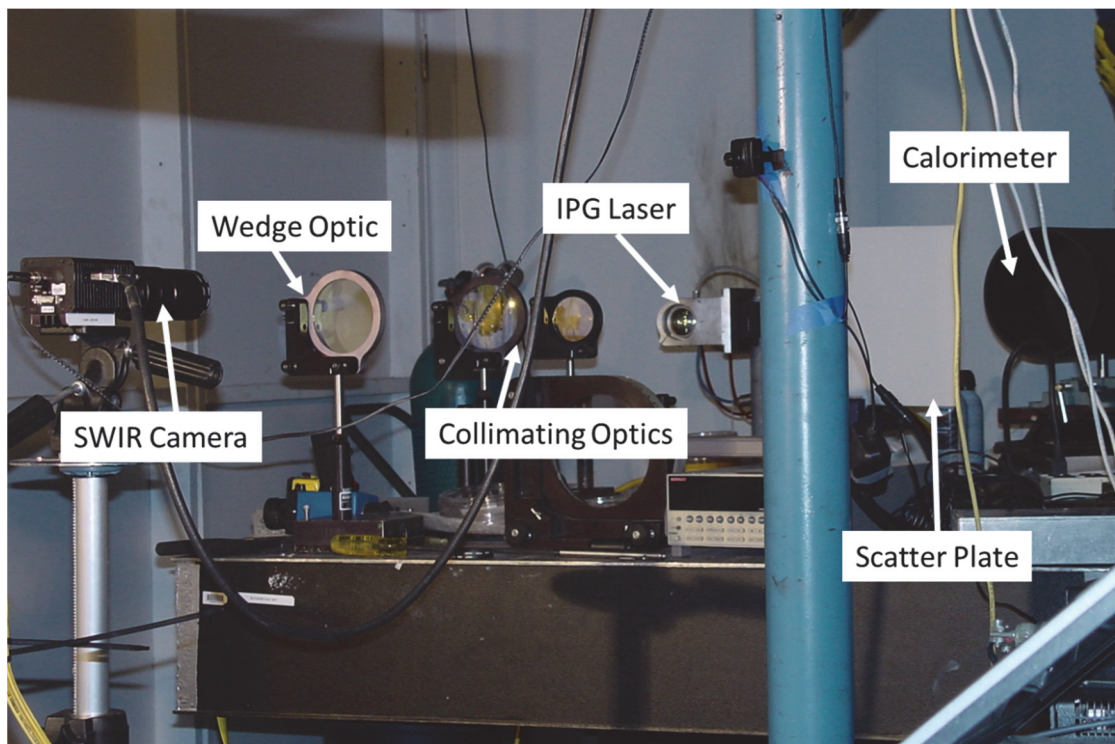


Figure 6.5: Laboratory configuration of optical elements and beam diagnostics for the panel tests

The test configuration also included eight cameras to document the panel response during transient heating and failure. The camera configuration is provided in Figure 6.6. The high speed Photron SA-1 camera was used to view the crack initiation and propagation during failure. The FLIR SC-4000 Mid-Wave Infrared (MWIR) camera was

used to measure the spatial variation in surface temperature. Four standard Sony mini-cameras were used to provide real-time video and situational awareness to the laser operator. Two Photron SA-1 cameras were setup in a stereoscopic configuration to enable a full-field strain measurement using the Correlated Solutions' non-contact deformation measurement technique. The full-field strain cameras were configured to provide 0.1 mm/pixel resolution at 5,400 frames per second. The alignment of the full-field strain cameras were in the plane of the neutral axis, as shown in Figure 6.6, while the remaining cameras were offset vertically to avoid the beam block or horizontally to increase viewing angle in the case of the Sony mini-cameras.

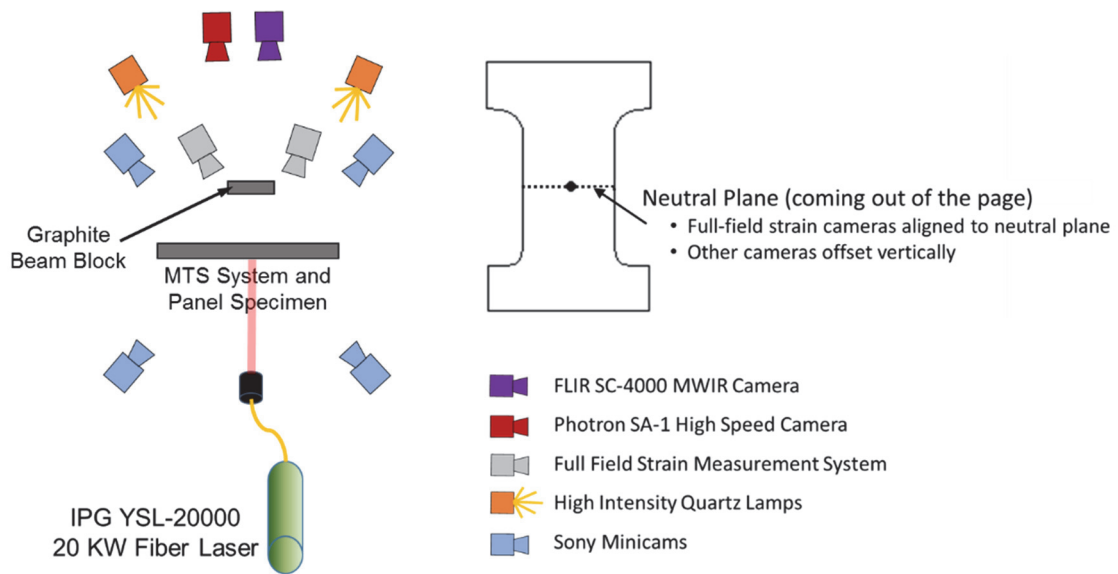


Figure 6.6: Camera configuration for panel experiments

An image of the general configuration is shown in Figure 6.7 with a panel specimen mounted in the MTS 810 materials testing system. A 20 kip load cell was used for the experiments which enabled the machine to operate in the middle third of the load range. The hydraulic system which powered the MTS system was controlled using a Test Star IIS

operating system. Prior to testing, the MTS system was calibrated with the clevis adapters and grips to characterize the load train compliance.

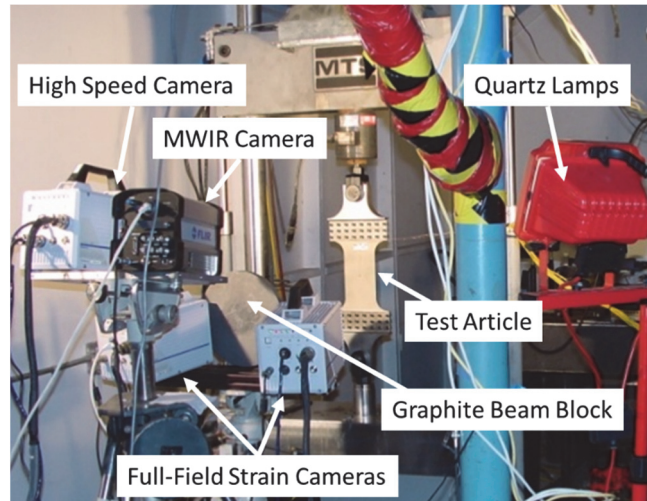


Figure 6.7: Laboratory configuration with panel sample mounted in the MTS machine

6.1.3 Panel Test Matrix

The initial load was selected to ensure the panels were in the elastic regime prior to laser heating. The yield and peak load for failure at room temperature were determined using the strength results found in Figure 4.18 and the geometry provided in Figure 6.1. The estimated load for first yield (F_y) was 90.7 kN and the peak load (F_p) was 132.7 kN. Two different initial loads, 60 and 70% of F_y , were used to induce failure at different peak temperatures. The lower load condition should result in a higher peak temperature at failure since additional weakening will be needed to cause rupture. In addition, two different laser irradiance levels were selected to further change the time-to-failure. A lower irradiance level (100 W/cm^2) was used for the lower loading condition, providing a heating rate of approximately 100°C/s . A higher irradiance level (200 W/cm^2) was selected for the higher loading condition, providing a heating rate of approximately

200°C/s. The spot size was selected to be as large as possible while depositing the majority (>95%) of the laser energy on the sample. A spot size diameter of 9 cm calculated at the $1/e^2$ ($2\text{-}\sigma$) point was found to best meet this criterion which minimizes energy losses and ensures the entire cross-section is at an elevated temperature during rupture.

A repeat shot of each test condition was planned, as shown in Table 2.1, to ensure a consistent panel response was captured. A third test would be considered if consistent results were not observed. However, only 6 test specimens were available to conduct this experiment which limited the opportunity to investigate a greater range of conditions or repeat tests.

Table 6.1: Panel test matrix including load and laser conditions

Test Name	Load Ratio (F/F_y)	Load (kN)	Peak Irradiance (W/cm²)	1/e² Diameter (cm)
PT1	0.6	54.4	100	9.0
PT2	0.6	54.4	100	9.0
PT3	0.7	63.5	200	9.0
PT4	0.7	63.5	200	9.0

6.1.4 Laser Beam Results

The test series was completed using the approximate laser conditions provided in the test matrix (Table 6.1). The time-averaged laser beam profiles for tests PT1 and PT2 as well as PT3 and PT4 are shown in Figure 6.8 and Figure 6.9, respectively. The first experiment, PT1, had a higher power setting which resulted in a peak irradiance of approximately 125 W/cm². The issue was corrected for PT2 resulting in an irradiance of

approximately 100 W/cm^2 , as prescribed in the test matrix. Even though the irradiance differed, the laser beam size was approximately 9 cm in diameter for both tests.

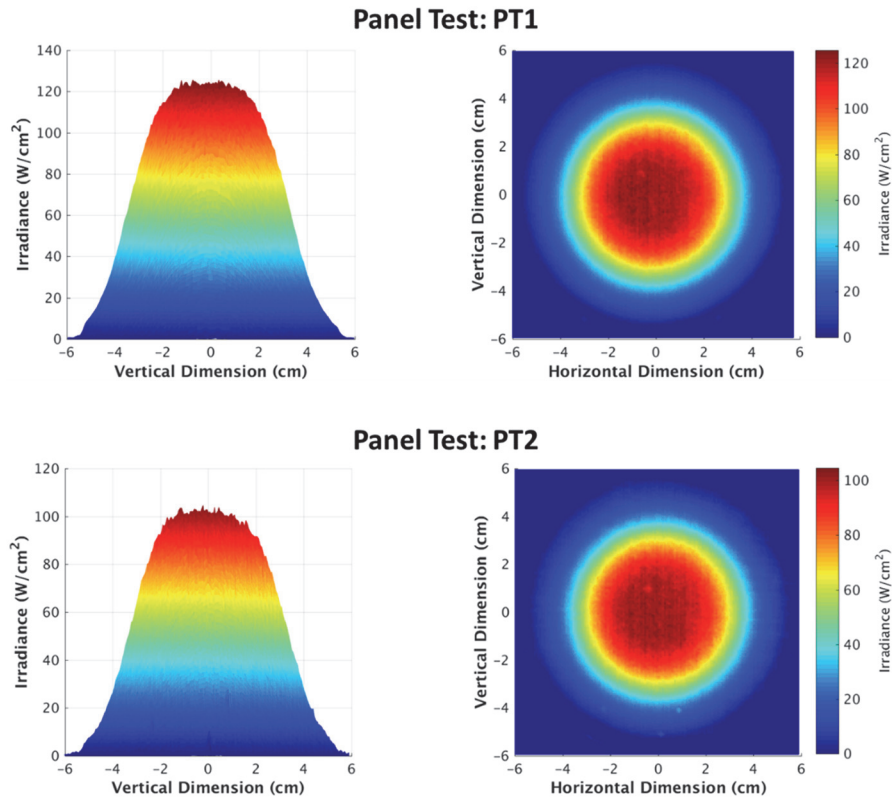


Figure 6.8: Laser beam profiles for panel test PT1 and PT2

The power setting was adjusted appropriately for PT3 and PT4 resulting in peak irradiance values of approximately 200 W/cm^2 , as prescribed in the test matrix. Again, the laser beam size was approximately 9 cm in both the horizontal and vertical directions. The beam symmetry is clear from the profile images and the benefit of using a laser source, as opposed to a fuel burning heater, is evident from the quality of the flux characterization.

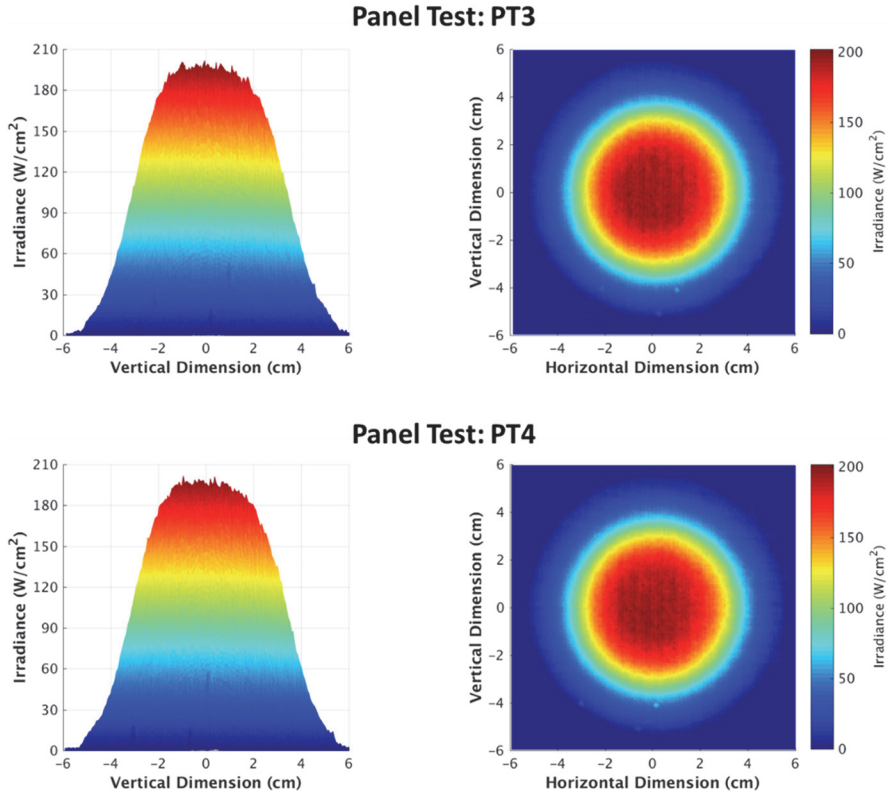


Figure 6.9: Laser beam profiles for panel test PT3 and PT4

A summary of the laser beam power, irradiance and spot size is provided in Table 6.2. The peak irradiance is provided as well as an average irradiance over a 1 cm diameter circular region surrounding the beam centroid. The horizontal and vertical diameter ($1/e^2$) are provided to assess the laser beam symmetry.

Table 6.2: Measured laser beam power, irradiance, and size

Test Name	Total Power (W)	Peak Irradiance (W/cm ²)	Average Irradiance, 1cm Φ (W/cm ²)	Horizontal Diameter, 1/e ² (cm)	Vertical Diameter, 1/e ² (cm)
PT1	4791	125.6	120.5	9.10	9.01
PT2	3899	104.6	100.1	8.96	8.93
PT3	7525	201.8	193.2	8.93	8.90
PT4	7487	201.6	193.8	8.98	8.90

The laser power and beam profile were stable during each shot allowing for the time-averaged beam to be used in the FEA model. The laser beam profiles were converted to a comma separated variable file to be read into the Abaqus DFLUX subroutine, which will be discussed in Section 6.2. In addition, an approximate beam profile estimate was generated to convey the beam profile information without providing the entire SWIR imagery. An example of the beam profile approximation is provided in Figure 6.10 with a comparison to the vertical profile for PT3.

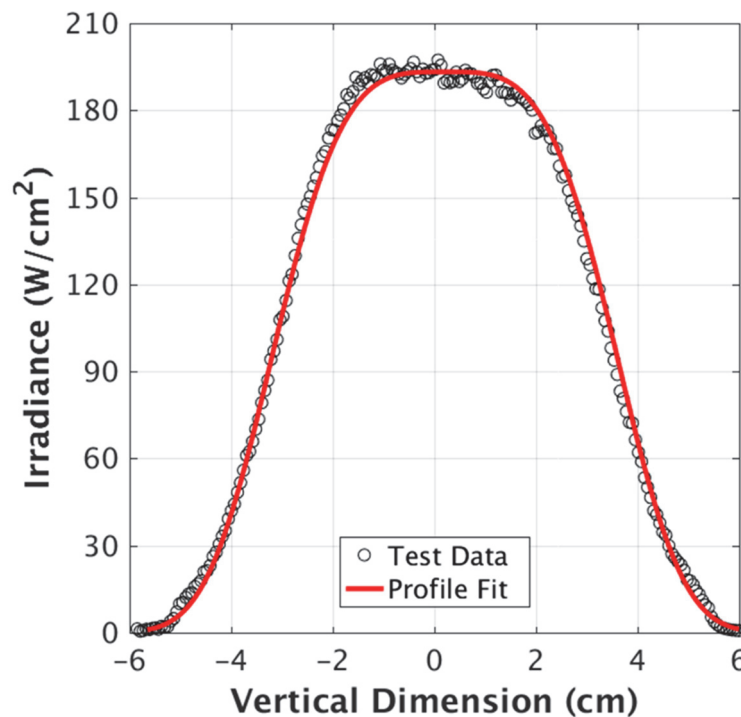


Figure 6.10: Beam profile data in the vertical dimension for PT3 with beam shape approximation

The beam profile approximation follows a super-Gaussian shape defined as follows:

$$I(r) = I_{avg} * \exp\left(-2 \left(\frac{r}{R_{avg}}\right)^{3.7}\right) \quad (6.1)$$

Where, r is the radial distance from the beam center, I_{avg} is the average irradiance (defined in Table 6.2), R_{avg} is the average of the vertical and horizontal “radius” (approximately 4.5 cm based on the diameters provided in Table 6.2), and the super-Gaussian exponent of 3.7 was determined to best fit the laser beam data.

6.1.5 Thermal Results

The panels were instrumented with two thermocouples (TC) closely welded to the center of the panel which is also the point used for laser beam alignment. The thermocouple response for PT1 and PT2 are shown in Figure 6.11. For panel test PT1, both thermocouples responded well up to approximately 850°C before strong signal noise is observed, most likely due to weld failure. In addition, the two readings were very consistent throughout the experiment. For panel test PT2, the first thermocouple (TC1) was non-responsive likely due to poor welding but the second thermocouple provided a reasonable reading up until panel failure. The lower heating rate observed for PT2 was a result of the decrease in power to match the 100 W/cm² test matrix condition.

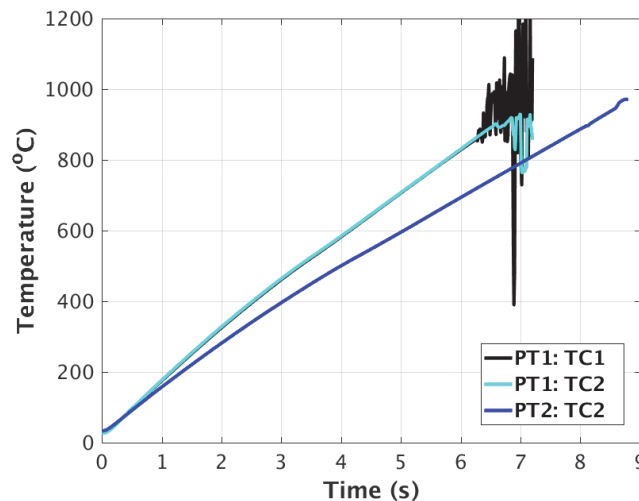


Figure 6.11: Temperature history of center thermocouples for panel tests PT1 and PT2

The temperature history for panel tests PT3 and PT4 are provided in Figure 6.12. For panel test PT3, the first thermocouple (TC1) was not responsive and the second thermocouple (TC2) had a large amount of noise after 0.75 seconds which limited the amount of thermal data available for this experiment. For panel test PT4, both thermocouples were responsive and measured consistently until approximately 750°C.

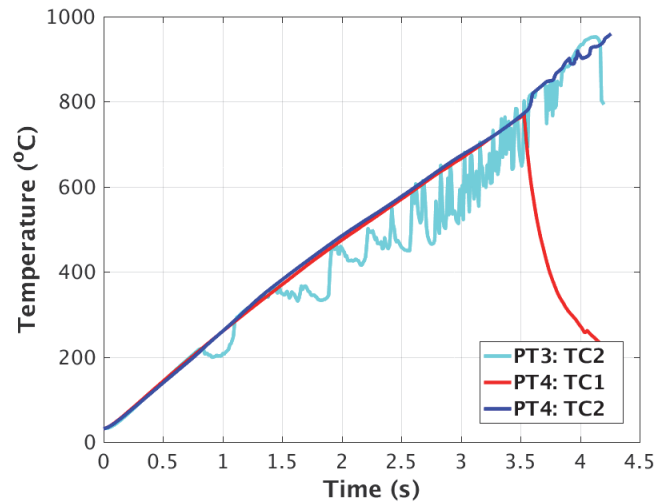


Figure 6.12: Temperature history of center thermocouples for panel tests PT3 and PT4

Since the irradiance and spot size are nearly identical for PT3 and PT4 it was expected that the temperature histories would be nearly equivalent. In fact, Figure 6.12 shows that the initial heating rate prior to 200°C and 0.75 seconds were very consistent between the two experiments. Since limited thermal data was available for the latter part of PT3, the results of PT4 will be used for modeling purposes.

6.1.6 Mechanical Results

The load and displacement histories for panel tests PT1 and PT2 are provided in Figure 6.13. Although the panel tests were intended to be tested at constant load, it can be seen that the MTS system was unable to maintain a constant load as the panel was

softened due to laser heating. The failure time was identified using the data point just prior to the sudden load drop as 7.1 seconds for RT1 and 8.6 seconds for RT2. The longer time-to-failure for RT2 is a result of having 20% lower irradiance which ultimately led to a 21% increase in time-to-failure.

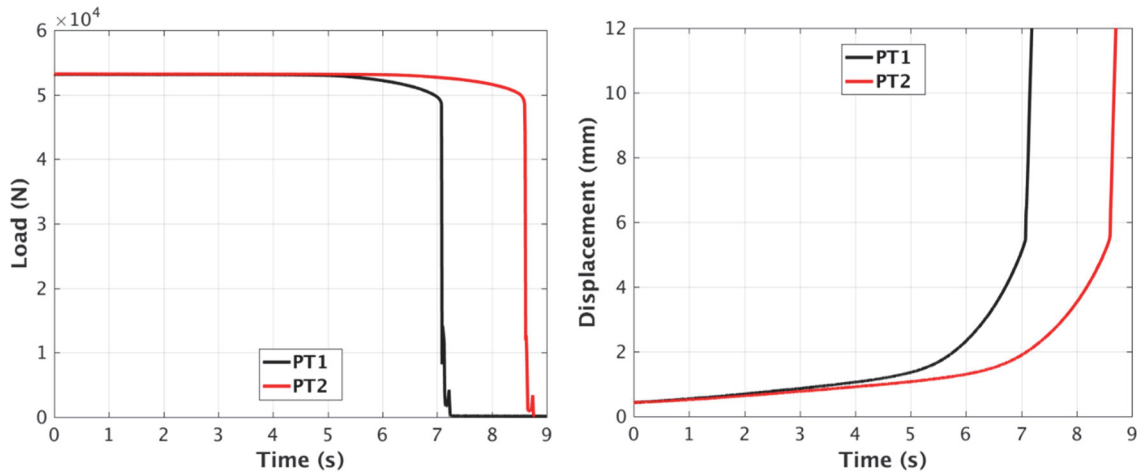


Figure 6.13: Load and displacement histories of panel tests PT1 and PT2

The fracture occurred near the edge of the heated zone, as shown in Figure 6.14, for both PT1 and PT2. The crack initiated on different sides of the heated zone but nearly equal distance from the panel edge, 1-1.9 cm from the panel edge. The variation may be due to a slight offset in the horizontal laser location. In Figure 6.14, the heated zone appears to be offset to the left for PT2. Some pointing variation can occur during high power operation even though the laser is aligned using a low power alignment laser.

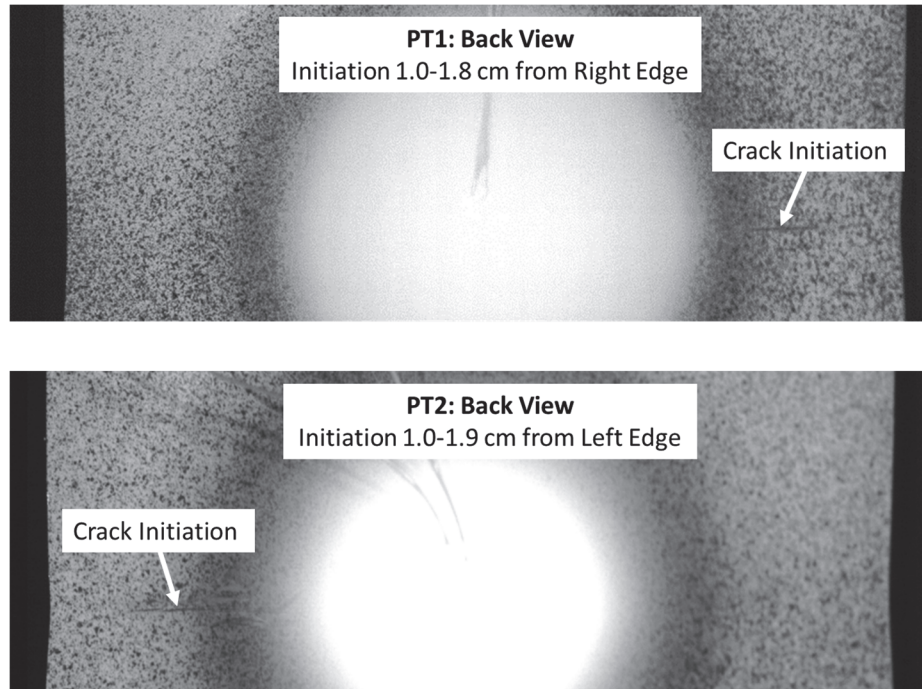


Figure 6.14: First frame of crack growth captured by the full-field strain camera for PT1 and PT2

After the crack initiated, it propagated to the nearest panel edge followed by propagation toward the center of the heated zone, as shown in Figure 6.15. In addition, a secondary crack appears to form on the opposite side of the heated zone before the crack propagates across the panel. However, the camera is nearly saturated in the center of the panel which makes it difficult to determine whether a fine crack exists in the central ligament.

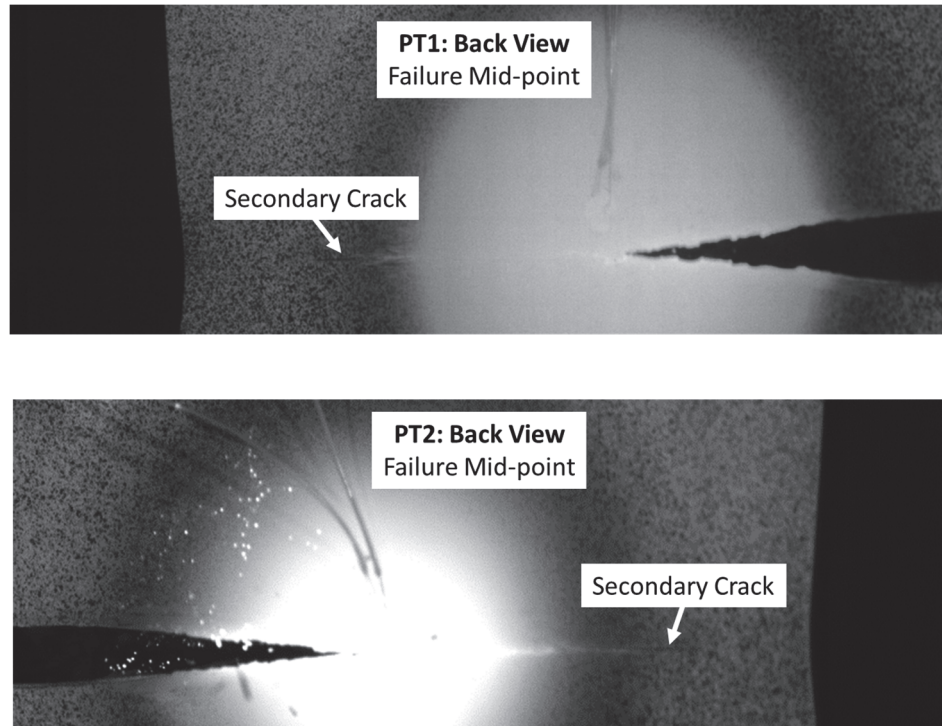


Figure 6.15: Image at the mid-point of failure process captured by the full-field strain camera for PT1 and PT2

The full-field strain measurement was limited due to the same saturation in the central region of the heated zone. However, the strain was calculated using digital image correlation near the panel edges where the speckle pattern was still visible during fracture. Using the Correlated Solutions software, the speckle pattern was triangulated into a mesh and the displacement of the speckle points were monitored during the experiment with a stereoscopic camera configuration. The corresponding evolution of strain was calculated for each triangle based on the displacement observations of the two

cameras. The axial strain calculated from the full-field strain device/software is provided in Figure 6.16 for the last frame prior to crack initiation in panel test PT1.

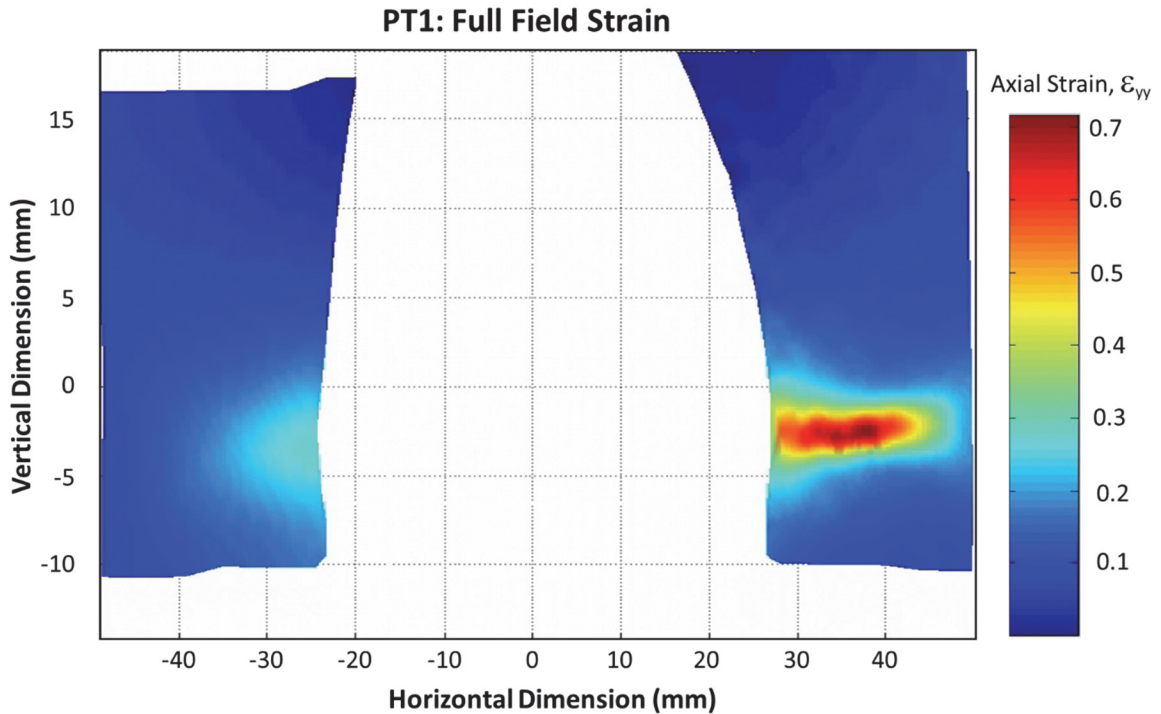


Figure 6.16: Full-field strain map in the final frame prior to crack initiation for PT1

The axial strain in the fracture zone is in the range of 0.55-0.7 and the localization band is approximately 3 mm in thickness. The corresponding temperature range for this region is 200-600°C based on MWIR and FEA analysis. The full field strain values prior to failure are in a range consistent with failure strains determined from the notched tensile tests shown in Figure 5.19 for this temperature range.

Although the edge strain and localization size may prove to be useful, the diagnostic did not perform as well as intended in the heated zone. A potential solution would be to use two sets of cameras with different neutral density filters to capture the lower temperature range and higher temperature range. Since the cameras were

saturated in the highest temperature region, it is still unclear whether the high temperature paint speckle pattern maintained enough contrast to enable strain calculations. The stove paint appears to work up to approximately 600°C based on the results of this experiment but the speckle material may need to be improved as well.

The load and displacement histories for panel tests PT3 and PT4 are provided in Figure 6.17, corresponding to an increase in laser intensity and initial tensile load. The failure times were found to be roughly half with an irradiance that is approximately double that of PT2. The mechanical response for both the PT3 and PT4 specimens during laser heating is remarkably close which is not surprising considering the initial load, beam irradiance and size were nearly identical between the two experiments.

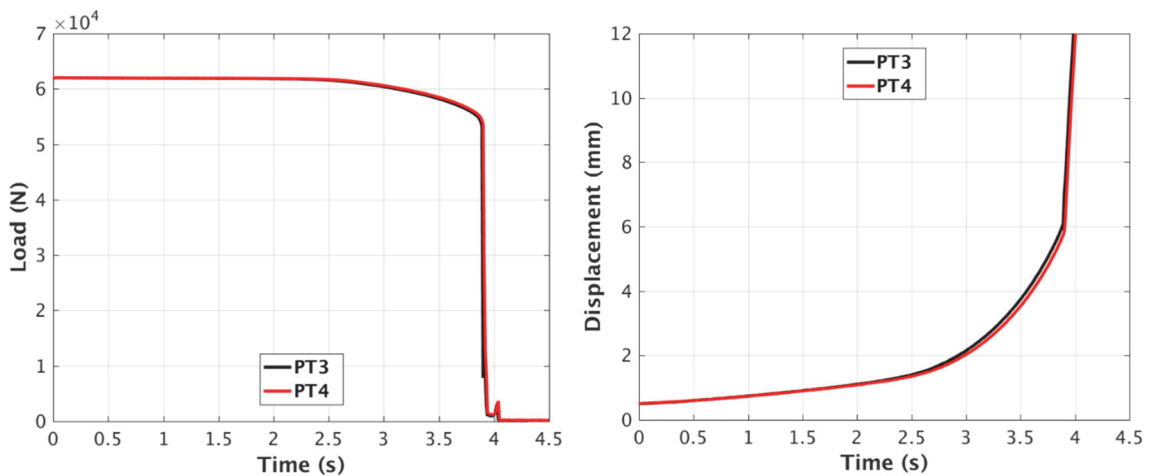


Figure 6.17: Load and displacement histories of panel tests PT3 and PT4

Similar to PT1 and PT2, the fracture occurred near the edge of the heated zone for PT3 and PT4, as shown in Figure 6.18. Again, the crack initiated on different sides of the heated zone but nearly equal distance from the panel edge for the two experiments which may be due to a slight off set in the horizontal laser location. On average, the crack

initiates further from the panel edge in PT3/PT4 than in PT1/PT2. Since the failure times are less in PT3/PT4, there is less time for thermal diffusion which results in a more compact thermal profile, causing the crack to initiation further from the panel edge.

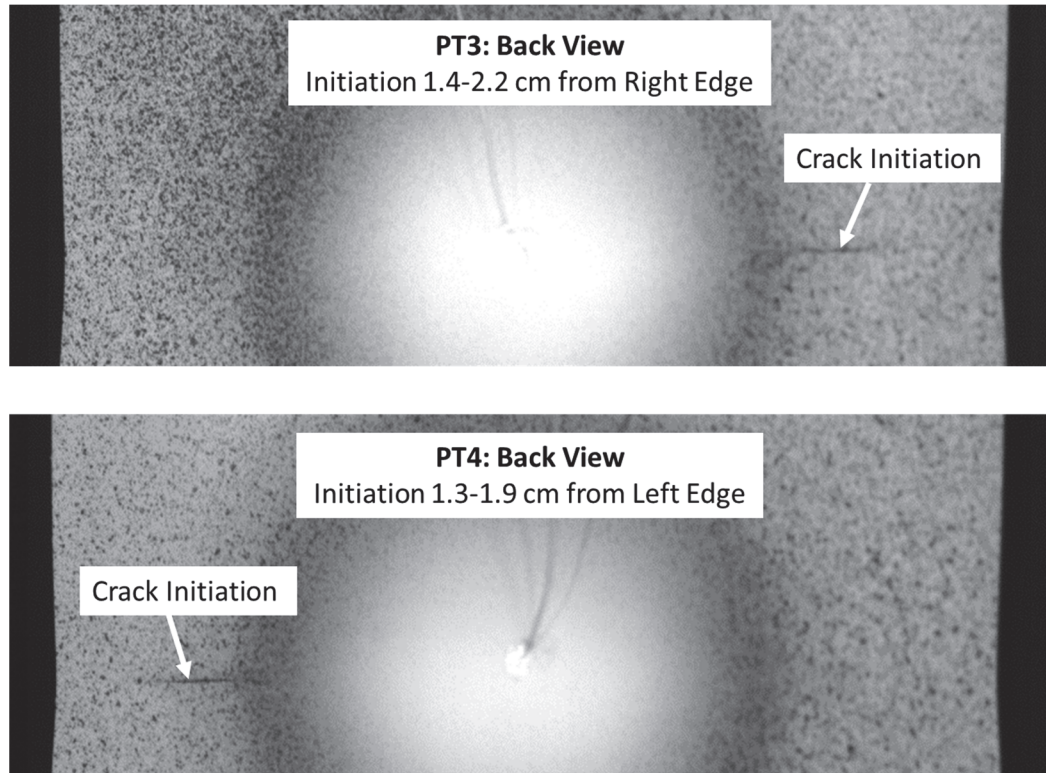


Figure 6.18: First frame of crack growth captured by the full-field strain camera for PT3 and PT4

Similar to PT1 and PT2, the crack still propagated to the nearest panel edge followed by propagation toward the center of the heated zone, as shown in Figure 6.19. The secondary crack is more clearly visible since the cameras are less saturated and it does not appear there is a connecting crack in the central ligament between the primary crack tip and the secondary crack, particularly for PT4. A close-up view of the central ligament in the image of PT4 is provided in Figure 6.20. A secondary crack does appear to form prior to the crack propagating across the heated zone.

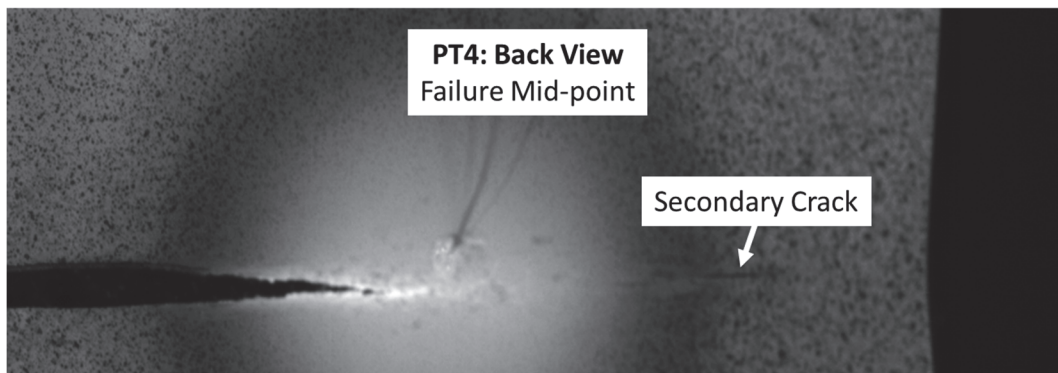
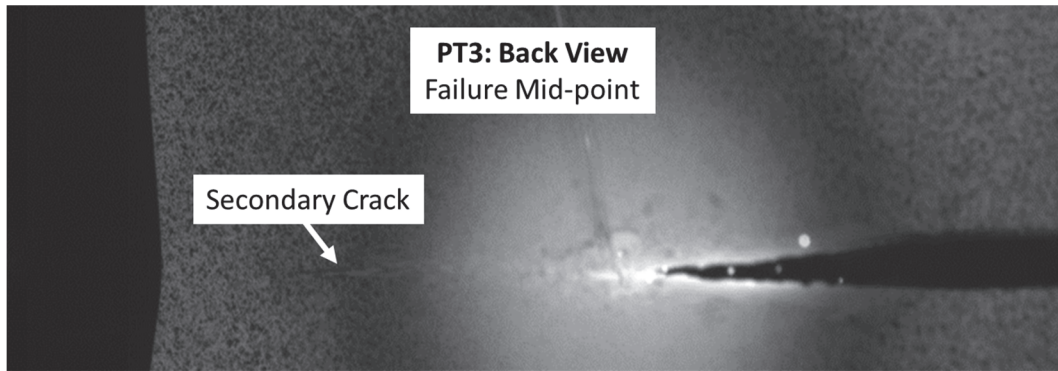


Figure 6.19: Image at the mid-point of failure process captured by the full-field strain camera for PT3 and PT4

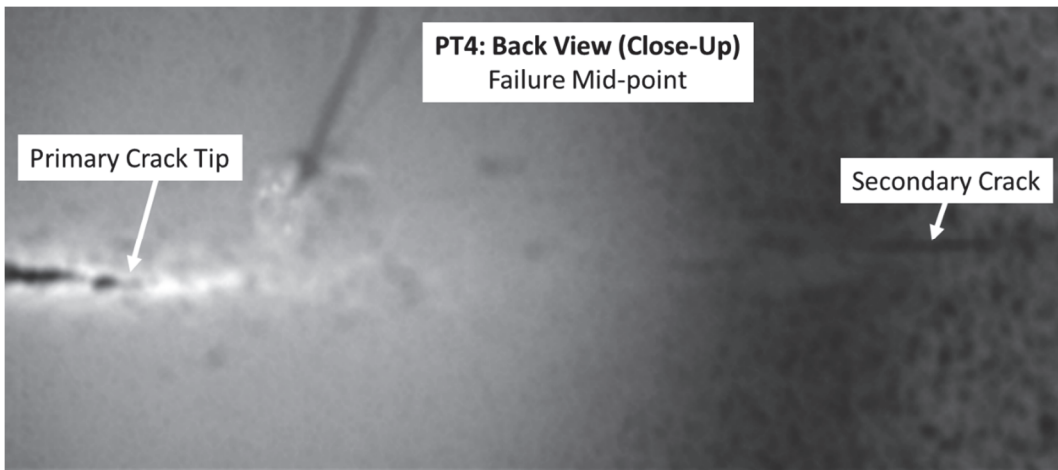


Figure 6.20: Close-up of the image at the mid-point of failure process captured by the full-field strain camera for PT4

The two cracks then have a tendency to coalesce quickly, leading to rapid panel failure. A fracture time duration of approximately 0.15 seconds was estimated using the time between crack initiation and final panel separation. The corresponding nominal crack speed was around 70 cm/s which is in the quasi-static failure regime for steel.

6.1.7 Panel Validation Test Summary

The panel validation experiments were successfully conducted using two different combinations of laser intensity and tensile loading conditions. The laser irradiance was well characterized, both spatially and temporally, using SWIR imagery. The rear surface peak temperature history was captured well with the exception of PT3 where TC failure was apparent in both readings. The load and displacement histories were captured which led to the discovery that the MTS system was unable to maintain a constant load during the failure process. Nonetheless, failure was achieved for each panel and the failure times were consistent and nearly proportional to the peak irradiance value. The high speed imagery was used to identify the crack initiation location and led to the identification of a secondary crack which formed during the failure process. The experiment was successful at collecting the necessary data for simulating the experiment and enabling validation comparison. To the author's knowledge, this is a first-of-its-kind dataset in the literature for thermo-mechanical failure of DSS in a transient heating environment where fracture occurs in a high thermal gradient zone.

6.2 Panel Validation Models

The panel experiments provide a unique dataset for simulating a complex thermal-mechanical response. The loading conditions are relatively simple yet provide a progression in complexity from the isothermal tensile testing, presented in Chapter 4, to a transient heating environment with high thermal gradients. The panel experiments are used here to validate the PDM model for failure predictions under complex thermal states. The PDM model will be evaluated in its ability to predict failure time, failure temperature, failure displacement, crack initiation location and propagation with no modification to the material model defined in Chapter 5.

6.2.1 Thermal Model

The temperature state of the panel can be considered an input loading condition or forcing function for the thermal-mechanical damage which will be predicted by the PDM model. Since the complete spatial and temporal thermal state cannot be easily measured, ensuring the appropriate thermal state becomes challenging from a validation standpoint. The PDM model cannot be evaluated properly unless there is confidence in the transient thermal solution. Given the panel experiment results presented in Section 6.1, the most reliable thermal data is provided by the thermocouples used to measure the peak temperature on the rear surface of the panel.

The absorption of laser energy is also critical as it drives the temperature change and thermal distribution within the panel. The SWIR imagery and laser beam power measurements provide a well characterized laser beam irradiance, as defined in Section

6.1.4. However, most finite element software cannot directly incorporate arbitrary heat flux distributions. As a result, user subroutines were required to incorporate the laser irradiance distribution in Abaqus. The SWIR imagery provides regularly spaced data corresponding to the sensor array size and field of view. The irradiance is characterized at uniform horizontal (Δx) and vertical spacing (Δy), as shown in Figure 6.21, which do not necessarily correspond to the finite element mesh size or distribution.

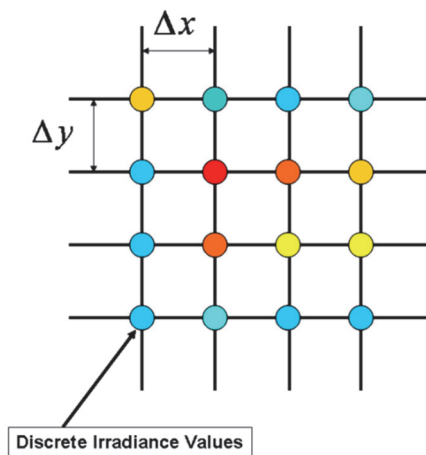


Figure 6.21: Diagram of uniformly spaced irradiance values from SWIR imagery

Since the FEA mesh and irradiance may be irregular in future studies, a generalized irregular beam profile algorithm was developed to provide greater flexibility. An inverse distance weighting method was selected since it does not impose any restrictions on the irradiance sampling. Figure 6.22 shows four randomly located irradiance points, one in each quadrant of the laser beam plane, and the discrete point for which an irradiance value is sought.

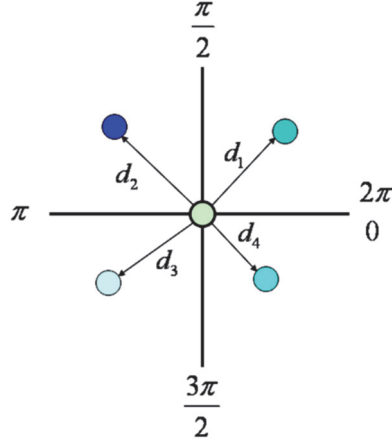


Figure 6.22: Inverse distance weighting method applied to the four closest irradiance points with one per quadrant

To determine the interpolated irradiance value from the experimental irradiance data, a weighting function (w) is defined in terms of the distance (d) between the data point and the interpolation point as follows:

$$w(d) = \frac{1}{d^n} \quad (6.2)$$

Where n is a user defined power factor which is taken to be unity for this study. The weighted irradiance (I_w) can then be determined for the point of interest using the following equation:

$$I_w = \frac{\sum_{i=1}^N \frac{I_i}{d_i^n}}{\sum_{i=1}^N \frac{1}{d_i^n}} \quad (6.3)$$

Where N is the total number of data points contributing to the point of interest and I_i is the experimental irradiance at data point i located at a distance d_i from the point of interest.

The irregular beam algorithm, defined above, was implemented using several user-defined subroutines available in Abaqus. The subroutine UEXTERNALDB was used to read the FEA mesh and laser beam information (scaled SWIR image) followed by computation of the weighted laser irradiance for each element surface. The weighted irradiance calculation is only conducted once at the beginning of the analysis since the laser beam is not moving. The irradiance is then adjusted based upon the temperature dependent surface absorption and applied to the model using the DFLUX subroutine at every iteration. Pre-calculating the irradiance in UEXTERNALDB is more computationally efficient than performing the calculation at each iteration within DFLUX. However, an iterative calculation may be required if the laser beam was moving during the analysis, which one might expect in additive manufacturing or laser welding applications, or if the irradiance profile is not temporally stable. The final subroutine used in the irregular beam implementation was USDFLD, which was used to create a user-defined field variable for viewing the irradiance in the output database. The pseudo-code showing the function call and a list of calculations is provided in Appendix B.

Using the irregular beam subroutine, the time averaged SWIR image was used for each individual experiment and mapped to the panel mesh which was created to match the 1x1x0.5 mm element size from the PDM characterization. The thermal model was conducted using the Abaqus/Standard (Implicit) solver using a DC3D8 heat transfer brick element which provides a compatible thermal solution to the C3D8R element used in the sequentially coupled thermal-mechanical simulation. The thermal solution is stored during the heat transfer analysis using the keyword “*Node File” and read by the

mechanical analysis using keyword “*Temperature”. The analysis must be sequentially coupled because the user defined flux subroutine “DFLUX” was not available in the Abaqus/Explicit solver. During the preparation of this manuscript, the most recent release of Abaqus is said to have an initial implementation of “VDFLUX”, the explicit variant of the subroutine “DFLUX”, which would enable the use of a fully coupled element (C3D8RT). However, the deformation is small relative to the beam size which suggests a sequentially coupled approach is feasible even though it introduces a source of error in the thermal distribution. An example of the beam profile and mesh mapping is shown in Figure 6.23 along with an example thermal distribution on the panel. An Abaqus input file for the heat transfer simulation is provided in Appendix B which shows the call to the user defined DFLUX routine.

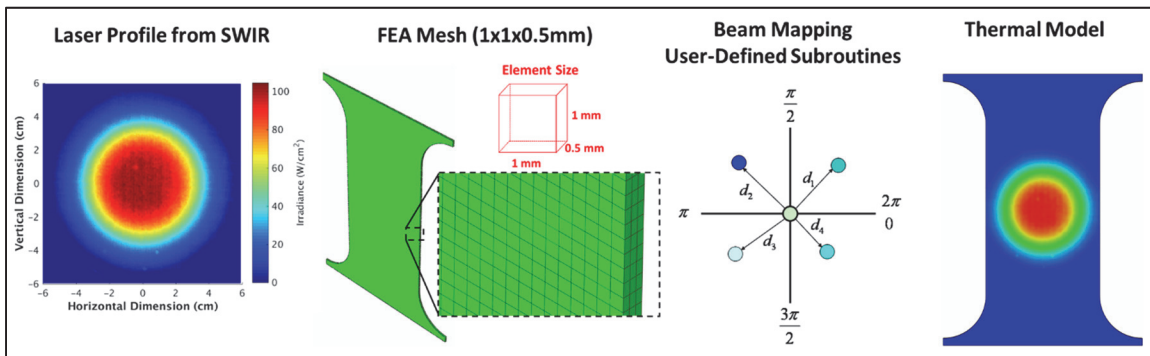


Figure 6.23: Panel mesh and laser beam mapping applied to thermal model

Prior to conducting the thermal analysis, the laser position was determined by analyzing the rear-surface MWIR imagery. The centroid of the laser beam was determined from an unsaturated image early in the test and the panel edges were determined from the saturated image later in the test, as shown in Figure 6.24. The

horizontal beam shift was estimated to be $\pm 4\text{mm}$ based on the MWIR resolution and edge finding algorithm.

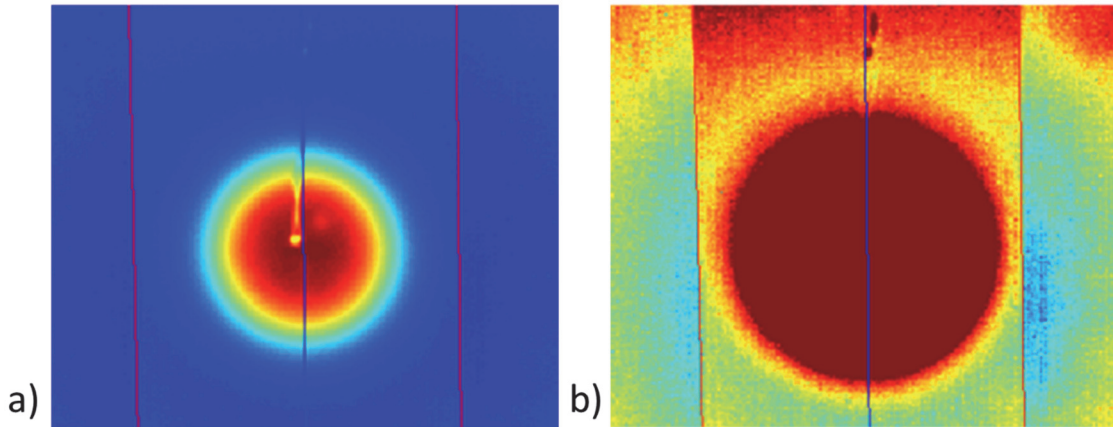


Figure 6.24: MWIR imagery used to determine horizontal shift of laser position; a) prior to saturation used to determine laser centroid b) image after saturation used to determine panel edge locations

The thermal analysis was performed with the horizontal beam shift and experimentally determined laser beam profile implemented via user-subroutine. Surface radiation was modeled on the front and rear surfaces of the panel with an emissivity of 0.8 and ambient temperature set to the initial temperature of the panel. The absorptance was initially set to the temperature dependent absorptance determined from the TRAM experiment, provided in Section 3.5, and extrapolated to 1000°C . The absorption was then modified in order to best fit the thermal conditions observed in the experiment. The temperature history at the TC location was compared to the temperature data for PT1 in Figure 6.25. The thermal profile along a horizontal path is also provided in Figure 6.26 for several times during the heating process. The edge temperatures reached as high as 200°C while the center temperature stayed below 1000°C . The thermal profile

encompasses the entire temperature range for which the PDM model was characterized, which is ideal for validation purposes.

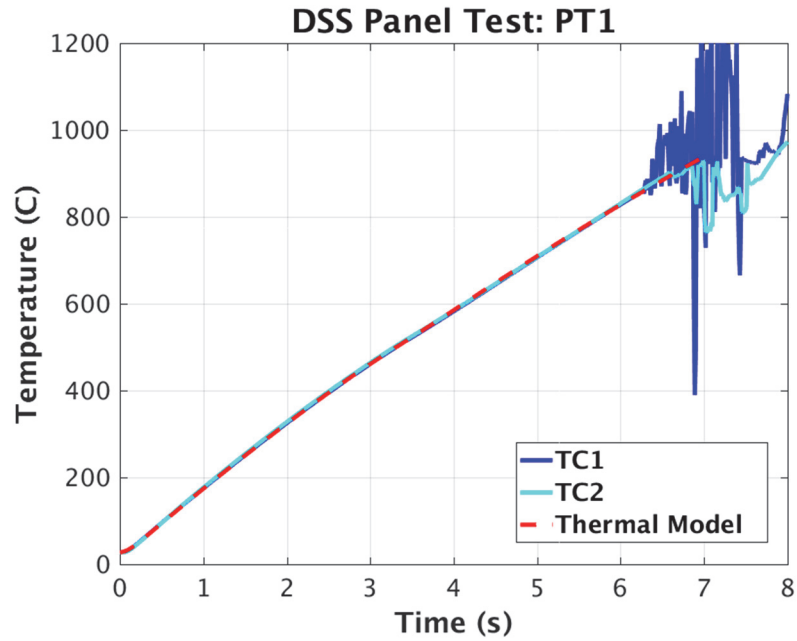


Figure 6.25: Temperature history comparison of the Abaqus thermal model to the thermocouple data for PT1

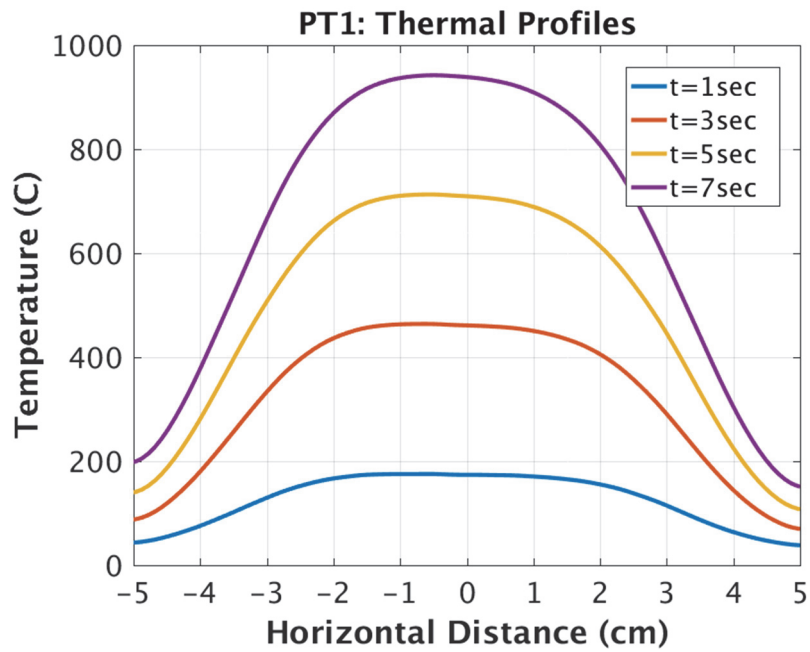


Figure 6.26: Thermal profiles from the Abaqus simulation at select times during the laser heating of PT1

Similar to PT1, the temperature history and profiles are provided for PT2, PT3, and PT4 in Figure 6.27, Figure 6.28, and Figure 6.29, respectively. Again, the temperature history is captured by adjusting the temperature dependent absorption curve. Given the poor temperature history data for PT3, as discussed in Section 6.1.5, it seemed reasonable to use PT4 as a surrogate since they correlated well prior to TC failure (Figure 6.12). The absorption optimization was performed on PT4 first then applied to PT3 since they had nearly identical test conditions. Ideally, the MWIR camera would have allowed for temperature history and thermal profile comparisons of PT3. However, the MWIR cameras saturated near the center of the heated zone for all experiments and the temperature dependent emissivity was not well characterized. Therefore, the center TC measurement became the most critical measurement for comparing the thermal model.

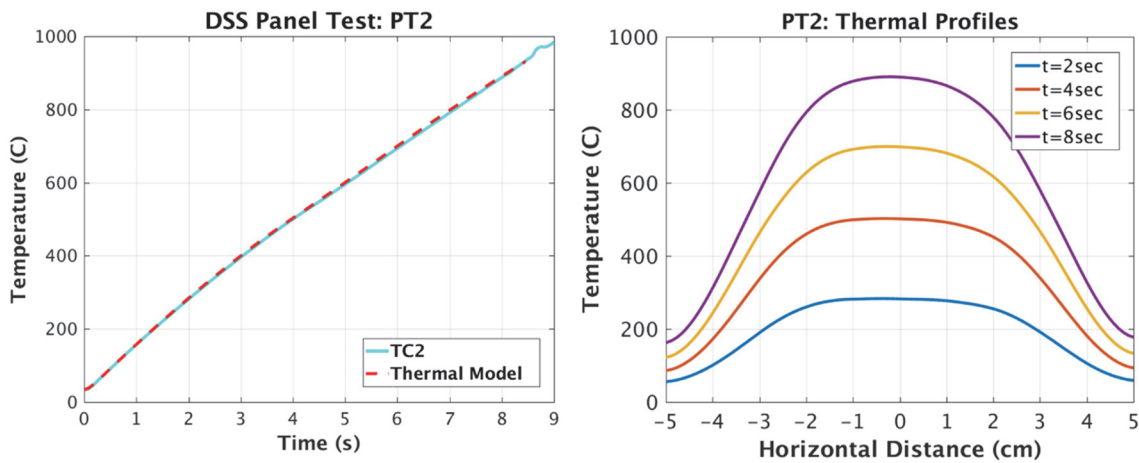


Figure 6.27: Temperature history comparison and thermal profiles from the Abaqus thermal model of PT2

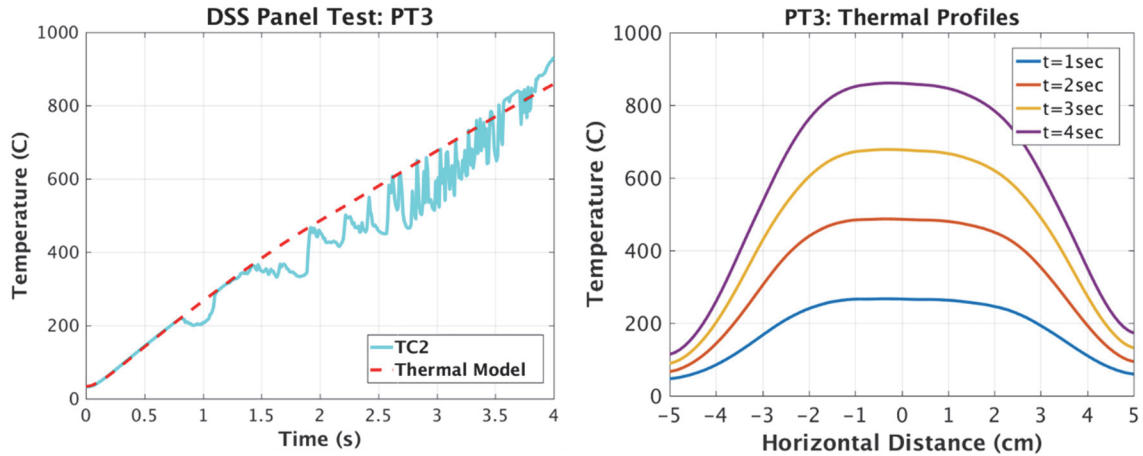


Figure 6.28: Temperature history comparison and thermal profiles from the Abaqus thermal model of PT3

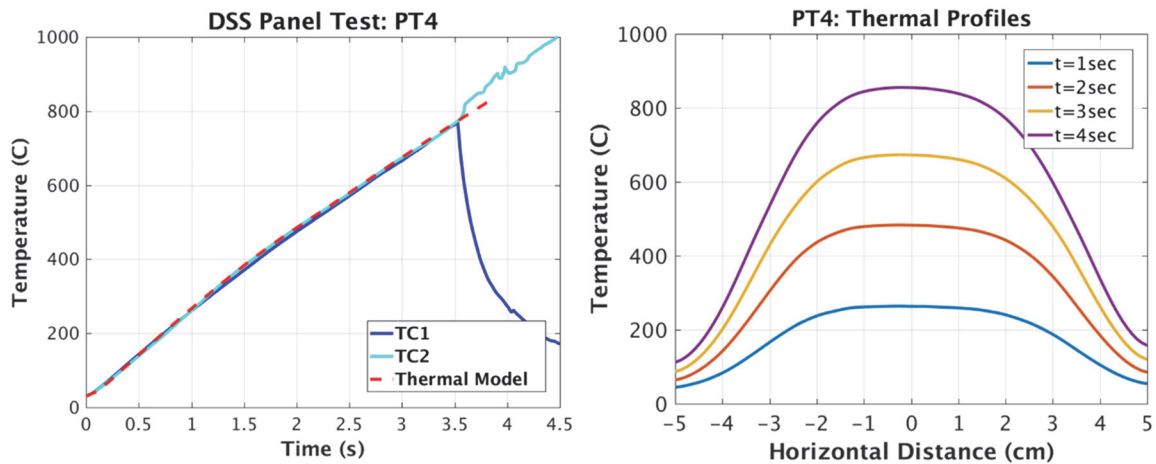


Figure 6.29: Temperature history comparison and thermal profiles from the Abaqus thermal model of PT4

The optimized absorption curve used to capture the thermocouple history for each panel experiment is shown in Figure 6.30 with a comparison to the TRAM absorption data, including uncertainties. The initial absorption is within the experimental uncertainty but required a decrease in the 400-625°C range. This may be related to the solid-solid phase change which is seen in the specific heat curve (Figure 3.3). The need to decrease absorption may indicate that the latent heat is underestimated in the DSC data.

Above this range, the optimized curves increased to near the room temperature value however no data was available for comparison. The degradation of the paint above 600°C and statistical variation of absorption was not well characterized in this study but could be the focus of further investigation.

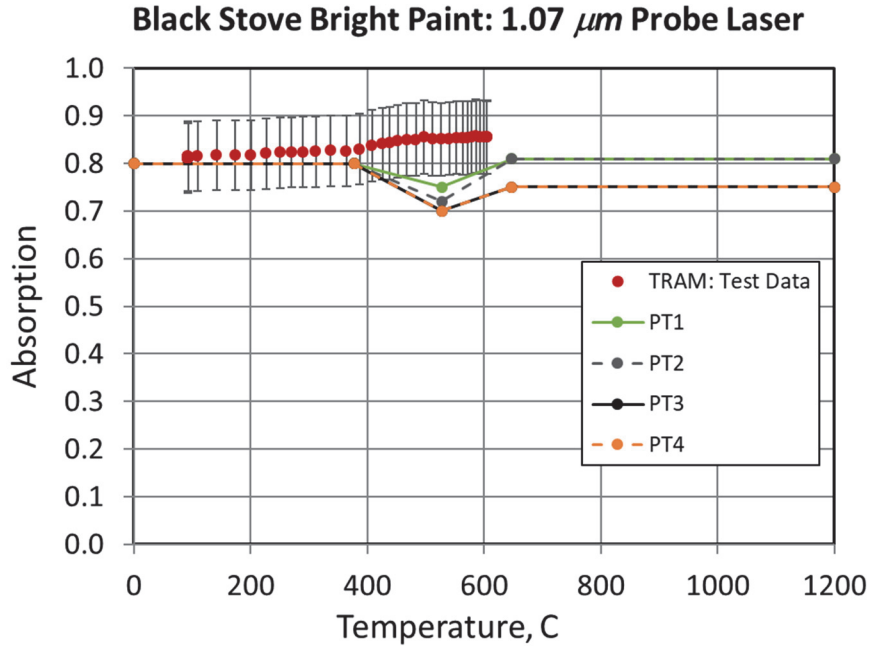


Figure 6.30: Optimized absorption used in the Abaqus model compared to the elevated temperature absorption, including uncertainty estimate, from the TRAM experiment when using a 1.07 μm probe laser

Although the temperature data was not ideal, it was sufficient to optimize the thermal model to best fit the panel measurement of peak rear surface temperature. The thermal solutions for the panels were stored to an Abaqus results file using the keyword “*NODE FILE”. The thermal solution was then used as an input for the thermal-mechanical model discussed in the following section.

6.2.2 Thermal-Mechanical Model

In addition to the temperature state of the panel, the mechanical load for each experiment must be applied to the model to provide a representative loading condition for predicting damage with the PDM model. Since the MTS machine was unable to maintain a constant load through the failure process, as described in Section 6.1.6, the complete load history must be used within the simulation. However, the final load drop was not incorporated into the loading function, $F(t)$, since the model would never predict failure in the event where the PDM model predicts a later time-to-failure. The loading and boundary conditions are shown graphically in Figure 6.31 with a pin tie connection to a rigid reference node. The reference nodes are used to apply the boundary conditions and loading function while enabling the rotational degree of freedom on the pin similar to the clevis adapter.

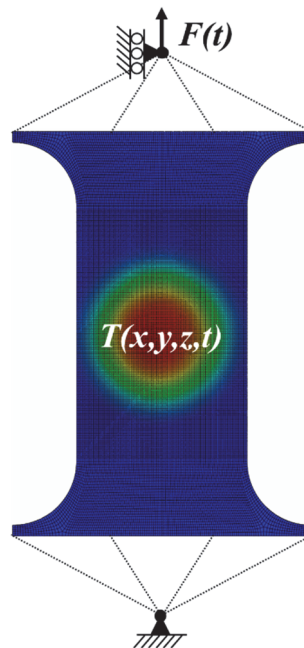


Figure 6.31: Loading and boundary conditions for the Abaqus thermal-mechanical model of the panel experiments

The load history curve for PT1 is shown in Figure 6.32 along with the predicted load response from the PDM simulation. In this case, the predicted failure occurs earlier than the experiment which allows for the exact load history to be used for the model input. The predicted failure time using the PDM model was 6.86 seconds while the experimental failure was observed at 7.08 seconds, a difference of -3.1%. The corresponding failure loads were 49.9 kN for the PDM Model and 48.6 kN for the experiment, a difference of 2.7%.

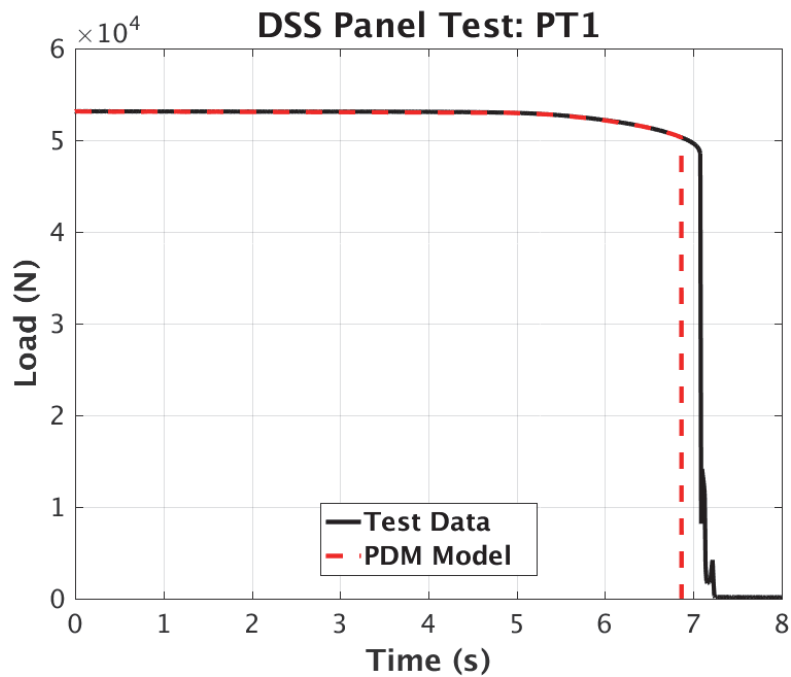


Figure 6.32: Load history results from Abaqus PDM simulation compared to experimental results for PT1

The displacement history is provided in Figure 6.33 which shows close correlation with the experiment until just prior to failure in the model. The failure displacement was 5.7 mm in the PDM model in comparison to 5.5 mm in the experiment, a difference of 3.6%.

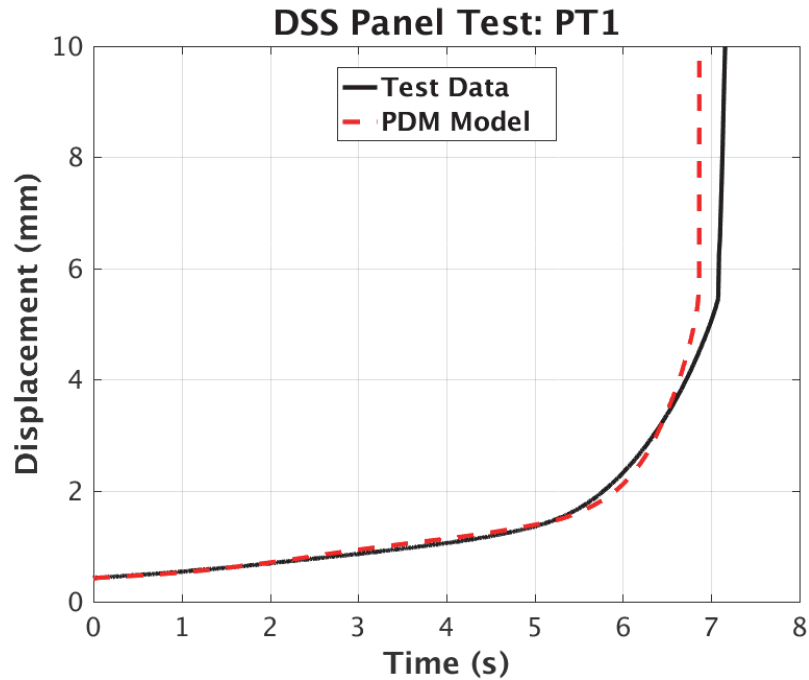


Figure 6.33: Displacement history from the Abaqus PDM simulation compared to experimental results for PT1

The temperature distribution in the panel at the first increment of crack initiation is shown in Figure 6.34. The temperature is approximately 618°C at the location where the crack initiates and 924°C at the thermocouple location. A direct comparison to the TC data is not possible since the signal degraded prior to failure. However, if you take the temperature of the thermal model at the experimental failure time you get 945°C, a difference of -2.2%. This approach will be used for comparing temperature in the other panel tests as well.

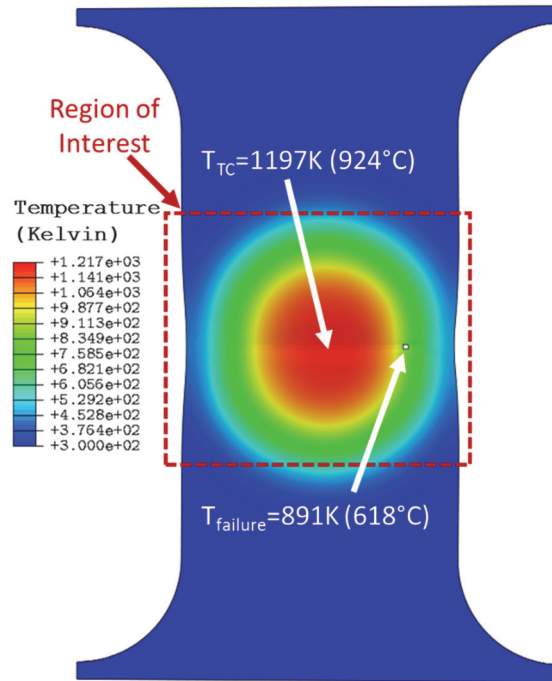


Figure 6.34: Temperature solution at crack initiation time for PT1

A region of interest is outlined in Figure 6.34 which will be used to look at the solution contours for other field variables. The damage initiation criterion (DUCTCRT), damage variable (SDEG), equivalent plastic strain (PEEQ), and the von Mises stress (SMISES) are all shown in Figure 6.35 for the region of interest. The localization zone can be clearly seen in the equivalent plastic strain contours with maximum strain levels approaching 60%. Some localization along the shear bands can also be seen near the edge of the heated zone. Interestingly, the damage level is fairly localized around the fracture initiation point and a similar location on the opposite side of the heated zone. The damage did not accumulate in the center region where it is hottest due to the delayed initiation criteria, discussed in Section 5.3.2, which was required to best capture the diffuse necking.

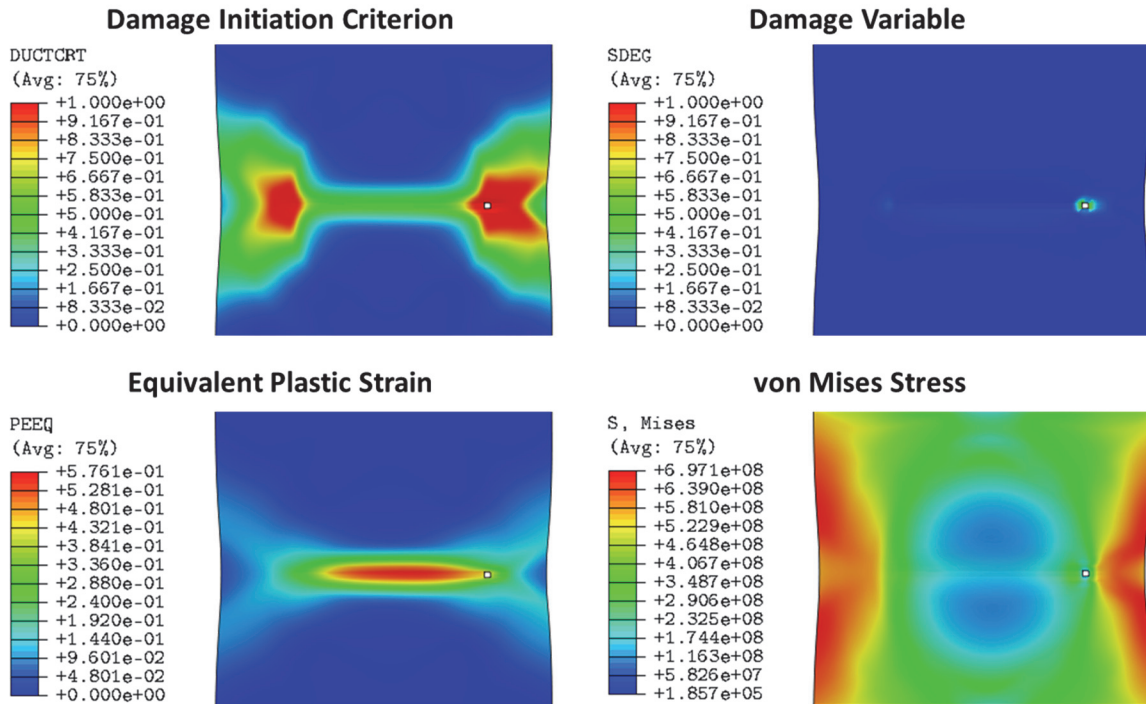


Figure 6.35: Damage initiation criterion, damage variable, equivalent plastic strain and von Mises stress solutions at crack initiation time for PT1 (Solution only shown for region of interest defined in Figure 6.34)

The fracture initiation point is compared to the experimental results in Figure 6.36. The crack initiates over two elements which spans a distance of 1.7-1.9 cm from the right edge, as viewed from the back of the panel. The experimental results show a crack in the range of 1.0-1.8 cm in the first frame where a crack is discernable. An overlaid image is provided in Figure 6.36 which shows very similar width reduction and deformed shape on the edges as well as close correlation between the crack initiation points. Given that the crack first propagates toward the nearest edge in the experiment, it is reasonable to assume that the experimental initiation point is closer to 1.8 cm which is within the range of the numerical prediction.

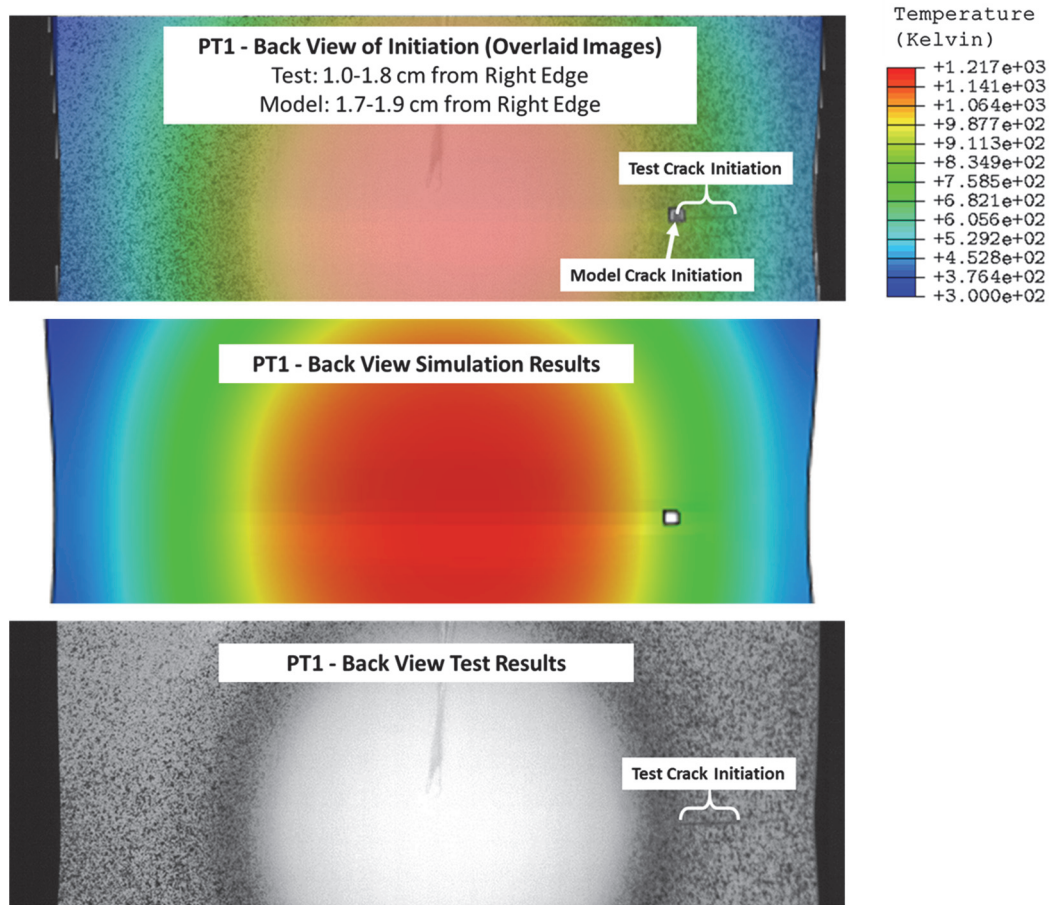


Figure 6.36: Fracture initiation prediction for PT1 compared to the experimental results

The crack is obviously less sharp in the model since element deletion is used to simulate crack initiation and growth. However, the initiation point compares well to the experiment. The secondary crack which is observed in the experiments was also captured in the model. A similar overlaid image is provided in Figure 6.37 for a later time increment when the second crack is formed on the opposite side of the heated zone. Again, the location of the secondary crack matches closely. However, at this point in time the size of the primary crack was not as large in the simulation as the experiment.

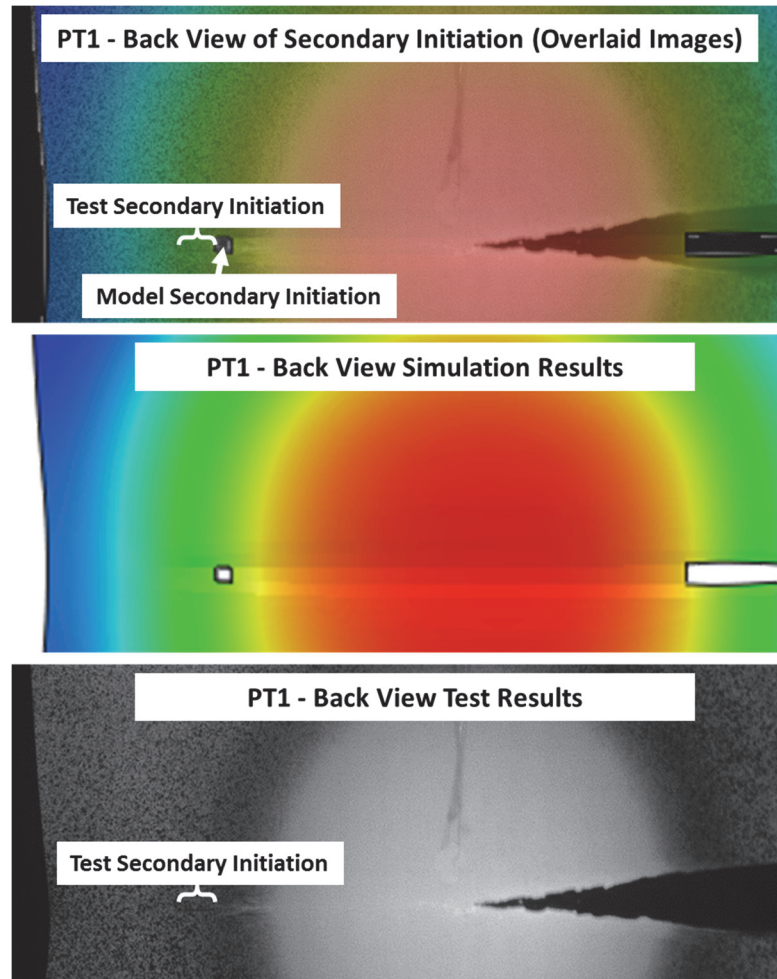


Figure 6.37: Secondary crack initiation prediction for PT1 compared to the experimental results

A summary of the model comparison is shown in Table 6.3. The model predictions are within 4% for all metrics which indicates the PDM model is capable of capturing thermal-mechanical fracture initiation during localized heating. Simulation results for the remaining 3 panels had a similar level of agreement with the experimental results.

Table 6.3: PDM model comparison to PT1 results

PT1	Temp (C)	Time (sec)	Displacement (mm)	Load (kN)	Initiation Location (cm)
Test	945	7.08	5.5	48.6	1.0-1.8
Model	924	6.86	5.7	49.9	1.7-1.9
Difference	-21	-0.22	0.4	1.3	Overlap
% Difference	-2.2%	-3.1%	3.6%	2.7%	

The comparison for PT2, which had a lower irradiance than PT1, is shown in Figure 6.38. Again, the predicted failure time was prior to the experimental load drop which allowed for the experimental load history to be used as the model input. Similar to PT1, the displacement history is close to the experimental curve until just prior to failure. The predicted failure time using the PDM model was 8.47 seconds while the experimental failure was observed at 8.60 seconds, a difference of -1.5%. The corresponding failure loads were 50.4 kN for the PDM Model and 48.7 kN for the experiment, a difference of 3.5%. The failure displacement was 5.8 mm in the PDM model in comparison to 5.6 mm in the experiment, a difference of 3.6%.

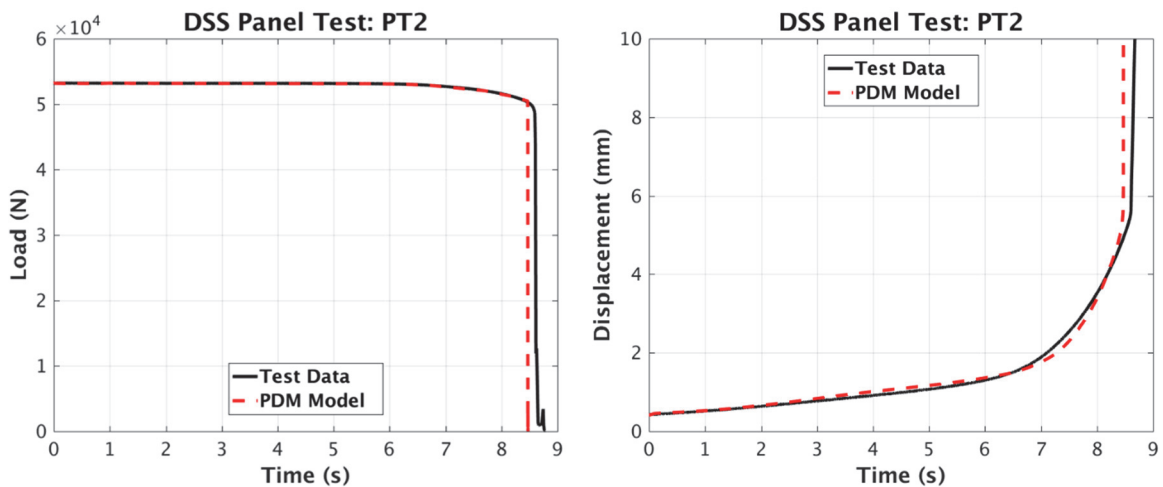


Figure 6.38: Load and displacement history for PT2 compared to the PDM model results

The fracture initiation location is again compared to the experiment using overlaid images of the high speed camera and the thermal contours from the PDM model, as shown in Figure 6.39. The crack initiates over three elements which spans a distance of 1.7-2.0 cm from the left edge, as viewed from the back of the panel. The experimental results captured a crack in the range of 1.0-1.9 cm in the first frame where a crack was discernable. Again, the crack initiation location is predicted well and the temperature was approximately 613°C at the initiation location which is consistent with the model results for PT1. The temperature at the initiation location is reasonable since the material response at 600°C provides a combination of lower ductility and strength in comparison to the room temperature response, as shown in Figure 4.12. Although the strength drops further at temperatures above 600°C, the ductility also increases considerably, allowing the material in the center of the heated zone to stretch and redistribute the load toward the cooler material near the panel edges.

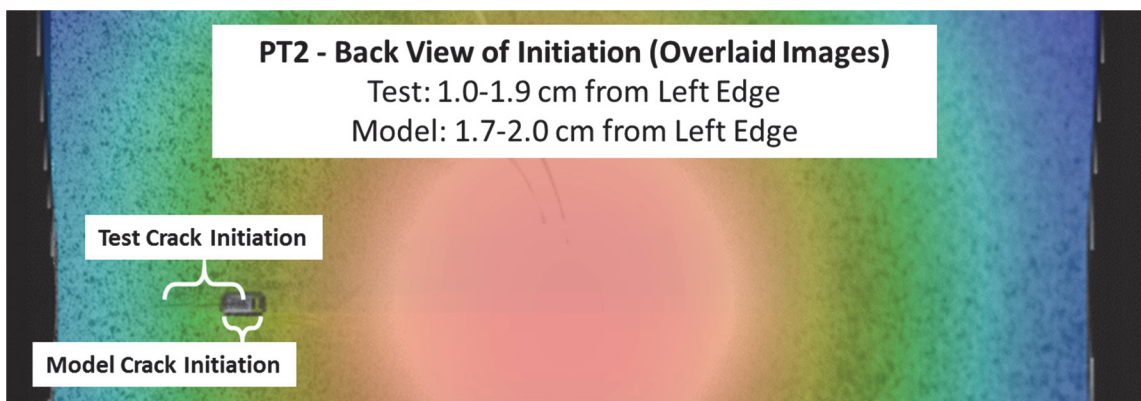


Figure 6.39: Overlaid image of the PDM model and PT2 test result for the crack initiation location

A summary of the PDM model and experimental results for PT2 are provided in Table 6.4. The model compares well across all metrics. The contour results for the stress, strain and damage variables are similar to the distributions seen in Figure 6.35 prior to initiation.

Table 6.4: PDM model comparison to PT2 results

PT2	Temp (C)	Time (sec)	Displacement (mm)	Load (kN)	Initiation Location (cm)
Test	944	8.60	5.6	48.7	1.0-1.9
Model	933	8.47	5.8	50.4	1.7-2.0
Difference	-11	-0.13	0.2	1.7	Overlap
% Difference	-1.2%	-1.5%	3.6%	3.5%	

Panel tests PT3 and PT4 had an increase in irradiance ($\sim 200 \text{ W/cm}^2$) resulting in less thermal diffusion and lower failure times. The model comparison for PT3 is provided in Figure 6.40, Figure 6.41, and Table 6.5. The comparison with PT4 is provided in Figure 6.42, Figure 6.43, and Table 6.6. In both cases, the predicted failure time was slightly longer than observed in the experiment. As a result, no failure would occur in the PDM simulation if the loading function, $F(t)$, exactly followed the experimental load history. Therefore, the gradual portion of the load decrease was extrapolated in time, as shown in Figure 6.40 and Figure 6.42. The failure load and times were then within 4% of the experimental values for both tests as well as the load and displacement at failure. The crack initiation locations, derived from the high speed camera and the PDM model, were again overlapping. The temperature at the initiation location was approximately 620°C which is consistent with the lower irradiance experiments.

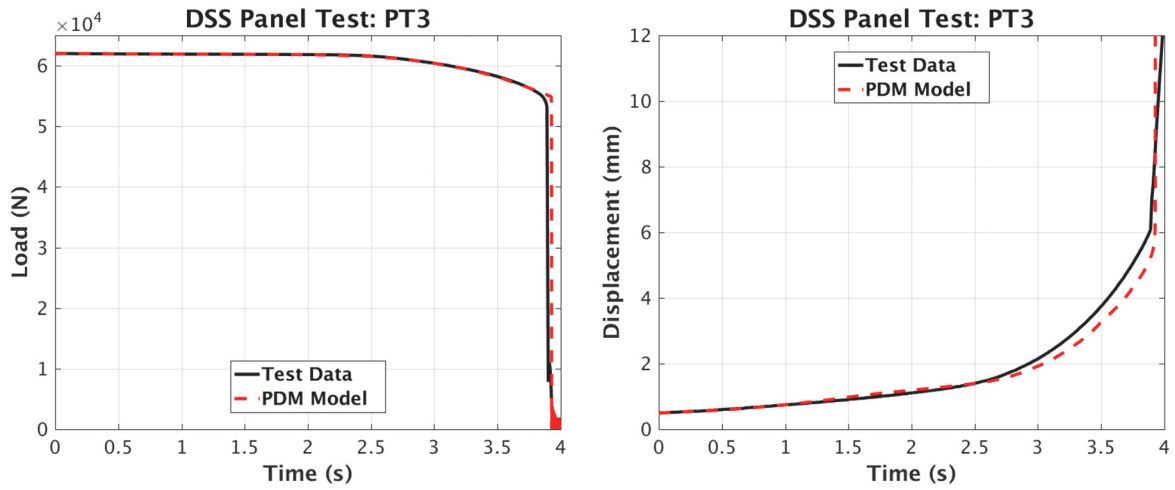


Figure 6.40: Load and displacement history for PT3 compared to the PDM model results

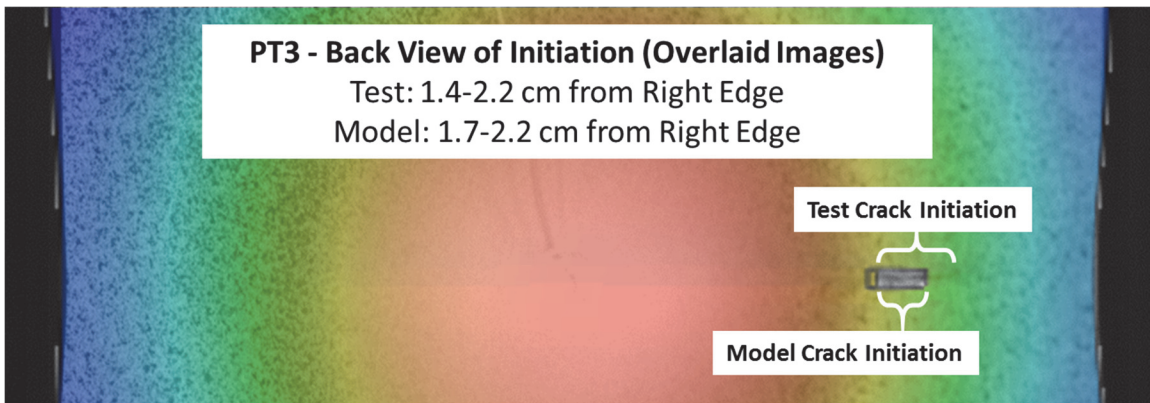


Figure 6.41: Overlaid image of the PDM model and PT3 test result for the crack initiation location

Table 6.5: PDM model comparison to PT3 results

PT3	Temp (C)	Time (sec)	Displacement (mm)	Load (kN)	Initiation Location (cm)
Test	842	3.89	6.1	53.3	1.4-2.2
Model	850	3.93	6.2	54.1	1.7-2.2
Difference	8	0.04	0.1	0.8	Overlap
% Difference	1.0%	1.0%	1.6%	1.5%	

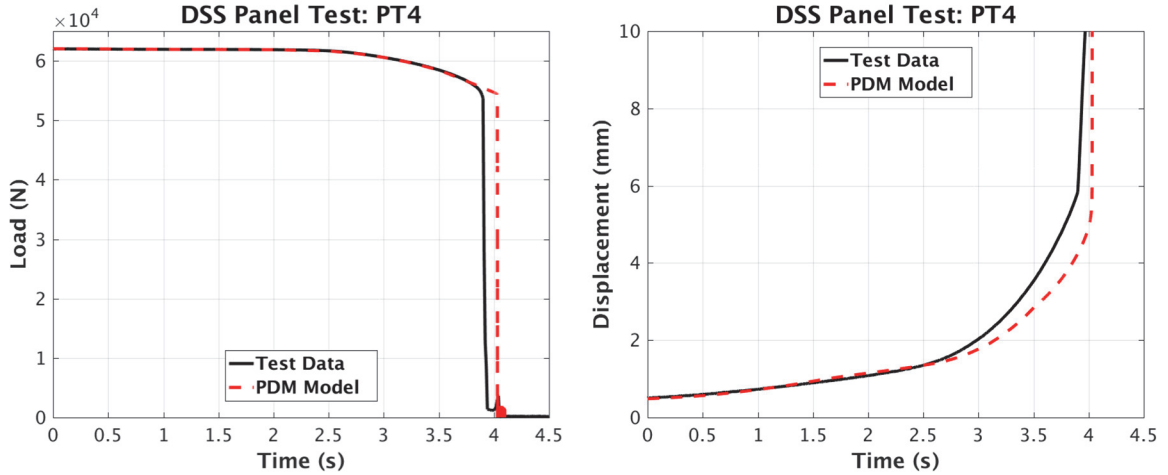


Figure 6.42: Load and displacement history for PT4 compared to the PDM model results

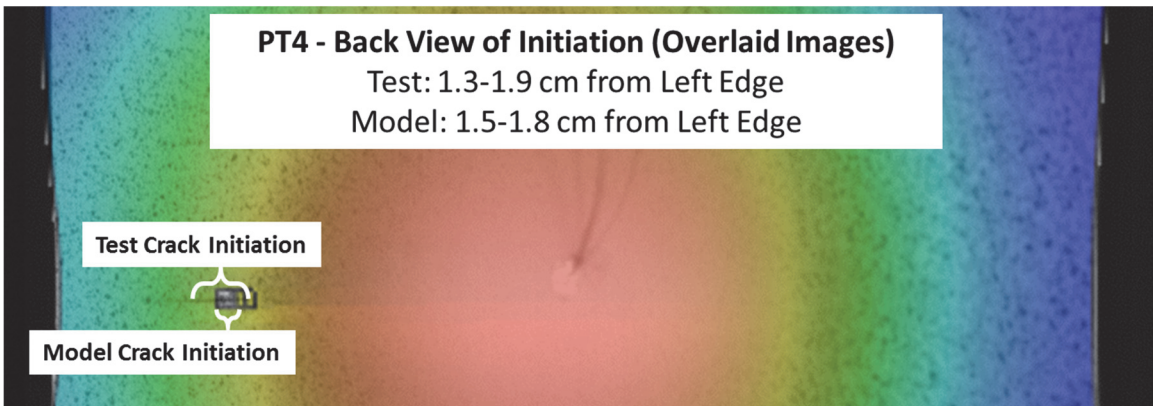


Figure 6.43: Overlaid image of the PDM model and PT4 test result for the crack initiation location

Table 6.6: PDM model comparison to PT4 results

PT4	Temp (C)	Time (sec)	Displacement (mm)	Load (kN)	Initiation Location (cm)
Test	839	3.90	5.8	53.7	1.3-1.9
Model	863	4.03	5.6	54.3	1.5-1.8
Difference	24	0.13	-0.2	0.6	Overlap
% Difference	2.9%	3.3%	-3.4%	1.1%	

Although the experimental results were nearly identical for PT3 and PT4, as shown in Figure 6.17, the simulation results differed slightly. The primary difference in the simulations was the horizontal offset of the laser beam impinging on the panel. The high

speed and MWIR camera data were used to estimate the horizontal offset for each test case. PT4 was assessed to have a slightly larger offset and in the opposite direction than PT3, which is the cause of the initiation being on opposite sides of the heated zone. The slightly higher irradiance used in PT3 and PT4 resulted in lower failure times and less thermal diffusion which leads to greater sensitivity to beam location. Given the uncertainty in the offset calculation and the consistency of the experimental results, the magnitude of the offset may have been closer than the estimation.

The uncertainty of the horizontal offset turned out to be one of the most sensitive input parameters for crack initiation, but had minimal impact on other metrics. The centroid offset was estimated to be ± 5 mm from the panel centerline. Changing the centroid location within this range resulted in a change in the initiation location from the left to right side of the heated zone or in some cases the initiation could occur simultaneously on both sides of the heated zone. However, the initiation location relative to the nearest panel edge changed by less than 3 mm for each of these cases.

The comparison of all other metrics (time, temperature, displacement, and load) were within 4% for the four panel experiments. When input uncertainties were considered, the temperature and time were still within 6% and the displacement and load were within 8% of the experimental results. Overall, the PDM model appears capable of capturing the failure response of DSS due to rapid localized heating and uniaxial tension.

6.2.3 Panel Validation Modeling Summary

The PDM model provided close correlation with the experimental results for time, temperature, displacement and load for each of the panel experiments. The predicted crack initiation location was also overlapping with the experimental crack observations. The comparison was somewhat limited since the experimental crack was only captured within 6-9 mm due to framerate limitations and the model only captured the initiation within 2-5 mm due to output frequency. The temperature at the fracture initiation location was found to be in the range of 600-620°C even when the irradiance was doubled. Although the temperature was not directly measured for comparison purposes, this temperature range seems reasonable when comparing the strength and ductility changes as a function of temperature presented in Chapter 4. Successful comparison of the validation metrics provides confidence in the PDM model for simulating elevated temperature fracture. In addition, the correlation also increases confidence in the modeling approach with respect to element type, solver approach, boundary conditions, user defined flux subroutine, mass scaling, and material properties interpolations associated with tabular input data.

However, an area of potential concern is the crack propagation. The initiation location was captured well but the crack morphology was not representative of the experimental crack propagation. The crack tip was blunter in the simulation due to the element deletion method used for initiating and propagating the crack. In addition, when the secondary crack was formed there was less propagation into the center of the heated zone in the model than observed in the experiment (Figure 6.37). This may be due to a

greater influence of triaxiality at the elevated temperature crack tip, which was not adequately characterized with the V-Notch specimen, or due to the delayed initiation needed to capture the diffuse necking at higher temperatures. Nevertheless, the model response closely correlates with the experiment and the differences in the crack propagation can be attributed to fundamental challenges in simulating ductile fracture within a traditional continuum mechanics framework based on the Finite Element Method.

Chapter 7 : Pressure Vessel Validation

The results of the panel experiment and model comparison provided confidence in the PDM approach for simulating elevated temperature fracture of DSS during rapid localized heating. The second validation experiment was used to evaluate the predictive capability for pressure vessel failure during rapid heating. The catastrophic failure of pressure vessels subjected to accidental fire has been shown to be very destructive when a boiling liquid expanding vapor explosion (BLEVE) occurs (Birk et al., 2006). Pressure vessel failure can occur in less than 20 minutes when exposed to fully engulfing fuel fires, resulting in a significant hazard for industrial fires in petroleum and chemical processing plants, among others.

The failure of pressure vessels at room temperature has been investigated in the literature using finite element simulations (Hampton and Nelson, 2003; Oh et al., 2011) and using empirically based predictions of critical crack length for pipeline and pressure vessel evaluation (Hahn et al., 1969). Most of the literature is devoted to criticality assessment for evaluating existing cracks in pipelines or pressure vessels. However, very limited research has been published on predicting elevated temperature pressure vessel failure.

Pressure vessel failure due to localized heating, as opposed to fully engulfing fuel fire, has been shown to result in different failure modes depending on the size of the heated zone relative to the pressure vessel diameter (Li et al., 1994). When the heated zone is large, the failure is catastrophic and approaches the response of a fully engulfing

fuel fire. However, as the heated zone becomes more localized the failure also becomes more localized and the internal pressure is relieved through a small fracture without catastrophic damage. The localized failure being more representative of the failure observed when a thermal protection system is locally degraded. The catastrophic and local failure are also termed BLEVE and non-BLEVE failures, respectively, within the context of liquid propane pressure vessels (Birk et al., 2006). Since the progressive damage model is capable of simulating crack initiation and propagation, the validation testing will be conducted to identify the transition from local failure to catastrophic failure. Predicting the failure mode transition is a more stressing validation case since the crack must arrest for local failures when conditions are below a critical combination of internal pressure and heated zone size.

7.1 Elevated Temperature Pressure Vessel Experiments

Prior research has shown that increasing internal pressure will decrease the critical crack length to cause failure in room temperature pressure vessels (Hahn et al., 1969). Similarly, the critical heated zone size to cause catastrophic failure should also decrease with increasing internal pressure. Figure 7.1 provides a graphical representation of the heated zone size versus internal pressure. The square shaped markers indicate a catastrophic failure mode and circular markers indicate a local failure mode where the crack is arrested prior to exiting the heated zone.

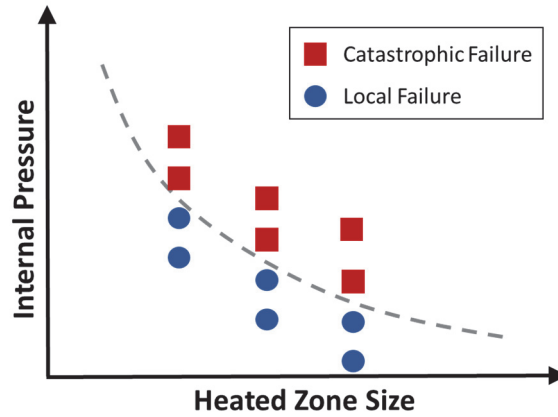


Figure 7.1: Notional plot of the failure response as a function of heated zone size and internal pressure

The pressure vessel experiments in this study were conducted at a fixed heated zone (laser spot) size and the internal pressure was increased or decreased for each subsequent test until the change in failure mode was observed. The test series consisted of 12 failure events over three heated zone sizes. The internal pressure was slowly increased to a set condition using a custom remote pressurization system then a high energy fiber laser was used to achieve heating rates in excess of 100°C/sec. The test was designed to capture the following critical measurements; pressure history, failure mode, temperature history, irradiance distribution, crack initiation location and crack propagation. The irradiance distribution and temperature history are critical for characterizing the transient thermal state of the pressure vessels during the experiment while the pressure history (used for failure time), crack morphology and failure mode are critical measurements for model comparison.

7.1.1 Pressure Vessel Test Articles

Twelve pressure vessels were built for this test series using the same sheet stock of duplex stainless steel used for model calibrations, with a thickness of 1.5 ± 0.1 mm, and manufactured such that the rolling direction of the sheet is along the circumferential direction of the pressure vessel. The sheets were rolled to a 10 inch diameter which is on the smaller side for a pressure vessel and an intermediate size for pipeline. The roll and weld process used a laser welding system with 2205 DSS weld wire. The thickness of each cylinder was measured after completion of the rolling process and prior to the longitudinal (axial) weld, as tabulated in Table 7.1. The cylinders were 1 meter in length with circular flanges at each end, as shown in Figure 7.2.

Table 7.1: Cylindrical pressure vessel test article thicknesses

Test #	Avg. Thickness (mm)	Std. Deviation (mm)
1	1.483	± 0.009
2	1.484	± 0.011
3	1.475	± 0.008
4	1.487	± 0.014
5	1.499	± 0.011
6	1.472	± 0.012
7	1.486	± 0.010
8	1.503	± 0.018
9	1.512	± 0.020
10	1.497	± 0.011
11	1.471	± 0.012
12	1.512	± 0.012

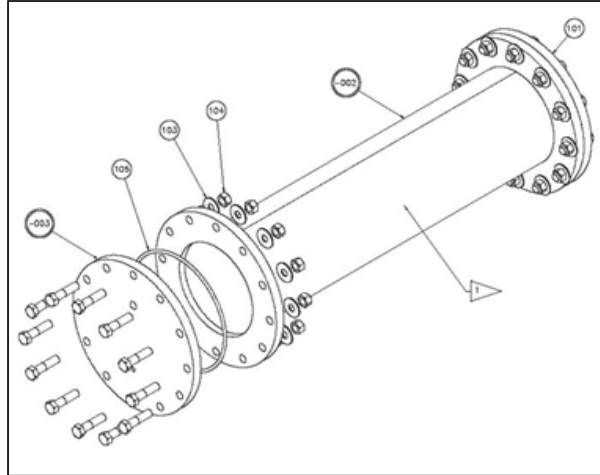


Figure 7.2: CAD geometry drawing for cylindrical pressure vessel with reusable end flanges

The flanges and end caps were grooved to accommodate an O-ring which enabled removal for instrumenting the interior of the test articles. The top flange was also machined to have one port for the pressurization system and a second port for a thermocouple feedthrough, allowing for 27 thermocouple pairs to be wired into the cylinder while maintaining internal pressure, as shown in Figure 7.3.

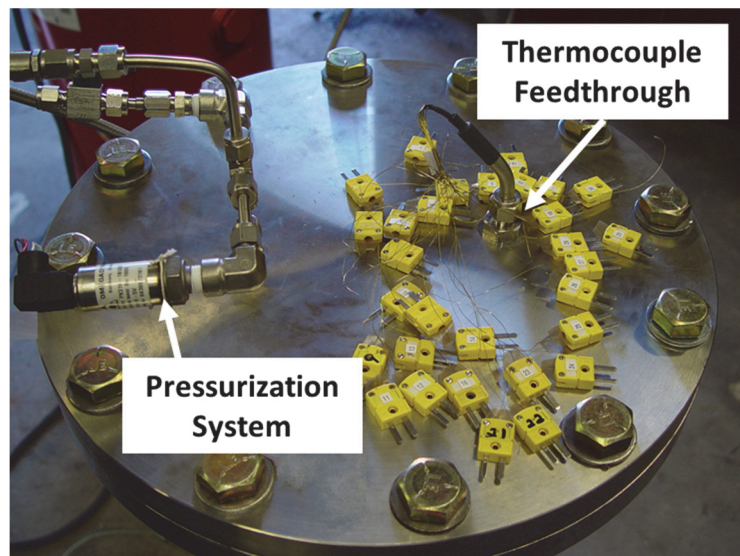


Figure 7.3: Pressure vessel top flange with thermocouple feedthrough and pressurization system

The thermocouples were welded to the interior surface using the pattern shown in Figure 7.4. The larger grid spacing was at 5 cm intervals in the axial and circumferential direction and the smaller pattern near the beam center was at 2 cm spacing. The thermocouples were K-type from Omega Engineering providing a measurement range up to 1250°C with standard error of 2.2°C or 0.75% of the reading, whichever is greater. The TC array was mounted using a conformal template and the continuity of each channel was checked prior to testing. The TC data was collected using a National Instruments data acquisition system at 100 Hz.

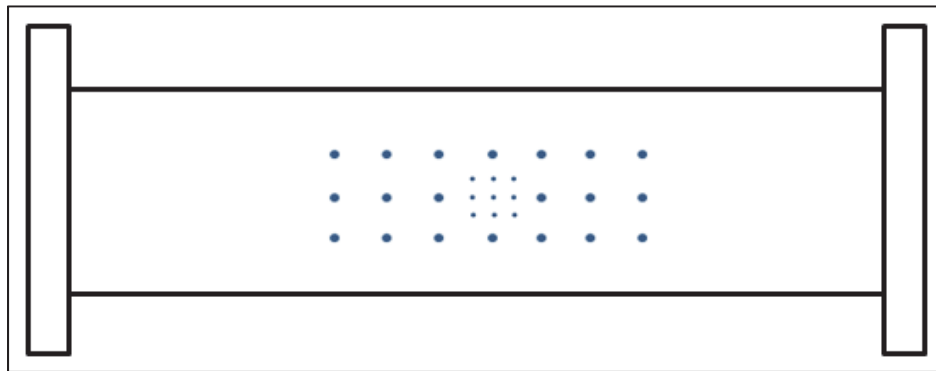


Figure 7.4: Thermocouple pattern for the interior surface of the pressure vessels

Following the manufacturing of each pressure vessel, a dye penetration and leak test was performed using ASTM E-515 at a pressure of 75 psi for 5 minutes. In addition, the longitudinal welds were inspected via radiographic inspection. An example of one of the finished cylinders is shown in Figure 7.5 without the end caps attached to the flanges.



Figure 7.5: Example of one of the cylinders after rolling and welding without the end caps attached

Similar to the panel test articles, the front side (180° from the axial weld) of each cylinder was painted with Forrest Paint “Stove Bright” high temperature stove paint (Flat Black #6304) to help increase the surface absorption of the samples at the laser wavelength ($1.07 \mu\text{m}$). The painted region was approximately ± 20 cm from the centerline in the axial direction and $\pm 90^\circ$ in the circumferential direction, where 180° represents the axial weld location. Painting the panels helped to increase the laser energy absorption from 50% to roughly 85%. The paint also provides a near uniform surface finish across the sample which reduces spatial variation in absorption commonly seen with unfinished materials in the as-received condition.

7.1.2 Test Configuration

The failure of the pressurized cylinders was expected to be destructive, particularly when the pressure and heated zone size were high enough to generate a catastrophic failure. In order to mitigate safety hazards to equipment and personnel, a concrete enclosure was constructed of $2' \times 2' \times 4'$ concrete blocks with a reinforced steel

grating placed over the enclosure. The grating allowed light into the test area while reducing the hazards associated with flying debris. The test enclosure with the test article stand and lighting are shown in Figure 7.6.



Figure 7.6: Enclosure for the pressure vessel experiments

The test article stand was constructed from $\frac{1}{4}$ -inch thick, 3"x3" square steel tubing using a welded construction. A reinforced steel top plate was used to attach the top cylinder cap to the test stand, such that the cylinder was suspended from above. This allowed for the cylinder and top plate to be easily installed into the stand using a hydraulic lift. The lower cylinder cap/flange were slipped through a hole in the lower plate allowing the base to drop upon failure. A fully instrumented test article mounted into the test fixture is shown in Figure 7.7. The pressurization lines, pressure transducer wiring and thermocouple wires are shown going through the grating to the data acquisition and pressurization control unit outside of the enclosure.



Figure 7.7: Instrumented pressure vessel mounted in the test fixture

The internal pressure was provided by a 6000 psi “K” bottle of Argon gas, controlled by a regulator and valves. The pressurization equipment was placed outside the enclosure wall and only a small gas line was passed through the grating to the top of the pressure vessel. Both the regulator and pressure transducer at the top of the pressure vessel were monitored during initial pressurization and during laser irradiation. The argon bottle with pressure regulator, the pressure transducer and gauge, as well as the remote operation switches are shown in Figure 7.8. The remote switching capability added an additional safety measure in the event the test articles were unable to hold the rated pressure. The remote pressurization system was also designed to release the pressure in the event of an aborted test, which was necessary for the final experiment. Once each cylinder was sealed and mounted into the test fixture, the test article was remotely pressurized to 30 psi for a minimum of 30 minutes to test for leaks. The test articles were

then pressurized to the full experimental pressure 5 minutes prior to laser heating and the valves were closed to isolate the test article from the argon bottle.

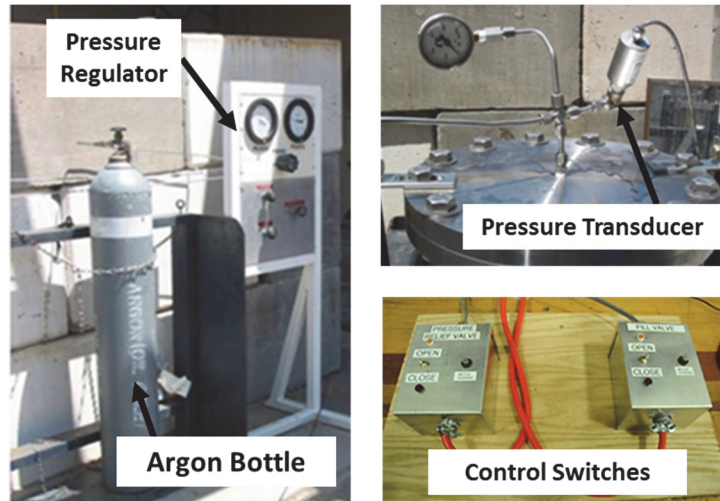


Figure 7.8: Pressurization system with remote operation switches

The pressure was measured using an Omega Engineering transducer with a range of 0-1000 psi (Omega PX303-1KG5V) and uncertainty of 1% of full scale. The pressure was monitored at a rate of 100 Hz. The pressure history was used to identify initial pressure (stress state) in the tank and the pressure at the time of failure. Due to heating of the tank wall, a slight increase in pressure (a few psi) was observed during the test. The failure time was identified by a rapid drop in tank pressure. In general, the failure time indicated by the pressure transducer was complimentary to the time identified by the high speed camera but more reliable and prompt than other measurements such as the thermocouples or MWIR camera.

The test articles were illuminated using high intensity quartz lamps to improve the imagery during the failure event. A Photron SA-1 high speed camera (operating at 40,000 fps) and FLIR SC-4000 MWIR camera were positioned behind concrete blocks and viewed the test article using turning mirrors, as shown in Figure 7.9. Several small Sony mini-cameras were also placed throughout the test area to provide situational awareness to the laser operator. Similar to the panel experiments, the IPG Photonics YLS-20000 fiber laser system was used to provide heating to the pressure vessels. A custom collimator system was used in conjunction with beam expanding optics to tailor the beam size (heated zone size) for the different test conditions. A wedge optic was used to extract partial reflections of the laser energy to measure power with an 8 inch Scientech calorimeter and the beam profile was imaged from a Macor scatterplate using a Sensors Unlimited Inc. SWIR camera. A secondary power estimate was provided by a photo-detector (Judson J22 InGaAs) viewing the reflected energy from the scatter plate. The power measurements were calibrated to a NIST traceable ball calorimeter (BB2GP1), along the primary beam path, to determine the split ratio of the partial reflection.

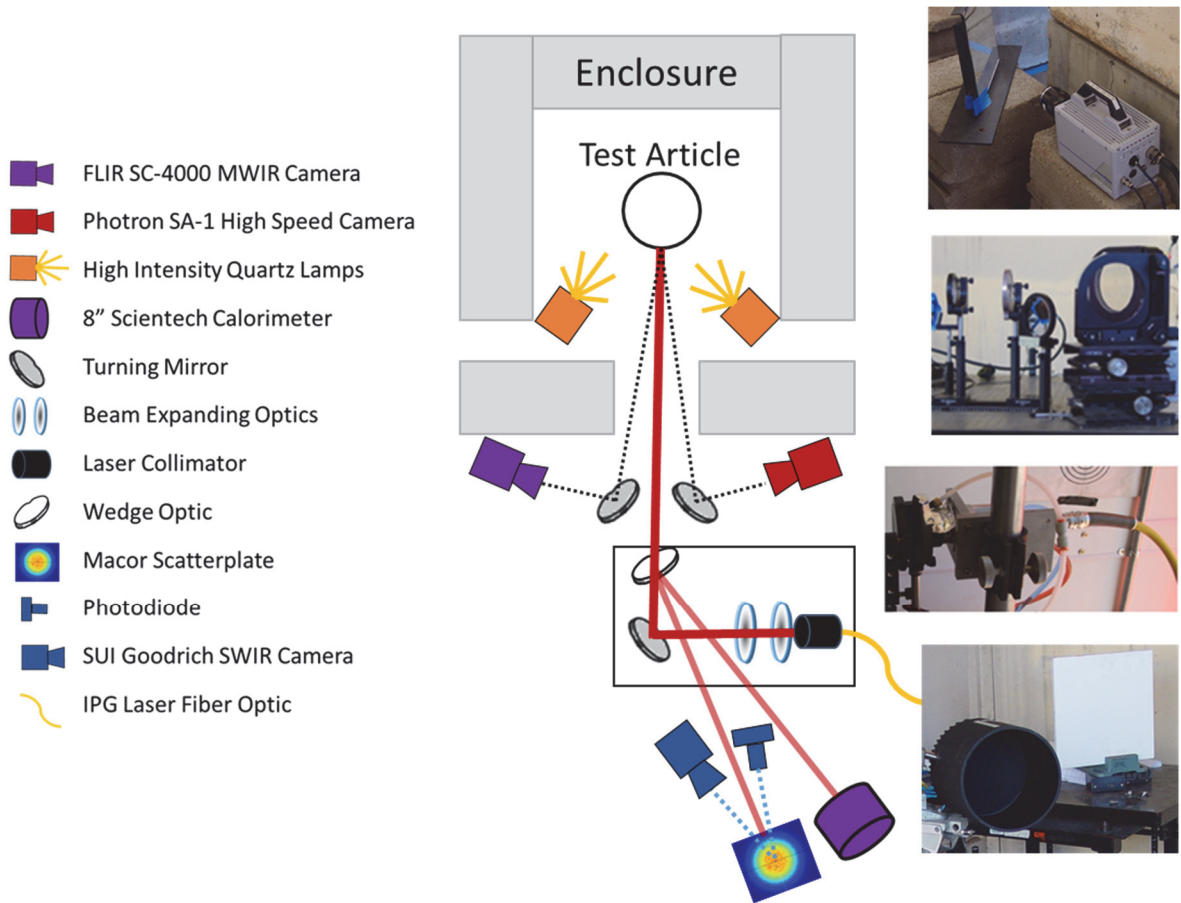


Figure 7.9: Test configuration for elevated temperature pressure vessel experiments

7.1.3 Pressure Vessel Test Conditions

Only twelve pressure vessels were constructed for the test series which limited the number of pressure and heated zone size conditions that could be explored. In order to select the optimal test conditions, the PDM model was used to predict the transition line between local to catastrophic failure. The predicted failure mode transition is shown in Figure 7.10, plotted in terms of pressure ratio and heated zone ratio. The pressure ratio is defined as the initial pressure divided by the room temperature hydrostatic burst pressure. The burst pressure, P_b , is determined from shell theory using the room temperature tensile strength (σ_{ult}) and cylinder geometry as follows:

$$P_b = \frac{\sigma_{ult} \cdot t}{R} \quad (7.1)$$

where t is the cylinder thickness and R is the cylinder radius. The pressure ratio is also the inverse of the Factor-Of-Safety (FOS) when considering the operational/rated pressure for pipeline or pressure vessels. The heated zone ratio is defined as the $1/e^2$ laser beam diameter divided by the cylinder diameter. Using the normalized quantities accounts for the strength and geometry of the pressure vessel which may result in a more general characterization of the failure mode transition for potential application to other materials and geometries.

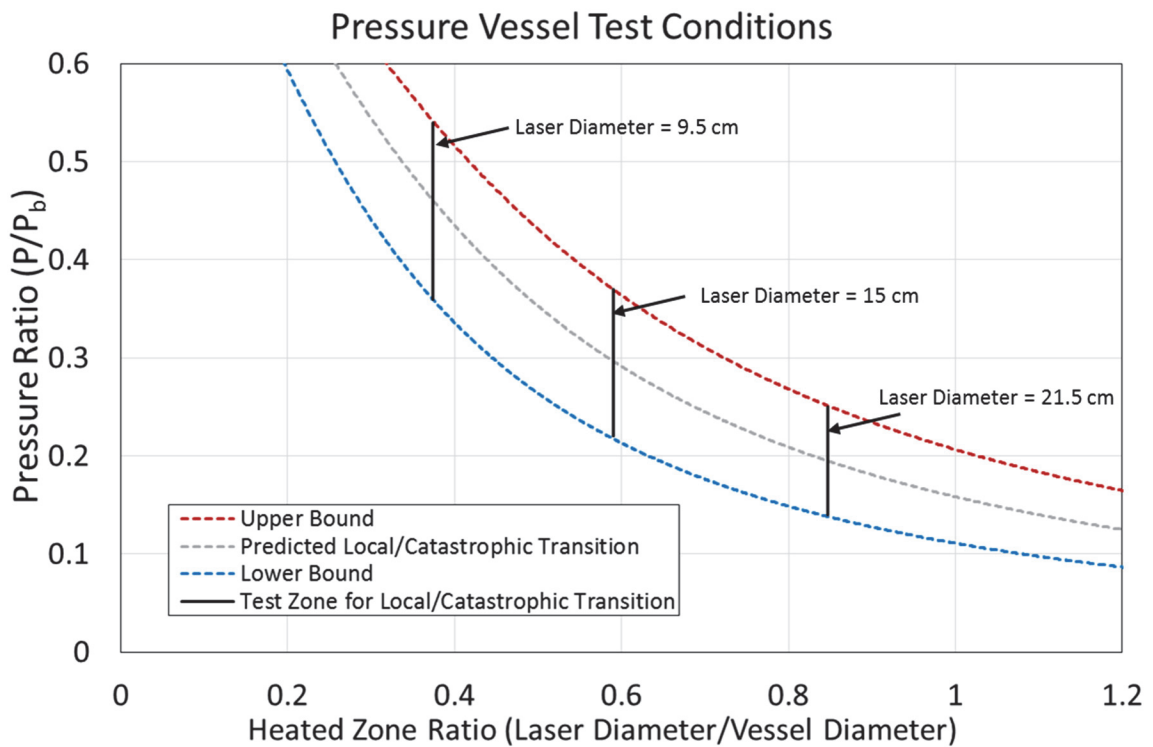


Figure 7.10: Predicted failure mode transition line and test ranges for three different laser beam sizes

The predicted failure mode transition using the PDM model was conducted using an idealized Gaussian laser beam profile and mass scaling of 10,000 which significantly

reduced the computation time. However, the impact of mass scaling on the failure mode prediction was not quantified so an upper and lower bound were estimated using $\pm 25\%$ of the heated zone ratio, as shown in Figure 7.10. The experiments were then selected to investigate pressure and heated zone ratio combinations within these upper and lower bounds. The spot sizes of 9.5, 15, and 21.5 cm diameters were chosen for this study because they roughly span the pressure ratio range of 0.2 to 0.5 which equates to a factor-of-safety range of 5 to 2. The irradiance level was selected at 100 W/cm^2 based on the available laser power (20 kW) and largest anticipated laser diameter (21.5 cm).

Since twelve pressure vessels were manufactured for this test series, four test articles were available for each laser diameter. The initial pressure was changed for each test to help identify the transition from local to catastrophic failure. If a local failure was observed, the pressure would be increased for the subsequent test. Likewise, if a catastrophic failure was observed the pressure would be decreased on the subsequent test. Due to budget limitations, there were not enough test articles to perform repeat experiments to quantify random uncertainties associated with shot-to-shot variations.

7.1.4 Pressure Vessel Test Results

All twelve cylinders were successfully tested using various combinations of heated zone ratio and pressure ratio, as shown in Table 7.2, resulting in both local and catastrophic failure modes. The experimental irradiance conditions were within $\sim 25\%$ of the planned value of 100 W/cm^2 for all experiments. The variability was primarily caused by remote laser operations which increased the time and difficulty of irradiance

calibrations when the optics locations were modified to change the laser spot size. The peak irradiance was lower than anticipated for the largest spot size due to power limitations, resulting in an overall irradiance range of 80-126 W/cm². However, the irradiance levels were more tightly grouped for a given laser beam diameter.

Table 7.2: Results summary for elevated temperature pressure vessel failures

Test #	Peak Irradiance (W/cm ²)	Laser Diameter 1/e ² (cm)	Heated Zone Ratio	Pressure (psig)	Pressure Ratio (P/P _b)	Failure Time (s)	Peak Thermocouple Temperature (°C)	Failure Mode
1	113.9	13.6	0.54	362	0.24	8.14	1092	Local
2	109	13.5	0.53	535	0.36	6.27	886	Catastrophic
3	105.7	13.4	0.53	444	0.30	7.43	1005	Local
4	118.8	13.1	0.52	487	0.33	6.79	1007	Catastrophic
5	122.2	9.4	0.37	617	0.41	6.81	1014	Local
6	123.2	9.4	0.37	740	0.50	5.41	852	Catastrophic
7	125.8	9.3	0.37	678	0.46	5.89	931	Catastrophic
8	126.5	9.3	0.37	648	0.43	6.35	990	Local
9	119.9	17.4	0.69	340	0.23	7.14	1012	Local
10	79.6	21.1	0.83	348	0.23	9.88	979	Catastrophic
11	83.3	21.1	0.83	300	0.20	10.46	1040	Catastrophic
12	80.6	20.8	0.82	276	0.19	11.13	1034	Local

The laser diameters used during the experiments were close to the planned values of 9.5, 15, and 21.5 cm. Although the intermediate spot size of 15 cm was not easily achievable with the optical layout. A laser diameter of 13.5 cm was used to simplify the test configuration and reduce the number of modifications to the beam train. The small and large spot sizes were close to the planned values of 9.5 cm and 21.5 cm, with the exception of test #9, which was caused by a beam diagnostics issue.

The failure time and peak rear surface temperature reading for each experiment are also shown in Table 7.2, corresponding to heating rates in the range of 90-160°C/s. For each laser beam size, both a local and catastrophic failure were observed by varying the initial pressure, allowing for the failure mode transition to be estimated. The

experimental results are presented in Figure 7.11 with a comparison to the pre-test analysis, previously shown in Figure 7.10.

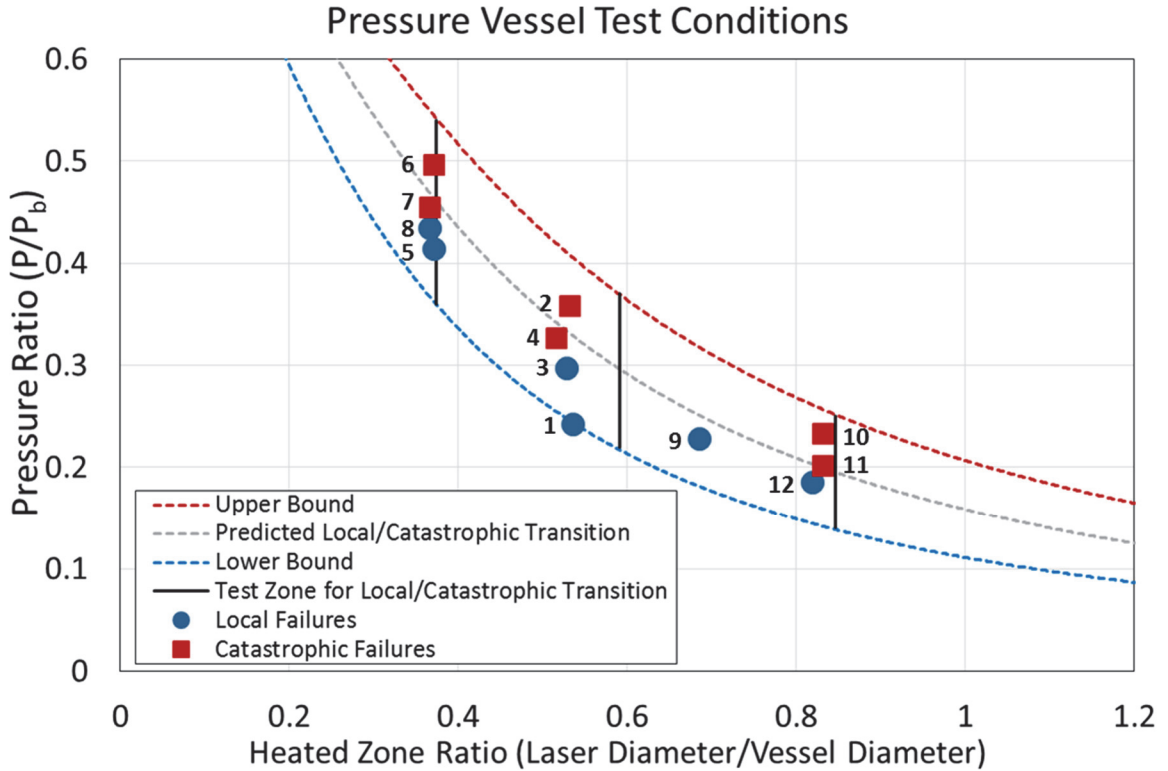


Figure 7.11: Experimental results showing the failure mode transition as the pressure ratio is increased

The experimentally determined failure mode transition was slightly lower than the pre-test analysis although the initial predictions were conducted with a mass scaling of 10,000 and an idealized Gaussian profile. An unscaled model comparison using the measured beam profile and pressure conditions will be presented in Section 7.2. Nevertheless, the pre-test predictions proved to be vital in determining the test conditions for each experiment. The failure mode transition was captured within a pressure ratio difference of 0.03 even with only four experiments for each heated zone size. In addition, the transition point was still captured at the largest heated zone size

even with test #9 being an outlier due to laser diagnostics issues. Figure 7.12 shows an image of the failure mode for each experiment, as captured by a standard video camera. The difference between a catastrophic and local failure can be clearly discerned.

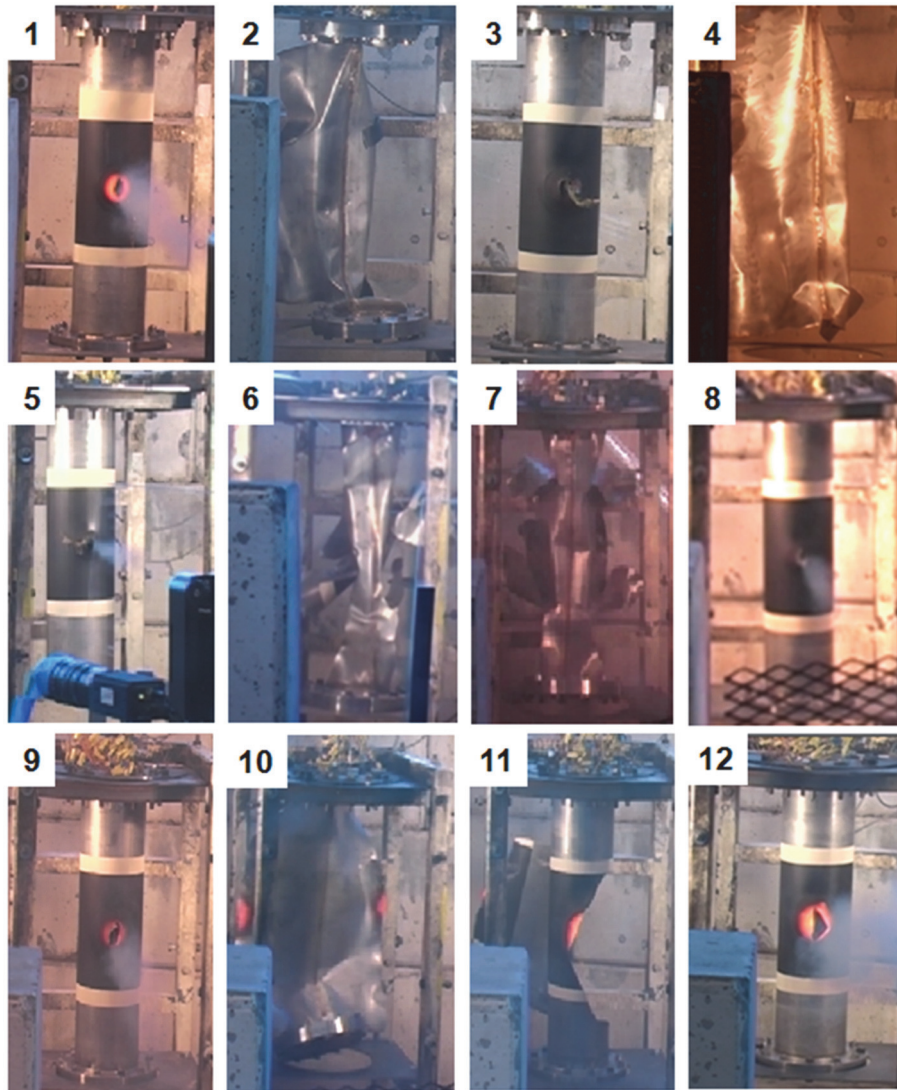


Figure 7.12: Images of the failure mode for each pressure vessel experiment

The only noteworthy discrepancy during the pressure vessel experiments was during test #12. The test article was pressurized using the procedure outlined in Section 7.1.2 and the laser heating was initiated. Following approximately 6 seconds of laser

heating, the laser operator noted a potential issue with the laser health sensors and terminated operation to protect equipment. The test article was depressurized using the remote valve system and allowed to cool back to ambient conditions. The temperature history is provided in Figure 7.13 for the two highest thermocouple readings, showing a peak rear surface temperature near 500°C.

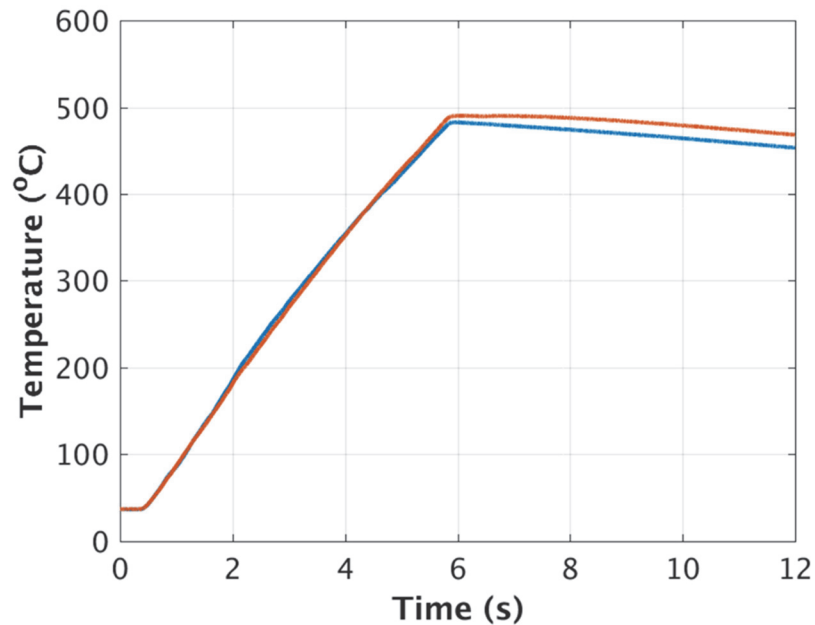


Figure 7.13: Temperature history for highest thermocouple readings from test #12 when laser operation was aborted

The material was approaching the solid-to-solid phase transformation which occurs in the temperature range of 450-700°C, which can be estimated using the specific heat curve provided in Figure 3.3. Damage to the painted surface was clearly visible, as shown in Figure 7.14, but the extent to which the material strength and surface absorption changed was not determined.

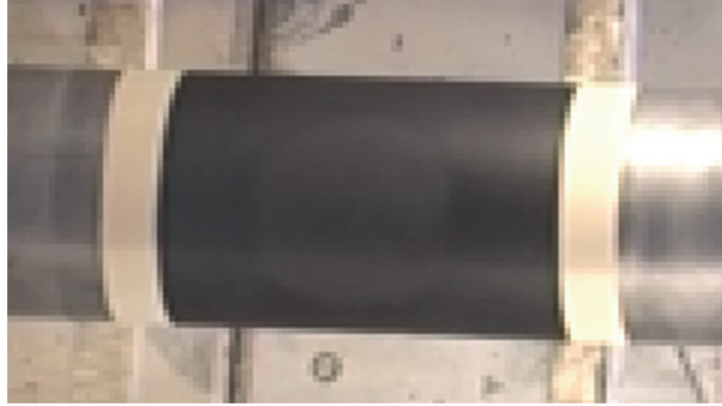


Figure 7.14: Test article used in test #12 showing damage to the painted surface caused by laser heating prior to the test being terminated over laser health concerns

Once the laser was checked and approved for operation, the decision was made to re-attempt the experiment on the same test article. The peak temperature was on the lower end of the phase transformation range and the test article was also the final pressure vessel available for the test series. Heating another region on the cylinder was considered but not implemented due to time constraints, since the internal thermocouples would need to be re-welded in a new location. Ultimately, the experiment was conducted again without further issues and a local failure was observed. The conditions and results presented in Table 7.2 and any additional descriptions of test #12 found later in this manuscript are for the final experiment. While the outcome of test #12 was consistent with the experimental trend, the discrepancy was worth noting.

An example of a typical laser beam profile, generated for this test series using the IPG Photonics laser, is shown in Figure 7.15 for test #1. The beam is nearly axisymmetric with a profile that is somewhat flatter in the central portion than a true Gaussian distribution. Similar to the panel validation experiments, the profile can be estimated using Equation 5.1 with a super-Gaussian exponent in the range of 3.1-3.7.

Pressure Vessel Test #1

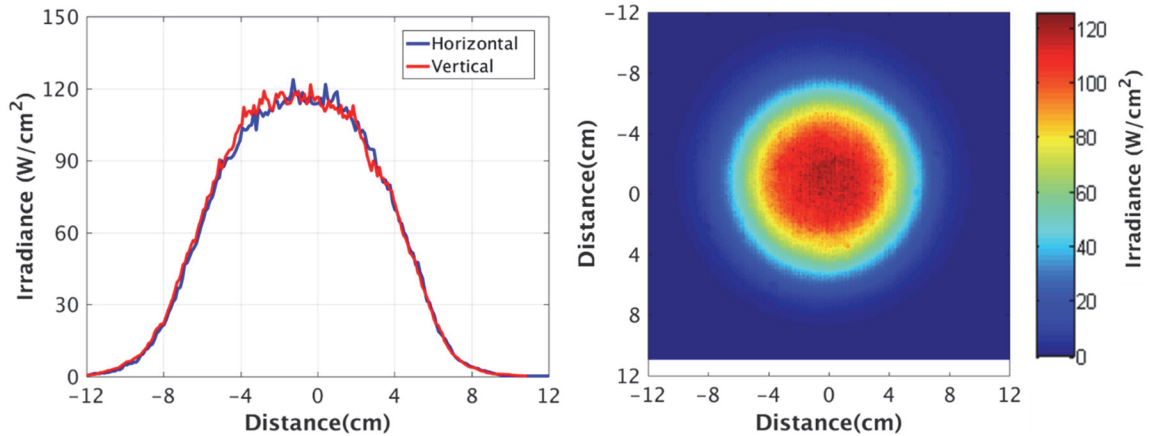


Figure 7.15: Laser beam profile for pressure vessel test #1

The laser beam profiles for a subset of the experiments used during the PDM model validation are shown in Figure 7.16. Test numbers 2, 6 and 10 were not analyzed since a catastrophic failure was also achieved using a lower pressure in test numbers 4, 7 and 11. Similarly, test numbers 1 and 5 could have been neglected since a local failure was also achieved with a higher pressure in test numbers 3 and 8. Ideally, all of the experiments would be used in the validation process but the simulations took approximately 2000 CPU-hours of computation time per case which required the study to focus around the failure mode transition.

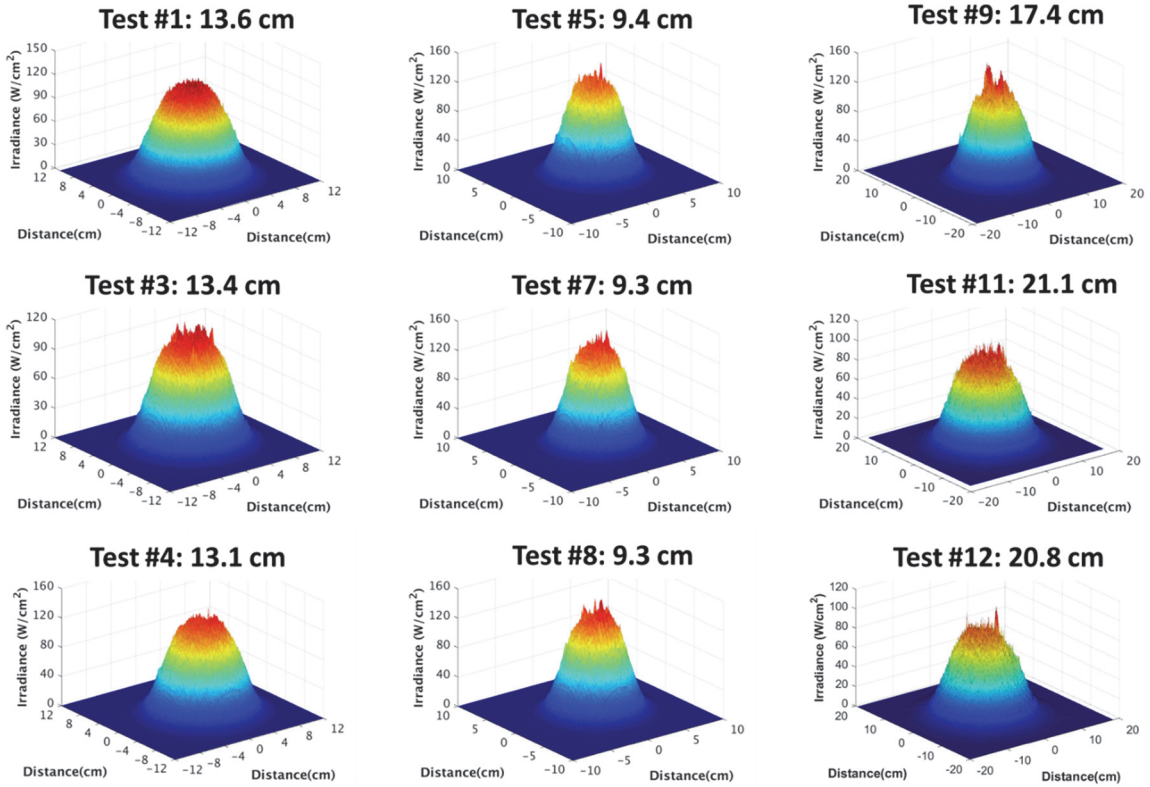


Figure 7.16: Laser beam profiles for the pressure vessel experiments which were analyzed with the PDM model

The beam profiles were relatively smooth for the intermediate spot size (13.5 cm), as shown in Figure 7.16. As the optics were adjusted to the smaller beam size a “hot spot” formed in the laser beam profile and persisted as the beam size was increased to the largest size. The hot spot may have formed due to damage of the laser fiber or block during early testing or a damage site may have formed on one of the optical elements. The hot spot is clearly visible in the laser profile of the horizontal and vertical cross-sections of test #9, shown in Figure 7.17. Although some scintillation and noise from the scatter plate uniformity is common, a hot spot of nearly 20% indicates an issue arising from the laser or a component within the beam train. Hot spots are not ideal for the validation experiments, however the ability to characterize the hot spots makes the laser

heating method superior to broadband IR heating or fuel burning methods. Due to schedule limitations, the root cause of the hot spots was not identified and corrected during the test series.

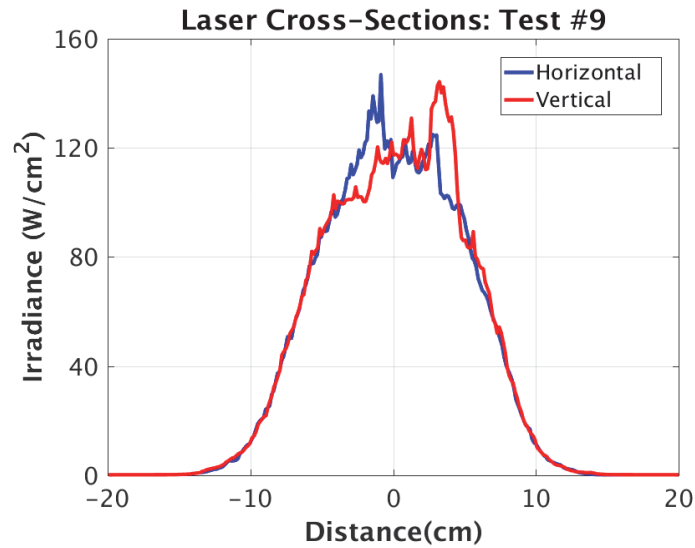


Figure 7.17: Horizontal and vertical profile of the laser beam for pressure vessel test #9 showing hot spots

The hot spot can be seen in the high speed imagery of test #12 in the first frame shown in Figure 7.18. Several less-intense hot spots are also visible which may be due to paint deterioration. In this case, the crack initiates near the hot spot location and then propagates toward the center before being arrested near the lower edge of the heated zone.

Test 12

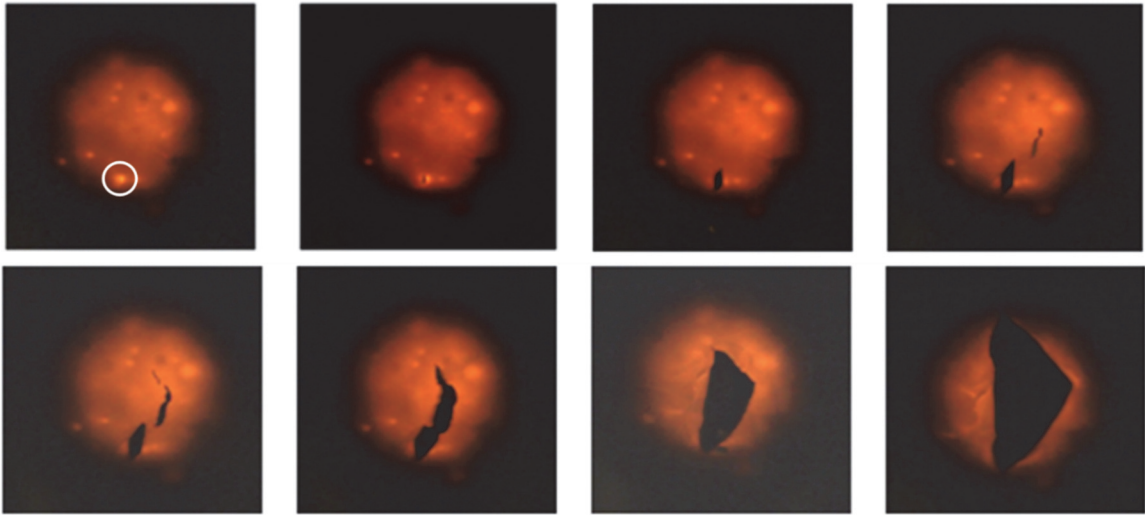


Figure 7.18: High speed imagery of fracture process for test #12

Similarly, the crack initiates near a hot spot in test #9 and propagates across the heated zone to a secondary hot spot on the opposite side, as shown in Figure 7.19. The crack is arrested and the pressure is released through the failure opening.

Test 9

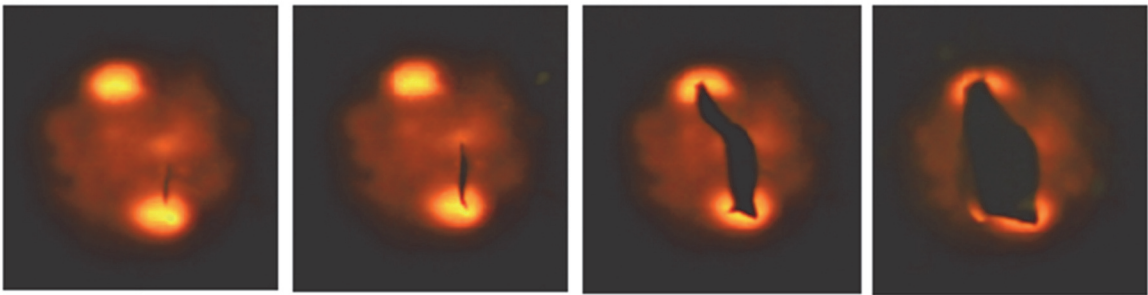


Figure 7.19: High speed imagery of the fracture process for test #9

An example of a catastrophic failure is provided in Figure 7.20 for test #6. The yellow markers represent the estimated crack tip locations, determined from the magnified images. The crack speed was calculated to be in the range of 200-250 m/s using the estimated crack tip locations and known length of the painted region. As the crack

becomes wider in the last two frames, increasing amounts of argon emerge from the cylinder which obscures the view of the central region of the crack. The imagery for test #6 and earlier experiments were impacted by the reflected laser energy, appearing green on the camera sensor, even though the laser is in the near infrared. A narrow line notch filter around $1.07 \mu\text{m}$ was added to the camera for later experiments to reduce the amount of reflected laser energy which ultimately improved the high speed imaging of the fracture process, as previously shown for tests #9 and #12.

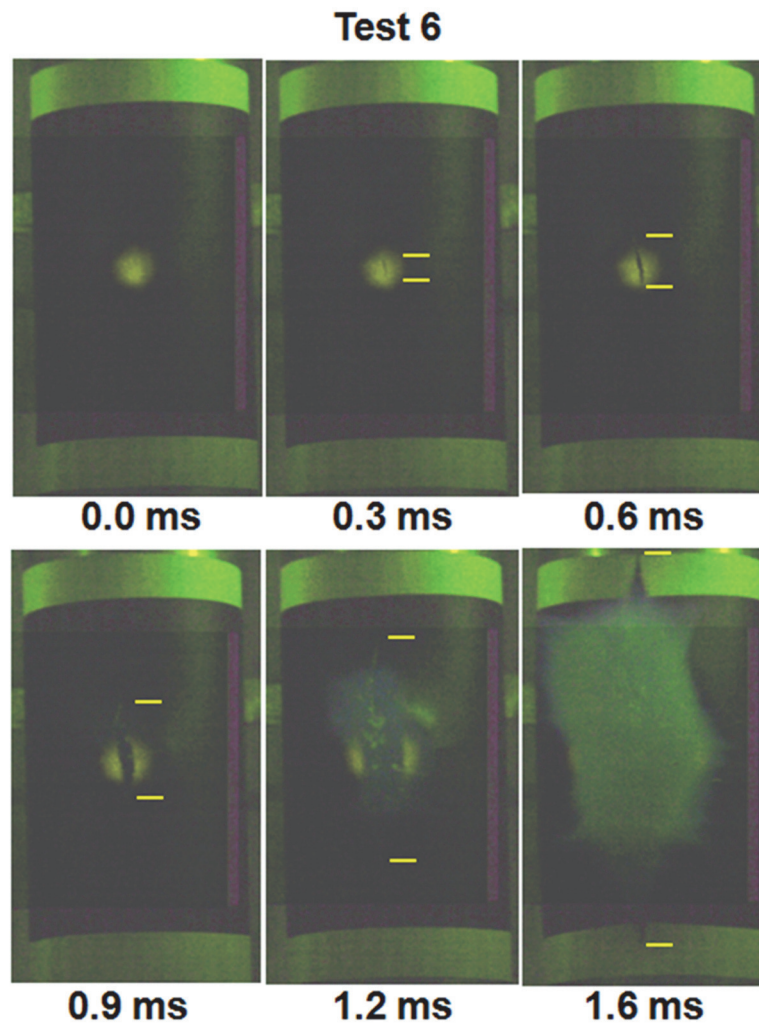


Figure 7.20: High speed imagery of the fracture process for test #6

Although hot spots were apparent in the beam profile and the high speed camera images for several experiments, the thermocouple measurements were consistent with a smooth beam profile. The centermost thermocouple (TC-15) had the highest reading in the majority of the cases with only two cases having a peak reading at the TC located 2 cm below center (TC-16). The hotspot location appears to be offset vertically in eight cases but that was not typically reflected in the peak TC location. However, the hot spot may have been located between TC locations or the thermal diffusion may have reduced the non-uniformity on the rear surface. An example of the thermocouple traces are shown in Figure 7.21 for test #1 and Figure 7.22 for test #12.

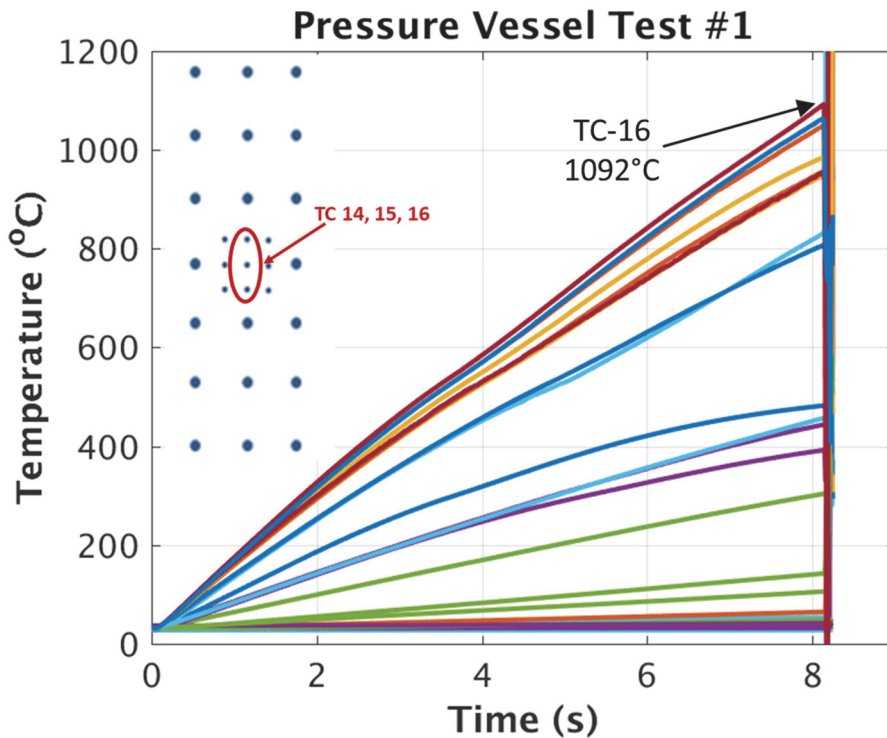


Figure 7.21: Thermocouple histories for pressure vessel test #1

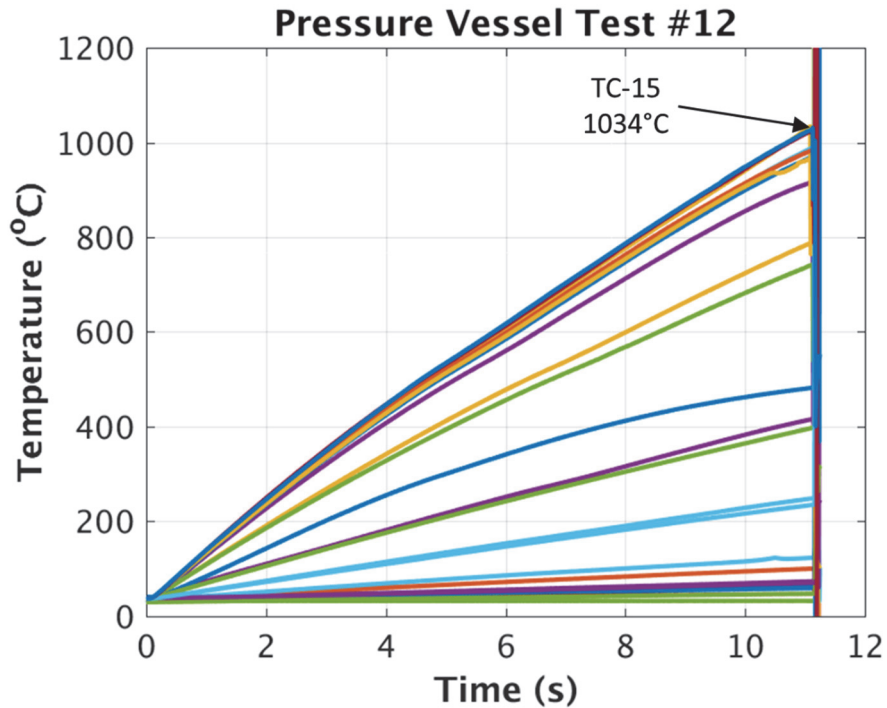


Figure 7.22: Thermocouple histories for pressure vessel test #12

In both cases, the center column of thermocouples (TC-14 orange, TC-15 blue, and TC-16 maroon) were the hottest and within 50°C of one another during failure. The overall trend and quality of the thermocouple data was similar for the remaining experiments however some variation in heating rate and distribution was seen as a result of the laser beam size, irradiance and beam alignment.

The laser beam centroid location relative to the TC pattern proved to be important for later comparison to the finite element simulations. In order to estimate the beam alignment shift relative to the TC pattern, a brute force optimization method was developed to compare the normalized beam profile to the normalized thermal profile, as measured by the thermocouples.

A flow chart of the algorithm used to determine the beam shift is provided in Figure 7.23. The algorithm begins with the measured laser beam profile and thermocouple data. For a given beam centroid location, the beam was projected onto the cylinder surface and the irradiance was determined at the TC locations. Both datasets were then normalized to the peak value and the residual was calculated at various times. The times were selected to be early in the heating process to reduce the impact of thermal diffusion. The centroid was then adjusted to a new location and the process was repeated until the residual was minimized. In general, the estimated beam shifts were within 1 cm of the TC pattern center for both the horizontal and vertical directions. As a result, the beam centroid was always within the finer (2 cm) TC grid.

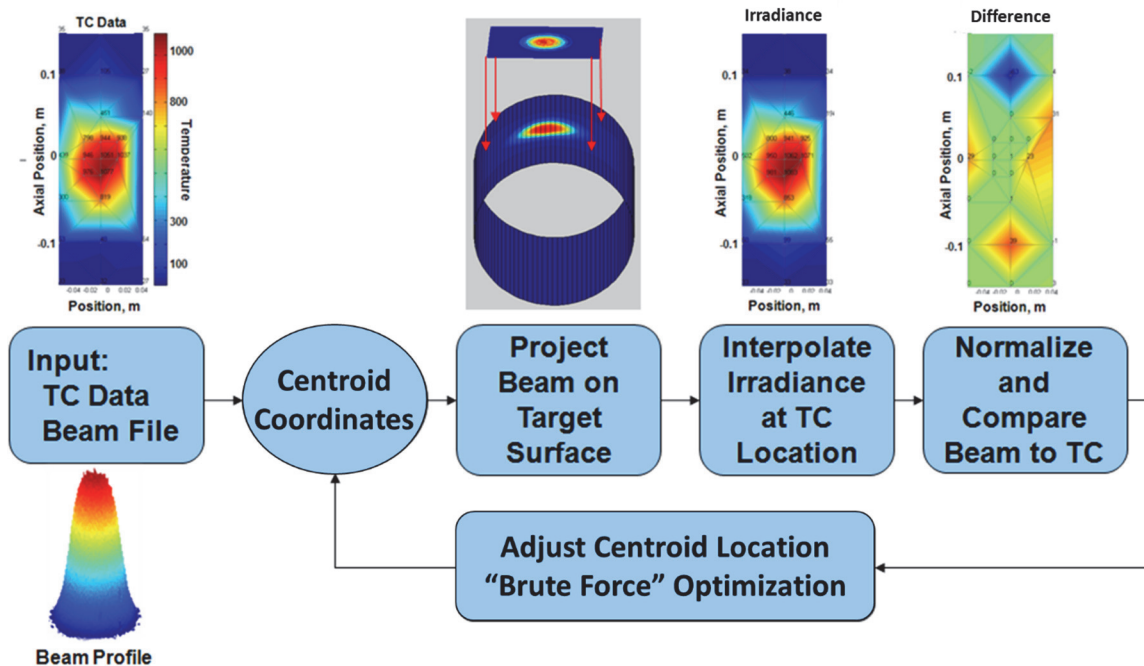


Figure 7.23: Flow chart for identifying the laser beam centroid location using the beam profile and TC data

In each experiment, the peak thermocouple temperature was extracted and recorded in Table 7.2. As one might expect, the temperature at failure tends to increase as you move away from the transition line toward a lower pressure ratio, as seen in test #1, and tends to decrease as you move away from the transition line toward a higher pressure ratio, as seen in tests #2. In addition to temperature, the thermocouple readings were also used as a secondary measurement for failure time. Failure was identified by an erratic temperature reading as the thermocouple welds detach during depressurization, as shown in Figure 7.22 around 11.1 seconds. Fortunately, this approach was not needed as the pressure transducers were very reliable.

An example pressure transducer history is shown in Figure 7.24. The pressure history shows a stable internal pressure prior to failure and a low signal-to-noise ratio. The failure time was identified by a rapid decrease in pressure and cross-correlated to the high speed imagery using an IRIG timestamp. The pressure at failure is recorded in Table 7.2 based on a 100 Hz data acquisition rate.

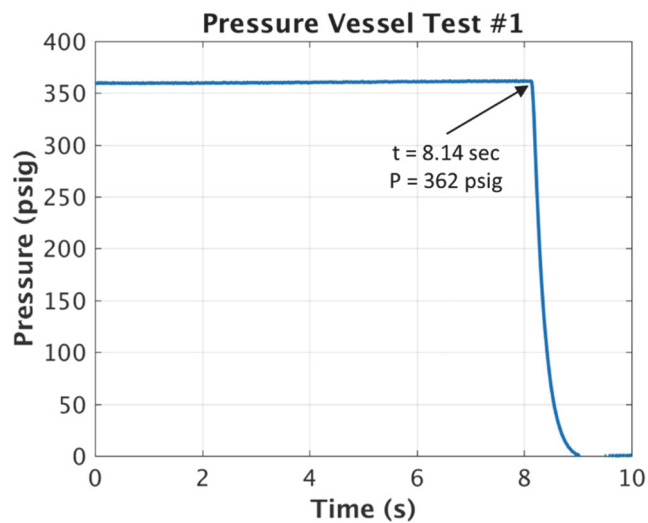


Figure 7.24: Pressure history for test #1 showing stable pressure and low single-to-noise ratio

The pressure history for a local (test #1) and catastrophic (test #6) failure are shown in Figure 7.25 and Figure 7.26, respectively. The plots are zoomed in on the pressure reading over a one second interval near the failure time which shows a drastic difference in the depressurization rate between the two failure modes. The local failures tend to depressurize in approximately 1 second while the catastrophic failure depressurizes in less than 50 milliseconds. The final deformed shapes are also shown in the inset pictures of the pressure histories.

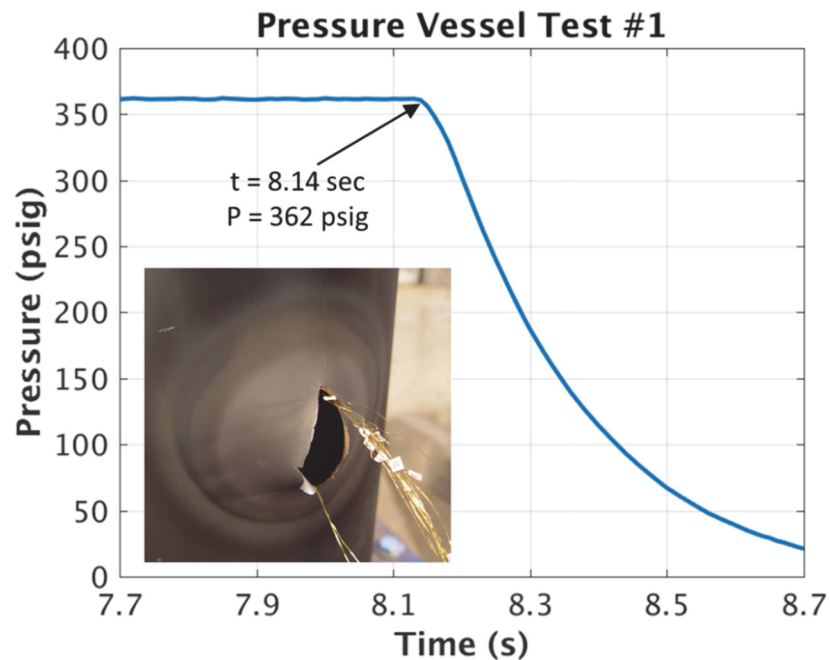


Figure 7.25: Pressure history for test #1 showing a decay in pressure following local failure

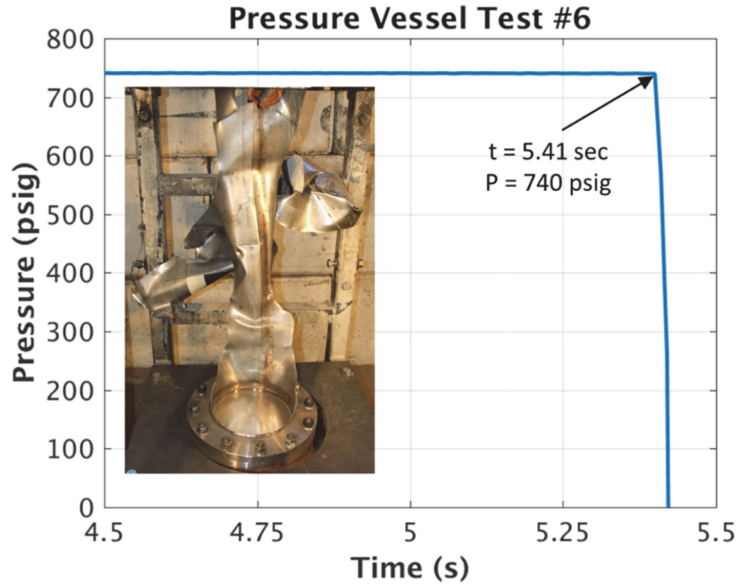


Figure 7.26: Pressure history for test #6 showing a rapid decrease in pressure following a catastrophic failure

The pressure was found to increase slightly as the cylinder walls were heated, as shown in Figure 7.27, due to heating and expansion of the argon gas. The failure pressures recorded in Table 7.2 reflect this phenomena although it's relatively small for the heating times in these experiments.

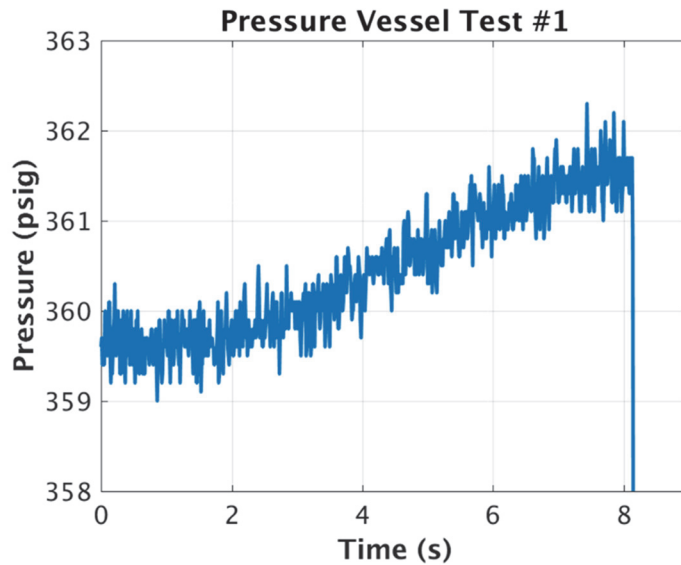


Figure 7.27: Pressure history for test #1 zoomed to show the gradual pressure increase as the cylinder is heated

A plot of the applied energy and relative internal pressure increase is provided in Figure 7.28, showing a maximum change of approximately 2%. However, the pressure change may be more significant for lower heat fluxes (longer exposure durations), fully engulfing fire conditions (greater heated area) or liquid filled pressure vessels where vapor is generated from boiling at the heated surface.

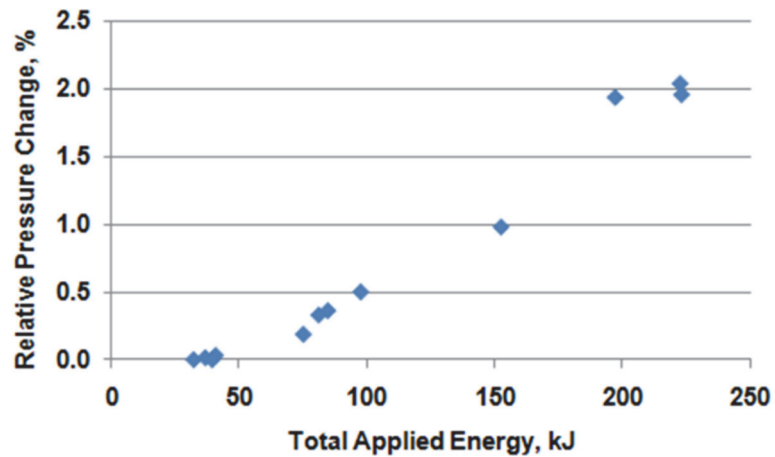


Figure 7.28: Relative pressure increase before failure as a function of the applied laser energy

The pressure vessel validation experiments resulted in a comprehensive dataset for validation of the PDM model for predicting crack initiation and growth at elevated temperatures and high thermal gradients. As previously mentioned, the failure mode transition from local to catastrophic failure was captured within a pressure ratio difference of 0.03 across several heated zone sizes, as shown in Figure 7.29. An equation was fit to the experimental results to estimate the pressure ratio (β) as a function of the heated zone ratio (η) at the failure mode transition.

The use of pressure ratio and heated zone ratio is intended to provide a normalized response for potential application to other materials and geometries (radius

and thickness). The polynomial equation is provided in Figure 7.29 with an experimental domain of $0.37 < \eta < 0.83$. Although the polynomial fit may provide a reasonable estimate outside this range, only a moderate extrapolation to the domain of $0.3 \leq \eta \leq 0.9$ is recommended without further experimentation. The corresponding range of pressure ratio is approximately $0.15 \leq \beta \leq 0.5$ which roughly covers an operational factor-of-safety of $2 \leq FOS \leq 5$. While a fully engulfing fire ($\eta > 1$) may be more representative of industrial hazards, local defects or localized failures in thermal protection system (TPS) can result in lower heated zone ratios. For instance, Birk et al. (2006) investigated the impact of TPS defect size on the BLEVE failure of liquid propane containment vessels.

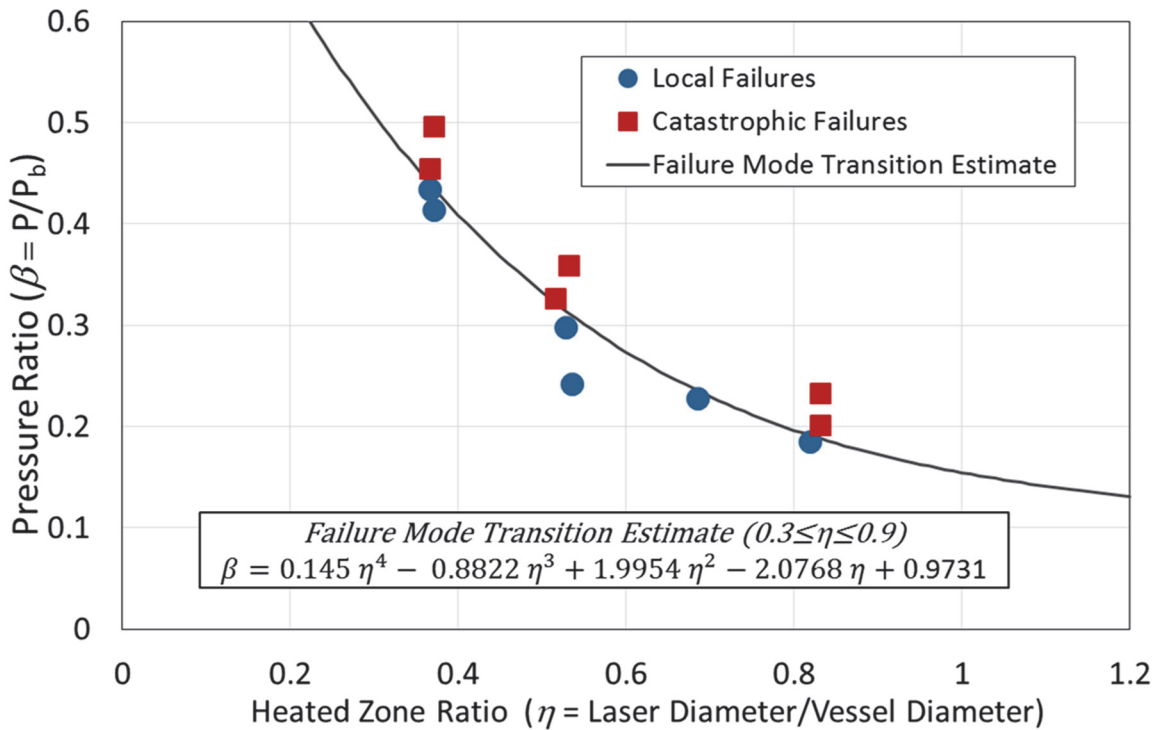


Figure 7.29: Failure mode transition estimate for heated pressure vessels

In addition to the failure mode transition estimate, the experiments also provided the irradiance distribution, temperature history, pressure history, failure time, and failure temperature to be used for validation comparisons.

7.1.5 Pressure Vessel Test Summary

Twelve pressure vessels were successfully heated until failure at different initial pressure conditions and heated zone sizes. The experiments were successful in identifying the failure mode transition at three different heated zone sizes with pressure ratios corresponding to factor-of-safety values in the range of 2 to 5. To the author's knowledge, this data is the first-of-its-kind for identifying the failure mode transition in DSS pressure vessels due to localized heating. A polynomial equation was developed for estimating the critical heated zone ratio as a function of operational pressure ratio where the failure mode transitions from local to catastrophic failure. The normalized quantities enable extrapolation to other materials and geometries, although additional experiments are needed to validate this concept.

The pressure vessel experiments also provided key measurements and diagnostics to enable PDM model validation. The in-situ total power and beam profile measurements were captured such that the spatial and temporal irradiance distribution could be quantified for the thermal model input. The rear surface temperature was captured with a large array of thermocouples, enabling the temperature history and distribution to be compared with heat transfer simulations. In addition, the peak surface temperature at failure can be estimated from the thermocouple data and used as a validation metric. The

pressure history was measured via pressure transducer, providing both the mechanical load for the coupled thermal-mechanical simulation and the failure time which will be used as a validation metric. The failure process was captured via high speed and standard video which enables comparison of the crack morphology. Further description of the model comparison is provided in the following section.

7.2 Pressure Vessel Validation Models

The pressure vessel experiments provide a unique dataset for simulating a complex thermal-mechanical response, representing a more stressing case for simulating crack initiation and propagation than previous models of the uniaxial tension panel experiments. The loading conditions are relatively simple yet provide a progression in complexity from the panel experiments, presented in Chapter 6, to a biaxial stress state which evolves into a more complex three dimensional stress state as bulging occurs in the heated zone due to internal pressure loads and thermal expansion. In addition, multiple failure modes can occur depending on the heated zone size whereas a complete failure and separation was always observed in the panel experiments. The pressure vessel experiments will be used here to validate the PDM model for failure predictions under complex thermal and mechanical loading, specifically whether the failure mode transition can be captured. The PDM model will also be evaluated for predicting failure time and temperature with no modification to the material model defined in Chapter 5.

7.2.1 Pressure Vessel Mesh

Similar to the panel test articles, the pressure vessel models were constructed to have the same approximate mesh size (1x1x0.5 mm) as the notched tension specimens for which the PDM model was calibrated. However, meshing the entire cylinder to the specified size would result in a model with approximately 2.5 million elements and lengthy computation times. As a result, transition meshing and shell-to-solid coupling strategies were used to reduce the number of elements and analysis time.

Transition meshing is a strategy for increasing the mesh size along a predefined edge/surface. A transition with a 2:1 ratio (Figure 7.30) was used to minimize the element aspect ratio along the transition, even though strategies for faster transitions could have been used. The TrueGrid meshing software, by XYZ Scientific Applications, simplifies the incorporation of a transition mesh through the use of the keyword “trbb” which describes the transition across block boundaries. The transition is completely automated, provided the user defines the proper ratio of elements along each block boundary interface. TrueGrid also provides a parameterized mesh file which simplifies the modification of geometry and mesh refinement. A comparable mesh would be relatively difficult to generate in Abaqus/CAE, requiring extensive solid partitioning and patterning.

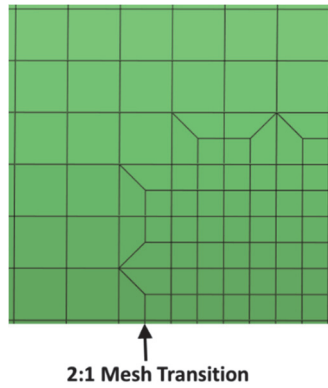


Figure 7.30: Example of 2:1 transition mesh

The cylinder mesh was constructed to maintain the desired size (1x1x0.5 mm) beyond the region of localized heating for the largest beam size used in the experiment. As a result, the first mesh transition was located approximately ± 25 cm from the laser beam center in the axial direction and $\pm 65^\circ$ in the circumferential direction. The first mesh transition increased the mesh size to 2x2x0.5 mm and the second transition further increased the size to 4x4x0.5 mm, as shown in Figure 7.31. The symmetry plane is shown in Figure 7.31 for illustrative purposes however the full pressure vessel geometry was used for the validation simulations due to the asymmetric laser profile.

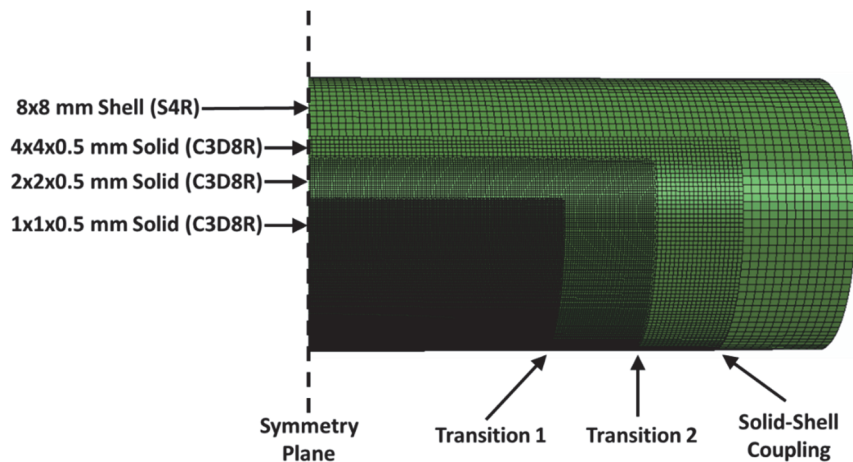


Figure 7.31: Pressure vessel mesh showing the transition mesh and solid-shell coupling locations along with the approximate mesh size

A solid-shell coupling interface was then used to transition the mesh to an 8x8 mm shell element with a virtual thickness of 1.5mm. The shell mesh was constructed to be at the mid-thickness radius of the solid structure, as shown in Figure 7.32. The shell element reference plane was then set to the middle integration point to ensure consistency in the geometry definition.

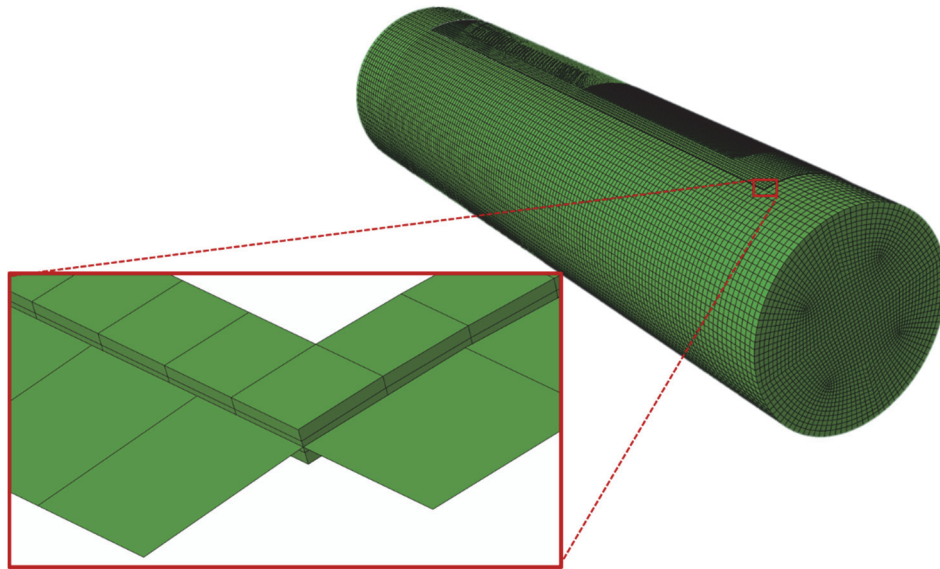


Figure 7.32: Solid to shell coupling interface used to reduce pressure vessel mesh

The shell and solid part instances were then connected using the Abaqus keyword “*Shell to Solid Coupling” which defines the interface connection between the shell edges and the solid face. Using shell elements allowed for the non-critical regions of the pressure vessel to be discretized with only 13,000 elements. The remainder of the pressure vessel, which includes the heat affected zone, was discretized with approximately 500,000 solid elements. The final mesh was approximately 20% of the 2.5 Million elements required to mesh the entire pressure vessel with 1x1x0.5 mm elements,

significantly reducing computational requirements. The complete pressure vessel mesh is shown in Figure 7.33 along with the maximum heated zone size overlaid on the image.

Upon completion of the mesh, the structure was pressurized within the elastic regime to compare the axial and circumferential stress to the analytical solution using shell theory. The numerical results were consistent with the analytical solution which provided confidence in the solid-shell coupling methodology. In addition, no abnormalities were observed in the transition or solid-to-shell coupling regions.

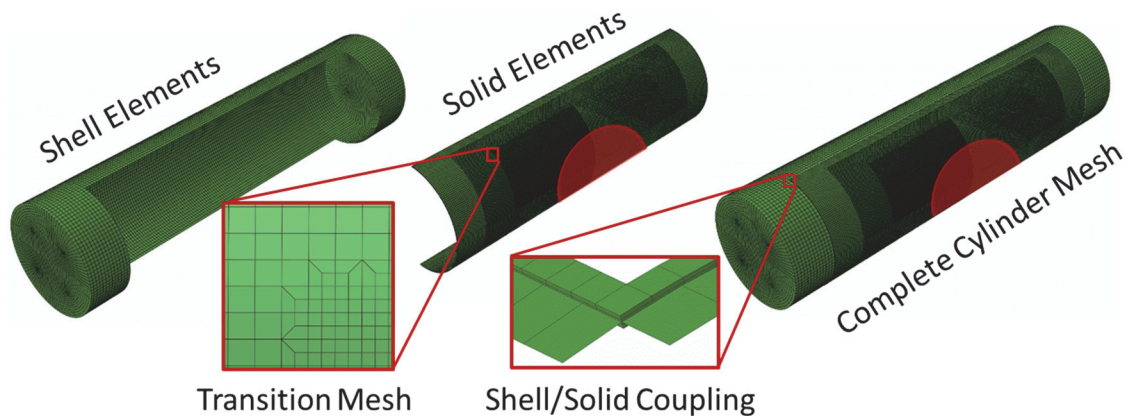


Figure 7.33: Complete pressure vessel mesh with approximate heated zone size

7.2.2 Thermal Model for Laser Heating of Pressure Vessels

Similar to the panel validation models, the temperature state of the pressure vessel can be considered an input loading condition or forcing function for the thermal-mechanical damage predicted by the PDM model. Since the complete spatial and temporal thermal state cannot be easily measured, ensuring the appropriate thermal state is captured becomes challenging from a validation standpoint. Given the pressure vessel experimental configuration presented in Section 7.1.2, the most reliable thermal

data is provided by the thermocouple array used to measure the temperature of the internal surface. Therefore, the thermal model was correlated to the thermocouple response prior to the thermal mechanical simulation using a similar approach to the panel simulations.

The distribution and absorption of laser energy in the material is critical for correlating the thermal model to the experiment as it drives the temperature change and thermal distribution within the pressure vessel. Fortunately, the SWIR imagery and laser beam power measurements provide a well characterized laser beam irradiance, as shown in Section 7.1.4. Similar to the panel validation models, user subroutines were required to incorporate the laser irradiance distribution in Abaqus. However, the subroutines developed for the panel models were modified to account for the cylinder curvature. When using the flux based loading method in Abaqus, as opposed to energy based methods such as ray tracing, the energy deposition can be inadvertently overestimated on a curved surface.

As the incidence angle between the laser direction and the element surface normal is increased, the total energy applied to the system artificially increases when calculated by the sum of the interpolated surface flux (irradiance) times the element surface area. In order to account for this discrepancy the so-called “cosine correction” is applied to the irradiance to maintain a consistent laser energy when applied to curved surfaces. Figure 7.34 shows a graphical representation in two dimensions for the cosine correction. I_o and L_o represent the interpolated irradiance and projected length in the beam plane, respectively. I_e and L_e represent the effective irradiance and effective area

on the element plane, respectively. The effective irradiance can be determined by equating the energy in both the beam and element planes which results in a cosine correction using the angle between the laser beam direction and element surface normal.

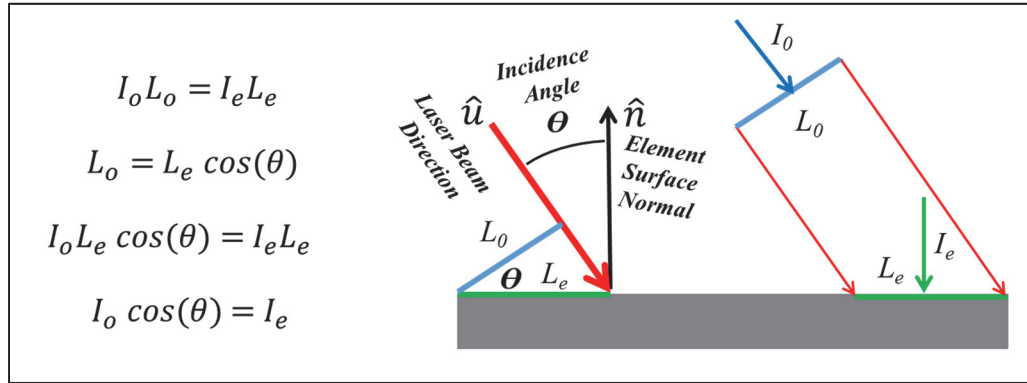


Figure 7.34: Cosine correction for flux based energy deposition for elements on a curved surface

The interpolated irradiance, I_o , cosine correction and effective irradiance, I_e , can all be preprocessed in the subroutine UXTERNALDB and passed to the DFLUX subroutine using a common block, provided the beam is temporally and spatially stable. Otherwise, the surface normal can be processed in UEXTERNALDB and the effective irradiance calculation must be performed in DFLUX at every solver increment. An example subroutine is provided in Appendix C.1 which can accommodate temporally stable axisymmetric beam profiles. A more general subroutine was used to simulate the pressure vessel experiments which includes the surface centroid calculation, transformation to the beam plane, and inverse distance weighting interpolation scheme.

The thermal analysis was performed using the modified user subroutine to apply the cosine correction to the measured laser profile prior to depositing energy on the cylinder surface. The thermal analysis was only performed on the solid elements since

the shell elements were outside of the heated zone where no heat transfer was anticipated. During the thermal-mechanical analysis the shell elements were then initialized to the ambient temperature, providing a consistent temperature across the solid-shell coupling interface. An example heat transfer input file can be found in Appendix C.2.

Example results from the Abaqus heat transfer simulations are shown in Figure 7.35 for three different laser beam sizes, color-coded to the nodal temperature (NT11). The non-uniform heat flux was applied using the custom subroutines which is evident in the thermal solution provided at the first time increment. The laser beam profiles were shown previously in Figure 7.16, with the intermediate beam size (Test #4) having the least number or irregularities. However, the thermal contours become relatively smooth by the last increment due to thermal diffusion, even when considering the largest laser beam profile (Test#11) which has a higher number irregularities.

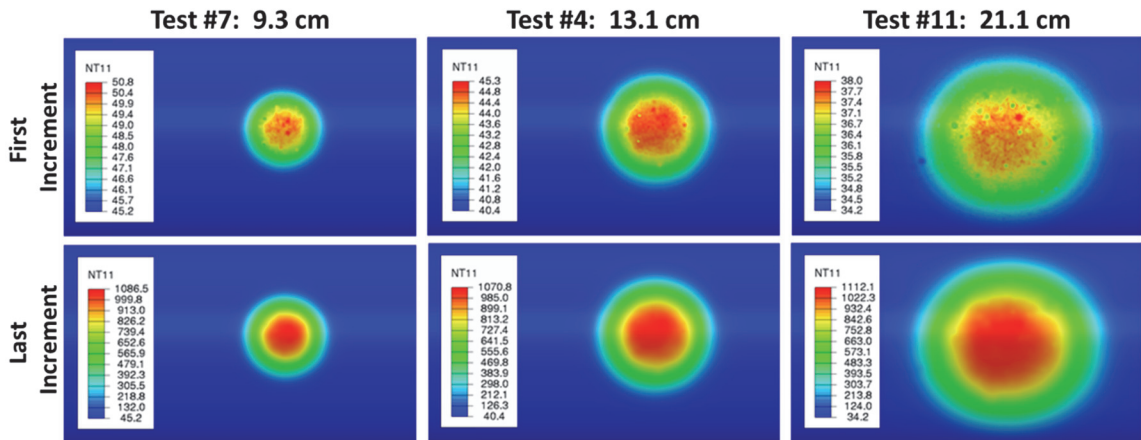


Figure 7.35: Thermal contours from the Abaqus heat transfer analysis of 3 pressure vessel experiments with various laser beam sizes, shown after the initial increment and final increment of the analysis

In order to compare the Abaqus solution to the experiments, a python script was written to extract the temperature history of nodes in the vicinity of the interior thermocouple locations. An example python script is provided in Appendix C.3. The thermal solution was then used to adjust the temperature dependent surface absorption to capture the peak rear-surface thermocouple history, using a similar approach to the panel simulations. A comparison of the peak thermocouple trace (TC-15 and TC-16) and the Abaqus thermal solution is provided in Figure 7.36 for test #4. In addition, the complete set of thermocouple data (solid colored lines) is plotted against the corresponding nodal temperature histories (dashed black lines) from the Abaqus thermal model.

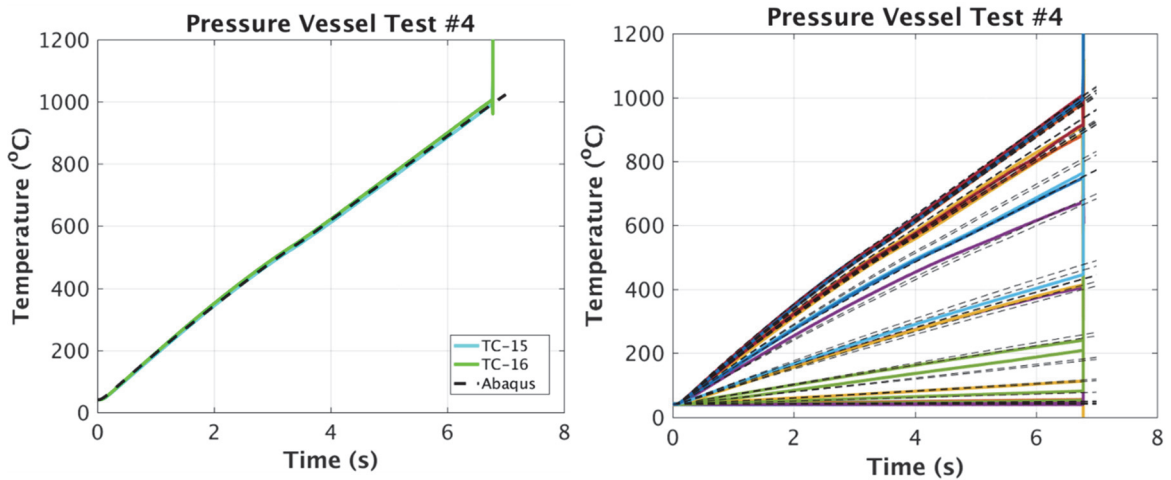


Figure 7.36: Temperature history comparison between thermocouple readings and Abaqus thermal model results

While the general trends seem to be captured in the Abaqus solution, it can be difficult to conduct a comparison of the spatial distribution from the temperature histories alone. In order to improve the spatial comparison, the nodal temperatures were extracted from the Abaqus model along an axial path at several times throughout the

heating process. The thermocouple measurements were then extracted along the centerline of the grid pattern and compared at corresponding times, as shown in Figure 7.37 for test #4.

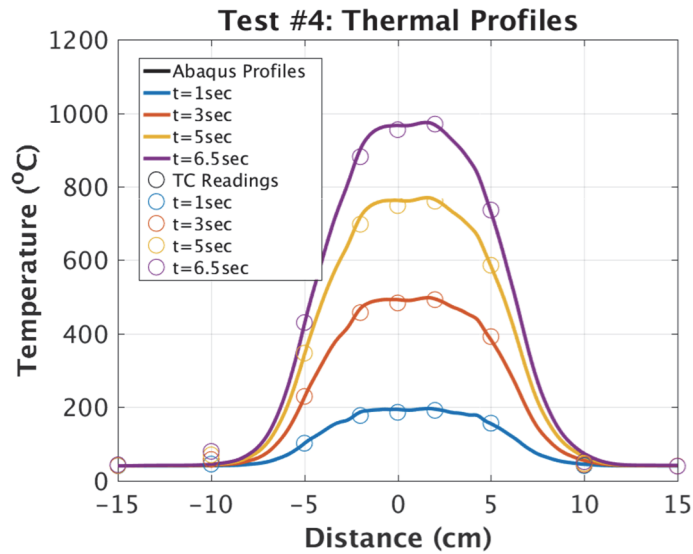


Figure 7.37: Comparison of the Abaqus thermal profile and the thermocouple measurements along an axial path at various times in the heating process for pressure vessel test #4

The model captures the temperature distribution well, however some discrepancies exist near the extents of the beam profile. Overall it provides confidence in the spatial and temporal thermal solution which will be used for the sequentially coupled thermal-mechanical simulation. Similar comparisons are shown in Figure 7.38 for tests #7.

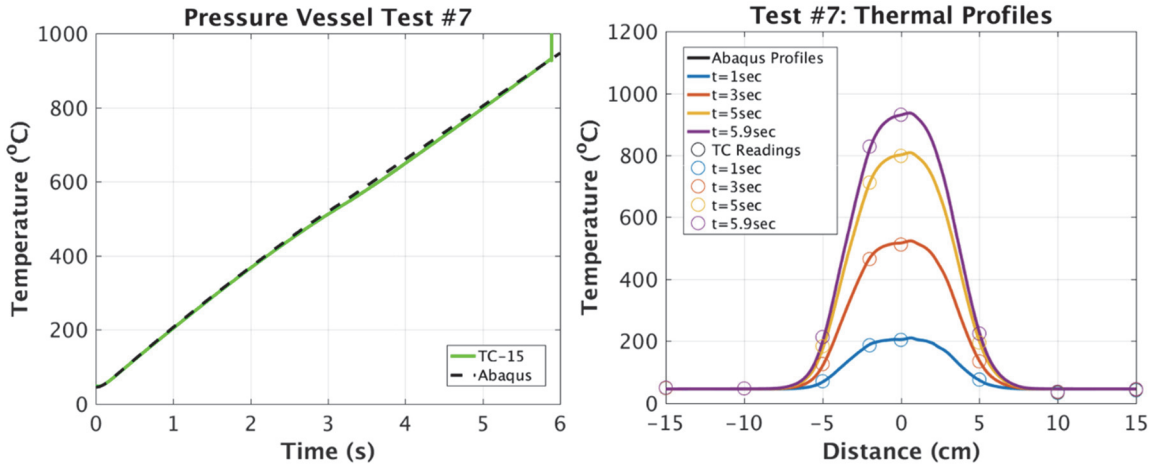


Figure 7.38: Temperature history and thermal profile comparison between the Abaqus thermal solution and thermocouple measurements for test#7

Test #7 had the least number of thermocouples in the heated zone due to the size of the laser beam diameter (9.3 cm). In addition, the thermocouple located at +2 cm (TC-16) failed early in the experiment which further reduced the number of measurements in the heated zone. Nevertheless, the model closely correlates to the thermocouple measurements even for a limited dataset.

The peak temperature history and the thermal profiles for test #11 are provided in Figure 7.39 and Figure 7.40, respectively. Test #11 had the largest beam size (21.1 cm) which resulted in seven thermocouples being located within the heated zone. Again, the Abaqus thermal profile closely correlates to the thermocouple measurements with some small discrepancies near the outer thermocouples located in the high gradient zone (± 10 cm).

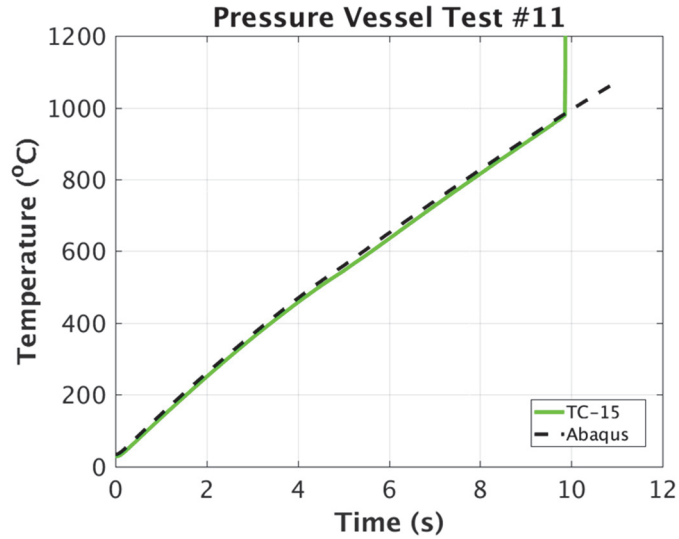


Figure 7.39: Temperature history comparison between Abaqus simulation and center thermocouple trace for test #7

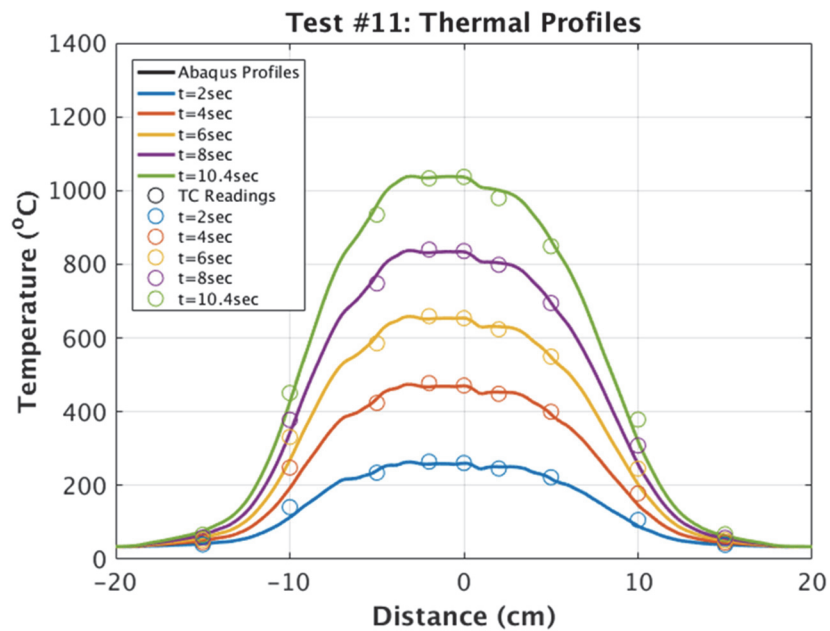


Figure 7.40: Abaqus thermal profile comparison to thermocouple data along an axial path for test #11

A similar process was used for the remainder of the experiments to capture the peak thermal history and evaluate the thermal distribution prior to the mechanical simulations. As previously mentioned, pressure vessel tests 2, 6 and 10 were not analyzed since a catastrophic failure was also achieved using a lower pressure in test numbers 4, 7

and 11. The emphasis was placed on analyzing the test conditions near the transition between local and catastrophic failure modes. For the remaining nine experiments which were analyzed, the optimized absorption curves are provided in Figure 7.41 with a comparison to the absorption curve determined from the TRAM experiment.

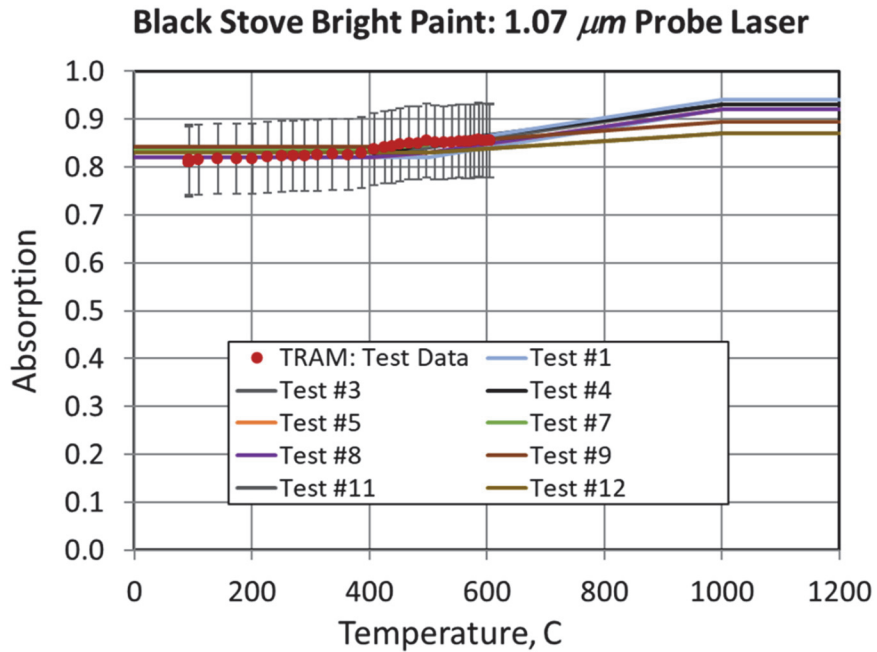


Figure 7.41: Temperature dependent laser absorption used in Abaqus thermal models compared to TRAM data

The absorption curves are all tightly grouped within the uncertainty of the TRAM measurement up to 600°C. The absorption continued to trend up for temperatures above 600°C, reaching values in the range of 87-92%. The optimized pressure vessel thermal models resulted in more consistent absorption curves when compared to the TRAM data than previously seen in the panel simulations. The surface preparation, paint application, and paint batch may have contributed to the variation. Nevertheless, the objective to match the experimentally measured thermal response was achieved in both cases.

7.2.3 Thermal-Mechanical Model of Pressure Vessel Failure

The temporal and spatial thermal solution provides a critical input to the thermal-mechanical simulation where the PDM model will be used for predicting crack initiation and propagation. Since the pressure is nearly constant, the temperature change can be considered the driving condition which induces material softening and ultimately leads to failure of the pressure vessel. The pressure measurement just prior to crack initiation was applied to the internal surface of the cylinder and end caps during the initial loading step. The thermal solution was then applied in a time synchronized manner using the keyword “*Temperature” within each thermal-mechanical load step until material failure occurred. The mass scaling was then progressively reduced as the model approached failure to ensure no mass scaling was applied to the model during the final prediction of crack initiation. A flow chart is provided in Figure 7.42 showing the overall simulation process for a sequentially coupled thermal-mechanical simulation.

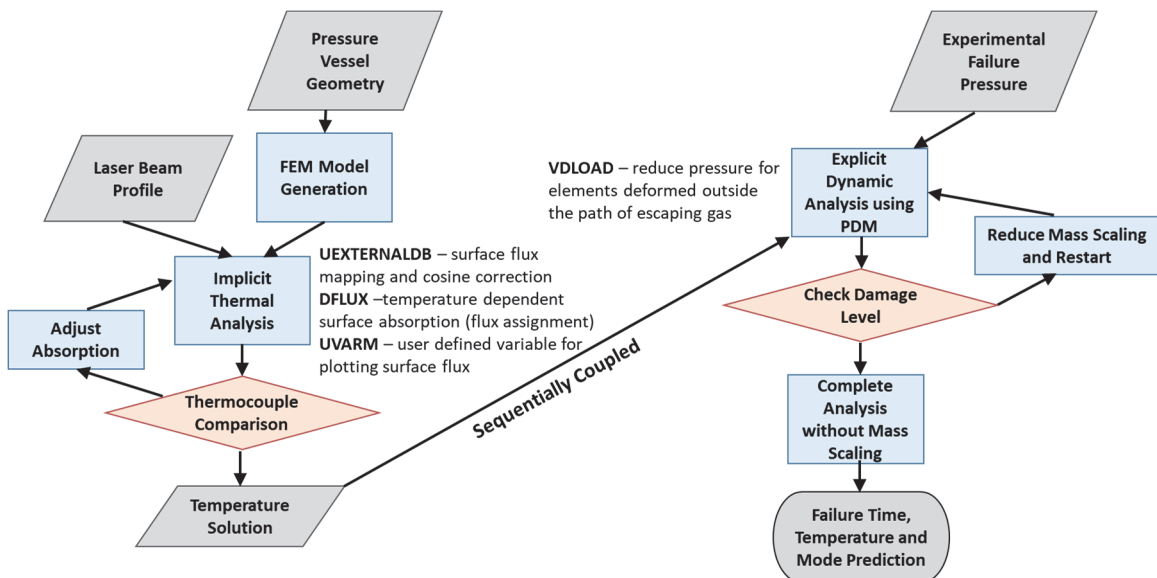


Figure 7.42: Flow chart describing the sequentially coupled thermal-mechanical analysis of pressure vessel failure induced by localized heating

Similar to the panel validation models, mass scaling enabled the pressure vessel simulations to run faster when small deformations and accelerations were occurring early in the analysis. The simulations were then “restarted” from an intermediate solution using a progressively lower mass scaling level. An example modeling sequence is provided in Table 7.3 for Test #7, including the mass scaling level, simulation time, failure time estimate and run time (computation time).

Table 7.3: Example analysis sequence including computation time associated with each mass scaling level

Test #7				
Analysis Type	Mass Scaling	Simulation Time (s)	Failure Time (s)	Run Time (CPU-hrs)
Heat Transfer	N/A	0 - 6.5	N/A	19
Explicit Dynamic	10,000	0 - 6.5	6.2 - 6.3	684
Explicit Dynamic	1,000 - 100	5 - 6.3	6.09	780
Explicit Dynamic	100 - 1	6 - 6.15	6.08	495
TOTAL				1978 CPU-hrs

The total computation time for Test #7 was 1978 CPU-hrs or 82.4 CPU-days, even with transition meshing, shell-solid coupling, and mass scaling used to speed up the computation. The longest simulation time, associated with the lowest irradiance level, was approximately 50% longer at 128 CPU-days. Parallel execution on 8-16 CPU cores allowed for faster wall clock execution but the analysis time was still significant. As a result, the mass scaling approach was a critical aspect of the analysis process outlined in Figure 7.42. In the future, the analysis time may be reduced if Abaqus improves the ability to transition from implicit to explicit analysis for a broader range of element types and model features.

The Abaqus subroutines utilized in the implicit thermal and explicit dynamic solvers were also critical to analyzing the pressure vessel failure, as shown in the flow chart (Figure 7.42) next to the respective analysis blocks. The subroutines for the thermal analysis were discussed in previous sections, therefore VDLOAD is the only new subroutine introduced for this analysis. The surface based pressure load in Abaqus is applied in the direction normal to the surface, even as the element deforms, causing unrealistic loads once the surface is no longer in the path of escaping gas. Due to this limitation, the pressure was reduced using the VDLOAD subroutine for elements which deform such that the surface normal is greater than 90° from the laser direction. Using this simple approach provides a more realistic load on the failure surface without the inclusion of gas dynamics. An example of a predicted local failure with and without the VDLOAD subroutine is shown in Figure 7.43 in comparison to a local failure observed in the experiment.

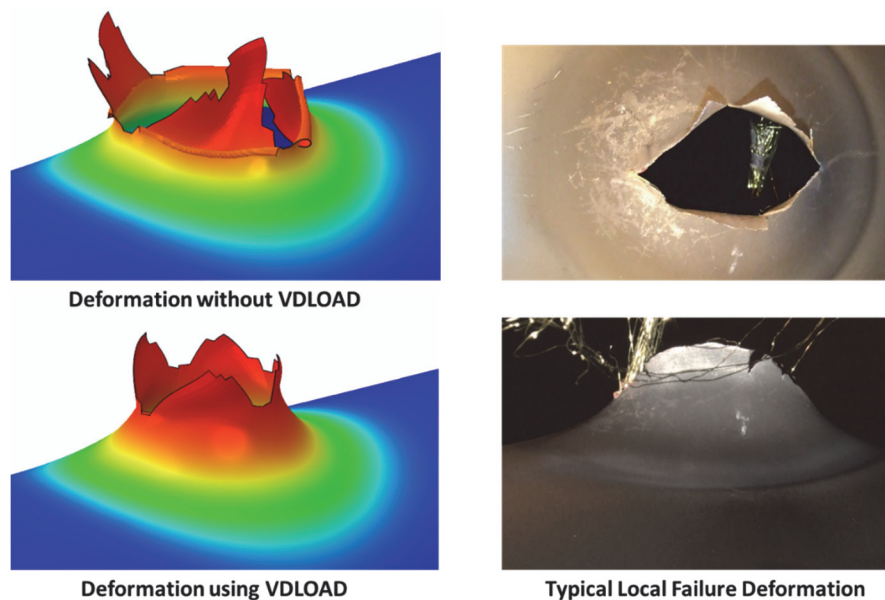


Figure 7.43: Example of a local failure prediction with and without the use of VDLOAD compared to a typical failure observed in the experiments

The simulation without the VDLOAD subroutine shows the failure surface deforming backward and through the cylinder before wrapping around itself. The deformation through the cylinder surface is unrealistic and could be prevented with the inclusion of a general contact scheme. However, the underlying cause of the unrealistic deformation is related to the pressure load “following” the surface as it deforms outward. The inclusion of the VDLOAD routine reduces the pressure loads on the failure surface as the normal vector approaches 90° from the laser direction, improving the correlation with the final deformed shape. Interestingly, the inclusion of VDLOAD had no impact on the failure mode prediction since the crack would typically arrest or propagate out of the heated zone before the surface normal reached the point where pressure was reduced.

The predicted failure time, temperature and mode for each experiment is provided in Table 7.4, showing close correlation with the experiments. The majority of the cases were within 4% in failure time and temperature with the exception of test #8 which had a difference of 5.4% in failure time. In addition, the predicted failure mode was matched for all cases except Test #12. However, test #12 was performed using a test article which was previously heated to approximately 500°C, as discussed in section 7.1.4. The simulation of Test #12 will be discussed in more detail later in this section.

Table 7.4: Comparison of Abaqus failure predictions using PDM with experimental results

Test #	Peak Irradiance (W/cm ²)	Laser Diameter 1/e ² (cm)	Pressure (psig)	Experimental Failure Time (s)	PDM Model Failure Time (s)	Time Difference	Experimental Failure Temp. (°C)	PDM Model Failure Temp. (°C)	Temp. Difference	Experimental Failure Mode	PDM Model Failure Mode
1	113.9	13.6	362	8.14	7.94	-2.5%	1092	1064	-2.6%	Local	Local
3	105.7	13.4	444	7.43	7.70	3.6%	1005	1021	1.6%	Local	Local
4	118.8	13.1	487	6.79	6.68	-1.6%	1007	982	-2.5%	Catastrophic	Catastrophic
5	122.2	9.4	617	6.81	6.99	2.6%	1014	1022	0.8%	Local	Local
7	125.8	9.3	678	5.89	6.08	3.2%	931	959	3.0%	Catastrophic	Catastrophic
8	126.5	9.3	648	6.35	6.69	5.4%	990	1016	2.6%	Local	Local
9	119.9	17.4	340	7.14	6.86	-3.9%	1012	979	-3.3%	Local	Local
11	83.3	21.1	300	10.46	10.31	-1.4%	1040	1019	-2.0%	Catastrophic	Catastrophic
12	80.6	20.8	276	11.13	10.89	-2.2%	1034	1013	-2.0%	Local	Catastrophic

The pre-test prediction for the failure mode transition was shown to be higher than the experimental results (Figure 7.11). However, the post-test analysis using reduced mass scaling along with the measured beam profile and internal pressure significantly improved the correlation with the experiment. Removing mass scaling prior to crack initiation led to an increased likelihood of a local failure near the transition line. In addition, using the measured beam profiles led to more realistic thermal profiles for experiments where hot spots were observed.

The crack initiation location and propagation path were sensitive to the localized hot spots, as shown in Figure 7.44 for Test #9. The crack initiates in a location offset from the center of the heated zone toward a localized hot spot. The crack then propagates into the center of the hot spot as it also propagates across the heated zone to a second hot spot on the opposite side. The crack is arrested on both sides of the heated zone as it approaches the cooler material, as seen in the experiment and simulation. The predicted crack shape is not as sharp as the experiment due to the element deletion method used to initiate and propagate the crack, similar to the findings for the panel tests.

However, the crack initiation location and general crack morphology are comparable. The ability of the PDM model to capture arresting of the crack is particularly notable.

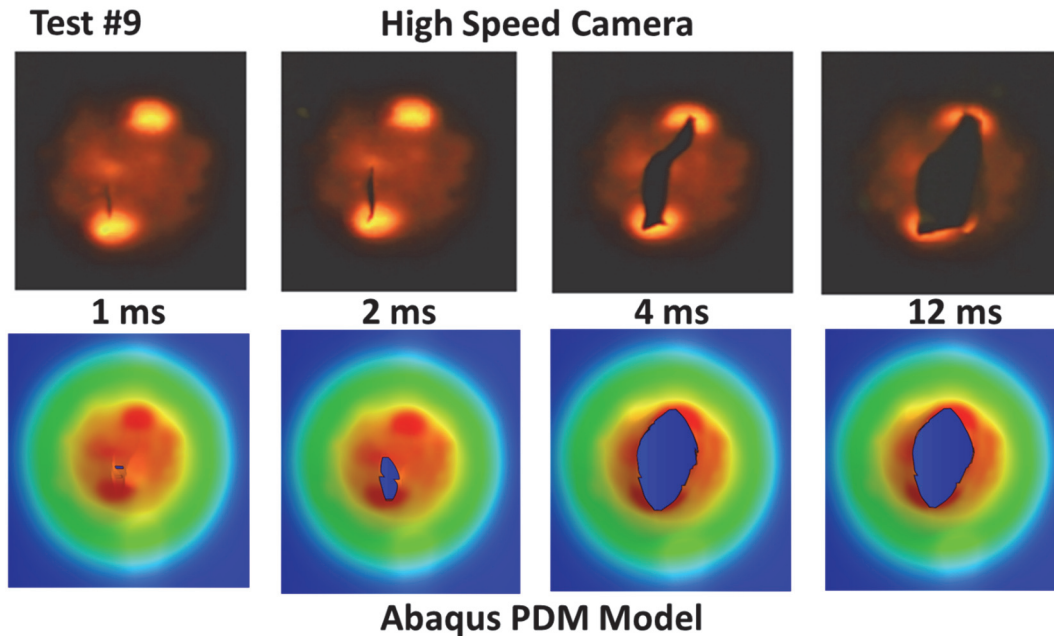


Figure 7.44: Test #9 fracture comparison between high speed video and Abaqus predictions (temperature contours)

The temperature, Mises stress, equivalent plastic strain, damage imitation criteria, and damage variable contours are shown in Figure 7.45 - Figure 7.49, respectively. The peak temperature at failure for the entire model is approximately 1053°C, as shown in Figure 7.45, which is slightly above the highest temperature for which the PDM model was calibrated (1000°C). However, the material has very low strength and high ductility in this temperature range. The failure temperature reported in Table 7.4 (979°C) corresponds to the rear surface of the pressure vessel in the location of the peak thermocouple reading.

Test #9: Temperature (°C)

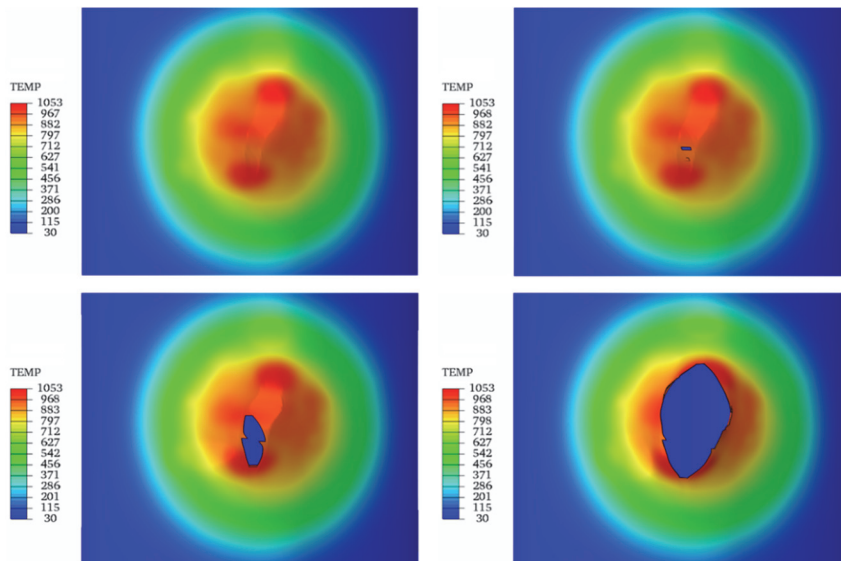


Figure 7.45: Temperature contours for Test #9 during failure

The Mises stress contours (Figure 7.46) reveal that the highest stress is actually near the edge of the heated zone. As the material is heated the strength decreases and the material above 600°C becomes more ductile, resulting in a radial bulge due to internal pressure. The stress redistributes around the heated zone causing the stress to be largest near the edges. However, the equivalent plastic strain contours (Figure 7.47) clearly show strain localization parallel to the pressure vessel axis in a narrow region connecting the hot spots through the central portion of the heated zone. This response is reasonable considering a limited amount of strain hardening was observed at 800°C and above (Figure 4.12). The crack then initiates and propagates across the localization zone until the crack is finally arrested as it reaches the cooler material.

Test #9: Mises Stress (N/m²)

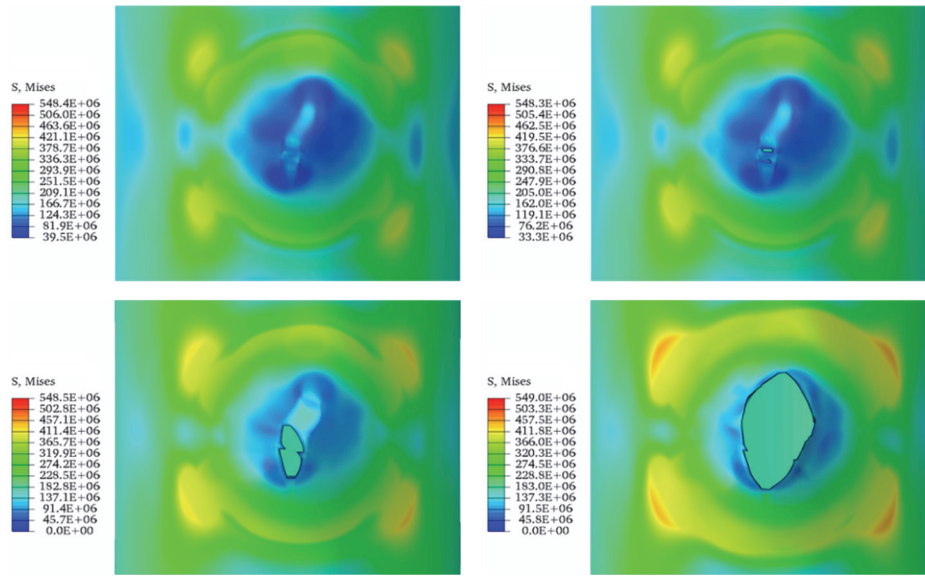


Figure 7.46: Mises stress contours for Test #9 during failure

Test #9: Equivalent Plastic Strain (m/m)

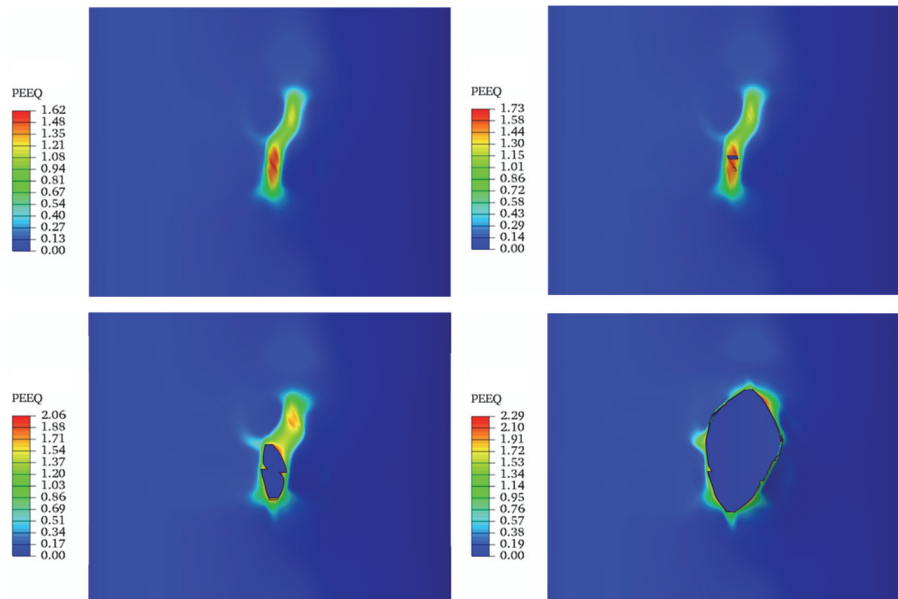


Figure 7.47: Equivalent plastic strain contours for Test #9 during failure

Since damage initiation is directly proportional to the plastic strain and stress triaxiality, the contours for the initiation criterion (Figure 7.48) are very similar to

equivalent plastic strain. As the crack initiates, the Mises stress and triaxiality begin to increase near the crack tip which in turn increases the damage initiation criterion.

Test #9: Damage Initiation Criterion, ω_D

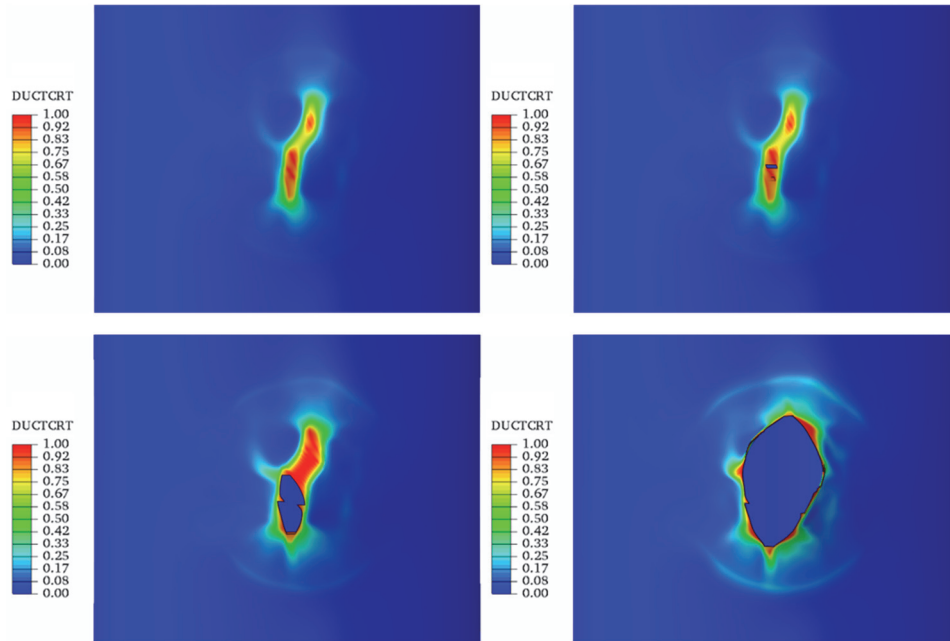


Figure 7.48: Damage initiation criteria contours for Test #9 during failure

The damage variable (Figure 7.49) does not follow the same trend as the initiation criterion since damage does not accumulate until the criterion is met. Furthermore, the damage tends to increase rapidly near the crack tip and the element is removed once the damage variable reaches unity which only leaves a sparse number of elements which have both met the damage criterion and are below the element removal threshold.

Test #9: Damage Variable, D

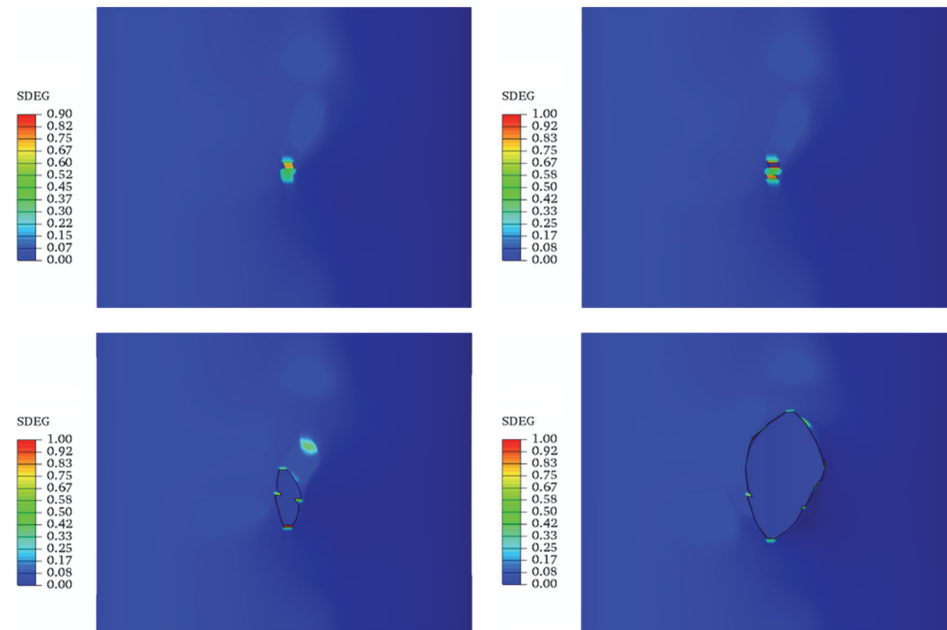


Figure 7.49: Damage variable contours for Test #9 during failure

The PDM approach proved to be capable of modeling the crack initiation and propagation in Test #9 and was remarkable in its ability to predict arresting of the crack, leading to a local failure prediction. Similar results were also achieved for tests 1, 3, 5 and 8 as highlighted in Table 7.2. This is the first known capability to predict local failure in un-cracked pressure vessels and pipelines due to localized heating to be presented in the literature, which has historically focused on the criticality of existing cracks under ambient conditions.

The ability to predict the transition to a catastrophic failure was also demonstrated, as shown in Figure 7.50 for Test #4. The crack tended to propagate faster for conditions where a catastrophic failure was achieved and the crack was not arrested as it exited the heat affected zone. The crack propagated to the end flanges before

turning along the circumferential weld line. The images in Figure 7.50 show a comparison at two instances in time during the failure. The high speed camera was saturated for many of the early shots which only made it possible to view/estimate the crack shape for a few select frames. The high speed imagery was improved for later experiments by using a narrow line notch filter. Nevertheless, the comparison was reasonable for Test #4 and the simulation led to a catastrophic failure prediction.

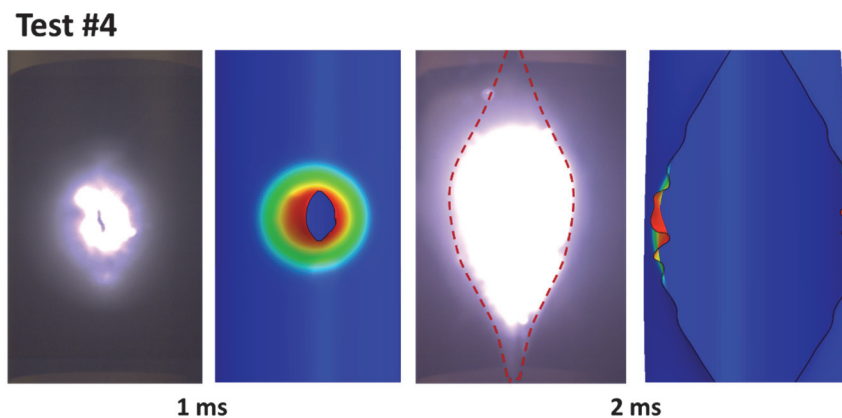


Figure 7.50: Comparison of failure response between the experiment and PDM simulation for Test #4

The temperature, Mises stress, equivalent plastic strain, damage initiation criteria, and damage variable contours are provided in Figure 7.45 - Figure 7.49, respectively. Again, the peak temperature at failure for the entire model is approximately 1022°C, as shown in Figure 7.51Figure 7.45, which is slightly above the highest temperature for which the PDM model was calibrated (1000°C). The failure temperature reported in Table 7.4 is 982°C which corresponds to the rear surface of the pressure vessel in the location of the peak thermocouple reading.

Test #4: Temperature (°C)

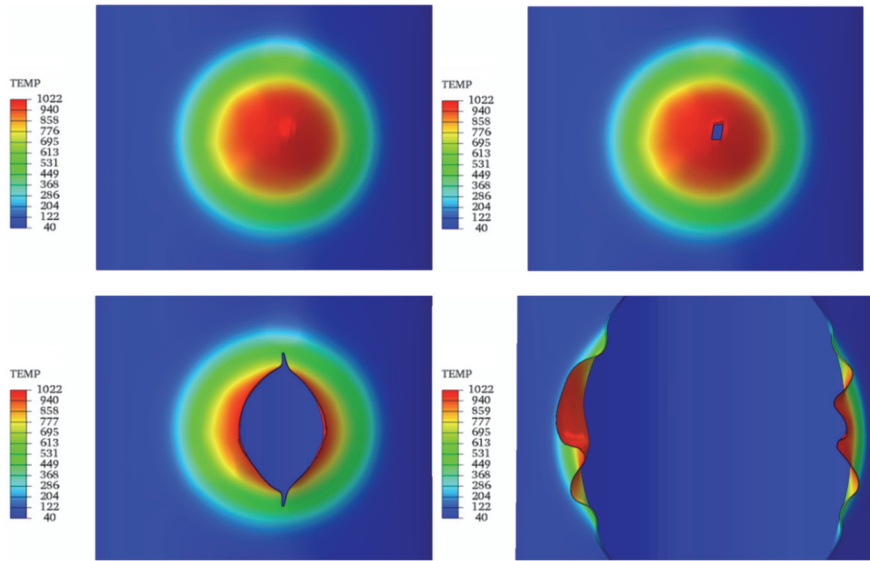


Figure 7.51: Temperature contours for Test #4 during failure

The predicted crack becomes sharper as it exits the heated zone since the fracture strain decreases substantially as the material approaches 400°C (Figure 4.15). The stress also becomes noticeably more concentrated near the crack tip in the lower-left image of Figure 7.52.

Test #4: Mises Stress (N/m²)

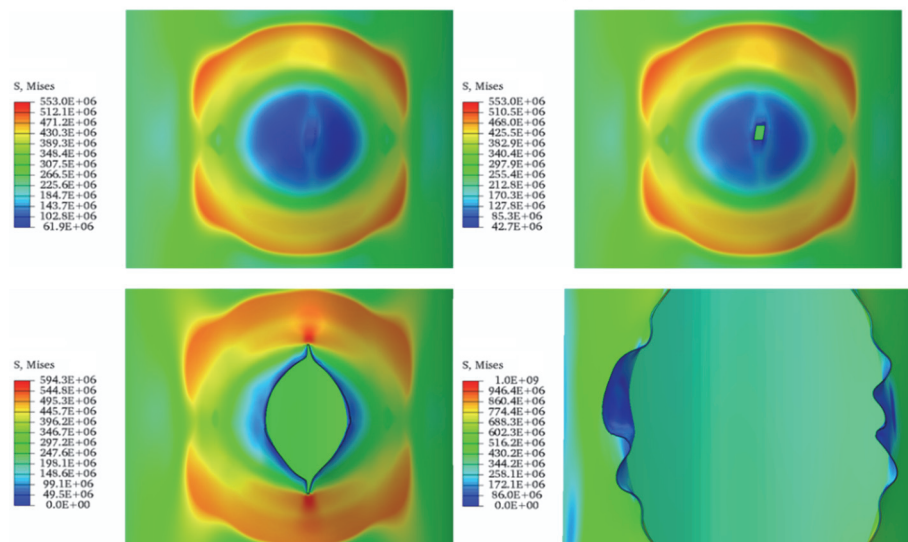


Figure 7.52: Mises stress contours for Test #4 during failure

Similar to the local failure, the strain tends to localize in the direction parallel to the axial direction since the stress is higher in the hoop direction and local bulging occurs due to internal pressure. The crack continues to propagate outside the original localization zone and the effective plastic strain at failure is reduced as it approaches the edge of the heated zone.

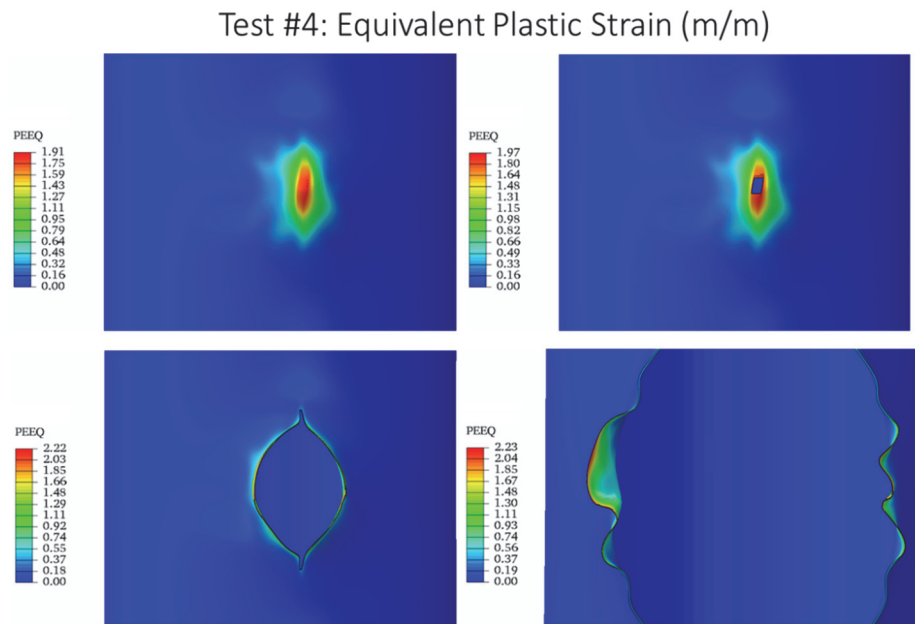


Figure 7.53: Equivalent plastic strain contours for Test #4 during failure

The damage initiation criterion is shown in Figure 7.54 to be higher near the edge of the heated zone than previously seen for the local failure (Figure 7.48). The higher pressure ratio leads to greater stress redistribution and higher plastic strain near the edge of the heated zone which in turn increases the likelihood of damage onset prior to the crack tip reaching the edge. The lower-left image of Figure 7.54 shows the crack tip interacting with the circular shaped region where the damage initiation criterion was nearly 60% prior to crack initiation.

Test #4: Damage Initiation Criterion, ω_D

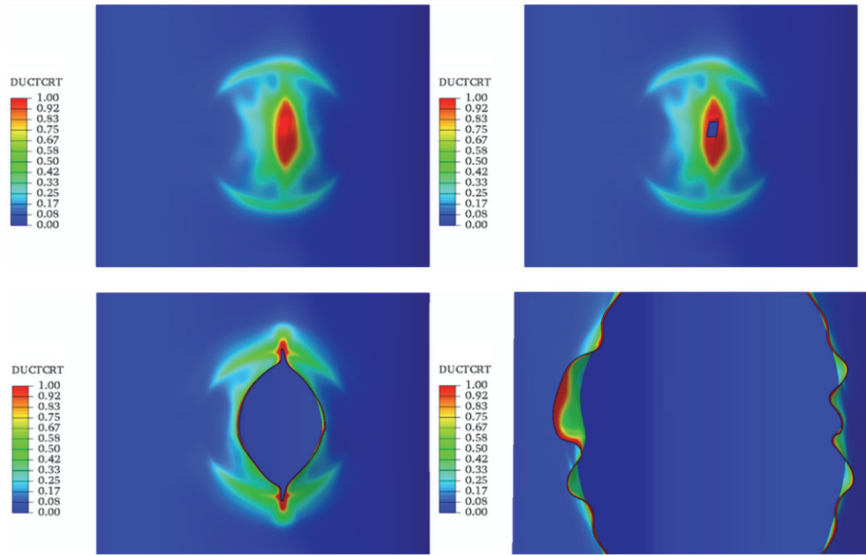


Figure 7.54: Damage initiation criterion contours for Test #4 during failure

The corresponding damage variable is similar to the local failure case, where only a sparse number of elements have both met the damage criterion and are below the element removal threshold.

Test #4: Damage Variable, D

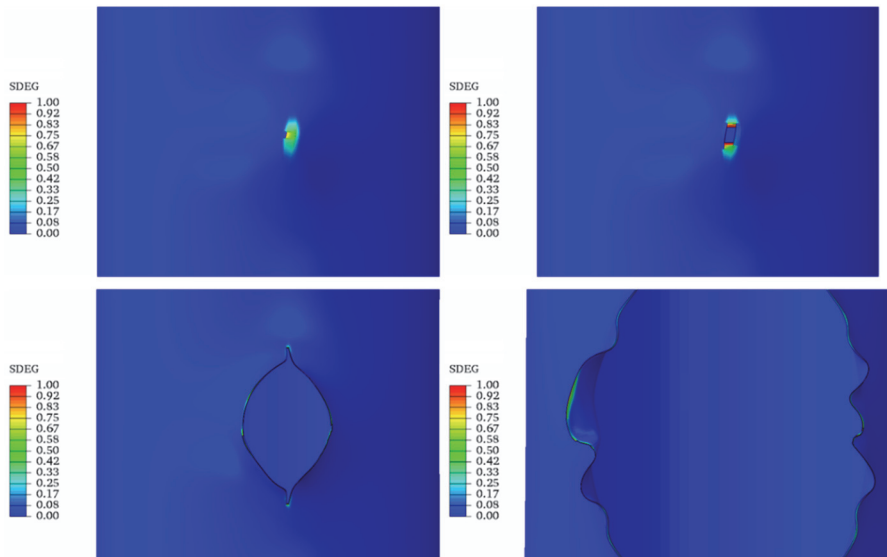


Figure 7.55: Damage variable contours for Test #4 during failure

The PDM approach proved to be capable of modeling the crack initiation and propagation in Test #4, leading to a catastrophic failure prediction. Similar results were also achieved for tests 7 and 11 as highlighted in Table 7.2. These results further validate the PDM approach for predicting the failure time, failure temperature and failure mode transition in pressure vessels and pipeline subjected to localized heating.

However, the model did not capture the failure mode for test #12 even though the failure time and temperature were predicted within 2% of the measurements. The predicted and experimental failure response of Test # 12 are compared in Figure 7.56. The high speed imagery is slightly more zoomed than the simulation results but the crack appears to initiate in a similar location. Then a secondary crack forms before coalescing and propagating toward the edge of the heated zone. The crack propagates faster in the simulation than observed in the experiment, although slower than the catastrophic failure in Test #4. Interestingly, the predicted crack slows significantly as it reaches the edge of the heated zone and only propagates a small distance between 1 ms and 4 ms. This indicates the crack was nearly arrested before finally propagating along the entire pressure vessel by 6 ms. As a result, the conditions associated with Test #12 were assessed to be very close to the true failure mode transition line where greater statistical variability can be expected.

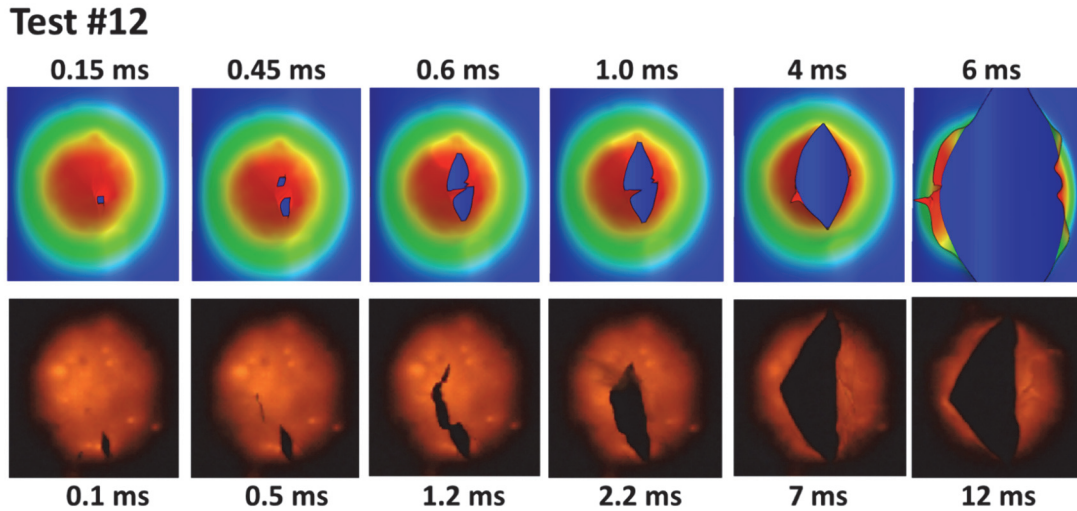


Figure 7.56: Comparison of failure response between the experiment and PDM simulation for Test #12

In order to evaluate the model sensitivity, two additional simulations of Test #12 were performed. One simulation used a 2% smaller laser beam profile and one used a 2% lower pressure ratio. A local failure was predicted for both cases, indicating the conditions for Test #12 were indeed very close to the predicted failure transition line. In addition, Test #12 was performed using a test article which was previously heated to approximately 500°C, as discussed in section 7.1.4, which may have also played a role in the failure mode difference. Nevertheless, the PDM approach captured the failure response well for all of the validation metrics (time, temperature and failure mode) and the one outlier was very close to the predicted failure mode transition line.

7.2.4 Pressure Vessel Validation Modeling Summary

A sequentially coupled thermal-mechanical model for predicting failure of rapidly heated pressure vessels was developed in Abaqus using the calibrated PDM model presented in Chapter 5. Modeling strategies such as mass scaling, transition meshing and

shell-to-solid coupling were used to speed up computations while maintaining the calibrated element size in the heat affected zone. Customized user subroutines (UEXTERNALDB, DFLUX, USDFLD, VDLOAD) were created to apply the spatially non-uniform flux profile onto the curved surface of the pressure vessel and to reduce the pressure loads on the failure surface as it deformed outside the path of escaping gas.

The PDM based approach for simulating elevated temperature fracture in uncracked bodies was then validated for predicting the failure time, temperature and mode within approximately 5% for the failure of pressure vessels subjected to localized heating. The model was able to simulate local failure conditions that lead to arresting of the crack near the edge of the heated zone as well as conditions that lead to unsteady crack growth and catastrophic failure. To the author's knowledge, this is a first-of-its-kind capability for predicting the failure mode transition in pressure vessels due to localized heating. Based on these results, the model could be expanded to evaluate pressure vessels or pipelines containing liquid propane or crude oil products to evaluate hazards during refinery, oil platform, tanker or ship fires. The method could also be used to evaluate the criticality of thermal protection system damage.

Chapter 8 : Summary and Recommendations

8.1 Summary

The research presented in this dissertation led to the characterization of elevated temperature thermo-physical properties for duplex stainless steel; including specific heat, thermal diffusivity, optical absorption and coefficient of thermal expansion. The density, Poisson's ratio, chemical composition and micro-structural analysis for phase determination were also measured.

Elevated temperature tensile tests were conducted using various isothermal conditions and edge notched tensile specimen geometries to examine the temperature dependency of material stiffness, yield strength, ultimate strength, and hardening response of DSS as it approaches failure. A unique experimental method using broadband InfraRed heating was developed to enable deformation measurements in the localization zone, using digital image correlation, that could not otherwise be achieved using resistive or furnace heating. The effect of temperature and stress triaxiality associated with the two different notch radii were captured in the experiment, including the post-peak response of the specimens as diffuse and localized necking occurred. The thermal embrittlement near 475°C, associated with the decomposition of ferrite and increased tendency for precipitation of nitrides and carbides, was also captured.

The conjugate fracture surfaces were evaluated using the FRASTA technique which revealed the micro-void formation and failure propagating from the area with the

highest confinement in the center of the sample toward the sample edges. The uncertainty in the cross-sectional area, associated with bow-tie deformation in the rectangular cross-sections, was also quantified using SEM images of the final deformed shape. The experimental uncertainties in the load and deformation measurements were also characterized.

A comprehensive literature review was conducted for ductile failure modeling techniques both at ambient and elevated temperature conditions. A large number of approaches were identified in the literature with varying degrees of success for simulating ductile fracture. In some instances, relatively unsophisticated phenomenological models were found to outperform more complicated approaches based on dislocation mechanics and void growth. The Continuum Damage Mechanics approach to fracture was identified in the literature as being capable of predicting ductile fracture using a relatively simple phenomenological formulation which could be expanded to include the effect of temperature. The literature also revealed limited information on elevated temperature failure models and even less model validation. In this dissertation, the objective was to fill the gap in the literature by characterizing an elevated temperature CDM model for ductile DSS and validate the model for predicting failure time, failure temperature, crack initiation and propagation in elevated temperature environments with high thermal gradients.

The Progressive Damage Model in Abaqus was selected and characterized to estimate the onset of material damage as a function of temperature and stress triaxiality. The evolution of damage as a function of temperature and effective plastic displacement

was then calibrated to match the load-displacement response of both the C-Notch and V-Notch specimens. The loss in load carrying capacity during diffuse and localized necking was captured, providing a first-of-its-kind capability for simulating crack initiation and propagation in initially un-cracked bodies constructed of duplex stainless steel.

Validation experiments were then conducted using panel specimens under constant uniaxial tensile load and irradiated by a laser source to induce spatial and temporal thermal gradients. The pre-load and heating rates were varied to induce different failure times and temperatures. The PDM model was then used to analyze the experimental conditions with excellent agreement for the crack initiation location, failure displacement, load, and temperature. However, the crack morphology was not as representative due to the element deletion method used in this study, particularly in regions where temperatures exceeded 800°C.

The second validation experiment was used to evaluate the predictive capability for pressure vessel failure during rapid heating. The catastrophic failure of pressure vessels subjected to accidental fire can be very destructive when a boiling liquid expanding vapor explosion (BLEVE) occurs, resulting in a significant hazard for industrial fires in petroleum and chemical processing plants, among others. The experiments were designed to identify the critical pressure ratio when the failure mode transitions from a local to catastrophic failure for a given heated zone size, providing insight into the criticality analysis of thermal protection system failure. The tests resulted in an empirical correlation between critical pressure ratio and heated zone ratio for potential application to other geometries and materials.

The PDM model was capable of predicting the failure time, temperature and failure mode transition. Most notably, the model was able to capture the crack arresting near the edge of the heated zone for conditions leading to local failures. This is the first known capability to be presented in the literature for predicting local and catastrophic failure in un-cracked pressure vessels and pipelines due to localized heating, which has historically focused on the criticality of existing cracks under ambient conditions.

8.2 Recommendations and Future Work

Although the research presented in this dissertation was largely successful, there are several recommendations for improvements. Ideally, each experiment would have been repeated multiple times to allow for characterization of the statistical variation in the material response. The uncertainties characterized in this dissertation primarily focus on measurement uncertainties with no consideration for random uncertainty associated with test-to-test variation. Furthermore, propagating the uncertainties through the damage characterization and validation simulations would provide a better understanding of the prediction variability. Although this would take a significant amount of computation time given the analysis time required for each pressure vessel simulation.

In addition, the notched tensile specimen experiments could have been improved with the inclusion of a high temperature extensometer for a redundant measurement of the shoulder displacement. Although the digital image correlation method was required for capturing area reduction, an additional measurement of the axial displacement would have been beneficial. In addition, the MWIR and high speed cameras were saturated in a

number of the experiments which could have been avoided by using calibration experiments to identify the appropriate filters. Since the MWIR camera was often saturated for the panel experiments it would have been useful to have an array of thermocouples similar to the approach used in the pressure vessel experiments. Otherwise, the majority of the measurements were satisfactory for this study.

Several additional experiments are recommended in order to expand the PDM model to be more generally applicable. A room temperature V-notch specimen should be tested to quantify the change in the damage initiation criterion with higher triaxiality, similar to the experiments conducted at elevated temperatures in this study. In addition, investigation of elevated temperature response should be expanded into a wider range of triaxiality ratios, strain rates and lode angles. An elevated temperature butterfly specimen experiment may be the most feasible approach for sheet material.

Given the successful validation of the PDM model for predicting failure of DSS, the approach should be applied to other metals to evaluate the empirical correlation for failure mode transition which was identified in Figure 7.29 for more general use. The approach could also be applied to realistic system containing liquid or compressed gas with the inclusion of the thermal losses associated with nucleate and film boiling on the interior surface. The change in the failure mode transition and predicted failure times could also be investigated along with the impact of damaged and un-damaged thermal protection systems and coatings. The research presented in this dissertation lays the groundwork for investigating the failure of metals in extreme thermal environments.

REFERENCES

- Alegre, J. M., & Gutierrez-Solana, F. (2004). A Gurson–Tvergaard based model to simulate the fracture of aged duplex stainless steels. *Fatigue & Fracture of Engineering Materials & Structures*, 27(12), 1171-1182.
- Antoun, B. R. (2004). Temperature effects on the mechanical properties of annealed and HERF 304L stainless steel. *Sandia National Laboratories*. SAND2004-3090
- Ashtiani, H. R. R., & Shahsavari, P. (2016). Strain-dependent constitutive equations to predict high temperature flow behavior of AA2030 aluminum alloy. *Mechanics of Materials*, 100, 209–218.
- ASTM E1269. (2005). Standard Test Method for Determining Specific Heat Capacity by Differential Scanning Calorimetry. ASTM International, West Conshohocken, PA
- ASTM E1461. (2007). Standard Test Method for Thermal Diffusivity by the Flash Method. ASTM International, West Conshohocken, PA.
- ASTM E18. (2003). Standard Test Methods for Rockwell Hardness and Rockwell Superficial Hardness of Metallic Materials. ASTM International, West Conshohocken, PA.
- ASTM E21. (2009). Standard test method elevated temperature tension test of metallic materials. ASTM International, West Conshohocken, PA.
- ASTM E228. (1995). Standard Test Method for Linear Thermal Expansion of Solid Materials with a Vitreous Silica Dilatometer. ASTM International, West Conshohocken, PA.
- ASTM E8. (2001). Standard test methods for tension testing of metallic materials. ASTM International, West Conshohocken, PA
- Azuma, S., & Ogawa, K. (1997). "Duplex stainless steel excellent in corrosion resistance." *U.S. Patent No. 5,672,215*. Washington, DC: U.S. Patent and Trademark Office.
- Baaser, H., & Gross, D. (2000). Crack analysis in ductile cylindrical shells using Gurson's model. *International Journal of Solids and Structures*, 37(46), 7093-7104.
- Bäker, M. (2006). Finite element simulation of high-speed cutting forces. *Journal of Materials Processing Technology*, 176(1–3), 117–126.
- Banerjee, B. (2007). The Mechanical Threshold Stress model for various tempers of AISI 4340 steel. *International Journal of Solids and Structures*, 44(3–4), 834–859.
- Bao, Y. (2004). Dependence of fracture ductility on thickness. *Thin-Walled Structures*, 42(8), 1211–1230.
- Barenblatt, G. I. (1962). The mathematical theory of equilibrium cracks in brittle fracture. In *Advances in Applied Mechanics*, 7, 55-129. Elsevier.
- Barton, D. C., Mirza, M. S., Sturges, J. L., & Waheed, M. (1994). Effect of temperature on the high strain-rate fracture characteristics of ductile metals. *Le Journal de*

Physique IV, 4(C8), C8–659.

- Bažant, Z. P. (2002). Concrete fracture models: testing and practice. *Engineering Fracture Mechanics*, 69(2), 165–205.
- Becker, R. (2002). Ring fragmentation predictions using the Gurson model with material stability conditions as failure criteria. *International Journal of Solids and Structures*, 39(13–14), 3555–3580.
- Belytschko, T., & Bindeman, L. P. (1993). Assumed strain stabilization of the eight node hexahedral element. *Computer Methods in Applied Mechanics and Engineering*, 105(2), 225–260.
- Belytschko, T., Liu, W. K., Moran, B., & Elkhodary, K. (2013). *Nonlinear finite elements for continua and structures*. John Wiley & Sons.
- Belytschko, T., & Tsay, C. S. (1983). A stabilization procedure for the quadrilateral plate element with one-point quadrature. *International Journal for Numerical Methods in Engineering*, 19(3), 405–419.
- Benzerga, A. A., Leblond, J.-B., Needleman, A., & Tvergaard, V. (2016). Ductile failure modeling. *International Journal of Fracture*, 201(1), 29–80.
- Bergstrom, D. S., Dunn, J. J., Grubb, J. F., & Pratt, W. A. (2003). "Duplex stainless steel." *U.S. Patent No. 6,551,420*. Washington, DC: U.S. Patent and Trademark Office.
- Besson, J., Steglich, D., & Brocks, W. (2003). Modeling of plane strain ductile rupture. *International Journal of Plasticity*, 19(10), 1517–1541.
- Birk, A. M., Poirier, D., & Davison, C. (2006). On the thermal rupture of 1.9m³ propane pressure vessels with defects in their thermal protection system. *Journal of Loss Prevention in the Process Industries*, 19(6), 582–597.
- Bonora, N. (1997). A nonlinear CDM model for ductile failure. *Engineering Fracture Mechanics*, 58(1–2), 11–28.
- Bonora, N. (1999). Identification and measurement of ductile damage parameters. *The Journal of Strain Analysis for Engineering Design*, 34(6), 463–478.
- Bonora, N., Gentile, D., Pirondi, A., & Newaz, G. (2005). Ductile damage evolution under triaxial state of stress: theory and experiments. *International Journal of Plasticity*, 21(5), 981–1007.
- Bonora, N., & Milella, P. P. (2000). *Strain Rate And Temperature Effect in Ductile Failure Process: Characterization and Modeling Using Continuum Damage Mechanics*. CASSINO UNIV (ITALY) DIPARTIMENTO DI MECCANICA STRUTTURE AMBIENTE E TERRITORIO.
- Børvik, T., Hopperstad, O. S., & Berstad, T. (2003). On the influence of stress triaxiality and strain rate on the behaviour of a structural steel. Part II. Numerical study. *European Journal of Mechanics - A/Solids*, 22(1), 15–32.
- Børvik, T., Hopperstad, O. S., Berstad, T., & Langseth, M. (2001). A computational model

- of viscoplasticity and ductile damage for impact and penetration. *European Journal of Mechanics-A/Solids*, 20(5), 685–712.
- Børvik, T., Hopperstad, O. S., Dey, S., Pizzinato, E. V., Langseth, M., & Albertini, C. (2005). Strength and ductility of Weldox 460 E steel at high strain rates, elevated temperatures and various stress triaxialities. *Engineering Fracture Mechanics*, 72(7), 1071–1087.
- Børvik, T., Hopperstad, O. S., Langseth, M., & Malo, K. A. (2003). Effect of target thickness in blunt projectile penetration of Weldox 460 E steel plates. *International Journal of Impact Engineering*, 28(4), 413–464.
- Børvik, T., Langseth, M., Hopperstad, O. S., & Malo, K. A. (1999). Ballistic penetration of steel plates. *International journal of impact engineering*, 22(9-10), 855-886.
- Bouchard, P.-O., Bourgeon, L., Fayolle, S., & Mocellin, K. (2011). An enhanced Lemaitre model formulation for materials processing damage computation. *International Journal of Material Forming*, 4(3), 299–315.
- Boyce, B. L., Kramer, S. L. B., Bosiljevac, T. R., Corona, E., Moore, J. A., Elkhodary, K., ... Xue, L. (2016). The second Sandia Fracture Challenge: predictions of ductile failure under quasi-static and moderate-rate dynamic loading. *International Journal of Fracture*, 198(1–2), 5–100.
- Boyce, B. L., Kramer, S. L. B., Fang, H. E., Cordova, T. E., Neilsen, M. K., Dion, K., ... Wierzbicki, T. (2014). The Sandia Fracture Challenge: blind round robin predictions of ductile tearing. *International Journal of Fracture*, 186(1–2), 5–68.
- Boyer, H. E., & Gall, T. L. (1985). *Metals handbook*; desk edition.
- Bridgman, P. W. (1952). *Studies in large plastic flow and fracture* (Vol. 177). New York: McGraw-Hill.
- Bron, F., Besson, J., & Pineau, A. (2004). Ductile rupture in thin sheets of two grades of 2024 aluminum alloy. *Materials Science and Engineering: A*, 380(1–2), 356–364.
- Brozzo, P., Deluca, B., & Rendina, R. (1972). A new method for the prediction of formability in metal sheets, sheet material forming and formability. In *Proceedings of the Seventh Biennial Conference of the IDDRG*.
- Cabezas, E. E., & Celentano, D. J. (2004). Experimental and numerical analysis of the tensile test using sheet specimens. *Finite Elements in Analysis and Design*, 40(5–6), 555–575.
- Calamaz, M., Coupard, D., & Girod, F. (2010). Numerical simulation of titanium alloy dry machining with a strain softening constitutive law. *Machining Science and Technology*, 14(2), 244-257.
- Camanho, P. P., & Dávila, C. G. (2002). Mixed-mode decohesion finite elements for the simulation of delamination in composite materials. *National Aeronautics and Space Administration*. NASA/TM-2002-211737

- Chaboche, J. L. (1984). Anisotropic creep damage in the framework of continuum damage mechanics. *Nuclear Engineering and Design*, 79(3), 309–319.
- Chandrakanth, S., & Pandey, P. C. (1993). A new ductile damage evolution model. *International Journal of Fracture*, 60(4), R73–R76.
- Chen, J., & Young, B. (2006). Stress–strain curves for stainless steel at elevated temperatures. *Engineering Structures*, 28(2), 229–239.
- Chen, J., Young, B., & Uy, B. (2006). Behavior of high strength structural steel at elevated temperatures. *Journal of Structural Engineering*, 132(12), 1948–1954.
- Choe, H., Chen, D., Schneibel, J. H., & Ritchie, R. O. (2001). Ambient to high temperature fracture toughness and fatigue-crack propagation behavior in a Mo–12Si–8.5 B (at.%) intermetallic. *Intermetallics*, 9(4), 319–329.
- Chow, C. L., & Wang, J. (1987). An anisotropic theory of continuum damage mechanics for ductile fracture. *Engineering Fracture Mechanics*, 27(5), 547–558.
- Chu, C. C., & Needleman, A. (1980). Void nucleation effects in biaxially stretched sheets. *Journal of Engineering Materials and Technology*, 102(3), 249–256.
- Chung, H. M. (1992). Aging and life prediction of cast duplex stainless steel components. *International Journal of Pressure Vessels and Piping*, 50(1-3), 179–213.
- Clausen, A. H., Børvik, T., Hopperstad, O. S., & Benallal, A. (2004). Flow and fracture characteristics of aluminium alloy AA5083–H116 as function of strain rate, temperature and triaxiality. *Materials Science and Engineering: A*, 364(1–2), 260–272.
- Cockcroft, M. G., & Latham, D. J. (1968). Ductility and the workability of metals. *Journal of the Institute of Metals*, 96(1), 33–39.
- Coër, J., Bernard, C., Laurent, H., Andrade-Campos, A., & Thuillier, S. (2011). The Effect of Temperature on Anisotropy Properties of an Aluminium Alloy. *Experimental Mechanics*, 51(7), 1185–1195.
- Colley, L. J., Wells, M. A., & Maijer, D. M. (2004). Tensile properties of as-cast aluminum alloy AA5182 close to the solidus temperature. *Materials Science and Engineering: A*, 386(1–2), 140–148.
- Cornec, A., Scheider, I., & Schwalbe, K.-H. (2003). On the practical application of the cohesive model. *Engineering Fracture Mechanics*, 70(14), 1963–1987.
- Cowan, M., & Khandelwal, K. (2014). Modeling of high temperature creep in ASTM A992 structural steels. *Engineering Structures*, 80, 426–434.
- Cowper, G. R., & Symonds, P. S. (1957). *Strain-hardening and strain-rate effects in the impact loading of cantilever beams* (No. TR-C11-28). Brown University: Providence, RI.
- Dempsey, J. F., Antoun, B. R., Romero, V. J., Wellman, G. W., Scherzinger, W. M., & Grange, S. (2013). Temperature dependent ductile material failure constitutive

- modeling with validation experiments. In *Challenges in Mechanics of Time-Dependent Materials and Processes in Conventional and Multifunctional Materials*, 2, 7–15. Springer.
- Dorn, J. E. (1955). Some fundamental experiments on high temperature creep. *Journal of the Mechanics and Physics of Solids*, 3(2), 85–116.
- Dowling, N. E. (1999). *Mechanical Behaviour of Materials*. Upper Saddle River, NJ: Prentice-Hall Inc.
- Dugdale, D. S. (1960). Yielding of steel sheets containing slits. *Journal of the Mechanics and Physics of Solids*, 8(2), 100–104.
- Elices, M., Guinea, G. V., Gomez, J., & Planas, J. (2002). The cohesive zone model: advantages, limitations and challenges. *Engineering Fracture Mechanics*, 69(2), 137–163.
- Erice, B., Gálvez, F., Cendón, D. A., & Sánchez-Gálvez, V. (2012). Flow and fracture behaviour of FV535 steel at different triaxialities, strain rates and temperatures. *Engineering Fracture Mechanics*, 79, 1–17.
- Farabi, E., Zarei-Hanzaki, A., & Abedi, H. R. (2015). High Temperature Formability Prediction of Dual Phase Brass Using Phenomenological and Physical Constitutive Models. *Journal of Materials Engineering and Performance*, 24(1), 209–220.
- Flanagan, D. P., & Belytschko, T. (1981). A uniform strain hexahedron and quadrilateral with orthogonal hourglass control. *International journal for numerical methods in engineering*, 17(5), 679–706.
- Florando, J. N., Margraf, J. D., Reus, J. F., Anderson, A. T., McCallen, R. C., LeBlanc, M. M., ... Lowdermilk, W. H. (2015). Modeling the effect of laser heating on the strength and failure of 7075-T6 aluminum. *Materials Science and Engineering: A*, 640, 402–407.
- Follansbee, P. S., & Kocks, U. F. (1988). A constitutive description of the deformation of copper based on the use of the mechanical threshold stress as an internal state variable. *Acta Metallurgica*, 36(1), 81–93.
- García-Garino, C., Gabaldón, F., & Goicolea, J. M. (2006). Finite element simulation of the simple tension test in metals. *Finite Elements in Analysis and Design*, 42(13), 1187–1197.
- Gastbled, O. J., & May, I. M. (2000). Bifurcation in the numerical simulation of softening mechanisms. *Computers & Structures*, 78(6), 745–755.
- Gerberich, W. W., Martens, H. E., & Boundy, R. A. (1962). Tensile Properties of Five Low-Alloy and Stainless Steels Under High-Heating-Rate and Constant-Temperature Conditions. *California Institute of Technology Jet Propulsion Laboratory*, Technical Report 32-222
- Goto, D. M., Garrett, R. K., Bingert, J. F., Chen, S.-R., & Gray, G. T. (2000). The mechanical

- threshold stress constitutive-strength model description of HY-100 steel. *Metallurgical and Materials Transactions A*, 31(8), 1985–1996.
- Griffith, A. A., & Eng, M. (1921). VI. The phenomena of rupture and flow in solids. *Philosophical Transactions of the Royal Society London A*, 221(582-593), 163-198.
- Grytten, F., Daiyan, H., Polanco-Loria, M., & Dumoulin, S. (2009). Use of digital image correlation to measure large-strain tensile properties of ductile thermoplastics. *Polymer Testing*, 28(6), 653–660.
- Guo, W.-G., & Nemat-Nasser, S. (2006). Flow stress of Nitronic-50 stainless steel over a wide range of strain rates and temperatures. *Mechanics of Materials*, 38(11), 1090–1103.
- Gurson, A. L. (1977). Continuum theory of ductile rupture by void nucleation and growth: Part I—Yield criteria and flow rules for porous ductile media. *Journal of Engineering Materials and Technology*, 99(1), 2-15.
- Hahn, G. T., Sarrate, M., & Rosenfield, A. R. (1969). Criteria for crack extension in cylindrical pressure vessels. *International Journal of Fracture Mechanics*, 5(3), 187-210.
- Haigh, J. R. (1975). The growth of fatigue cracks at high temperatures under predominantly elastic loading. *Engineering Fracture Mechanics*, 7(2), 271–284.
- Hampton, R. W., & Nelson, D. (2003). Stable crack growth and instability prediction in thin plates and cylinders. *Engineering Fracture Mechanics*, 70(3–4), 469–491.
- Hancock, J. W., & Mackenzie, A. C. (1976). On the mechanisms of ductile failure in high-strength steels subjected to multi-axial stress-states. *Journal of the Mechanics and Physics of Solids*, 24(2–3), 147–160.
- Harrison, C. B., & Sandor, G. N. (1971). High-temperature crack growth in low-cycle fatigue. *Engineering Fracture Mechanics*, 3(4), 403–420.
- Hawkyard, J. B., Eaton, D., & Johnson, W. (1968). The mean dynamic yield strength of copper and low carbon steel at elevated temperatures from measurements of the “mushrooming” of flat-ended projectiles. *International Journal of Mechanical Sciences*, 10(12), 929-930.
- Heimerl, G. J. (1957). Tensile Properties of Some Structural Sheet Materials Under Rapid-Heating Conditions. In *Proceedings of Fourth Sagamore Ordnance Materials Research Conference*.
- Heimerl, G. J., & Inge, J. E. (1955). Tensile Properties of 7075-T6 and 2024-T3 Aluminum-Alloy Sheet Heated at Uniform Temperature Rates Under Constant Load. *National Aeronautics and Space Administration*. Technical Note 3462
- Heimerl, G., Kurg, I. M., & Inge, J. E. (1956). Tensile Properties of Inconel and RS-120 Titanium-alloy Sheet Under Rapid-heating and Constant-temperature Conditions. *National Aeronautics and Space Administration*. Technical Note 3731

- Hillerborg, A., Modéer, M., & Petersson, P. E. (1976). Analysis of crack formation and crack growth in concrete by means of fracture mechanics and finite elements. *Cement and Concrete Research*, 6(6), 773-781.
- Hor, A., Morel, F., Lebrun, J.-L., & Germain, G. (2013). Modelling, identification and application of phenomenological constitutive laws over a large strain rate and temperature range. *Mechanics of Materials*, 64, 91–110.
- Huang, Y. Y. (1990). Cavitation and localization in plastic flow. PhD Dissertation. Harvard University, Cambridge, Massachusetts, USA.
- Huang, Y. (1991). Accurate dilatation rates for spherical voids in triaxial stress fields. *Journal of Applied Mechanics*, 58, 1084.
- Hutchinson, J. W. (1997). Linking scales in fracture mechanics. *Advances in Fracture Research*, 1, 1-14.
- International Molybdenum Association. (2009). Practical guidelines for the fabrication of duplex stainless steels. London, UK, 1-64.
- Irwin, G. R. (1957). Analysis of stresses and strains near the end of a crack traversing a plate. *Journal of Applied Mechanics*, 24, 361-364
- James, L. A. (1972a). Fatigue-Crack Growth in 20% Cold-Worked Type 316 Stainless Steel at Elevated Temperatures. *Nuclear Technology*, 16(1), 316–322.
- James, L. A. (1972b). The Effect of Stress Ratio on the Elevated Temperature Fatigue-Crack Propagation of Type 304 Stainless Steel. *Nuclear Technology*, 14(2), 163–170.
- Jirásek, M., & Rolshoven, S. (2003). Comparison of integral-type nonlocal plasticity models for strain-softening materials. *International Journal of Engineering Science*, 41(13-14), 1553-1602.
- Johnson, G. R., & Cook, W. H. (1983). A constitutive Model and Data for Metals Subjected to Large Strains, High Strain Rates and High Temperature. *Proceedings of the 7th International Symposium On Ballistics*.
- Johnson, G. R., & Cook, W. H. (1985). Fracture characteristics of three metals subjected to various strains, strain rates, temperatures and pressures. *Engineering Fracture Mechanics*, 21(1), 31-48.
- Kachanov, L. M. (1958). On the creep fracture time. *Izv Akad, Nauk USSR Otd Tech*, 8, 26-31. Translated Version: Kachanov, L. M. (1999). Rupture time under creep conditions. *International Journal of Fracture*, 97(1-4), 11-18.
- Kanninen, M. F., Popelar, C. H., & Broek, D. (1981). A critical survey on the application of plastic fracture mechanics to nuclear pressure vessels and piping. *Nuclear Engineering and Design*, 67(1), 27-55.
- Khamei, A. A., & Dehghani, K. (2015). Effects of strain rate and temperature on hot tensile deformation of severe plastic deformed 6061 aluminum alloy. *Materials Science and Engineering: A*, 627, 1–9.

- Kobayashi, H., & Dodd, B. (1989). A numerical analysis for the formation of adiabatic shear bands including void nucleation and growth. *International Journal of Impact Engineering*, 8(1), 1-13.
- Kutt, L. M., Pifko, A. B., Nardiello, J. A., & Papazian, J. M. (1998). Slow-dynamic finite element simulation of manufacturing processes. *Computers & structures*, 66(1), 1-17.
- Lassen, T., & Récho, N. (2006). Short Overview of the Foundations of Fracture Mechanics. *Fatigue Life Analyses of Welded Structures*, 381-391.
- Lava, P., Cooreman, S., & Debruyne, D. (2010). Study of systematic errors in strain fields obtained via DIC using heterogeneous deformation generated by plastic FEA. *Optics and Lasers in Engineering*, 48(4), 457–468.
- Lechler, J., Merklein, M., & Geiger, M. (2008). Determination of Thermal and Mechanical Material Properties of Ultra-High Strength Steels for Hot Stamping. *Steel Research International*, 79(2), 98-104.
- Lee, K. Y., & Park, J. S. (1992). J-integral under transient temperature state. *Engineering Fracture Mechanics*, 43(6), 931-940.
- Lemaitre, J. (1972). Evaluation of dissipation and damage in metals submitted to dynamic loading. *Mechanical Behavior of Materials*, 540-549.
- Lemaitre, J. (1984). How to use damage mechanics. *Nuclear Engineering and Design*, 80(2), 233-245.
- Lemaitre, J. (1985). A continuous damage mechanics model for ductile fracture. *Journal of Engineering Materials and Technology*, 107(1), 83-89.
- Lemaitre, J., & Chaboche, J. L. (1978). Phenomenological approach of damage rupture. *Journal de Mecanique Appliquee*, 2(3), 317-365.
- Lemaître, J., & Desmorat, R. (2005). *Engineering damage mechanics: ductile, creep, fatigue and brittle failures*. Berlin ; New York: Springer.
- Li, S., Chen, Y., Zhang, G., & Li, Z. (1994). The failure of shells subjected to internal pressure and irradiated by CW CO2 laser beam. In *AIAA, Plasmadynamics and Lasers Conference, 25th*, Colorado Springs, CO.
- Liaw, P. K., & Swaminathan, V. P. (1989). Elevated-temperature fatigue crack growth behavior of a rotor steel. *Engineering Fracture Mechanics*, 34(2), 457-463.
- Lin, Y. C., Xia, Y.-C., Chen, X.-M., & Chen, M.-S. (2010). Constitutive descriptions for hot compressed 2124-T851 aluminum alloy over a wide range of temperature and strain rate. *Computational Materials Science*, 50(1), 227–233.
- Ling, Y. (1996). Uniaxial true stress-strain after necking. *AMP Journal of Technology*, 5, 37-48.
- Litonski, J. (1977). *Bulletin de l'Academie Polonaise des Sciences. Sciences Tech.*, 25, 7.

- Ludwik, P. (1909). *Element der Technologischen. Mechanik*, Berlin, Germany: Springer Verlag
- Mackenzie, A. C., Hancock, J. W., & Brown, D. K. (1977). On the influence of state of stress on ductile failure initiation in high strength steels. *Engineering fracture mechanics*, 9(1), 167-188.
- Manu, C. C. (2008). Finite element analysis of stress rupture in pressure vessels exposed to accidental fire loading. MS Thesis. *Queen's University*, Kingston, Ontario, Canada.
- Manu, C. C., Birk, A. M., & Kim, I. Y. (2009). Stress rupture predictions of pressure vessels exposed to fully engulfing and local impingement accidental fire heat loads. *Engineering Failure Analysis*, 16(4), 1141–1152.
- McClintock, F. A. (1968). A criterion for ductile fracture by the growth of holes. *Journal of Applied Mechanics*, 35(2), 363-371.
- Mills, W. J. (1980). The effect of heat treatment on the room temperature and elevated temperature fracture toughness response of Alloy 718. *Journal of Engineering Materials and Technology*, 102(1), 118-126.
- Motoya, D., Hamada, M., Amaya, H., Nagayama, H., & Yamada, K. (2017). "Duplex stainless steel and production method therefor." U.S. Patent No. 9,771,628. Washington, DC: U.S. Patent and Trademark Office.
- Mukherjee, A. K., Bird, J. E., & Dorn, J. E. (1968). Experimental correlations for high-temperature creep. *University of California, Lawrence Radiation Laboratory*, UCRL-18526
- Mulyadi, M., Rist, M. A., Edwards, L., & Brooks, J. W. (2006). Parameter optimisation in constitutive equations for hot forging. *Journal of Materials Processing Technology*, 177(1–3), 311–314.
- Nahshon, K., & Hutchinson, J. W. (2008). Modification of the Gurson Model for shear failure. *European Journal of Mechanics - A/Solids*, 27(1), 1–17.
- Needleman, A. (1972). A numerical study of necking in circular cylindrical bar. *Journal of the Mechanics and Physics of Solids*, 20(2), 111-127.
- Needleman, A. (1988). Material rate dependence and mesh sensitivity in localization problems. *Computer Methods in Applied Mechanics and Engineering*, 67(1), 69-85.
- Oh, C.-S., Kim, N.-H., Kim, Y.-J., Baek, J.-H., Kim, Y.-P., & Kim, W.-S. (2011). A finite element ductile failure simulation method using stress-modified fracture strain model. *Engineering Fracture Mechanics*, 78(1), 124–137.
- Oyane, M., Sato, T., Okimoto, K., & Shima, S. (1980). Criteria for ductile fracture and their applications. *Journal of Mechanical Working Technology*, 4(1), 65-81.
- Park, Y. S., Kim, S. T., & Lee, I. S. (2005). "High-grade duplex stainless steel with much

- suppressed formation of intermetallic phases and having an excellent corrosion resistance, embrittlement resistance castability and hot workability". *U.S. Patent Application No. 10/507,069*. Washington, DC: U.S. Patent and Trademark Office.
- Peerlings, R. H. J., De Borst, R., Brekelmans, W. A. M., & Geers, M. G. D. (2002). Localisation issues in local and nonlocal continuum approaches to fracture. *European Journal of Mechanics-A/Solids*, 21(2), 175-189.
- Peerlings, R. H. J., Geers, M. G. D., De Borst, R., & Brekelmans, W. A. M. (2001). A critical comparison of nonlocal and gradient-enhanced softening continua. *International Journal of Solids and Structures*, 38(44-45), 7723-7746.
- Prager, W. (1938). On isotropic materials with continuous transition from elastic to plastic state. *Proceedings of the 5th International Congress on Applied Mechanics*, Cambridge, Massachusetts, 234-237.
- Provenzano, V., Gilmore, C.M., Smidt, F.A., & Hawthorne, I.R., (1981). Thickness and Temperature Effects on the J-Integral COD Relationship. *Navy Research Laboratory*. NRL Memorandum Report 4696.
- Puso, M. A. (2000). A highly efficient enhanced assumed strain physically stabilized hexahedral element. *International Journal for Numerical Methods in Engineering*, 49(8), 1029-1064.
- Puttick, K. E. (1959). Ductile fracture in metals. *Philosophical magazine*, 4(44), 964-969.
- Rabczuk, T., & Belytschko, T. (2004). Cracking particles: a simplified meshfree method for arbitrary evolving cracks. *International Journal for Numerical Methods in Engineering*, 61(13), 2316-2343.
- Rabotnov, Y. N., Leckie, F. A., & Prager, W. (1970). Creep problems in structural members. *Journal of Applied Mechanics*, 37, 249.
- Raj, R., & Ashby, M. F. (1975). Intergranular fracture at elevated temperature. *Acta Metallurgica*, 23(6), 653-666.
- Rajput, S. K., Chaudhari, G. P., & Nath, S. K. (2016). Characterization of hot deformation behavior of a low carbon steel using processing maps, constitutive equations and Zener-Hollomon parameter. *Journal of Materials Processing Technology*, 237, 113-125.
- Ramaswamy, S., & Aravas, N. (1998a). Finite element implementation of gradient plasticity models Part I: Gradient-dependent yield functions. *Computer Methods in Applied Mechanics and Engineering*, 163(1-4), 11-32.
- Ramaswamy, S., & Aravas, N. (1998b). Finite element implementation of gradient plasticity models Part II: Gradient-dependent evolution equations. *Computer Methods in Applied Mechanics and Engineering*, 163(1-4), 33-53.
- Reese, S., & Wriggers, P. (2000). A stabilization technique to avoid hourglassing in finite elasticity. *International Journal for Numerical Methods in Engineering*, 48(1), 79-

109.

- Reusch, F., & Svendsen, B. (2004). On the investigation of material stability during the simulation of ductile damage in metallic materials. In *Proceedings of the Seventh International Conference on Computational Structures Technology*, 123, 1-13.
- Rhines, W. J. (1961). Ductile fracture by the growth of pores. PhD Dissertation. *Harvard University*, Cambridge, Massachusetts, USA.
- Rice, J. R. (1968). A path independent integral and the approximate analysis of strain concentration by notches and cracks. *Journal of Applied Mechanics*, 35(2), 379-386.
- Rice, J. R., & Tracey, D. M. (1969). On the ductile enlargement of voids in triaxial stress fields*. *Journal of the Mechanics and Physics of Solids*, 17(3), 201-217.
- Rogers, H. C. (1960). The tensile fracture of ductile metals. *AIME trans*, 218(3), 498-506.
- Romero, V. J., Dempsey, J. F., Antoun, B., Wellman, G., & Sherman, M. (2014). Handling Bias and Uncertainty in Model Verification and Validation associated with Heated Pipes Pressurized to Failure. *American Institute of Aeronautics and Astronautics. 16th AIAA Non-Deterministic Approaches Conference*
- Rousselier, G. (1987). Ductile fracture models and their potential in local approach of fracture. *Nuclear Engineering and Design*, 105(1), 97-111.
- Sajjadi, S. A., Nategh, S., & Guthrie, R. I. (2002). Study of microstructure and mechanical properties of high performance Ni-base superalloy GTD-111. *Materials Science and Engineering: A*, 325(1-2), 484-489.
- Sakumoto, Y., Nakazato, T., & Matsuzaki, A. (1996). High-temperature properties of stainless steel for building structures. *Journal of Structural Engineering*, 122(4), 399-406.
- Samantaray, D., Mandal, S., Borah, U., Bhaduri, A. K., & Sivaprasad, P. V. (2009). A thermo-viscoplastic constitutive model to predict elevated-temperature flow behaviour in a titanium-modified austenitic stainless steel. *Materials Science and Engineering: A*, 526(1-2), 1-6.
- Saxena, A. (1991). Creep crack growth in high temperature ductile materials. *Engineering Fracture Mechanics*, 40(4-5), 721-736.
- Scheider, I., & Brocks, W. (2003). Simulation of cup-cone fracture using the cohesive model. *Engineering Fracture Mechanics*, 70(14), 1943-1961.
- Scheider, I., Brocks, W., & Cornec, A. (2004). Procedure for the Determination of True Stress-Strain Curves From Tensile Tests With Rectangular Cross-Section Specimens. *Journal of Engineering Materials and Technology*, 126(1), 70.
- Schreyer, H. L., & Neilsen, M. K. (1996). Analytical and numerical tests for loss of material stability. *International Journal for Numerical Methods in Engineering*, 39(10), 1721-1736.

- Schreyer, H. L., & Maudlin, P. J. (2005). Thermodynamically consistent relations involving plasticity, internal energy and thermal effects. *Philosophical Transactions of the Royal Society of London A: Mathematical, Physical and Engineering Sciences*, 363(1836), 2517-2541.
- Schweizer, C. (2016). Evolution equations for the $C(t)$ -integral and the crack-tip opening displacement CTOD for elastic–viscoplastic material behavior and temperature dependent material properties. *Engineering Fracture Mechanics*, 157, 125–140.
- Seidt, J. D., & Gilat, A. (2013). Plastic deformation of 2024-T351 aluminum plate over a wide range of loading conditions. *International Journal of Solids and Structures*, 50(10), 1781–1790.
- Sokolowsky, V. (1948). Propagation of elasto-viscoplastic waves in bars. *Prikladnaya Matematika i Mekhanika*, 12, 261-280.
- Swift, H. (1952). Plastic instability under plane stress. *Journal of the Mechanics and Physics of Solids*, 1(1), 1-18.
- Tai, W. H., & Yang, B. X. (1987). A new damage mechanics criterion for ductile fracture. *Engineering Fracture Mechanics*, 27(4), 371-378.
- Tane, M., Ichitsubo, T., Ogi, H., & Hirao, M. (2003). Elastic property of aged duplex stainless steel. *Scripta Materialia*, 48(3), 229-234.
- Tang, B. T., Bruschi, S., Ghiotti, A., & Bariani, P. F. (2016). An improved damage evolution model to predict fracture of steel sheet at elevated temperature. *Journal of Materials Processing Technology*, 228, 76–87.
- Tanguy, B., & Besson, J. (2002). An extension of the Rousselier model to viscoplastic temperature dependent materials. *International Journal of Fracture*, 116(1), 81-101.
- Tari, D. G., & Worswick, M. J. (2015). Elevated temperature constitutive behavior and simulation of warm forming of AZ31B. *Journal of Materials Processing Technology*, 221, 40–55.
- Tarigopula, V., Hopperstad, O. S., Langseth, M., Clausen, A. H., & Hild, F. (2008). A study of localisation in dual-phase high-strength steels under dynamic loading using digital image correlation and FE analysis. *International Journal of Solids and Structures*, 45(2), 601–619.
- Taylor, B. N., & Kuyatt, C. E. (1994). Guidelines for evaluating and expressing the uncertainty of NIST measurement results. Gaithersburg, MD: US Department of Commerce, Technology Administration, *National Institute of Standards and Technology*.
- Tinet, H., Klöcker, H., & Le Coze, J. (2004). Damage analysis during hot deformation of a resulfurised stainless steel. *Acta Materialia*, 52(13), 3825–3842.
- Tipper, C. F. (1949). The fracture of metals. *Metallurgia*, 39(231), 133-137.

- Tran, D. K., Kobayashi, A. S., & White, K. W. (2001). Crack growth in alumina at high temperature. *Engineering Fracture Mechanics*, 68(2), 149-161.
- Tucker, J. D., Miller, M. K., & Young, G. A. (2015). Assessment of thermal embrittlement in duplex stainless steels 2003 and 2205 for nuclear power applications. *Acta Materialia*, 87, 15-24.
- Tvergaard, V. (1981). Influence of voids on shear band instabilities under plane strain conditions. *International Journal of Fracture*, 17(4), 389-407.
- Tvergaard, V., & Hutchinson, J. W. (1992). The relation between crack growth resistance and fracture process parameters in elastic-plastic solids. *Journal of the Mechanics and Physics of Solids*, 40(6), 1377-1397.
- Tvergaard, V., & Needleman, A. (1984). Analysis of the cup-cone fracture in a round tensile bar. *Acta Metallurgica*, 32(1), 157-169.
- Ulacia, I., Salisbury, C. P., Hurtado, I., & Worswick, M. J. (2011). Tensile characterization and constitutive modeling of AZ31B magnesium alloy sheet over wide range of strain rates and temperatures. *Journal of Materials Processing Technology*, 211(5), 830-839.
- Umbrello, D. (2008). Finite element simulation of conventional and high speed machining of Ti6Al4V alloy. *Journal of materials processing technology*, 196(1-3), 79-87.
- Umbrello, D., Hua, J., & Shivpuri, R. (2004). Hardness-based flow stress and fracture models for numerical simulation of hard machining AISI 52100 bearing steel. *Materials Science and Engineering: A*, 374(1-2), 90-100.
- van den Boogaard, A. H., & Huétink, J. (2006). Simulation of aluminium sheet forming at elevated temperatures. *Computer Methods in Applied Mechanics and Engineering*, 195(48-49), 6691-6709.
- Vinh, T., Afzali, M., & Roche, A. (1980). Fast fracture of some usual metals at combined high strain and high strain rate. In *Mechanical Behaviour of Materials*, 633-642.
- Voce, E. (1948). The relationship between stress and strain for homogeneous deformation. *Journal of the Institute of Metals*, 74, 537-562.
- Voyiadjis, G. Z., & Abed, F. H. (2005). Microstructural based models for bcc and fcc metals with temperature and strain rate dependency. *Mechanics of Materials*, 37(2-3), 355-378.
- Wang, T. J. (1992). Unified CDM model and local criterion for ductile fracture—I. Unified CDM model for ductile fracture. *Engineering Fracture Mechanics*, 42(1), 177-183.
- Wang, T. J. (1992). Unified CDM model and local criterion for ductile fracture—II. Ductile fracture local criterion based on the CDM model. *Engineering Fracture Mechanics*, 42(1), 185-193.
- Wellman, G. W. (2012). A simple approach to modeling ductile failure. *Sandia National Laboratories*. SAND2012-1343.

- Wells, A. A. (1963). Application of fracture mechanics at and beyond general yielding. *British Welding Journal*, 10, 563-570.
- Wierzbicki, T., Bao, Y., Lee, Y.-W., & Bai, Y. (2005). Calibration and evaluation of seven fracture models. *International Journal of Mechanical Sciences*, 47(4–5), 719–743.
- Wriggers, P., & Reese, S. (1996). A note on enhanced strain methods for large deformations. *Computer Methods in Applied Mechanics and Engineering*, 135(3-4), 201-209.
- Xia, L., Shih, C. F., & Hutchinson, J. W. (1995). A computational approach to ductile crack growth under large scale yielding conditions. *Journal of the Mechanics and Physics of Solids*, 43(3), 389-413.
- Xue, L. (2007). Damage accumulation and fracture initiation in uncracked ductile solids subject to triaxial loading. *International Journal of Solids and Structures*, 44(16), 5163–5181.
- Xue, L., & Wierzbicki, T. (2008). Ductile fracture initiation and propagation modeling using damage plasticity theory. *Engineering Fracture Mechanics*, 75(11), 3276–3293.
- Yamada, K., Nagayama, H., Hamada, M., Motoya, D., & Amaya, H. (2013). " Duplex Stainless Steel". U.S. Patent Application No. 13/984,327. Washington, DC: U.S. Patent and Trademark Office.
- Zener, C., & Hollomon, J. H. (1944). Effect of strain rate upon plastic flow of steel. *Journal of Applied Physics*, 15(1), 22-32.
- Zener, C., & Hollomon, J. H. (1946). Problems in Non-Elastic Deformation of Metals. *Journal of Applied Physics*, 17(2), 69–82.
- Zerilli, F. J., & Armstrong, R. W. (1987). Dislocation-mechanics-based constitutive relations for material dynamics calculations. *Journal of Applied Physics*, 61(5), 1816-1825.
- Zerilli, F. J., & Armstrong, R. W. (1996). Constitutive relations for titanium and Ti-6Al-4V. In *American Institute of Physics Conference Proceedings*, 370(1), 315-318. American Institute of Physics.
- Zhang, B., & Baker, T. N. (2004). Effect of the heat treatment on the hot deformation behaviour of AA6082 alloy. *Journal of Materials Processing Technology*, 153–154, 881–885.
- Zhang, Z. L., Hauge, M., Ødegård, J., & Thaulow, C. (1999). Determining material true stress–strain curve from tensile specimens with rectangular cross-section. *International Journal of Solids and Structures*, 36(23), 3497-3516.
- Zhang, P., & Lee, H. (1993). Creep damage and fracture at high temperature. *Engineering Fracture Mechanics*, 44(2), 283-288.
- Zhao, H., & Gary, G. (1996). The testing and behaviour modelling of sheet metals at strain rates from 10⁻⁴ to 10⁴ s⁻¹. *Materials Science and Engineering: A*, 207(1), 46-50.

Appendix A: Example Files for the Analysis of Notched Specimens

A.1 Abaqus Input File Example for C-Notch Specimen

```
*Heading
  Analysis of C-Notch specimen R=1cm
**=====
** Load Mesh from files
**=====
*NODE,NSET=NODEALL,INPUT=NODES_Cnotch_1x1x0pt5mm.inp
*ELEMENT,TYPE=C3D8R,ELSET=ELEMALL,INPUT=MESH_Cnotch_1x1x0pt5mm.inp
**=====
** Define BC node sets and set element controls
**=====
*NSET,NSET=top
17,37,57,77,97,117,137,157,177,197,217,237,18,38,58,78,
98,118,138,158,178,198,218,238,19,39,59,79,99,119,139,159,
179,199,219,239,20,40,60,80,100,120,140,160,180,200,220,240
*NSET,NSET=bot
241,261,281,301,321,341,361,381,401,421,441,461,242,262,282,302,
322,342,362,382,402,422,442,462,243,263,283,303,323,343,363,383,
403,423,443,463,244,264,284,304,324,344,364,384,404,424,444,464
**
*Section      Controls,      name=EC-1,      HOURGLASS=RELAX      STIFFNESS,max
degradation=1,element deletion=yes
1., 1., 1.
**
*Solid Section, elset=ELEMALL, material=DSS, controls=EC-1
1.,
**=====
** Define material properties
**=====
*MATERIAL,NAME=DSS, RTOL=0.003
**-----
*Elastic
** N/m^2, Poisson, temp(C)
19.50E+10, 0.18, 23.
**-----
*Plastic
** True Stress N/m^2,PEEQ, temp(C)
546938961.44 , 0.00000, 23.0
591627634.88 , 0.00952, 23.0
618404579.84 , 0.01410, 23.0
639522046.81 , 0.02368, 23.0
653314126.52 , 0.02830, 23.0
671842748.87 , 0.04730, 23.0
731223762.00 , 0.09062, 23.0
789832036.29 , 0.11042, 23.0
845682802.99 , 0.13048, 23.0
905255665.61 , 0.15078, 23.0
962287096.38 , 0.17662, 23.0
1016676716.84 , 0.20829, 23.0
1051252510.30 , 0.24071, 23.0
```

```

1085119968.85 , 0.29582, 23.0
1123420912.50 , 0.35420, 23.0
1131224695.41 , 0.38405, 23.0
1159066355.69 , 0.43272, 23.0
1159315710.14 , 0.45766, 23.0
1159636593.29 , 0.48975, 23.0
1161348788.10 , 0.55077, 23.0
1162027014.06 , 0.61859, 23.0
**-----
*Density
** kg/m3
 7685., 200.0
**-----
*Damage Initiation, criterion=ductile
**PEEQ, Triaxiality, Strain Rate (/sec), Temp(C)
0.26, 0.4, 0.025, 23.0
**-----
*Damage Evolution, type=displacement,softening=tabular
** Damage, Eff. Plastic Displacement (Upl), temp(C)
0.00, 0.0, 23.
0.05, 7.93701E-05, 23.
0.12, 0.000119055, 23.
0.25, 0.000198425, 23.
1.00, 0.000214299, 23.
**=====
** Define initial temperature, BC's, and smooth step amp.
**=====
*Initial Conditions, type=TEMPERATURE
NODEALL,23.0
**
*Boundary
BOT, Encastre
TOP, 1, 1
TOP, 3, 3
**
*Amplitude, name=ramp,definition=smooth step
0.0,0.0,0.6,1.0
**=====
** Define initial step with smooth step velocity increase
**=====
*Step, name=Step-1,NLGEOM=YES
loading
*Dynamic, explicit
, 0.6
**
*FIXED MASS SCALING,FACTOR=1000,ELSET=ELEMALL
**
*Boundary,type=velocity, amplitude = ramp
TOP, 2, 2, 0.000255
**
*Restart,WRITE,OVERLAY
*Output, field, number interval=6
*Node Output
U,RF,V,A
*Element Output
S,LE,E,PEEQ,STATUS,DMICRT,SDEG
** HISTORY OUTPUT: H-Output-1

```

```

**
*Output, history, variable=PRESELECT
*ENERGY OUTPUT,VARIABLE=ALL
*End Step
**=====
** Define step with constant velocity until failure
**=====
*Step, name=Step-2,NLGEOM=YES
loading
*Dynamic, explicit
, 9.4
**
*FIXED MASS SCALING,FACTOR=1000,ELSET=ELEMALL
**
*Restart,WRITE,OVERLAY
*Output, field, number interval=94
*Node Output
U,RF,V,A
*Element Output
S,LE,E,PEEQ,STATUS,DMICRT,SDEG
** HISTORY OUTPUT: H-Output-1
**
*Output, history, variable=PRESELECT
*ENERGY OUTPUT,VARIABLE=ALL
*End Step

```

A.2 Abaqus Python Script to Extract C-Notch Model Results

```

#####
# SCRIPT: Extract load-disp, thickness, width, PEEQ for Cnotch specimen
# SYNTAX: abaqus python scriptName.py runIdentifier
#####
import os, sys, string
import glob, csv
import time
import shutil
sys.path.append('/usr/lib64/python2.6/site-packages')
from numpy import *
from scipy import io, assio
from string import *
from odbAccess import *
from abaqusConstants import *

print "Entering extraction script"
print "File:",sys.argv[-1]
f=sys.argv[-1] # Read runIdentifier (job name) from command line arg.

odbFile='/home/user/'+f+'.odb'
odb = openOdb(path='%s'%odbFile)

makeSet=1
if makeSet==1:
    # Generate node set of four shoulder corners on the top
    nLabels=[529,532,1045,1048]

```



```

topNodeSet=odb.rootAssembly.instances['PART-1-1'].NodeSetFromNodeLabels(
    name='topShldr',nodeLabels=nLabels)

# Generate node set of four shoulder corners on the bottom
nLabels=[489,492,1017,1020]
botNodeSet=odb.rootAssembly.instances['PART-1-1'].NodeSetFromNodeLabels(
    name='botShldr',nodeLabels=nLabels)

makeSet2=1
if makeSet2==1:
    # Generate node set of front of center row
    nLabels=[916,920]
    frontNodeSet=odb.rootAssembly.instances['PART-1-1'].NodeSetFromNodeLabels(
        name='front',nodeLabels=nLabels)

    # Generate node set of back of center row
    nLabels=[913,917]
    backNodeSet=odb.rootAssembly.instances['PART-1-1'].NodeSetFromNodeLabels(
        name='back',nodeLabels=nLabels)

    # Generate node set of left of center row
    nLabels=[660,664]
    leftNodeSet=odb.rootAssembly.instances['PART-1-1'].NodeSetFromNodeLabels(
        name='left',nodeLabels=nLabels)

    # Generate node set of right of center row
    nLabels=[916,920]
    rightNodeSet=odb.rootAssembly.instances['PART-1-1'].NodeSetFromNodeLabels(
        name='right',nodeLabels=nLabels)

makeSet3=1
if makeSet3==1:
    # Generate element set for center row

eLabels=[394,395,396,397,398,459,460,461,462,463,524,525,526,527,528]
centerElemSet=odb.rootAssembly.instances['PART-1-1'].ElementSetFromElementLabels(
    name='centerElem',elementLabels=eLabels)

centerElem = odb.rootAssembly.instances['PART-1-1'].elementSets['centerElem']
botShldr = odb.rootAssembly.instances['PART-1-1'].nodeSets['botShldr']
topShldr = odb.rootAssembly.instances['PART-1-1'].nodeSets['topShldr']
front = odb.rootAssembly.instances['PART-1-1'].nodeSets['front']
back = odb.rootAssembly.instances['PART-1-1'].nodeSets['back']
left = odb.rootAssembly.instances['PART-1-1'].nodeSets['left']
right = odb.rootAssembly.instances['PART-1-1'].nodeSets['right']
nodeSetTop = odb.rootAssembly.instances['PART-1-1'].nodeSets['TOP']

F=[]
U=[]

```

```

w=[]
t=[]
timeVals=[]
PEEQ=[]
maxPEEQ=-1.

# Loop through each step
for step in odb.steps.values():
    # Loop through each frame for current step
    for frame in step.frames:
        # Extract total time of frame
        # =====
        totalTime=frame.frameValue
        timeVals.append(totalTime)

        # Extract/calculate total reaction force
        # =====
        fieldRF = frame.fieldOutputs['RF']
        topRF = fieldRF.getSubset(region=nodeSetTop)
        sumRF=0
        for rf in topRF.values:
            nodeRF=rf.data[1]
            sumRF=sumRF+nodeRF
            #print 'rf:', nodeRF
        F.append(sumRF)
        #print 'sumRF:', sumRF

        # Extract relative shoulder displacement
        # =====
        fieldU = frame.fieldOutputs['U']
        topU = fieldU.getSubset(region=topShldr)
        botU = fieldU.getSubset(region=botShldr)
        sumTopU=0
        for u in topU.values:
            sumTopU=sumTopU+u.data[1]
        sumBotU=0
        for u in botU.values:
            sumBotU=sumBotU+u.data[1]
        # Calculate average relative displacement of shoulders
        avgTopU=sumTopU/4
        avgBotU=sumBotU/4
        U.append((avgTopU-avgBotU)*1000)

        # Extract instantaneous thickness
        # =====
        fieldU = frame.fieldOutputs['U']
        frontU = fieldU.getSubset(region=front)
        backU = fieldU.getSubset(region=back)
        sumFront=0
        for u in frontU.values:
            sumFront=sumFront+u.data[2]
        sumBack=0
        for u in backU.values:
            sumBack=sumBack+u.data[2]
        # Calculate thickness based on displacements
        avgFrontU=sumFront/2
        avgBackU=sumBack/2

```

```

t.append(1.5-abs((avgFrontU-avgBackU))*1000)

# Extract instantaneous width
# =====
fieldU = frame.fieldOutputs['U']
rightU = fieldU.getSubset(region=right)
leftU = fieldU.getSubset(region=left)
sumRight=0
for u in rightU.values:
    sumRight=sumRight+u.data[0]
sumLeft=0
for u in leftU.values:
    sumLeft=sumLeft+u.data[0]
# Calculate width based on displacements
avgRightU=sumRight/2
avgLeftU=sumLeft/2
w.append(5.0-abs((avgRightU-avgLeftU))*1000)

# Extract the maximum PEEQ on cross-section
# =====
fieldPEEQ = frame.fieldOutputs['PEEQ']
centerPEEQ =
fieldPEEQ.getSubset(region=centerElem,position=CENTROID,
elementType='C3D8R')
for p in centerPEEQ.values:
    if(p.data>maxPEEQ):
        maxPEEQ=p.data
PEEQ.append(maxPEEQ)

# Save data to Matlab database file (.mat)
# =====
data= {'time': timeVals, 'F': F, 'U': U, 't': t, 'w': w, 'PEEQ':PEEQ}
sio.savemat(f+'.mat',{f:data})
odb.close()

```

A.3 Abaqus File for Thermal and Mechanical Properties of DSS

```

**=====
** COMPLETE DSS MATERIALS FILE
**=====
*MATERIAL,NAME=DSS, RTOL=0.015
*****
*Density
** kg/m^3
*****
7685.0
*****
*Elastic
** Modulus N/m^2, Poisson, Temp(C)
*****
1.95E+11, 0.18, 23.0
1.80E+11, 0.18, 200.0
6.00E+10, 0.18, 400.0
5.50E+10, 0.18, 600.0
3.00E+10, 0.18, 800.0

```

```

9.78E+09,    0.18, 1000.0
7.76E+09,    0.18, 1200.0
*****
*Plastic
** True Stress N/m^2,PEEQ,Temp (C)
** 500C & 1200C from Gleeble Test
*****
546938961.44 , 0.00000, 23.0
591627634.88 , 0.00952, 23.0
618404579.84 , 0.01410, 23.0
639522046.81 , 0.02368, 23.0
653314126.52 , 0.02830, 23.0
671842748.87 , 0.04730, 23.0
731223762.00 , 0.09062, 23.0
789832036.29 , 0.11042, 23.0
845682802.99 , 0.13048, 23.0
905255665.61 , 0.15078, 23.0
962287096.38 , 0.17662, 23.0
1016676716.84 , 0.20829, 23.0
1051252510.30 , 0.24071, 23.0
1085119968.85 , 0.29582, 23.0
1123420912.50 , 0.35420, 23.0
1131224695.41 , 0.38405, 23.0
1159066355.69 , 0.43272, 23.0
1159315710.14 , 0.45766, 23.0
1159636593.29 , 0.48975, 23.0
1161348788.10 , 0.55077, 23.0
1162027014.06 , 0.61859, 23.0
**
396000000.00 , 0.00000, 200.0
460000000.00 , 0.00800, 200.0
515000000.00 , 0.03270, 200.0
577000000.00 , 0.06440, 200.0
624000000.00 , 0.09550, 200.0
685000000.00 , 0.15660, 200.0
770000000.00 , 0.30000, 200.0
810000000.00 , 0.50000, 200.0
**
377869439.67 , 0.00000, 400.0
408153907.41 , 0.00500, 400.0
479258203.88 , 0.02890, 400.0
540203263.69 , 0.07291, 400.0
582175550.62 , 0.11848, 400.0
605418034.73 , 0.15063, 400.0
625809851.28 , 0.19882, 400.0
642516138.83 , 0.24330, 400.0
661824604.81 , 0.30112, 400.0
670362402.97 , 0.34324, 400.0
672096990.10 , 0.37409, 400.0
673360550.53 , 0.43236, 400.0
**
3.50E+08,    0.00,      500.0
3.80E+08,    0.0085,     500.0
4.16E+08,    0.0231,     500.0
4.67E+08,    0.0460,     500.0
5.04E+08,    0.0690,     500.0
5.53E+08,    0.1114,     500.0

```

```

6.63E+08,    0.35, 500.0
**
320000000.00 , 0.00000, 600.0
405000000.00 , 0.10200, 600.0
475000000.00 , 0.24100, 600.0
536000000.00 , 0.48400, 600.0
549000000.00 , 0.58000, 600.0
550000000.00 , 0.85200, 600.0
**
160254226.02 , 0.00000, 800.0
176354395.83 , 0.01040, 800.0
179391066.40 , 0.01540, 800.0
191080602.11 , 0.05412, 800.0
193788983.23 , 0.07455, 800.0
201885336.67 , 0.13144, 800.0
213186046.10 , 0.24100, 800.0
222292982.19 , 0.34717, 800.0
236593168.05 , 0.49405, 800.0
261224653.44 , 0.74133, 800.0
290099350.86 , 1.00714, 800.0
297439790.32 , 1.07471, 800.0
302322818.55 , 1.11967, 800.0
**
42246000.00 , 0.00000, 1000.0
48530168.76 , 0.00500, 1000.0
50598608.19 , 0.01000, 1000.0
52140560.47 , 0.01500, 1000.0
53422117.84 , 0.02000, 1000.0
54542085.06 , 0.02500, 1000.0
55549750.69 , 0.03000, 1000.0
56473790.06 , 0.03500, 1000.0
57332576.10 , 0.04000, 1000.0
58138693.01 , 0.04500, 1000.0
58901193.57 , 0.05000, 1000.0
59626840.20 , 0.05500, 1000.0
60320837.52 , 0.06000, 1000.0
60987289.75 , 0.06500, 1000.0
61629499.09 , 0.07000, 1000.0
63260307.20 , 0.09395, 1000.0
71233683.34 , 0.23395, 1000.0
82624220.70 , 0.43395, 1000.0
94014758.05 , 0.63395, 1000.0
105405295.41 , 0.83395, 1000.0
116795832.76 , 1.03395, 1000.0
128186370.11 , 1.23395, 1000.0
139576907.47 , 1.43395, 1000.0
150967444.82 , 1.63395, 1000.0
162357982.17 , 1.83395, 1000.0
173748519.53 , 2.03395, 1000.0
185139056.88 , 2.23395, 1000.0
196529594.23 , 2.43395, 1000.0
**
1.77E+07,    0.00,      1200.0
1.85E+07,    0.0059,     1200.0
1.90E+07,    0.0099,     1200.0
3.14E+07,    1.00,       1200.0
5.02E+07,    2.50,       1200.0

```

```

**
*****
*Damage Initiation, criterion=ductile
**PEEQ, Triaxiality, Strain Rate (/sec), Temp(C)
**Combined C notch and V notch
**V-Notch has higher triaxiality
*****
0.28, 0.4, 0.025, 23.0
0.15, 0.4, 0.025, 200.0
0.07, 0.7, 0.025, 200.0
0.14, 0.4, 0.025, 400.0
0.11, 0.7, 0.025, 400.0
0.14, 0.4, 0.025, 600.0
0.1, 0.7, 0.025, 600.0
0.85, 0.7, 0.025, 800.0
0.48, 0.9, 0.025, 800.0
1.50, 0.7, 0.025, 1000.0
0.7, 0.9, 0.025, 1000.0
*****
*Damage Evolution, type=displacement,softening=tabular
** Damage, PEEQ*Char_length (meter), Temp(C)
** Char_length (m) = (0.001 * 0.001 * 0.0015/3)^(1/3)
*****
0.00, 0.0, 23.
0.05, 0.00007937, 23.
0.12, 0.00011906, 23.
0.25, 0.00019842, 23.
1.00, 0.00021430, 23.
**
0.00, 0.0, 200.
0.15, 0.00015874, 200.
0.21, 0.00017461, 200.
0.30, 0.00020636, 200.
0.40, 0.00023811, 200.
0.50, 0.00025002, 200.
0.88, 0.00027383, 200.
1.00, 0.00027779, 200.
**
0.00, 0.0, 400.
0.07, 0.000063, 400.
0.14, 0.000135, 400.
0.22, 0.000198, 400.
1.00, 0.000235, 400.
**
0.00, 0.0, 600.
0.08, 0.00007937, 600.
0.18, 0.00015874, 600.
0.32, 0.00023811, 600.
1.00, 0.00027543, 600.
**
0.00, 0.0, 800.
0.10, 0.000079, 800.
0.32, 0.000159, 800.
1.00, 0.000222, 800.
**
0.00, 0.0, 1000.
0.10, 0.00031748, 1000.

```

```

0.35, 0.00051590, 1000.
0.65, 0.00067464, 1000.
1.00, 0.00071433, 1000.
*****
*Conductivity
**W/m-K, Temp(C)
*****
14.2, 23.
14.8, 50.
15.8, 100.
17.4, 200.
18.5, 300.
20.3, 400.
23.25, 500.
24.6, 600.
24.9, 700.
26.1, 800.
26.4, 900.
26.6, 1000.
26.9, 1100.
28.9, 1200.
*****
*Specific Heat
** J/kg-C, Temp(C)
*****
480.5,      23
488.4,      50
501.3,     100
513.1,     150
523.8,     200
533.4,     250
545.2,     300
562.3,     350
586.5,     400
598.6,     420
612.3,     440
627.9,     460
645.3,     480
669.7,     500
707.1,     520
767.4,     540
807.6,     560
777.2,     580
734.1,     600
700.2,     620
685.1,     640
672.9,     660
661.3,     680
651.5,     700
647.7,     720
656.4,     740
660.7,     750
657.1,     900
656.1,    1200
656.1,    1466
57656.1,  1471
656.1,    1476

```

```
*****
*Expansion
**m/m-C,  Temp (C)
*****
1.300E-5,  23.0
1.310E-05, 100.0
1.362E-05, 200.0
1.394E-05, 300.0
1.416E-05, 400.0
1.459E-05, 500.0
1.511E-05, 600.0
1.591E-05, 700.0
1.642E-05, 800.0
1.656E-05, 900.0
1.606E-05, 1000.0
1.493E-05, 1100.0
```


Appendix B: Example Files for the Analysis of Panel Specimens

B.1 Pseudo-code for Irregular Beam Subroutine Implementation

```
c ===== UEXTERNALDB SUBROUTINE =====
c      subroutine uexternaldb(lop,lrestart,time,dtime,kstep,kinc)
c =====
c This subroutine is called once at the beginning of the
c analysis, at the beginning of each increment, at the end of
c each increment, and at the end of the analysis.
c
c Used to precalculate the irradiance on each element face
c exposed to the laser so it only executes when lop=0
c
c      Irregular Beam Profile : Stationary beam direction
c =====
c              DESCRIPTION OF VARIABLES
c
c              Variables from UEXTERNALDB subroutine
c      lop:      lop = 0 is start of analysis
c      lrestart: indicates if restart is written for this increment
c      time(2):  time(1) --> step time; time(2) --> total time
c      dtime:    time increment
c      kstep:    step number
c      kinc:     increment number
c
c =====
1) Define filename which contains coordinates/connectivity
   Define filename which contains elements which may be heated
   Define filename which contains beam profile data
2) Define laser beam center
if(lop.ne.0 ) return !Only execute once in the beginning
3) Read nodal coordinates and element connectivity from file
4) Read heated element set from file
5) Read the beam profile (defined in the beam plane) from file
LOOP THROUGH HEATED ELEMENTS
6) Calculate the centroid of the heated element face and determine
location in the beam plane
7) Interpolate using the inverse distance weighting algorithm to get a
weighted irradiance value at the centroid of the element face
8) Store the irradiance for each element in a common block to be accessed
later by DFLUX
```

END LOOP

```
c ===== DFLUX SUBROUTINE =====  
      subroutine dflux(flux,sol,kstep,kinc,time,noel,npt,coords,  
      &                jltyp,temp,press,sname)
```

```
c =====  
c This subroutine is called at every iteration of the solver to  
c calculate the surface heat flux for the surface defined in the  
c input file.
```

```
c  
c Used to implement temperature dependent surface absorption  
c coefficient. Irradiance is read from pre-calculated values  
c stored in common block from UEXTERNALDB
```

```
c  
c Irregular Beam Profile : Stationary beam direction
```

```
c =====  
c DESCRIPTION OF VARIABLES
```

```
c  
c Variables from DFLUX subroutine  
c Variables to be defined  
c flux(1): Magnitude of surface flux  
c flux(2): Magnitude of body flux  
c  
c Variables provided in call from solver  
c sol: Temperature solution at current time  
c kstep: Step number  
c kinc: Increment number  
c time(1): Current step time  
c time(2): Current total time  
c noel: Element number  
c npt: Integration point number  
c coords: Coordinates of point being evaluated  
c jltyp: Identifies the flux type for which this call to DFLUX  
c is being made. Flux type may be body flux, surface-  
c based flux, or element-based surface flux. For  
c element-based surface fluxes, this variable  
c identifies the element face.
```

```
c =====
```

- 1) Define temperature dependent absorption data
- 2) Interpolate absorption value from data (1) using the current element temperature (sol)
- 3) Read interpolated irradiance for the current element (noel) from common block
- 4) Set flux(1) to the interpolated irradiance multiplied by the absorption value for the current element (which will be the surface flux returned to the Abaqus solver)
- 5) Store flux(1) and absorption for each heated element in a common block to be accessed later by USDFLD

```
c ===== USDFLD SUBROUTINE =====  
      SUBROUTINE USDFLD(FIELD,STATEV,PNEWDT,DIRECT,T,CELENT,
```

```

1 TIME, DTIME, CMNAME, ORNAME, NFIELD, NSTATV, NOEL, NPT, LAYER,
2 KSPT, KSTEP, KINC, NDI, NSHR, COORD, JMAC, JMATYP, MATLAYO, LACCFLA)
c =====
c This subroutine is called at every iteration of the solver to
c calculate field variables at the material point
c
c Used to generate a field for irradiance and/or absorption      c values
to enable the user to view the spatial distribution in      c the output
database
c
c      Irregular Beam Profile : Stationary beam direction
c =====
c              DESCRIPTION OF VARIABLES
c
c      Variables from DFLUX subroutine
c      Variables to be defined
c      field(n): Vector containing the user defined field variables
c
c      Variables that can be updated
c      statev: Solution dependent state variables
c      pnewdt: Suggested time increment ratio
c
c      Variables provided in call from solver
c      direct: Direction cosines of material dir. wrt global dir.
c      T: Direction cosines of material dir. wrt element basis dir.
c      CELENT: Characteristic element length
c      dtime: Time increment
c      time(1): Current step time
c      time(2): Current total time
c      CMNAME: Material name
c      orname: Local orientation
c      nffield: Number of field variables
c      nstatev: Number of solution dependent state variables
c      noel: Element number
c      npt: Integration point number
c      layer: Layer number for composite shells or layered solids
c      kpst: Section point number
c      kstep: Step number
c      kinc: Increment number
c      NDI: Number of direct stress components
c      NSHR: Number of shear stress components
c      JMAC, JMATYP, MATLAYO, LACCFLA: Variables for calling GETVRM
c =====
1) Read geometry and absorption corrected irradiance value from
common block for current element (noel)
2) Store irradiance value as field(1)
3) Store additional values such as cosine(theta) or absorption as
field(2) etc. for debugging purposes. Must be passed through
common block.

```

B.2 Abaqus Input File Example for Panel Specimen Thermal Model

```

*Heading
Analysis of Panel Test during laser irradiation

```

```

Thermal Model
**=====
** Load Mesh from files
**=====
*Node, nset=NODEALL, input=nodes.input
*Element, type=DC3D8, elset=ELEMALL, input=elements.input
*include, input=sets.input
**=====
** Define element controls
**=====
*Solid Section, elset=ELEMALL, material=DSS
1.,
**=====
** Define material properties
**=====
*Include, Input=DSS_1x1xpt5mm_C3D8R_Kelvin.txt
**=====
** Define initial temperature and physical constants
**=====
*Initial Conditions, type=TEMPERATURE
NODEALL,303.0
**
*Physical Constants, absolute zero=0.0, stefan boltzmann=5.669e-8
**=====
** Apply heating with user-defined subroutine
**=====
*Step, name=Heat-1, inc=100000, amplitude=step
Heat with user defined dflux subroutine
*Heat Transfer, end=PERIOD, deltmx=15
0.05, 3.0 , 1e-05, 0.1
**
** User defined surface heat flux (DFLUX)
*Dflux
  _HEAT_SURF_S6, S6NU, 0.
  _HEAT_SURF_S1, S1NU, 0.
**
** Surface radiation
*Radiate
  _HEAT_SURF_S6, R6, 303., 0.8
  _HEAT_SURF_S1, R1, 303., 0.5
**
*Restart, write, overlay
**
*Output, field
*Node Output
NT
*Element Output
TEMP, FV
**
*Output, history, frequency=1000
*Node file
NT

```

*End Step

B.3 Abaqus Input File Example for Panel Specimen Thermal-Mechanical Model

```
*Heading
Analysis of Panel Test during laser irradiation
Sequentially Coupled Thermal-Mechanical
**=====
** Load Mesh from files
**=====
*Node, nset=NODEALL, input=nodes.input
*Element, type=C3D8R, elset=ELEMALL, input=elements.input
*include, input=sets.input
**=====
** Define BC node sets and element controls
**=====
*Rigid Body, ref node=TOP_REF_NODE, pin nset=TOP_BC
*Rigid Body, ref node=BOT_REF_NODE, pin nset=BOT_BC
**
*Section Controls, name=EC-1, hourglass=RELAX STIFFNESS,max
degradation=1,element deletion=yes
1., 1., 1.
**
*Solid Section, elset=ELEMALL, material=DSS, control=EC-1
1.,
**=====
** Define material properties
**=====
*Include, Input=DSS_1x1xpt5mm_C3D8R_Kelvin.txt
**=====
** Define initial temperature, BC's, and smooth step amp.
**=====
*Initial Conditions, type=TEMPERATURE
NODEALL,303.0
**
*Amplitude, Name=Load_History, time=total time, value=Absolute
1,-62004, 1.5,-61968, 2,-61932, 2.5,-61921,
3,-61877, 3.5,-61666, 3.75,-61256, 4,-60578,
4.25,-59668, 4.5,-58455, 4.75,-56609, 5,-54699,
5.250,-52788, 5.5,-50877, 5.75,-48966, 6,-47055
**
*Boundary
TOP_REF_NODE, 1,5
BOT_REF_NODE, 1,1
BOT_REF_NODE, 3,5
***
*Amplitude, name=ramp,definition=smooth step
0.0,0.0,1.0,1.0
```

```

**=====
** Define initial step with smooth step load increase
**=====
*Step, name=ApplyLoad, nlgeom=YES
LOAD CONTROLLED TEST
*Dynamic, explicit
, 1.
**
*Fixed mass scaling, factor = 1.0e3
**
*Cloud, amplitude = ramp
BOT_REF_NODE, 2, -62035.84
**
*Restart, write, OVERLAY
*Output, field, NUMBER INTERVAL=10
*Node Output
U,NT
*Node Output, nset=BOT_REF_NODE
RF,RT
*Node Output, nset=TOP_REF_NODE
RF,RT
*Element Output
TEMP, S, LE, PE, PEEQ, THE, STATUS, DMICRT, SDEG, TRIAX
**
*Output, history, variable=PRESELECT
*ENERGY OUTPUT, VARIABLE=ALL
*End Step
**=====
** Apply heating with time-dependent load curve from test
**=====
*Step, name=Thermech-1, amplitude=step, nlgeom=yes
Hold Load and Heating Up
*Dynamic, explicit
, 3.0
**
*Cloud, amplitude = Load_History
BOT_REF_NODE, 2, 0.0
**
*Temperature, file=Heat_RT4_5, bstep=1, estep=1, binc=1, einc=60
**
*Restart, write, OVERLAY
**
*Output, field, NUMBER INTERVAL=300
*Node Output
U,NT
*Node Output, nset=BOT_REF_NODE
RF,RT
*Node Output, nset=TOP_REF_NODE
RF,RT
*Element Output
TEMP, S, LE, PE, PEEQ, THE, STATUS, DMICRT, SDEG, TRIAX
**
*Output, history, variable=PRESELECT

```

```
*ENERGY OUTPUT,VARIABLE=ALL  
*End Step
```

Appendix C: Example Files for the Analysis of Pressure Vessels

C.1 Abaqus User Subroutines for Axisymmetric Flux Profile on a Curved Surface

```
c=====
c=====
c ABAQUS Subroutines for user defined surface flux on curved surface
c
c DESCRIPTION:
c Subroutines to apply axisymmetric laser irradiance profiles to a curved
c surface with temperature dependent absorption. The more general case of
c arbitrary spatially and temporally varying profile is similar with the
c addition of a centroid calculation, transformation to the beam plane, and
c inverse distance weight interpolation scheme. The more general case adds a
c significant number of lines to the code which is cumbersome to include in
c this document.
c=====
c=====

c=====
c UEXTERANLDB subroutine
c -- Used to read mesh and heated set information
c -- Calculates surface normals for heated surface
c -- Only executes at beginning of analysis
c -- Interfaced to dflux via common blocks
c=====
      subroutine uexternaldb(lop,lrestart,time,dtime,kstep,kinc)
      implicit none

c   Abaqus Arguments
c   =====
      integer lop      ! specifically when lop=0, the subroutine is
c                       ! called at the start of analysis
      integer lrestart ! indicates if the restart file is
c                       ! written for this increment
      real*8 time(2)  ! time(1)--> step time; time(2)--> total time
      real*8 dtime    ! time increment
      integer kstep, kinc ! step number and increment number

c   Data files to read mesh and heated surface information
c   =====
      character*80 file_for_mesh           ! File containing mesh data
      character*80 file_for_heat_region1   ! File containing heated set data

      data file_for_mesh/'/home/darren/HSS/cylinder/SD_MESH.input'/
      data file_for_heat_region1/'/home/darren/HSS/cylinder/SD_HEAT_SET.input'/

c   User Variables
c   =====
      integer max_data
      integer unit_num, num_regions
```



```

parameter (max_data=250000)
parameter (num_regions=1)
real*8 x(3,max_data)          ! Spatial Coordinates of Each Node
real*8 coordinate(3,4)        ! 4 nodal coordinates of element face
real*8 edm(3,3)               ! Intermediate Vector to find surface normal
integer conn(8)               ! Connectivity of Element
integer num_nodes,num_elements ! Counters
integer loop,loop2,loop3,loop4,loop5 ! loop indices
integer elem,node,nd1,nd2,nd3,nd4,indx,incr1,i,ik,eln
integer num_heatelem          ! total number of heated elems
integer heat_elem_list(max_data) ! element #'s for heated elems
real*8 nvector(3,max_data)    ! Heat surface normal vectors
integer el(16),partition(num_regions),file_num

c      Common blocks for DFLUX
c      =====
common /K_heatelmlist/heat_elem_list
common /K_numheatelem/num_heatelem
common /K_normal_vector/nvector

character*132 line0,line
logical blank_line

if( lop.ne.0 ) return ! only execute when lop=0 (beginning of analysis)
write(6,*) '======'
write(6,*) 'Entering UEXTERNALDB'

c      Open data files
c      =====
write(6,*) 'Opening Mesh file'
open(unit=115,type='old',file=file_for_mesh)
write(6,*) 'Opening Heat file'
open(unit=101,type='old',file=file_for_heat_region1)

c      Read heated region data
c      =====
num_heatelem = 0
indx=0
! WARNING: Assumes each heat file starts with *ELSET, contains only one
! set, and has 16 element numbers per line (no generate sets), last line
! must be buffered with zeros so that 16 values are found

!Loop on all heated element files, one for each face
do file_num =1,num_regions
  write(6,*) 'Reading Heat file:', file_num
  ! Add 100 to file number to get unit number
  unit_num=file_num+100
  ! Read first line in heat file
  read(unit_num,'(a)', end=6001) line0 ! read a line
  ! Check if first line starts with *ELSET
  call change_case(line0,line)
  if(line(1:6) .ne. '*ELSET')then
    write(*,*) 'ERROR: *ELSET missing in heat file #',file_num
    goto 6001
  endif

  ! Read through the rest of the file which contains element set data
  do loop4 = 1,max_data

```

```

        read(unit_num,'(a)', end=6001) line0 ! read a line
        read(line0,*,err=5150) el(1),el(2),el(3),el(4),el(5),el(6),
&                                     el(7),el(8),el(9),el(10),el(11),el(12),
&                                     el(13),el(14),el(15),el(16)
        ! Only include non-zero elements
        incrl=0
        do i=1,16
            if(el(i) .gt. 0)then
                incrl=incrl+1
            endif
        enddo
        num_heatelem = num_heatelem + incrl
        ! write(6,*)'num_heatelem:', num_heatelem
        ! Store heat set elem #'s in common block
        do ik = 1, incrl
            indx = indx + 1
            heat_elem_list(indx) = el(ik) ! heat element list
            ! write(6,*)'Heated Elements:', heat_elem_list(indx)
        end do
    end do ! loop 4
6001 continue
    ! Store the last index for the current heat file
    partition(file_num)=indx
end do ! file loop

write(6,*) 'Partitions=', partition
write(6,*) 'Number heated element = ', num_heatelem

c Read the mesh file
c =====
num_nodes=0
num_elements=0
write(6,*) 'Reading Mesh File'
! Read first line in mesh file
read(115,'(a)', end=4001) line0 ! read a line

! Check if first line starts with *Node
call change_case(line0,line)
if(line(1:5) .ne. '*NODE')then
    write(*,*) 'ERROR: *NODE missing in mesh file #',file_num
    goto 4001
endif
! Read nodal data (node#,x,y,z)
do loop = 1,max_data+1
    ! Read a line of nodal data
    read(115,'(a)',end=4001) line0
    ! Check if line starts with *ELEM
    call change_case(line0,line)
    if(line(1:5) .eq. '*ELEM')then
        goto 2001
    else
        ! Read nodal data
        read(line0,*,err=5000) node,x(1,node),x(2,node),x(3,node)
        num_nodes = num_nodes + 1
        !write(6,'(i6,2x,3f12.7)', node,x(1,node),x(2,node),x(3,node)
    endif
end do ! loop

```

2001 continue

```
c Calculate surface normal for each heated element
c =====

! Check if at the beginning of the elem data, then read elem data
! (el#,connectivity)
if(line(1:5) .eq. '*ELEM')then
  do loop2 = 1,max_data+1
    ! Read element data line
    read(115,'(a)',end=4001) line0

    ! Read element number and nodal connectivity
    read(line0,*,err=5050) elem,conn(1),conn(2),conn(3),
&      conn(4),conn(5),conn(6),conn(7),conn(8)

    num_elements=num_elements+1

! Loop through all heated elements
do eln= 1,partition(num_regions)
  ! Check if the current element being evaluated is in
  ! the list of heated elements
  ! If heated element, pull appropriate nodes for cosine calc
  if(heat_elem_list(eln) .eq. elem) then
    ! WARNING: CHANGE HERE FOR EACH MODEL,
    ! Different nodes need to be pulled depending on the
    ! face you're heating, this is for face 4 on DC3D8
    nd1=conn(2) !store face 4 nodes
    nd2=conn(6)
    nd3=conn(7)
    nd4=conn(3)
  else
    write (6,*) 'ERROR: Reading Connectivity'
  endif
  ! Load the coords for the four nodes on the heated face

  coordinate(1,1) = x(1,nd1)
  coordinate(2,1) = x(2,nd1)
  coordinate(3,1) = x(3,nd1)
  coordinate(1,2) = x(1,nd2)
  coordinate(2,2) = x(2,nd2)
  coordinate(3,2) = x(3,nd2)
  coordinate(1,3) = x(1,nd3)
  coordinate(2,3) = x(2,nd3)
  coordinate(3,3) = x(3,nd3)
  coordinate(1,4) = x(1,nd4)
  coordinate(2,4) = x(2,nd4)
  coordinate(3,4) = x(3,nd4)

  ! construct two vectors in 3D space along two element edges
  edm(1,1) = coordinate(1,2) - coordinate(1,1)
  edm(2,1) = coordinate(2,2) - coordinate(2,1)
  edm(3,1) = coordinate(3,2) - coordinate(3,1)

  edm(1,2) = coordinate(1,4) - coordinate(1,1)
  edm(2,2) = coordinate(2,4) - coordinate(2,1)
  edm(3,2) = coordinate(3,4) - coordinate(3,1)
```

```

        ! calculate the normal using the cross product
        call kcrossp(edm(1,1),edm(1,2),edm(1,3))
        call knormv(edm(1,3),3)

        ! store element normal for cosine calculation in dflux
        nvector(1,eln) = edm(1,3)
        nvector(2,eln) = edm(2,3)
        nvector(3,eln) = edm(3,3)
    endif ! Elem List
  enddo ! Partition
enddo ! Loop2
else
  write(6,*) 'ERROR: *Elem Check'
endif ! *Elem

4001 continue
      write(6,*) 'Number of nodes = ', num_nodes
      write(6,*) 'Number of elements = ', num_elements

      ! error reading data
      goto 6000

5000 write(6,*) 'ERROR: Reading Nodal Data'
5050 write(6,*) 'ERROR: Reading Element Data'
5150 write(6,*) 'ERROR: Reading Heated Elements'
6000 continue

      ! Close data files
      close(unit=115)
      close(unit=101)

      write(6,*) 'Exiting UEXTERNALDB'
      write(6,*) '======'
      return
      end

c=====
c DFLUX subroutine
c -- Provides user defined surface flux back to analysis
c -- Called at each solver increment
c -- Interfaced with UEXTERNALDB and USDFLD via common blocks
c -- Supports axisymmetric flux distributions
c -- Projects to curved surface (cosine correction)
c -- Temperature dependent absorptivity
c=====
      subroutine dflux(flux,sol,kstep,kinc,time,noel,npt,coords,
& jltyp,temp,press,sname)

c      Abaqus Arguments
c      =====
      implicit none
      real*8 sol, temp, press
      real*8 flux(2), time(2), coords(3)
      integer kstep, kinc, noel, npt, jltyp
      character*80 sname

c      User Arguments
c      =====
      real*8 ct, dist,bcom(3),gflux,Io,beam_radius

```

```

integer max_data,num_heatelem,hlist
parameter (max_data=250000)
integer heat_elem_list(max_data)
integer k,indicator,ab_type,num_points
real*8 current_irrad(max_data),current_ct(max_data),nvector(3,max_data)
real*8 ab, ab_vals(18), ab_temp(18), temp_diff, ratio, const_ab

c      Common blocks from UEXTERNALDB
c      =====
common /K_numheatelem/num_heatelem
common /K_heatelmlist/heat_elem_list
common /K_normal_vector/nvector ! normal vector of heated element

c      Common blocks for USDFLD
c      =====
common /K_ct_current/current_ct
common /K_irrad_current/current_irrad

c      User parameters
c      =====
parameter (beam_radius = 0.0125d0 )      ! Beam radius
parameter (Io = 10000000.d0)            ! Peak intensity

data indicator/3/      !1 for flattop, 2 for Gaussian, 3 for 4th order

c      Absorptivity flag (Constant=1, Temp.Dependent=2)
parameter ( ab_type = 1)

c      Constant Absorptivity
parameter (const_ab = 0.85)

c      Temp. Dependent Absorptivity
parameter (num_points=5)
data ab_vals /0.82d0,0.82d0,0.85d0,0.93d0,0.93d0/
c      NOTE: Temperatures must be in increasing order for interpolation loop
data ab_temp /0.d0,400.d0,500.d0,1000.d0,1200.d0/

data origin/0.0d0, 0.0d0, 0.0d0/

c      Check if NOEL is a heated element then calc irradiance
c      =====
do hlist = 1, num_heatelem
  ! Check if heated element
  if (noel .eq. heat_elem_list(hlist)) then
    ! Calculate Absorptivity
    if(ab_type .eq. 1)then
      ab=const_ab
    elseif (ab_type .eq. 2)then
      if (sol.le.ab_temp(1)) then
        ab = ab_vals(1)
      else if (sol.ge.ab_temp(num_points)) then
        ab = ab_vals(num_points)
      else
        do k=2,num_points
          if (sol.le.ab_temp(k)) then
            temp_diff = ab_temp(k) - ab_temp(k-1)
            ratio = (sol-ab_temp(k-1))/temp_diff
            ab = (1.d0-ratio)*ab_vals(k-1)+ratio*ab_vals(k)
          end if
        end do
      end if
    end if
  end if
end do

```

```

        if (temp_diff.lt.1e-8) then
            write(6,*) 'error : will encounter division by zero'
        endif
        go to 8001
    endif
end do
8001 continue
endif
endif
c

! Calculate beam unit vector at current time (if moving)
! In this case it's assumed to be static
bcom(1)=-1.d0
bcom(2)=0.d0
bcom(3)=0.d0
call knormv(bcom,3)

! Calculate cosine theta using the dot product
ct = (nvector(1,hlist)*bcom(1) + nvector(2,hlist)*bcom(2)
&      + nvector(3,hlist)*bcom(3))
current_ct(noel)=ct
!write(6,*) 'Elem, CT =', noel, ct

! Irradiance calculation
if(ct.lt.0.d0)then
    flux(1)=0.d0
    current_ct(noel)=0.d0
else
    ! Calculate radius in the beam plane
    ! WARNING: ONLY works for axisymmetric beam shapes

    dist=dsqrt((origin(2)-coords(2))**2+(origin(3)-coords(3))**2)

    ! Check beam type and calculate irradiance
    if(indicator.eq.1)then ! Uniform distribution beam
        if(dist.le.beam_radius)then
            gflux=Io
        endif
    elseif (indicator.eq.2) then ! Gaussian beam
        gflux=Io*dexp(-2*dist**2/beam_radius**2)
    elseif (indicator.eq.3) then ! 4th order Gaussian
        gflux=Io*dexp(-2*dist**4/beam_radius**4)
    else
        write(6,*) 'ERROR with Beam Indicator in DFLUX'
    end if
    ! Correct irradiance for cosine theta and absorptance
    flux(1) = ct*ab*gflux
    current_irrad(noel)=flux(1)
endif
! Found flux for heated element (noel), go to return
go to 1002
endif
enddo ! do hlist

1002 return
end

```

```

c=====
c USDFLD subroutine
c -- Provides user fields back to analysis for plotting in CAE
c -- Called at every solver increment
c -- Interfaced with dflux via common blocks
c -- Stores user defined flux and cosine correction
c=====
      subroutine usdfd(field,statev,pnewdt,direct,t,celent,time,
&dttime,cmname,orname,nfield,nstatv,noel,npt,layer,kspt,kstep,kinc,
&ndi,nshr,coord,jmac,jmatyp,matlayo,laccfla)

      implicit none

      ! ABAQUS Parameters
      !=====
      real*8 field,statev,direct,t,celent,time(2),dttime
      real*8 coord,pnewdt,jmac,jmatyp,matlayo,laccfla
      character*80 cmname,orname
      integer nfield,npt,layer,kspt,kstep,kinc,ndi,nshr
      integer nstatv,noel
      dimension field(2),statev(nstatv),direct(3,3),t(3,3)
      dimension jmac(*),jmatyp(*),coord(*)

      ! User Parameters
      !=====
      integer max_data
      parameter (max_data=250000)

      real*8 current_irrad(max_data)
      real*8 current_ct(max_data)

      common /K_ct_current/current_ct
      common /K_irrad_current/current_irrad

      ! Store irradiance and cosine correction in field
      field(1)=current_irrad(noel)
      field(2)=current_ct(noel)

      return
      end

c=====
c check if the line being read is blank
c=====
      function blank_line(line)

      implicit none
      character*132 line
      logical blank_line
      integer i
      blank_line=.true.
      do i=1,132
         if(line(i:i).ne.' ') then
            blank_line=.false.
            return
         endif
      end do
end do

```

```

        return
        end
=====
c change the lower case letters to capitalized letters
=====
        subroutine change_case(line0,line)

        implicit none
        character*132 line0,line
        character*1 ch
        integer i,l

        l=0
        line = ' '
        do i = 1,132
            ch = line0(i:i)
            if('a'.le.ch.and.ch.le.'z') ch=char(ichar(ch)-32)
            if( ch.ne.' ')then
                l=l+1
                line(l:l) = ch
            endif
        end do

        return
        end
=====
c normalize a vector
=====
        subroutine knormv(a,n)

        implicit none
        integer n,i
        real*8 a(n), d

        d = 0.d0
        do i = 1,n
            d = d + a(i)*a(i)
        end do
        d = dsqrt(d)

        do i = 1,n
            a(i) = a(i)/d
        end do

        return
        end
=====
c cross product of 2 vectors, a and b
c match the column in Fortran
=====
        subroutine kcrossp(a,b,c)

        real*8 a(3),b(3),c(3)

        c(1) = a(2)*b(3) - a(3)*b(2)
        c(2) = a(3)*b(1) - a(1)*b(3)
        c(3) = a(1)*b(2) - a(2)*b(1)

```



```
return
end
```

C.2 Abaqus Input File Example for Pressure Vessel Thermal Model

```
*Heading
Analysis of Pressure Vessel during Laser Irradiation
Thermal Model
**=====
** Load Mesh from Files
**=====
*Part, name=solid
*End Part
*Assembly, name=Assembly
*Instance, name=solid, part=solid
**
** Load the node numbers and coordinates from file
*Node
*Include, Input=SD_NODES.input
**
** Load the element numbers and connectivity from file
*Element, type=DC3D8
*Include, Input=SD_ELEMENTS.input
**
** Load surfaces definitions and node/element sets from file
*Include, Input=SD_GEN_SETS.input
**
**=====
** Define element orientation and controls
**=====
*orientation, name=cylinder, system=cylindrical
0,0,0,0,0,1
**
*Solid Section, elset=ALL, orientation=cylinder, material=DSS
1.,
**
*End Instance
*End Assembly
**=====
** Define material properties (Load from file)
**=====
*Include, Input=DSS_1x1xpt5mm_C3D8R_Celcius.txt
**=====
** Define initial temperature and physical constants
**=====
*initial conditions, type=temperature
solid.all, 30.0
**
**Define Boltzmann constant in J/s-m^2-K^4
*Physical Constants, absolute zero=-273.15, stefan boltzmann=5.669e-8
**
**=====
** Apply heating with user-defined subroutine
**=====
*Step, name=Heat-1, inc=100000, amplitude=step
Heat with user defined dflux subroutine
*Heat Transfer, end=period, deltmx=15
0.005, 1., 1e-05, 0.1
**
** User defined surface heat flux (DFLUX)
```

```

*Dflux
solid.Heat_Set, S4NU, 0.0
**
** Surface radiation
*Radiate
solid.Heat_Set, R4, 30.0, 0.8
solid.innersur, R6, 30.0, 0.5
**
*Restart, write, overlay
**
*NODE FILE, NSET=solid.all
  NT
**
*Output, field
*Node Output
  NT
*Element Output
TEMP, HFL
*End Step

```

C.3 Abaqus Python Script for Extracting Temperature History at TC Locations

```

#####
# SCRIPT: Extract temperature history for nodes located at the approx.
#         location of the thermocouples (TCs) in the array of 29 TCs
#         The nodes were estimated from the mesh file and TC pattern
#         then written to a text file to be read by this python script
#         SYNTAX:          abaqus          python          scriptName.py
#####

from odbAccess import *
from abaqusConstants import *

# set filename/location containing node numbers corresponding to TC locations
tc_file='/home/user/test_12/tc_nodes.txt'
inFile=open('%s'%tc_file,'r')          # Open file to read node list
os.chdir('/home/user/test_12/')       # Directory where files are located
o_file='test12_heat'                  # Abaqus Odb file name to extract data
from
outFile=open('%s.Tvst'%o_file,'w')    # Open file to write TC history for each
node
odb = openOdb(path='%s.odb'%o_file, readOnly=True) # Open Abaqus odb
nvals = inFile.readlines()
nLabels = []
outFile.write('Time ')
for nval in nvals:
    nLabels.append(int(nval))
    outFile.write('%i '%(int(nval)))
outFile.write('\n')

# Create the set name TCS in Abaqus odb file containing nodes from tc_nodes.txt
nodeSet = odb.rootAssembly.instances['SOLID'].NodeSetFromNodeLabels(
    name='TCS',nodeLabels=nLabels)
# Get the node set info to set region later in the script
nset =odb.rootAssembly.instances['SOLID'].nodeSets['TCS']
# Specify the KEYS for the fields to be extracted
DesFields = ['NT11']                  # NT11 is the nodal temperature for DC3D8
for step in odb.steps.values():      # Loop through all steps
    stime=step.totalTime              # stime is the step time
    stepnum=step.number               # stepnum is the step number

```

```

for frame in step.frames:      # Loop through all frames in the step
    ttime=stime+frame.frameValue  # Calculate the total time
    first = 1
    for dfield in DesFields:      # Loop through all the desired fields
        if nset:                  # If node set then extract data
            # Get values in the node set
            value = frame.fieldOutputs[dfield].getSubset(region=nset)
            # Loop through value, i.e. all values for nodes in the set
            for vals in value.values:
                if first == 1:
                    outFile.write('%f'%(ttime))
                    first = 0
                outFile.write('%f'%(vals.data))      # Write the field data
                outFile.write('\n')
odb.close() # Close the Abaqus odb before exiting

```

C.4 Abaqus Input File Example for Pressure Vessel Thermal-mechanical Model

```

*Heading
Analysis of Pressure Vessel Failure during Laser Irradiation
Thermal-mechanical Model
**=====
** Define solid and shell element parts
**=====
*Part, name=solid
*End Part
*Part, name=shell
*End Part
*Assembly, name=Assembly
**=====
** Load solid element mesh (nodes, connectivity, and sets)
**=====
*Instance, name=solid, part=solid
*Node
*Include, Input=SD_NODES.input
*Element, type=C3D8R
*Include, Input=SD_ELEMENTS.input
*Include, Input=SD_GEN_SETS.input
**=====
** Define element orientation and controls
**=====
*orientation, name=cylinder, system=cylindrical
0,0,0,0,0,1
*Solid      Section,      elset=ALL,      orientation=cylinder,      material=DSS,
CONTROLS=SEC_CONTROL
1.,
*End Instance
**=====
** Load shell element mesh (nodes, connectivity, and sets)
**=====
*Instance, name=shell, part=shell
*Node
*Include, Input=SL_NODES.input
*Element, type=S4R
*Include, Input=SL_ELEMENTS.input
*Include, Input=SL_GEN_SETS.input
**=====
** Define element orientation and controls
**=====

```

```

*orientation, name=cylinder, system=cylindrical
0,0,0,0,0,1
*Shell Section, elset=innersur, orientation=cylinder, material=DSS, temperature=3
0.0015, 3
*Shell Section, elset=capinner, orientation=cylinder, material=DSS, temperature=3
0.01, 3
*End Instance
**=====
** Define shell-solid element coupling interface
**=====
*Shell to Solid Coupling, Constraint name=shell2solid
shell.Shell_Bound, solid.Solid_Bound
*End Assembly
**=====
** Define section controls for solid elements
**=====
*SECTION CONTROLS, NAME=SEC_CONTROL, HOURGLASS=RELAX STIFFNESS,max
degradation=1,element deletion=yes
1., 1., 1.
**=====
** Define material properties (Load from file)
**=====
*Include, Input=DSS_1x1xpt5mm_C3D8R_Celcius.txt
**=====
** Define initial temperature, BC's, and smooth step amp.
**=====
*initial conditions, type=temperature
shell.all, 30.0,30.0,30.0
*initial conditions, type=temperature
solid.all, 30.0
**
*Boundary
shell.ring, 1, 3
**
*Amplitude, name=ramp,definition=smooth step
0.0,0.0,1.0,1.0
**=====
** Define pressurization with smooth step load increase
**=====
*STEP, NAME=Pressurize, NLGEOM=YES, Amplitude=STEP
**
*DYNAMIC, EXPLICIT
,1.0
*fixed mass scaling, elset=solid.all,factor=1000
*fixed mass scaling, elset=shell.all,factor=1000
**
*Dload, amplitude=ramp
**
solid.innersur, P6, 1880890
shell.innersur, P, 1880890
shell.capinner, P, 1880890
, GRAV, 9.81, 0.0, 0.0, -1.0
**
*RESTART, WRITE, OVERLAY
**
*OUTPUT, FIELD, NUMBER INTERVAL=10
*Node Output
U, RF, A, V
**
*ELEMENT OUTPUT
STATUS,SDEG,temp,S,LE,peeq,DMICRT,P,Triax
*Output, history,variable=preselect, TIME INTERVAL=0.1

```

```

*energy output, variable=all
*energy output, variable=all, elset=solid.emonitor
*energy output, variable=all, elset=solid.center
*element output, elset=solid.center
SDEG,DMICRT
*End Step
**=====
** Apply heating
**=====
*STEP, NAME=Thermech-1, NLGEOM=YES
** Hold load and heat up pressure vessel
*DYNAMIC, EXPLICIT
,2.0
**
*TEMPERATURE, FILE=cylinder_heat, bstep=1,estep=2, binc=1, einc=10
**
*Dload
solid.innersur, P6NU
shell.innersur, P, 1880890
shell.capinner, P, 1880890
, GRAV, 9.81, 0.0, 0.0, -1.0
**
*RESTART, WRITE, OVERLAY
**
*OUTPUT, FIELD, NUMBER INTERVAL=20
*Node Output
U, RF, A, V
**
*ELEMENT OUTPUT
STATUS,SDEG,temp,S,LE,peeq,DMICRT,Triax
*Output, history,variable=preselect, TIME INTERVAL=0.001
*energy output, variable=all
*energy output, variable=all, elset=solid.emonitor
*energy output, variable=all, elset=solid.center
*element output, elset=solid.center
SDEG,DMICRT
*End Step

```